Directed self-assembly strategies for orientation-controlled block copolymers for advanced lithography.

Cindy Gomes Correia

université de BORDEAUX

THÈSE PRÉSENTÉE

POUR OBTENIR LE GRADE DE

DOCTEUR DE

L'UNIVERSITÉ DE BORDEAUX

ÉCOLE DOCTORALE des Sciences Chimiques

SPÉCIALITÉ : Polymères

Par Cindy GOMES CORREIA

DIRECTED SELF-ASSEMBLY STRATEGIES FOR ORIENTATION-CONTROLLED BLOCK COPOLYMERS IN ADVANCED LITHOGRAPHY

-

STRATÉGIES D'AUTO-ASSEMBLAGE DIRIGÉ POUR LE CONTRÔLE DE L'ORIENTATION DE DOMAINES DE COPOLYMÈRES À BLOCS EN LITHOGRAPHIE AVANCÉE

Sous la direction de Guillaume FLEURY et Christophe NAVARRO

Soutenue le 13 décembre 2019

Membres du jury :

Mme MARCELLAN Alba, Maître de Conférences, ESPCI - Paris	Rapportrice
M. ILIOPOULOS Ilias, Directeur de Recherche, Laboratoire PIMM, ENSAM - Paris	Rapporteur
Mme PONSINET Virginie, Directrice de Recherche, CRPP - Bordeaux	Présidente du jury
M. HADZIIOANNOU Georges, Professeur, Université de Bordeaux	Examinateur
M. CHEVALIER Xavier, Ingénieur de Recherche, Arkema	Invité
M. FLEURY Guillaume, Maître de Conférences, Université de Bordeaux	Directeur de thèse
M. NAVARRO Christophe, Ingénieur de Recherche, Arkema	Directeur de thèse

Remerciements

Tout d'abord, je tiens à remercier toutes les personnes sans qui je n'aurais jamais pu réaliser et défendre cette thèse.

Mes premières pensées vont au Professeur HADZIIOANNOU qui dirige l'équipe 4 du LCPO - Polymers Electronic Materials & Devices – et qui m'a permis d'effectuer ma thèse au B8 dans un environnement que tout doctorant rêverait d'avoir je pense ; que ce soit en termes d'infrastructures, équipements, instruments ou encore produits chimiques ! C'était un honneur de travailler dans votre équipe, de vous avoir eu dans mon jury et d'avoir pu interagir avec vous pendant ces trois ans. Je regrette de ne pas avoir toqué à votre porte plus souvent mais, je dois l'avouer, j'étais et serai toujours très (trop ?) impressionnée !

Je voudrais également remercier mes directeurs de thèse, Guillaume FLEURY et Christophe NAVARRO.

Guillaume, ces trois ans n'auront pas été un long fleuve tranquille. Je me souviendrai toujours de la fois où tu m'as dit que « pendant ces trois ans, nous serions presque comme un couple ! », et bien oui ce n'est pas tout à fait faux : il y a eu des hauts et des bas, des tensions, de la frustration, même des pleurs ! mais aussi beaucoup de joie et surtout, j'ai toujours pu compter sur toi dans les moments difficiles et cela jusqu'à la dernière minute ! C'est avec la gorge nouée que j'écris ces quelques lignes, qui ne sauront jamais assez te remercier. Je suis fière d'avoir été ta première doctorante et de ce qu'on a fait.

Christophe, je voudrais également vous remercier. Vous remercier de m'avoir accueillie au début de la thèse à Lacq, vous remercier également pour cette opportunité de faire ces deux séjours au CEA à Grenoble : tout cela m'a fait me sentir totalement intégrée dans l'équipe DSA ! Même loin, vous avez toujours gardé un œil sur moi notamment grâce à ces rapports mensuels qui me semblaient contraignants au début, mais qui se sont révélés très utiles lors de la rédaction

(et vous me l'aviez dit !). Je voulais également vous remercier pour vos conseils et votre bienveillance !

Je voudrais remercier mes encadrants officieux : Xavier CHEVALIER et Marc ZELSMANN.

Xavier, Xavier, Xavier ! Je n'oublierai jamais ce premier séjour au CEA qui a clairement marqué un moment fort à la fois dans mon travail de thèse et personnellement. On m'avait briefé au début : « ne t'inquiète pas, il est un peu particulier », « il n'est jamais satisfait mais faudra pas le prendre personnellement », « il râle souvent !». Alors c'est vrai que tu es quelqu'un d'unique ! Tu es très exigeant c'est vrai, mais c'est ce qui permet d'avancer et de repousser ses limites, oui tu râles (ou plutôt tu t'exprimes !) mais en fait t'es un vrai gentil. T'es une belle personne, tu n'es jamais méchant, toujours bienveillant et tu es de très bons conseils. Je suis très heureuse de t'avoir rencontré, d'avoir travaillé avec toi et je suis aussi très émue que tout cela s'arrête. J'espère vraiment que l'on gardera contact au-delà même du boulot.

Marc, merci de m'avoir accueillie pendant mes passages à Grenoble. Ton sourire et ta bonne humeur m'auront donné du baume au cœur. Merci également pour les discussions scientifiques toujours très enrichissantes et qui ont permis, à certains moments, de recentrer le débat sur les fondamentaux pour ces travaux à vocation industrielle.

Avant de remercier les personnes que j'ai côtoyé quotidiennement au laboratoire, je voudrais remercier les membres de mon jury pour avoir accepté d'évaluer mes travaux de thèse. Merci également d'être venu malgré les grèves et la tempête. Je voudrais également vous remercier pour la qualité de vos questions et remarques qui ont permis une discussion très enrichissante.

Je voudrais maintenant remercier les personnes grâce à qui j'ai été heureuse de me lever chaque matin pour venir travailler. Je tiens à remercier toutes les personnes du LCPO, et tout particulièrement B8. C'était vraiment un régal ces trois ans avec vous que ce soit pendant les pauses café, au labo, en salle blanche, à ElorPrinttec, pendant nos voyages et toutes nos sorties ! Je n'oublierai jamais tous ces moments et je suis vraiment contente de vous avoir rencontré.
Je crois qu'on est presque devenu une famille pour les plus anciens (Ségogo, Flo, Nicoo, Riiiim, KK, Ari, Alberto, Tommaso, Quentin) et pense qu'on est partis pour durer !

Je voudrais également remercier tous ceux que j'ai rencontré pendant ces trois ans avec une mention spéciale pour Solène : tu sais tout le bien que je pense de toi, t'es quelqu'un de super avec la main sur le cœur et je sais que tu feras une SU-PER thèse ! Petite pensée pour mon bureau : Ali, Nils, Naser, Lorenzo et Emin, merci de m'avoir supportée quand je me parlais à moi-même, quand je chantais et avec mon foutoir !^^ Je voudrais remercier les autres B8ers : Lauriane, Yanid, Camille, Micah, Silvia, Pane, Cian, Florent, Jérémy, Geoffrey, Pino, Antoine, Anirudh, Shekhar, Eunkyung, Alexander, Roland, Eleni, Mélanie, Aude, Ellena, Cyril, Eric, Sokha, Wiljan & Guillaume. Sans oublier aussi : Fio, Chris, Boris, Martin, Pauline, Quentin S., David, Anne & Cédric.

Je voudrais également remercier ceux qui m'ont formée à mon arrivée : Karim, qui a été mon encadrant en début de thèse - Pierre, avec qui j'ai fais mes premiers pas en salle blanche – Gillou, qui m'a formée sur l'AFM. Je voudrais également remercier les chimistes qui m'ont synthétisé de superbes polymères : Mumtaz et Benjamin -côté LCPO- Mumu et Célia -côté Arkema-.

J'ai également une pensée pour ceux que j'ai rencontré pendant mon passage au CEA : Philou, Gillou, Matthieu, Gwen et Vincent 😊

Petite pensée pour la team #*Shining Blue* !

Pour finir, je voudrais remercier ceux qui partagent ma vie depuis un moment déjà : Aurélie, Cha, Jess, J-T, Séb, Guigui, Bitch, Kim & Augustin.

Mon dernier mot sera pour la personne la plus importante de ma vie : **ma petite mère** 💔

Ce n'est pas la couleur de notre peau qui nous rend différent
c'est la couleur de nos pensées

Titre et résumé en français :

Stratégies d'auto-assemblage dirigé pour le contrôle de l'orientation de domaines de copolymères à blocs en lithographie avancée.

L'auto-assemblage de copolymères à blocs (CPBs) permet de générer des structures complexes avec des périodicités allant de quelques nanomètres à des centaines de nanomètres. Cet auto-assemblage est liée à l'incompatibilité thermodynamique entre les blocs de nature chimique différente ce qui est matérialisé par le paramètre d'interaction de Flory-Huggins, χ. Un fort degré d'incompatibilité entre les blocs va se traduire par une micro-séparation de phase des chaînes polymères en une panoplie de nanostructures. En particulier, les copolymères diblocs ont la capacité de s'auto-assembler en sphères, cylindres, gyroïdes ou encore lamelles. Grâce à cette habilité à former des réseaux denses et réguliers avec de petites dimensions, les CPBs peuvent être utilisés en tant que masques lithographiques pour l'industrie de la microélectronique.

Actuellement, des techniques de nano-fabrications permettent déjà de produire des objets à une si petite échelle. Les techniques de lithographies optiques conventionnelles ont été les premières technologies développées pour produire des objets à l'échelle nanométrique mais les dimensions accessibles restent limitées par la diffraction du faisceau. D'autres techniques, telles que la lithographie par immersion, la lithographie extrême ultra-violet, la lithographie par faisceau d'électrons ou encore la nanoimpression, ont ainsi été étudiées pour réduire ces dimensions. Cependant, leur coût et/ou leur défectivité limitent considérablement leur développement industriel à grande échelle. C'est pourquoi, l'industrie de la microélectronique envisage aujourd'hui de nouvelles façons de fabriquer des objets discrets, à l'échelle nanométrique, parfaitement organisés dans un réseau dense. L'utilisation de films CPBs auto-assemblés comme masques permettrait d'accéder aux dimensions caractéristiques de l'ordre du nanomètres (c.-à-d. aux dimensions caractéristiques des chaînes polymères). Par exemple, il serait possible d'obtenir un réseau de lignes parallèles à partir de lamelles perpendiculaires ou

encore, de cylindres parallèles ou un réseau de points hexagonal/carré à partir de cylindres perpendiculaires ou de sphères.

Le développement de cette approche requiert la formation de structures périodiques bien ordonnées en configuration de film mince. En effet, les dissimilarités chimiques entre les domaines permettent l'élimination sélective par plasma ou gravure humide de l'un des nanodomaines conduisant à un masque qui peut ensuite être utilisé pour définir les composants spécifiques à l'application microélectronique envisagée. Cependant, une structure polygrain avec un ordre à courte portée est généralement observée en film mince en raison de la cinétique lente de grossissement de grain. C'est pourquoi, les scientifiques ont développé des méthodes dites d'auto-assemblage dirigé (DSA) pour contrôler l'alignement et l'orientation des domaines par l'annihilation des défauts en limite de grains.

Dans ce contexte, un consortium français a été créé afin de fournir (i) des systèmes CPBs pour atteindre les nanostructures avec des périodicités en dessous de 20 nm, (ii) une compréhension de l'auto-assemblage des CPBs et (iii) des stratégies d'intégration des CPBs dans l'industrie de la microélectronique. Ce consortium réunit le Laboratoire de Chimie des Polymères Organiques (LCPO) et Arkema pour la synthèse de polymères en laboratoire et à l'échelle pilote, ainsi que le Laboratoire des Technologies de la Microélectronique (LTM) et le CEA-Leti pour la définition des procédés d'auto-assemblage compatible avec les pistes lithographiques.

Dans le cadre de ce consortium, le LCPO a mis au point une première génération de copolymères diblocs : le poly(styrène)-*b*-poly(méthacrylate de méthyle). Cette technologie mature a permis de définir des nanostructures avec des périodicités pouvant aller jusqu'à 22 nm. Pour diminuer encore d'avantage la dimension des nanostructures, il faut travailler avec des CPBs ayant un paramètre χ supérieur au PS-*b*-PMMA (0,03 à température ambiante). C'est pourquoi, le LCPO a développé un système CPB à base de polycarbosilane, le poly(1,1-diméthylsilacyclobutane)-*b*-poly(styrène) (PDMSB-*b*-PS), afin de répondre aux exigences de DSA. Ce projet de doctorat a donc

été consacré à l'auto-assemblage du PDMSB-*b*-PS pour des applications en nanolithographie avancée.

Dans un premier chapitre expérimental, nous avons étudié l'auto-assemblage du PDMSB-*b*-PS (voir Figure 1) en masse et en film mince pour démontrer la capacité de ce système à former des nanostructures bien définies avec des dimensions caractéristiques en dessous de 20 nm.

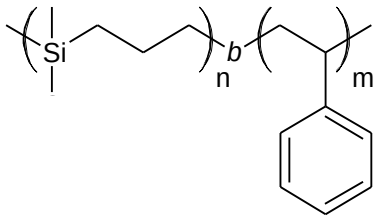

Figure 1 : Structure du PDMSB-*b*-PS.

Ce système a été développé car le bloc semi-cristallin contenant l'atome de silicium va permettre d'apporter un contraste chimique entre les deux blocs de façon à augmenter leur degré d'incompatibilité et ainsi obtenir un paramètre χ plus élevé que celui du système de référence, PS-*b*-PMMA. De plus, ce bloc inorganique fournira un contraste de gravure entre les domaines pour le retrait sélectif du PS et ainsi obtenir un masque de PDMSB oxydé qui sera suffisamment robuste pour permettre le transfert du motif du masque dans le substrat sous-jacent.

Une série de PDMSB-*b*-PS a été synthétisée par polymérisation anionique séquentielle du 1,1-diméthylsilacyclobutane et du styrène avec des masse moléculaire et fraction volumique variées de façon à obtenir une panoplie de structures comme le montre le tableau 1.

Tableau 1 : **Caractéristiques macromoléculaires des PDMSB-*b*-PS synthétisés.**

Polymères	M_n (g.mol^{-1})[a]	f_{PDMSB}[b]	N[c]	N_{Flory}[d]	$T_{g,PS}$ (°C)[e]	$T_{g,PDMSB}$ (°C)[f]	Structure[g]	*d* (nm)[h]
PDMSB$_{79}$-*b*-PS$_{76}$	9850	0.57	98	155	62	- 65	Lam	13
PDMSB$_{84}$-*b*-PS$_{123}$	13600	0.45	133	207	83	- 65	Lam	15.4
PDMSB$_{94}$-*b*-PS$_{125}$	14350	0.47	140	219	83	- 64	Lam	15.5
PDMSB$_{120}$-*b*-PS$_{143}$	17140	0.5	168	263	88	- 62	Lam	18.2
PDMSB$_{165}$-*b*-PS$_{195}$	23000	0.51	230	360	89	- 60	Lam	-
PDMSB$_{74}$-*b*-PS$_{224}$	19350	0.29	193	298	94	-73	Cyl	18.5
PDMSB$_{79}$-*b*-PS$_{251}$	21500	0.28	215	331	96	-74	Cyl	19.6
PDMSB$_{102}$-*b*-PS$_{245}$	22500	0.34	225	348	92	-71	Cyl	19.7
PDMSB$_{104}$-*b*-PS$_{330}$	28200	0.28	282	434	84	-77	Cyl	24.3
PDMSB$_{200}$-*b*-PS$_{636}$	54400	0.28	543	837	102	-74	Cyl	33.8
PDMSB$_{207}$-*b*-PS$_{906}$	72700	0.22	726	1114	101	-78	Cyl	-
PDMSB$_{54}$-*b*-PS$_{124}$	11500	0.35	115	178	83	-71	Gyr	15.8

a : Masse moléculaire déterminée par chromatographie d'exclusion stérique en utilisant les PS standards
b : Fraction volumique en PDMSB déterminée par résonance magnétique nucléaire du proton
c : Degré de polymérisation du CPB
d : Degré de polymérisation du CPB déterminé à partir du volume de référence, v_0 = 118 Å^3.
e & f: T_gs déterminés lors du second cycle de chauffe entre −160 et 150°C à 10°C.min^{-1}.
g : Structure des polymères déterminée par diffusion des rayons X aux petits angles.
h: Dimension caractéristique des structures formées déterminé à partir du pic de diffraction de 1er ordre.

La structure de ces polymères ainsi que leur dimension caractéristique ont été confirmées par diffusion des rayons X aux petits angles. Ainsi, des structures bien définies avec des dimensions pouvant descendre jusqu'à 13 nm ont été obtenues, ce qui démontre l'intérêt du PDMSB-*b*-PS à supplanter le PS-*b*-PMMA.

Pour compléter l'étude du PDMSB-*b*-PS en masse, nous avons déterminé le paramètre χ du système à l'aide des CPBs formant des lamelles. Ce paramètre a été estimé à 0,13 ± 0,06 à température ambiante. Cette valeur est quatre fois supérieure à celle du PS-*b*-PMMA ($\chi_{PS\text{-}b\text{-}PMMA}$ = 0,03 à température ambiante) ce qui confirme l'intérêt d'une utilisation du PDMSB-*b*-PS pour la définition de structures de moins de 20 nm de périodicité.

Dans un second temps, nous avons réalisé l'auto-assemblage du PDMSB-*b*-PS en film mince pour obtenir une nanostructuration du système en cylindre et gyroïde en utilisant un procédé compatible avec les prérequis industriels.

L'auto-assemblage des PDMSB-*b*-PS formant des cylindres a été réalisé en couches mince grâce à un recuit thermique. Nous avons étudié certains des paramètres qui ont été reportés dans la littérature pour la formation de nanostructures bien définies à savoir le temps du recuit thermique et la variation de l'épaisseur du film de CPB. Pour une épaisseur de film commensurable avec la période du CPB, il est possible d'obtenir un film plat de cylindres de PDMSB parallèles au substrat et avec une amélioration de l'organisation des domaines avec le temps de recuit (figure 2).

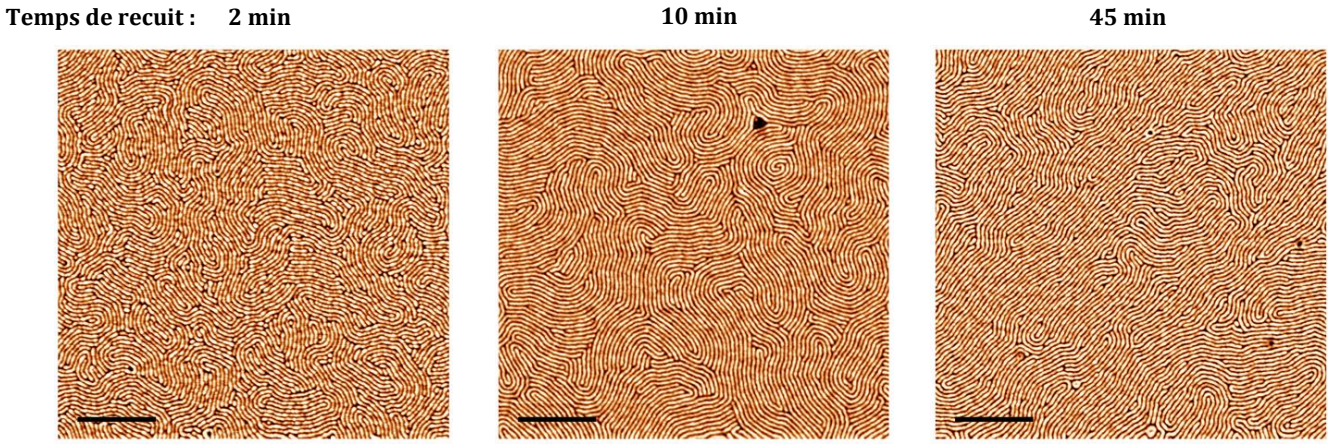

Figure 2 : Auto-assemblage du PDMSB$_{74}$-*b*-PS$_{224}$ en couche mince. Images topographiques obtenues par microscopie à force atomique (2 µm x 2 µm) d'un film de 42 nm d'épaisseur recuit pendant 2, 10 et 45 min à 180°C.

Dans le cas de ce système semi-cristallin, nous avons également mis en évidence l'effet de la cristallinité sur l'orientation des cylindres dans le film. En effet, en jouant sur la température de fusion du bloc PDMSB au regard de la température ambiante, il est possible de compenser les effets interfaciaux (thermodynamique) avec une cristallisation rapide du PDMSB pour piéger cinétiquement l'orientation perpendiculaire des cylindres. Par conséquent, il a été possible d'obtenir des cylindres perpendiculaires bien définis quel que soit l'épaisseur de film sans utiliser de sous-couches neutres comme le montre la figure 3.

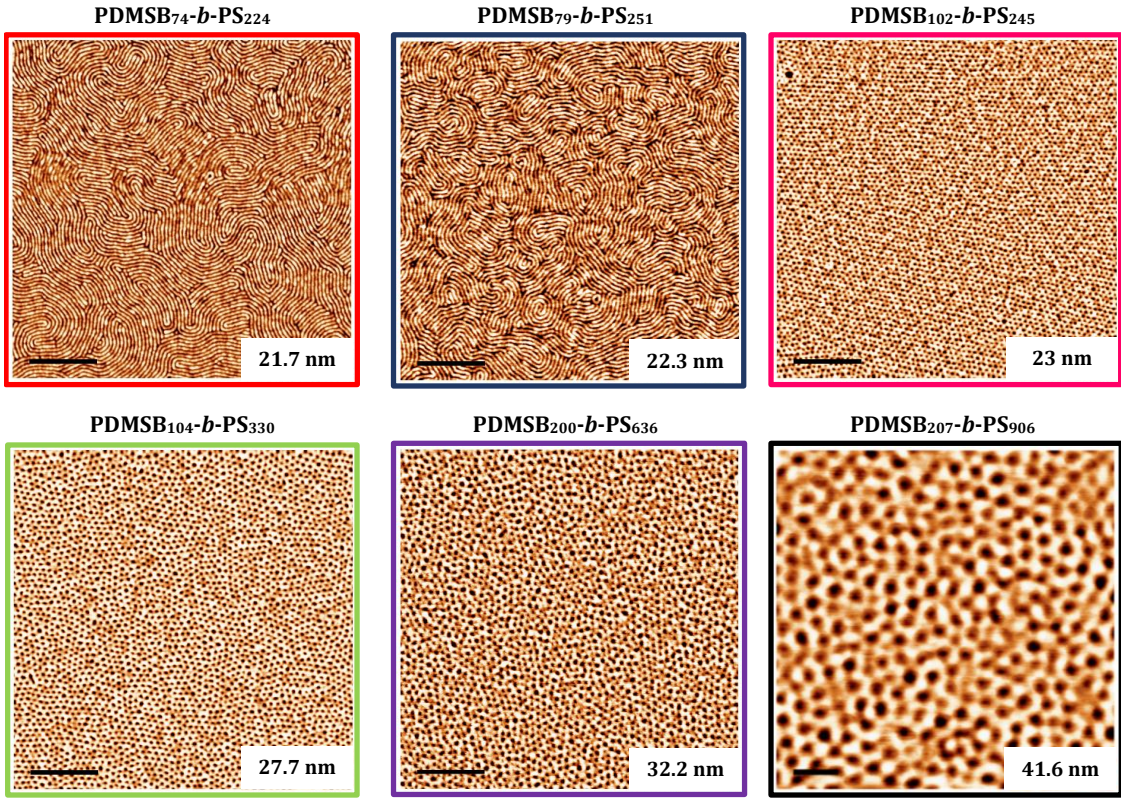

Figure 3 : Images topographiques par microscopie à force atomique des PDMSB-*b*-PS auto-assemblés formant des cylindres avec une masse moléculaire croissante. Échelle : 200 nm sauf pour le $PDMSB_{207}$-*b*-PS_{906} pour lequel la barre d'échelle est de 100 nm.

Après avoir étudié l'auto-assemblage du PDMSB-*b*-PS en cylindres, nous nous sommes intéressés à la phase gyroïde. Cette phase est une structure tridimensionnelle qui se distingue des autres structures par sa bicontinuité. En effet, elle consiste en deux réseaux continus d'un bloc minoritaire dans une matrice du bloc majoritaire dit double gyroïde (DG). Bien que de nombreuses études aient été réalisées sur le comportement de cette phase en masse, il n'existe que très peu d'études sur la DG en film mince car (i) elle se situe dans une fenêtre étroite du diagramme de phase ce qui rend la synthèse d'un CPB avec les caractéristiques macromoléculaires requises fastidieuse (ii) cette structure 3D est très difficile à stabiliser en film mince.

Nous avons démontré que la stabilisation d'une structure gyroïde du $PDMSB_{54}$-*b*-PS_{124} en film mince était possible dans une fenêtre étroite de procédé d'auto-assemblage comme le montre la figure 4. En effet, il faut que l'épaisseur du film soit au moins trois fois supérieure à la dimension de la cellule unité pour pouvoir développer la phase DG. De plus, il faut que l'énergie thermique

apporté par le recuit soit suffisante pour permettre la nucléation et croissance du nucléus. Cependant, cette température de recuit ne doit pas excéder une valeur seuil (180°C) au-delà de laquelle il y a transition de la DG vers une structure cylindrique. Grâce à ces conditions opératoires compatible l'échelle industrielle, nous avons obtenu une structuration en film mince du $PDMSB_{54}$-*b*-PS_{124} en DG avec un plan (211) parallèle à l'interface air/film. La dimension de la cellule unité, a_G = 35 nm, a été déterminée par SAXS et la structure et son orientation ont été confirmées par analyse GISAXS.

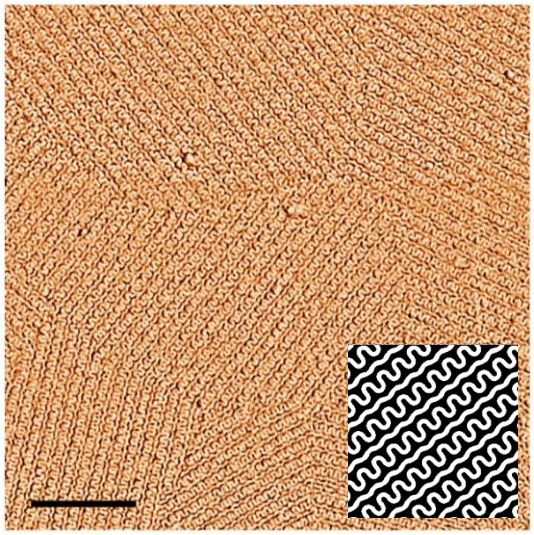

Figure 4 : Image obtenue par microscopie à force atomique du $PDMSB_{54}$-*b*-PS_{124} formant une phase DG avec un plan (211) parallèle à l'interface air/film. Échelle : 400 nm.

Dans un second chapitre expérimental, nous nous intéressés à l'obtention de lamelles perpendiculaires du PDMSB-*b*-PS en film mince. En effet, cette structure est la plus attrayante pour l'industrie des semi-conducteurs grâce à sa capacité à former des masques lithographiques de lignes parallèles. Cependant, une orientation parallèle des lamelles est généralement obtenue à cause de la différence d'énergie de surface importante entre les blocs PDMSB et PS (γ_{PS} = 43,5 $mN.m^{-1}$ et γ_{PDMSB}= 27,3 $mN.m^{-1}$). Pour surmonter cette problématique, nous avons donc développé un matériau réticulable qui, une fois déposé sur le film CPB, permettra un contrôle de l'énergie de surface à l'interface supérieure du film de façon à obtenir des lamelles de PDMSB-*b*-PS perpendiculaires. De plus, cette couche réticulée permet de maintenir mécaniquement le film CPB

pendant l'étape de recuit ce qui évite les problèmes de démouillage qui nuisent à l'homogénéité du film.

Ce matériau est un terpolymère composé de (i) méthacrylate hydroxylé pour permettre la solubilité du polymère dans les solvants polaires ce qui permettra son dépôt sur le film CPB sans le détériorer, (ii) méthacrylate de 2,2,2-trifluoroéthyle de façon à contrôler l'énergie de surface du polymère pour neutraliser les interactions préférentielles des blocs PDMSB et PS pour l'interface supérieure et (iii) méthacrylate de 2,3-époxypropyle pour permettre la réticulation du polymère (structure du polymère figure 5).

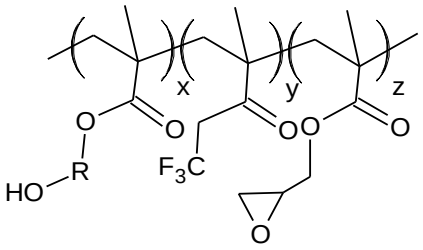

Figure 5 : Structure du terpolymère développé pour neutraliser les interactions préférentielles des blocs PDMSB et PS pour l'interface supérieure et ainsi obtenir des lamelles perpendiculaires.

Nous avons démontré la réticulation du polymère à l'aide d'un agent de réticulation thermique qui permet une réticulation rapide du matériau en 3 min. Cette couche réticulée a également été utilisée pour effectuer l'auto-assemblage du $PDMSB_{120}$-*b*-PS_{143} en film mince ce qui a conduit à l'obtention d'un film homogène non démouillé de lamelles perpendiculaires avec une périodicité de 17,2 nm comme le montre la figure 6.

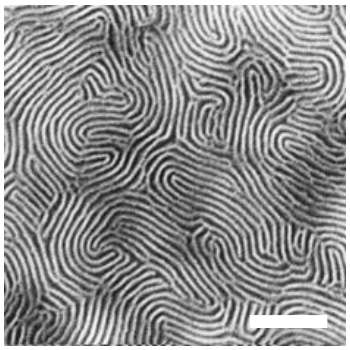

Figure 6 : Caractérisation par microscopie électronique à balayage du $PDMSB_{120}$-*b*-PS_{143} auto-assemblé en lamelles perpendiculaires avec 17,2 nm de périodicité. Échelle : 200 nm.

Ces résultats ont été étendus à deux autres systèmes PDMSB-*b*-PS ce qui a permis d'obtenir des films de lamelles perpendiculaires avec des périodicités de 14,6 nm et 22,7 nm comme le montre la figure 7.

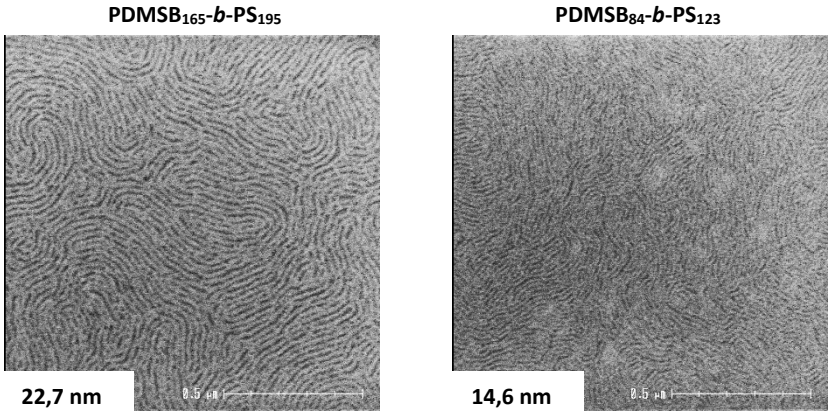

Figure 7 : Caractérisation par microscopie électronique à balayage des PDMSB$_{165}$-*b*-PS$_{195}$ et PDMSB$_{84}$-*b*-PS$_{123}$ auto-assemblés en lamelles perpendiculaires avec 22,7 nm et 14,6 nm de périodicité.

Grâce à la capacité de réticulation du matériau, il est possible d'utiliser le polymère réticulé en tant que nouveau substrat pour l'empilement d'une seconde couche de PDMSB-*b*-PS. De plus, en contrôlant l'énergie de surface du matériau réticulé aux interfaces inférieure et supérieure du film CPB, il est possible de contrôler l'orientation de chacune des couches de manière indépendante. Ainsi, nous avons réalisé l'empilement de lamelles parallèles du PDMSB$_{220}$-*b*-PS$_{238}$ sur des lamelles perpendiculaires du PDMSB$_{120}$-*b*-PS$_{143}$ comme le montre la figure 8.

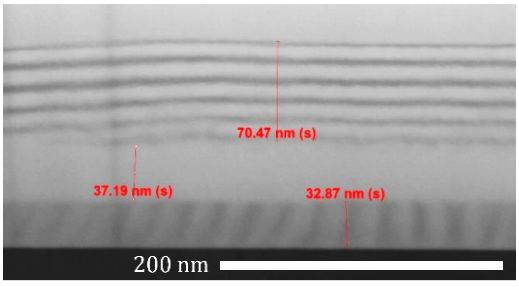

Figure 8 : Caractérisation par FIB-STEM de l'empilement de PDMSB$_{220}$-*b*-PS$_{238}$ (1ère couche) et PDMSB$_{120}$-*b*-PS$_{143}$ (2nd couche).

Finalement, dans un dernier chapitre expérimental, nous avons étendu le potentiel offert par ces sur-couches réticulables en obtenant un motif par photolithographie du matériau afin de guider l'auto-assemblage du CPB lamellaire à des zones spécifiques du film. Pour cela, nous avons

démontré la capacité des sur-couches à être photo-réticulée grâce à différents agents réticulant photosensibles. Trois stratégies ont été étudiées pour photo-réticuler la sur-couche dans l'UV profond et dans le visible. Nous avons comparé et optimisé l'efficacité de la réticulation du matériau avec divers agents de réticulation photosensibles pour obtenir des films entièrement réticulés après 2 min et 1 s d'exposition aux irradiations UV visible et UV profond, respectivement. Nous avons ensuite réalisé la lithographie de la sur-couche au-dessus du film de PDMSB$_{120}$-*b*-PS$_{143}$ ce qui a permis de contrôler l'orientation des lamelles dans des zones spécifiques du film avec une bonne résolution (figure 9).

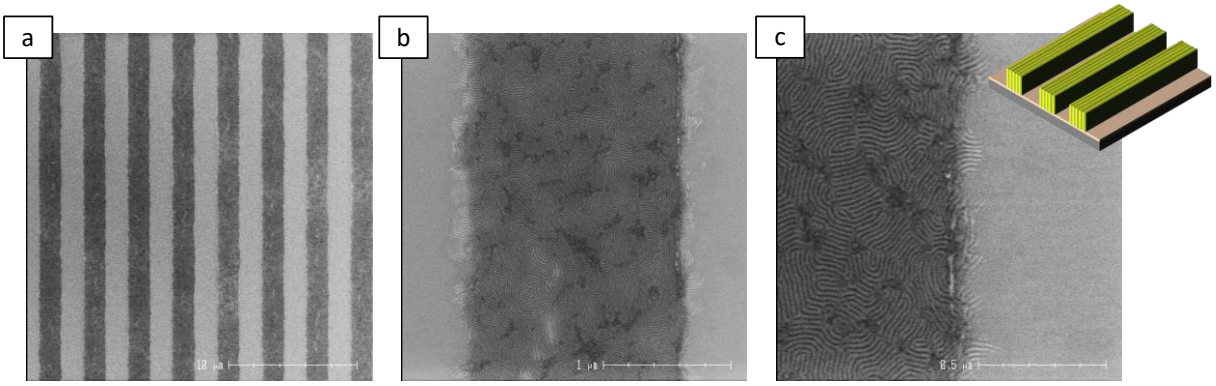

Figure 9 : Caractérisation par microscopie électronique à balayage du film de PDMSB$_{120}$-*b*-PS$_{143}$ obtenu après avoir effectué la lithographie de la sur-couche neutre. (a), (b) et (c) sont trois grossissements différents.

Au cours de ces travaux, nous avons fourni une compréhension du comportement d'auto-assemblage du PDMSB-*b*-PS en masse et en film mince. Nous avons mis en évidence le potentiel de ce copolymère semi-cristallin à former des nanostructures périodiques bien définies avec des périodicités inférieures à 20 nm grâce à un paramètre d'interaction de Flory-Huggins élevé (Chapitre 2). Nous avons par la suite proposé une approche pour obtenir des lamelles perpendiculaires du PDMSB-*b*-PS en film mince grâce à l'utilisation de sur-couches neutres réticulables. La polyvalence de cette approche a été démontrée à l'aide de CPBs de masses moléculaires différentes et s'est ensuite étendue à la formation d'empilements *via* un processus d'auto-assemblage itératif (chapitre 3). Enfin, nous avons réticulé la sur-couche neutre à l'aide d'agents photo-sensibles ce qui nous a permis d'obtenir un motif par lithographie. Ainsi, il a été possible de contrôler l'orientation du CPB à des endroits spécifiques du film.

Table of contents

General Introduction

Block copolymer (BCP) self-assembly is an elegant tool to generate complex periodic structures with exquisite symmetries. The driving force inherent to BCP phase behaviour is related to the thermodynamic incompatibility between the two or more chemically distinct building blocks allowing BCP chains to microphase-separate into a panoply of well-ordered nanostructures with periodicities ranging from a few nanometers to hundreds of nanometers. Innovative polymerization methods capable of generating on-demand BCP architectures associated to the conceptual framework of self-consistent field theory (SCFT) enable the rationalization of the rich bulk phase behaviour of BCPs over the last decades, with, for the simplest di-BCP phase diagram, a progression of morphologies from spheres arranged into a body-centered cubic lattice, hexagonally-packed cylinders, double gyroid, and lamellae. As virtually any combination of chemistry and sequencing is attainable by macromolecular design, BCPs offer tremendous opportunities for the design of functional materials with applications in biology, separation process and nanolithography among others.

Lithography (from the Greek words “lithos” meaning stone and “graphein” meaning to write) primarily refers to a printing technique that allows the creation and production of multiple copies of a drawing executed on a stone. Nowadays, this concept of lithography – specifically, nanolithography - evolved to describe more generally the design of nanometric structures and has become a fundamental technological requirement for semiconductor device fabrication. Indeed, the constant demand for data storage and performance capacity of electronic devices requires the miniaturisation of the components in order to increase their density within the devices, increasing thus the performance of the integrated circuits while reducing their manufacturing costs. As lithography is the step allowing the definition of the patterns, it is through this stage that it is possible to reduce the dimensions and thus to increase the density of the components on a given chip. This miniaturisation of electronic components was predicted by Moore’s law and is now one of the major challenges of the microelectronics industry. The development of lithography

techniques thus follows a precise timetable governed by the International Technology Roadmap for Semiconductors (ITRS). It describes the expected progression of technological nodes over the years as well as the corresponding transistor[1] grids width (pattern width). In addition, a lithography technique envisaged for the production of integrated circuits is associated with each technological node.

Optical lithography techniques were the first technologies developed in order to answer the ITRS roadmap but the accessible dimensions remain limited due to diffraction issues. Other techniques, such as immersion lithography, extreme ultraviolet lithography, electron-beam lithography or nanoimprint have thus been investigated to reduce these dimensions. These, so-called, "top-down" approaches have allowed to reach feature size down to 22 nm, but their expensive costs and/or defectivity severely limit their potential for industrial development on a large scale. On the other hand, the use of self-assembled BCP films as masks ("bottom-up" approach) would allow to access characteristic dimensions in the order of tenth of nanometres (i.e. characteristic dimensions of polymer chains). In this case, the ordered self-assembled nanopatterns could be used as lithographic masks for parallel line arrays (from perpendicular lamellae or parallel cylindrical structures) or hexagonal/square dot arrays (from perpendicular cylindrical or spherical structures, respectively).

Further opportunities in the development of BCP nanotechnologies are thus linked to the formation of well-ordered periodic nanoscale patterns in thin film configuration. Indeed, the chemical dissimilarities between the domains allow selective removal by plasma or wet etching of one of the BCP domains leading to a mask that can be subsequently used to define features in microelectronic applications. The formation of self-assembled patterns in thin film can also be combined with hybridization methods (i.e. sequential infiltration synthesis, inclusion of nanoparticles, electro- deposition or replication, lift-off process, aqueous metal reduction, sol-gel chemistry, etc.), thus converting the BCP patterns into functional structured surfaces such as bit-

[1] the transistor being the fundamental component of electronic devices and logical circuits.

patterned media, filed effect transistors, optical metamaterials or photonic structures. Most of these applications require the precise positioning or registration of the BCP nanostructure arranged within a highly-ordered nanoscale array. However, even if the equilibrium energy state of a BCP morphology would be reached for a uniform array of single-grain BCP features, a polygrain BCP structure is generally observed in thin film due to the prevalence of slow coarsening kinetics over the thermodynamic driving force. This weak thermodynamic driving force pushed scientists to develop directed self-assembly (DSA) methods providing means to control the domain alignment and orientation occurring through defect annihilation at grain boundaries. For instance, significant progresses were achieved in the DSA lithography by the synergistic combination of the "bottom-up" BCP self-assembly with the "top-down" fabrication of guiding patterned templates relying on chemoepitaxy and graphoepitaxy.

For these reasons, several DSA consortiums were organized worldwide including both industry and academia in order to provide (i) block copolymer systems to reach sub-20 nm structures, (ii) an understanding of the block copolymer self-assembly and (iii) strategies for the integration of the block copolymers in the microelectronics industry. In 2010, a European consortium was created to propose an effective integration of the DSA into commercial semi-conductor processes. This consortium involves the Laboratoire de Chimie des Polymères Organiques (LCPO) and Arkema for the synthesis of polymers at laboratory and pilot scales, as well as the Laboratoire des technologies de la Microélectronique (LTM) and the CEA-Leti for the definition of the process flows. In this context, the LCPO developed a polycarbosilane-based block copolymer system in order to fulfil the DSA requirements.

This PhD project was thus dedicated to the self-assembly of polycarbosilane-based block copolymers for nanolithography. The manuscript will be organized as follow:

Chapter 1 will describe the general context of the study. We will discuss the conventional lithography techniques and the limitations that led to the development of alternative methods. We will then introduce the general concept of the self-assembly of block copolymers in bulk and

in thin film as well as their interest for nanolithography. Finally, we will review the various block copolymers systems that were reported in the literature as well as the critical parameters for the integration of these systems in industry.

Chapter 2 will first provide an understanding of the self-assembly behaviour of the poly(1,1-dimethylsilacyclobutane)-*b*-poly(styrene) (PDMSB-*b*-PS) in bulk and in thin film. Using a series of PDMSB-*b*-PS BCPs with different compositions and molecular weights, we demonstrated the ability of the system to segregate into various nanostructures. Moreover, we highlighted the potential of PDMSB-*b*-PS for DSA applications by performing the self-assembly of the polymers in thin film using industrially-friendly processes. Additionally, we performed self-assembly studies on cylinder-forming and gyroid-forming PDMSB-*b*-PS BCPs in order to decipher the critical experimental parameters for the control of their phase separation behaviour in thin films.

Chapter 3 is devoted to the self-assembly of the PDMSB-*b*-PS BCPs into out-of-plane lamellae in thin film. Indeed, this structure is the most attractive for the semi-conductor industry thanks to its capability to form lithographic masks of parallel line arrays. However, the surface energy difference between the PDMSB and PS blocks being important, a parallel orientation of the lamellae is commonly obtained due to interfacial fields. To overcome this thermodynamic issue, we thus developed crosslinkable layers (top-coat) in order to control the surface energy at the top interface for the formation of out-of-plane PDMSB-*b*-PS lamellae. Moreover, this crosslinked layer allows to mechanically maintain the BCP film during the annealing step which avoid detrimental dewetting issues.

Finally, in the last **chapter**, we further extended the possibilities offered by this crosslinkable top-coat, notably by showing its potential in iterative BCP self-assembly. Using UV-sensitive species, we showed that it is possible to photocrosslink this layer, allowing thus the use of conventional lithography techniques for its patterning. Therefore, this layer can act as a

chemical guide to control the orientation of the lamellae-forming PDMSB-*b*-PS at specific locations of the film.

An **Annex** with the description of the techniques used in this study is provided at the end of the manuscript.

List of abbreviations

AFM: Atomic Force Microscopy
AIBN: 1,1'-azobisisobutyronitrile
ARXPS: Angle resolved X-Ray photoelectron spectroscopy
ArF: Argon fluoride
ATMS: Ammonium trifluoromethanesulfonate
ATR-FTIR: Attenuated total reflection-Fourier-transform infrared spectroscopy
BCC: Body Centered Cubic
BCP: Block Copolymer
BSEI: Backscattered electron imaging
CAR: Chemically Amplified Resins
CEA: Commissariat des Energies Atomiques
CPS: Close-Packed Spheres
DG: Double gyroid
DIS: Disordered phase
DMPAP: 2,2-dimethoxy-2-phenylacetophenone
DNQ: Diazonaphthoquinone
DNQ-5: Diazonaphthoquinone where the sulfonate group is in the 5th position
dPi-TS: diphenyl iodonium *p*-toluenesulfonate
dPi-PF$_6$: (4-methylphenyl) [4-(2-methylpropyl) phenyl] iodonium hexafluorophosphate
DPS: Decoupled Plasma Source
dPSPT-OTf: diphenyl (4-(phenylthio)phenyl) sulfonium trifluoromethanesulfonate
DSA: Directed Self-Assembly
DSC: Differential scanning calorimetry
DVB: Divinylbenzene
EdX: Energy-dispersive X-ray
EUV: Extreme ultraviolet
FCO: Face-Centered Orthorhombic
FFT: Fast Fourier Transform
GCIB-XPS: Gas Cluster Ion Beams - X-ray photoelectron spectroscopy
GISAXS: Grazing Incidence Small Angle X-ray Scattering
GMA: Glycidyl methacrylate
H: Hexagonal cylinders
HCP: Hexagonal Close-Packed
HDMS: Hexamethyldisilazane
HEMA: Hydroxyethyl methacrylate
HPMA: Hydroxypropyl methacrylate
ICP: Inductively Coupled Plasma
iCVD: Initiated Chemical Vapour Deposition
IR: Infrared
ISL: Intermediate Segregation Limit
ITRS: International Technology Roadmap for Semiconductors
KrF: Krypton fluoride
L: Lamellae
LCPO: Laboratoire de Chimie des Polymères Organiques
LTM: Laboratoire des technologies de la Microélectronique
MST: Microphase Separation Transition
N.A: Not attributed
NA: Numerical Aperture
ND-Tf: Norbornene dicarboxyimidyl triflate
NIL: Nanoimprint
NMR: Nuclear Magnetic Resonance
O^{70}: Orthorhombic
OBDD: Diamond phase
ODT: Order-Disorder Transition
OWRK: Owens, Wendt, Rabel and Kaelble
P2VP: Poly(2-vinylpyridine)
PAG: Photoacid generator
PBrS-*b*-PMMA: Brominated poly(styrene)-*b*-poly(methyl methacrylate)
PCHE: Poly(cyclohexylethylene)
PCHE-*b*-PMMA: Poly(cyclohexylethylene)-*b*-poly(methyl methacrylate)

PDMS: Poly(1,1-dimethylsiloxane)
PDMSB-*b*-PMMA: Poly(1,1-dimethylsilacyclobutane)-*b*-poly(methyl methacrylate)
PDVB: Poly(divinyl benzene)
PEB: Post-exposure bake
PGMEA: Propylene glycol methyl ether acetate
PHFA: Hexafluoroalcohol polymer
pI: Photoinitiator
PMMA-*b*-PMAPOSS: Poly(methyl methacrylate)-*b*-poly(methyl methacrylate hedral oligomeric silsesquioxane)
POSS: Polyhedral oligomeric silsesquioxane
pS: Photosensitizer
PS-*b*-P2VP: Poly(styrene)-*b*-poly(2-vinylpyridine)
PS-*b*-P4VP: Poly(styrene)-*b*-poly(4-vinylpyridine)
PS-*b*-PB: Poly(styrene)-*b*-poly(butadiene)
PS-*b*-PDMS: Poly(styrene)-*b*-poly(dimethylsiloxane)
PS-*b*-PEI: Partially epoxidized poly(styrene)-*b*-poly(isoprene)
PS-*b*-PEO: Poly(styrene)-*b*-poly(ethylene oxide)
PS-*b*-PI: Poly(isoprene)-*b*-poly(styrene)
PS-*b*-PLA: Poly(styrene)-*b*-poly(D,L-lactide)
PS-*b*-PLGA: Poly(styrene)-*b*-poly(lactide-co-glycolide)
PS-*b*-PMA: Poly(styrene)-*b*-poly(methyl acrylate)
PS-*b*-PMAPOSS: Poly(styrene)-*b*-poly(methyl methacrylate hedral oligomeric silsesquioxane)
PS-*b*-PMMA: Poly(styrene)-*b*-poly(methyl methacrylate)
PS-*b*-PTMC-Me: Poly(styrene)-*b*-poly(methyl 5-methyl-2-oxo-1,3-dioxane-5-carboxylate)
PtBS: Poly(4-*tert*-butylstyrene)
PtBS-*b*-P2VP: Poly(4-*tert*-butylstyrene)-*b*-poly(2-vinylpyridine)
PTMSS: Poly(trimethylsilylstyrene)
PTMSS-*b*-PLA: Poly(trimethylsilylstyrene)-*b*-poly(D,L-lactide)
PVA: Poly(vinyl alcohol)
PVBD-*b*-PDSS: Poly(5-vinyl-1,3-benzodioxole)-*b*-poly(pentamethyldisilylstyrene)
$\boldsymbol{Q_{Ia\bar{3}d}}$: Gyroid phase
$\mathbf{Q_{Im\bar{3}m}}$: Cubic phase
RIE: Reactive Ion Etching
***s*-BuLi:** *sec*-butyllithium
SAM: Self-Assembled Monolayer
SAXS: Small Angle X-ray Scattering
SCFT: Self-Consistent Field Theory
SEC: size-exclusion chromatography
SEI: Secondary Electron Imaging
SEM: Scanning Electron Microscopy
SiN_x: silicon nitride substrate
SOC: Spin-on carbon
SSL: Strong Segregation Limit
SVA: Solvent annealing
SVTA: Solvo-thermal annealing
TA: Thermal annealing
TBI-PFOS: bis-4-*tert* butylphenyl iodonium perfluorooctanesulfonate.
TBI-Tf: bis-4-*tert*-butylphenyl iodonium triflate
TEM: Transmission electron microscopy
THF: Tetrahydrofurane
TMAH: Tetramethylammonium hydroxide
TPO: Diphenyl(2,4,6-trimethylbenzoyl) phosphine oxide
tPS-Br: Triphenylsulfonium bromide
tPS-OTf: Triphenyl sulfonium trifluoromethanesulfonate
TPS-Tf: Triphenylsulfonium triflate
TSMC: Taiwan Semiconductor Manufacturing Company
UL: Underlayer
UV: Ultraviolet
VUV: Vacuum Ultraviolet
WCA: Weakly coordinating anions
WSL: Weak Segregation Limit
wt: weight

List of symbols

Symbol	Symbol name	Unit
A	Entropy contribution of the Flory-Hugging parameter	-
$\mathbf{A_t}$	Area of the C-O peak after exposure for a given time, t	(m^2)
$\mathbf{A_{t=0s}}$	Area of the C-O peak before exposure	(m^2)
$\boldsymbol{a}$	Length of the statistical segment	(m)
$\boldsymbol{a_G}$	Unit-cell dimension	(m)
$\boldsymbol{\alpha}$	Prefactor that depends on the BCP morphology	-
B	Enthalpy contribution of the Flory-Hugging parameter	(K)
β	Prefactor that depends on the BCP morphology	-
$\boldsymbol{C}$	Coulombic term	(J)
γ	Bond rocking (for the vibration peaks assignment)	(m^{-1})
γ	Strain (in the measurement of the elastic modulus)	(%)
$\boldsymbol{\gamma_i}$	Total surface energy of i	($N.m^{-1}$)
$\boldsymbol{\gamma_i^d}$	Dispersive component of the total surface energy of i	($N.m^{-1}$)
$\boldsymbol{\gamma_i^p}$	Polar component of the total surface energy of i	($N.m^{-1}$)
$\boldsymbol{\gamma_{i-j}}$	Interfacial energy between i and j	($N.m^{-1}$)
$\boldsymbol{d}$	Domain spacing	(m)
$\mathbf{\Delta G_{et}}$	Free energy of electron transfer process	(J)
$\mathbf{\Delta G_m}$	Gibbs free energy of mixing	(J)
$\mathbf{\Delta G_m^{ex}}$	Excess of free energy of mixing	(J)
$\mathbf{\Delta H_m}$	Enthalpy of mixing	(J)
$\mathbf{\Delta S_{m,conf}}$	Loss of configurational entropy	($J.K^{-1}$)
$\mathbf{\Delta S_{m,int}}$	Loss of entropy due to the covalent bonding	($J.K^{-1}$)
δ	Bond bending	(m^{-1})
$\boldsymbol{E^*}$	Excitation energy of the sensitizing molecule	(J)
$\boldsymbol{E_{ox}^{1/2}}$	Oxidation half-wave potential	(V)
$\boldsymbol{E_{red}^{1/2}}$	Reduction half-wave potential	(V)
$\boldsymbol{\varepsilon_{XY}}$	Interaction energy between the X and Y repeating units	(J)
$\boldsymbol{F}$	Faraday constant	($C.mol^{-1}$)
$\boldsymbol{F_{el}}$	Entropy contribution per chain	(J)
$\boldsymbol{F_{int}}$	Enthalpy contribution per chain	(J)
$\boldsymbol{f_i}$	Volume fraction of the component *i*	-

G'	Dynamic elastic modulus	(Pa)
H	Hildebrand solubility parameter	($Pa^{1/2}$)
θ	Angular aperture of the lens	(rad)
k_1	Parameter that depends on the resin and the apparatus	-
k_B	Boltzmann constant	($eV.K^{-1}$)
L_0	Natural periodicity of the BCP	(m)
λ_0	Wavelength of the incident source	(m)
λ_{eff}	Effective wavelength	(m)
λ_{max}	Wavelength of the maximum of absorbance	(m)
$\mathbf{M_n}$	Molecular weight	($kg.mol^{-1}$)
ν	Bond stretching	(m^{-1})
ν_0	Reference volume	(m^3)
N	Overall degree of polymerization	-
$\bar{N}$	Finite molecular weight correction to the composition fluctuation	
N_{Flory}	Overall Flory degree of polymerization	-
N_i	Degree of polymerization of the component *i*	-
n	Refractive index of the incident media	-
PDI	Dispersity	-
q	Wavevector	(m^{-1})
q^*	Wavevector of the first order peak	(m^{-1})
R	Resolution of the pattern in lithography in Rayleigh's law	(m)
R	Size of the domain	(m)
R^*	Theoretical period	(m)
R_G	Gyration radius	(m)
$\mathbf{T}$	Temperature	(K)/(°C)
$\mathbf{T_g}$	Glass transition temperature	(K)/(°C)
$\mathbf{T_m}$	Melting temperature	(K)/(°C)
$\mathbf{T_{ODT}}$	Order-Disorder transition temperature	(K)/(°C)
τ	Bond torsion	(m^{-1})
Φ	Local composition	-
χ_{AB}	Flory-Huggins parameter	-
ω	Pulsation (in the measurement of the elastic modulus)	($rad.s^{-1}$)
ω	Bond wagging (for the vibration peaks assignment)	(m^{-1})
z	Coordination number	-

CHAPTER 1: Bibliographical study

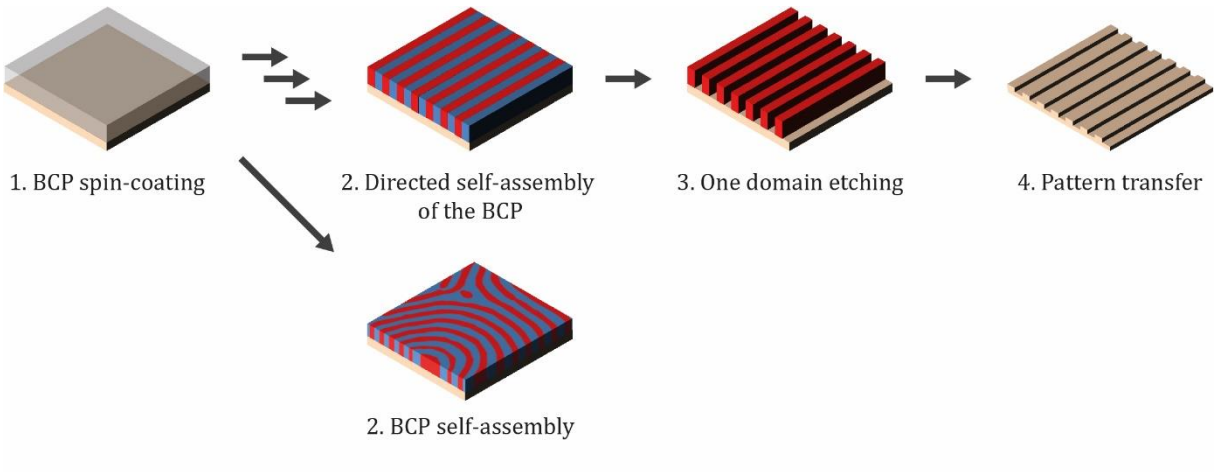

In this chapter, we present the general concept of this Ph.D. thesis. Firstly, we examine the background of "top-down" approaches for nanolithography. Although "top-down" techniques e.g. e-beam lithography, EUV lithography, nanoimprint lithography, have shown promise at the early stage of nanolithography development, their inherent limitations and expensive costs have led scientists to develop a "bottom-up" approaches. One particular approach relies on the use of BCPs as masks for pattern transfer, which offers another way for the achievement of smaller features in a cheap manner. Also, we outline the physics of BCPs from bulk to thin films and highlight the key challenges for the integration of these systems in industry that are, among others; the control of (i) organisation and (ii) orientation at long-range. Methods to direct the self-assembly in this regard include thermal and solvent vapour annealing, the use of surface energy modifiers and guiding patterns.

I. Principle of lithography

1. Conventional lithography techniques

a) Photolithography

As seen previously, the development of nanotechnology is based on the miniaturisation of electronic components. For this purpose, optical lithography (or photolithography) was the first technique developed for the semiconductor industry. Figure 1-1 depicts the general principle of the technique: (i) a photosensitive material, referred to a resin, is deposited on a substrate, (ii) the material is then exposed to a photon beam through a mask in order to crosslink or degrade the exposed parts depending on the type of resins (negative and positive resins, respectively) and finally (iii) the material is immersed into an appropriate solvent to reveal the pattern (development step).

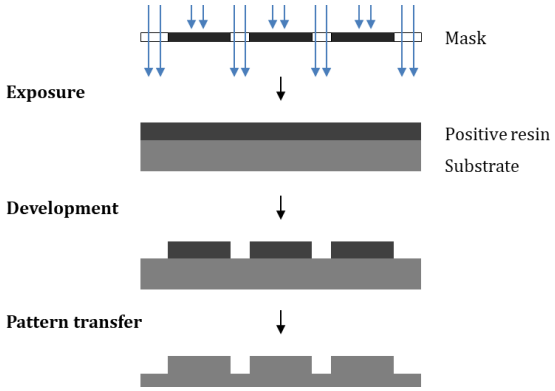

Figure 1-1: Principle of optical lithography using a positive photosensitive resin.

Indeed, the incident beam induces a change of the chemical properties (usually the solubility) into the exposed areas, which allow their further removal. These photosensitive resins can be positive or negative depending on their response to radiation. In the case of positive photosensitive resins, the exposed areas of the resin become soluble to solvents and can thus be selectively removed.

The resolution of the pattern is given by Rayleigh's law (equation 1-1):

$$\text{(eq. 1-1)} \quad \boldsymbol{R = k_1 \frac{\lambda_0}{n \sin \theta}}$$

where k_1 is a parameter that depends on the resin and the apparatus; λ_0 is the wavelength of the light source in the vacuum; n, the refractive index of the incident media and θ is the angular aperture of the lens.

The three parameters allowing an improvement of the resolution (*i.e.* a decrease of R) are the parameter k_1, λ_0 and $n \sin \theta$ (product denoted as *NA* for "Numerical Aperture"). Decreasing the wavelength of the source has been the main driving force of the semiconductor industry, starting from 436 nm with a "g-line" source and followed by 365 nm with a "i-line" source, 248 nm with a krypton fluoride (KrF) source and finally 193 nm with an argon fluoride (ArF) source [1]. To keep decreasing the size of the pattern, researchers have focused on methods to decrease k_1 by manipulating the illumination conditions (using a polarized source or sending light at an oblique angle, i.e. off-axis illumination), by modifying the mask architecture (use of phase-shifting masks) or by adding sub-resolution support functions (called sub-resolution assist features). More details on this non-exhaustive list of improvements are available in ref. [1], [2]. These technologies have greatly extended the life cycle of 248 nm and 193 nm lithography techniques. The lithography at 157 nm was then expected to succeed to the lithography at 193 nm but difficulties in its implementation (development of new resists sensitive at this particular wavelength, lenses, etc.) have slowed down its development. For this reason, a lithography derived from the 193 nm-lithography was developed to achieve similar resolutions to the lithography at 157 nm [1].

b) Immersion lithography at 193 nm

The immersion lithography at 193 nm emerged in 2002. The principle is the same as the classical optical lithography except that the beam at the exit of the projection lens passes through a medium whose refractive index is greater than the one of the air (Figure 1-2). In fact, by considering Rayleigh's law, one can understand that an increase of the refractive index will allow a decrease of the resolution. The "high refractive index" media is usually water because it is abundant, it is not toxic and it can be purified to remove metallic compounds (as contamination could create short circuits during the use of the final device) [3]. This allows the modification of the effective wavelength ($\lambda_{eff} = \lambda_0 / n_{media}$) of the incident light without changing the wavelength of the source in vacuum [1].

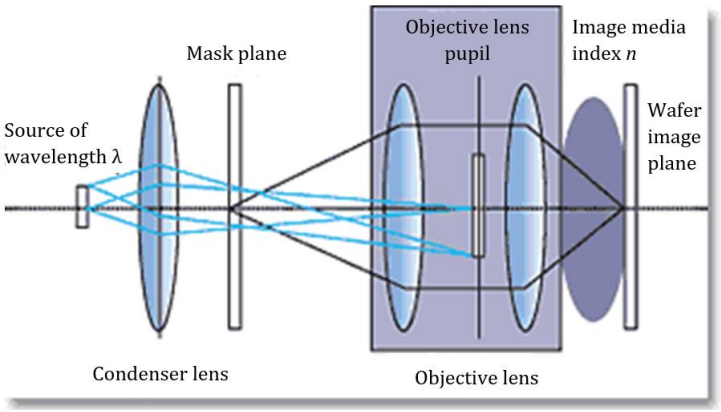

Figure 1-2: Principle of the immersion lithography at 193 nm [4].

The 193 nm immersion lithography has enhanced the lithographic resolution down to the 65 nm technology node in 2007. Double-exposed, double-patterned or double-step lithographic techniques were developed afterward to allow the definition of periods between 20 and 32 nm thanks to the use of sophisticated masks and newly developed resins. In addition, the 193 nm immersion lithography technique is performed on the same apparatus as the lithography at 193 nm, which was a strong asset to its implementation (no costly investment). However, the technique is still limited by diffraction and it is thus not possible to reach the technological nodes below 22 nm described on the ITRS roadmap for the semiconductor industry [5].

c) Commonly used resins

(1) Novalac/DNQ resins

The Novalac resin is the product of the acid-catalysed polycondensation of a formaldehyde and a mixture of meta- and para- cresol isomers (phenolic compounds can also be added) as shown in Figure 1-3. The diazonaphthoquinone (DNQ) derivatives, used for the activation of the Novalac resins, exist in several forms depending on the position of the sulfonate groups, even if the form with the sulfonate group in the 5th position (rated DNQ-5) is the most commonly used. The formulation of DNQ and Novalac form a positive resin [1], [6]. Indeed, before the exposure, DNQ is hydrophobic and prevents the dissolution of Novalac by selective solvents. When exposed to UV radiation, the DNQ undergoes a chemical modification whose product is an indene carboxylic acid. This transformation into a hydrophilic acid leads to the dissolution of the resin

during the development in a basic aqueous media. DNQ/Novalac resins have been the workhorse of the semiconductor industry for the lithography at 365 nm. However, the use of these resins is limited to sub-300 nm resolution patterns due to their low transparency at wavelengths below 300 nm [7]–[11].

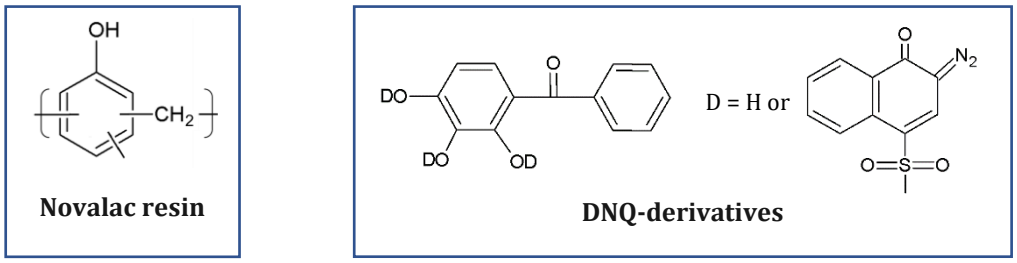

Figure 1-3: **General composition of a positive resin based on DNQ/Novolac.**

(2) Chemical amplification resin (CAR)

The use of smaller exposure wavelengths to improve the pattern resolution leads to a decrease of the sensitivity for Novalac/DNQ resins. Indeed, for a given dose, the number of available photons inducing the chemical modification decreases with the wavelength which renders the photosensitivity of the resins insufficient. For example, in the case of DNQ-based resins, several photons (three or four) are required to initiate the chemical transformation of a single molecule [12]. To overcome these issues, Ito, Willson and Fréchet proposed the concept of Chemical Amplified Resins (CARs) in 1982 [12]. These CARs are composed of a polymer matrix and a photoacid generator (PAG). The PAG is a specie that generates a strong acid (Lewis or Brønsted) upon irradiation that triggers a cascade of chemical reactions leading to the chemical modification of the polymer matrix. For example, such cascade reactions with the polymer can induce polymerization or depolymerization in the case of negative or positive resins, respectively. The chemical amplification resides in the catalytic nature of the initiation step. Indeed, a single photo-event will produce an acid that is not consumed during the initiation step and that can initiate several events allowing the improvement of the resin sensitivity [12]. These reactions, usually thermally-activated, require a subsequent thermal annealing to promote the diffusion of the acid called post-exposure bake.

- Polymer matrix

The principle of a positive resist is based on a deprotection mechanism catalysed by a photo-generated acid leading to a modification of the polymer solubility. Owing to this deprotection process, the polymer becomes soluble in the developer solvent.

Poly(phthalaldehyde) and poly(*p*-hydroxy methylstyrene) based resins have been developed for the lithography at 248 nm due to their transparency in deep UV. For instance, poly(phthalaldehyde) can be used as a polymer matrix for positive CARs. Indeed, this polymer has a ceiling temperature of -40°C, which means that it can rapidly depolymerized at room temperature. However, by protecting the polymer with acyl or alkyl groups, it can be stable up to 250°C. Taking advantage of this stable "dormant" state, an UV exposure is used to cleave the terminal function leading to a spontaneous depolymerization of the polymer chain [13]–[15]. However, poly(phthalaldehyde) has a poor plasma etching resistance which is problematic for its further use as mask. Moreover, the production of aldehyde gas during the exposure is detrimental as it can contaminate the lithographic tools [6]. On the other hand, poly(*p*-hydroxy methylstyrene) is obtained by cationic polymerization. It is usually hydroxyl or methyl end-terminated due to the quenching of the polymerization by water or methanol. These terminal groups can triggered through an acidolysis induced by irradiation the formation of carbocations leading to the depolymerization of the polymer from the end of the chain [1], [16].

Finally, poly(methyl methacrylate) based terpolymer has been developed for 193 nm lithography. Despite a good transparency, chemical modifications of poly(methyl methacrylate) resins were required for the improvement of its etching resistance and deprotection capability. As today, adamantyl methacrylate copolymer-based resists show the best sensitivity and resolution at 193 nm. It has also been reported that the incorporation of fluorine atoms in the polymer chain could provide a good transparency at 157 nm [17]–[20].

On the other hand, negative resins are based on the crosslinking reaction of the polymer chains under UV radiations. Initially, the design of the negative CARs focused on the ring-opening

polymerization of epoxy resins. The SU-8 resin, developed by Shell, is the most widespread. However, film swelling issues arose during the development in organic solvents which led to a decrease of the pattern resolution. To overcome these problems, phenolic resins were developed in basic aqueous solutions taking advantage of the intramolecular (aromatic) electrophilic substitution catalysed by the PAG. This substitution takes place within the polymer chain between a benzene that has been rendered electrophilic by the PAG and an electron-rich aromatic cycle. It is also possible to extend the system with multi-functional electrophiles with hydroxyl or acetoxy leaving groups [1], [21]–[25].

Another type of three-component system used as negative resin consists of a phenolic binder, a *N*-methoxymethylated melamine crosslinking agent and a PAG. Here, the photogenerated acid protonates the oxygen of the methoxy groups and then undergoes an electrophilic substitution in order to obtain a crosslinked network [25].

- Photoacid generator (PAG)

The first CAR system was developed for the cationic polymerization of epoxy resins by acid-initiated ring opening mechanism. For this purpose, aryldiazonium salts can be used as PAG because they are able to produce Lewis acids under UV. Consequently, through their formulation with epoxy resins, it is possible to obtain a negative resin with a sensitivity that can range from deep UV to visible wavelengths depending on the incorporated aromatic groups. However, such salts are thermally unstable and produce nitrogen under irradiation which damages the film due to degassing. Therefore, other salts such as diaryliodonium and triarylsulfonium have been developed [6]. Figure 1-4 shows the mechanism of the photolysis of a PAG based on triphenyl sulfonium salts. Such compounds have a better thermal stability (> 200°C), are non-volatile and have good absorbency properties at 248 nm. They can generate a wide variety of acids through the change of the nature of the counter-ion. Norbornene dicarboxyimidyl triflate (ND-Tf), triphenylsulfonium triflate (TPS-Tf), bis-4-*tert* butylphenyl iodonium perfluorooctanesulfonate (TBI-PFOS) and bis-4-*tert*-butylphenyl iodonium triflate (TBI-Tf) are PAG sensitive to 157 nm although generally used for KrF and ArF resins. Studies have shown that the iodonium salts are

the most sensitive with a sensitivity at 157 nm which varies according to: TBI-PFOS > TBI-Tf > ND-Tf > TPS-Tf (see Figure 1-5) [8], [9].

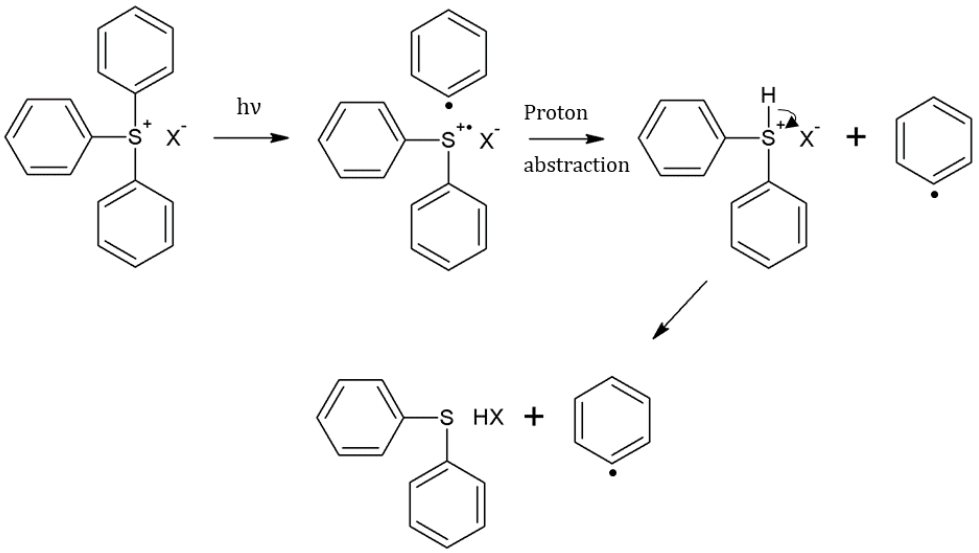

Figure 1-4: Mechanism of photolysis of PAG based on triphenyl sulfonium salts.

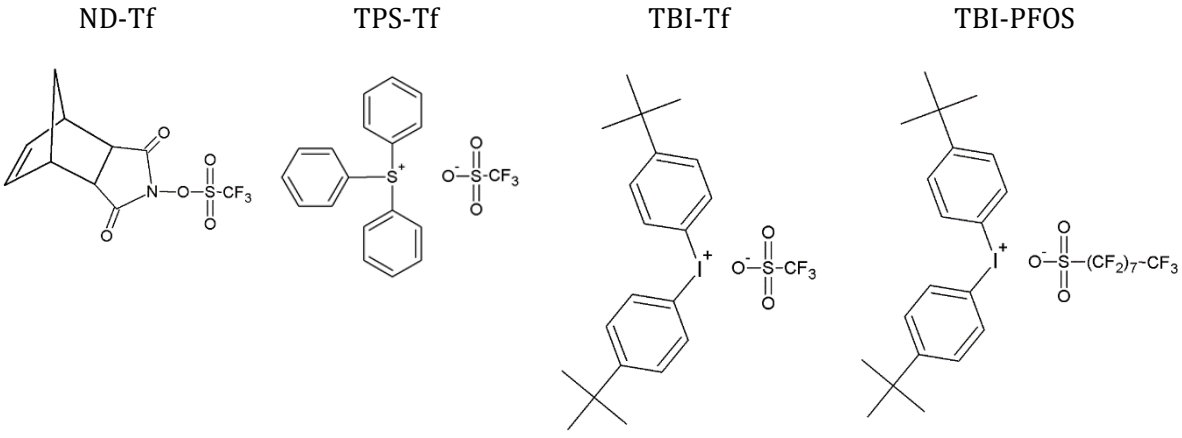

Figure 1-5: Series of onium salts used as PAGs for 157 nm lithography. ND-Tf refers to norbornene dicarboxyimidyl triflate, TPS-Tf refers to triphenylsulfonium triflate, TBI-Tf refers to bis-4-*tert*-butylphenyl iodonium triflate and TBI-PFOS refers to bis-4-*tert* butylphenyl iodonium perfluorooctanesulfonate.

It is also possible to UV-generate acids from non-ionic compounds. Non-ionic PAGs have a much wider range of solubility in organic solvents and polymer films than their onium salt analogs. Under UV illumination, these molecules can release an acid *via* the photolytic dissociation of their C-O, S-O and N-O bonds resulting in the formation of radicals extracting a hydrogen from the protic

solvent. Among the non-ionic PAGs, *o*-nitrobenzyl esters are the most known. They undergo intramolecular rearrangement to generate a nitrosobenzaldehyde and a sulfonic acid. Houlihan and Reichmanis were the first to synthesize these derivatives targeting their use as PAG. Such esters have good absorption properties at 248 nm and show a thermal stability up to 255°C [26]–[32]. There are other types of PAG based on diazomethane chemistry. As example, sulfonyldiazomethane can undergo photolysis in the same way than DNQ sulfonates to produce sulfonic acid. This reaction is very effective at high temperature and requires thus an annealing step. This PAG is sensitive at 254 nm [6]. One can also cite the use of halogenated compounds to produce halogenated acids when irradiated between 335 nm and 495 nm [33], [34] and disulfones to produce sulfinic acids between 255 nm and 338 nm. Despite many studies on the development of the non-ionic PAGs [35], their use in CAR formulations remains limited as compared to the ionic PAGs because of their low sensitivity below 240 nm and their thermal stability issues.

2. Emerging lithography techniques

a) Extreme ultraviolet lithography

Proposed in 1985, extreme ultraviolet (EUV) lithography is more complex than 193 nm immersion lithography as shown in the Figure 1-6 [36], [37]. The source used nowadays is a high-power laser striking a tin droplet to form a plasma emitting radiation at a wavelength of 13.5 nm. However, these wavelengths are absorbed by air and glass so that the optical system cannot work in transmission mode. The lenses are thus replaced by reflective Bragg mirrors to work in reflection mode and the masks have to undergo a complex transformation in order to operate under vacuum. The main drawback of using such mirrors is their low *NA* meaning that several mirrors have to be used (between 6 and 14 depending on the desired *NA*) to reach an acceptable aperture. Moreover, the mirrors are never fully reflective leading to photon losses and the more mirrors are used, the more losses are amplified. These losses have to be compensated with the power of the source that is limited today at 250 W in large-scale production facilities.

Although this technology is used in production for Samsung's "7 nm" node and will be soon used by TSMC (Taiwan Semiconductor Manufacturing Company), it is still limited by the absence of

material protecting the mirrors from degradation, which limits the lifetime of these very expensive machines (more than 250 million dollars per scanner). These issues will have consequently to be solved before moving to higher resolution EUV techniques [38], [39].

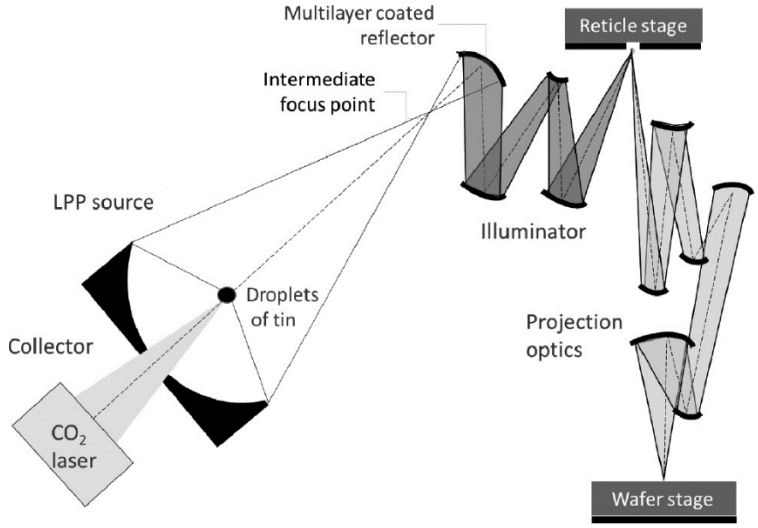

Figure 1-6: **Principle of the extreme ultraviolet lithography [37].**

b) Electron-beam lithography

Electron-beam lithography consists of an electron gun (operating between 50 and 100 keV) that writes patterns in an electron-sensitive resin (Figure 1-7). Electrons impacting the resin generate secondary electrons of lower energy that form free radicals and cation radicals (in the case of CARs). These intermediate species are then deactivated by fragmentation and/or reaction with the resin leading to chemical modifications of the resin structure. A rinsing step similar to the development step in the photolithography technique allows the removal of the irradiated areas. It is thus possible to write patterns down to 10 nm, ideally with a resolution of 2 nm [40], [41]. However, the diffusion and backscattering of the electrons impact the actual resolution. Another issue is related to the serial character of the technique which hinders its transposition to an industrial level. Nevertheless, the technique is widely used to provide the masks for immersion lithography and nanoimprint [42].

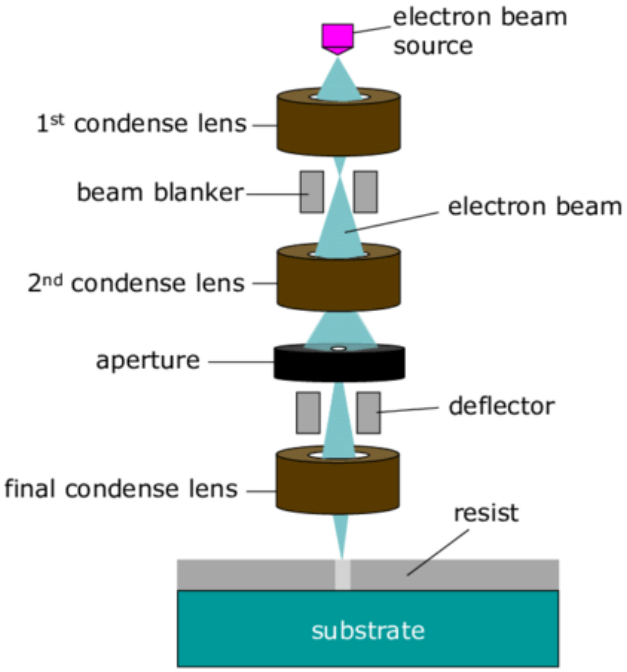

Figure 1-7: **Principle of electron-beam lithography [43].**

c) Nanoimprint lithography

Nanoimprint lithography (NIL) arose in the late 1990s and consists of replicating a predefined model in a soft material, generally a polymer resin. Its low manufacturing cost shows a high production capability potential that drew a great deal of interest. Moreover, the resolution of the technique is not limited by the diffraction issues outlined earlier as there is no need of an incident beam. The resolution mainly depends on the manufacturing method of the mold and on the resin being used for the transfer step. The mold is often made by electron-beam lithography on silicon or alumina substrates and transferred into a silicone material to obtain a "working" mold. There are two types of NIL techniques: the thermally-assisted NIL and the UV-assisted NIL. Thermally-assisted NIL was developed in 1995 and consists of heating the resin above its glass transition while embossing it with the mold. In this way, the polymer chains of the resin have sufficient mobility to follow the shape of the mold and its pattern. The mold is then cooled down below the glass transition of the resin before being removed so that its removal does not cause the resulting patterns to collapse [43].

The UV-assisted NIL uses a transparent mold that is pressed onto a photosensitive resin. Once in contact, the resin is irradiated leading to its photo-polymerization. The mold is then removed leaving a pattern printed in the resin (Figure 1-8). The polymer residues can eventually be removed with a soft plasma treatment (last step in Figure 1-8) [44]. This technique allows to work at room temperature and thus to avoid the degradation of the resin. However, the mold removal is critical as a strong adhesion with the crosslinked resin will result to an alteration of the pattern.

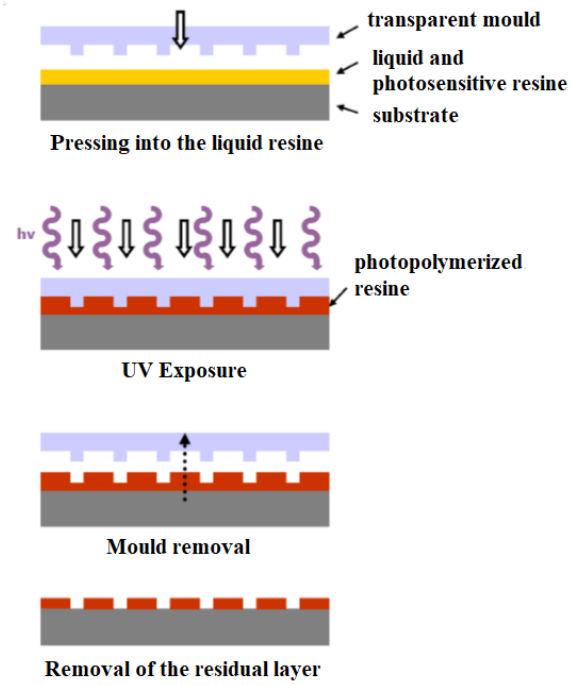

Figure 1-8: **Principle of the UV-assisted nanoimprint lithography [44].**

II. Directed self-assembly of block copolymers

1. Self-assembly of block copolymers

a) In bulk

(1) Theory of microphase separation

A system of two immiscible homopolymers tends to macroscopically phase separate to lower the repulsive interactions between the chemically distinct polymer chains. This process can be described with respect to the Gibbs free energy of mixing, ΔG_m, that has to be minimized to reach the equilibrium of the system. In the case of BCPs, the two incompatible chains are covalently bonded which prevent a macrophase separation. Nevertheless, the repulsive interactions between the two chemically distinct blocks (described by a mixing enthalpy, ΔH_m) will still lead to a minimization of the unfavourable contacts through the formation of microphase separated structures. This minimization of contacts between the two incompatible blocks is responsible of a loss of entropy, $\Delta S_{m,int}$, due to the confinement of the junction at the interface between the chemically distinct domains. This confinement is also responsible of a stretching of the chains that occurs in order to guaranty a constant chain density in the segregated domains. This loss of configurational entropy, $\Delta S_{m,conf}$, is the second entropic contribution acting against the microphase separation of the system.

As shown in equation 1-2 below, if the two entropic contributions, $\Delta S_{m,int}$ and $\Delta S_{m,conf}$, are not high enough to balance the enthalpy term, the free energy of mixing is positive leading to microphase separation.

$$\Delta G_m = \Delta H_m - T\Delta S_{m,int} - T\Delta S_{m,conf} \quad \textbf{(eq. 1-2)}$$

One can also consider the Gibbs free energy of mixing derived from the Flory-Huggins theory that drives the BCP microphase separation as shown in the equation 1-3:

$$\frac{\Delta G_m}{k_B T} = \boxed{\frac{f_A}{N_A} * lnf_A + \frac{f_B}{N_B} * lnf_B} + \boxed{f_A f_B \chi_{AB}} \quad \textbf{(eq. 1-3)}$$

Entropic term Enthalpic term

where k_B is the Boltzmann constant; T is the temperature; $f_{A,B}$ is the volume fraction of the blocks A and B, and $N_{A,B}$ is the degree of polymerization of the blocks A and B, respectively.

As shown the equation 1-3, the entropy of mixing is inversely proportional to the degree of polymerization of the blocks. It means that for a high degree of polymerization (i.e. copolymers of high molecular weight), the entropy term is low and the enthalpy term becomes predominant. This latter term will thus drive the thermodynamic behaviour of the BCP system and will be the source of the microphase separation. The mixing enthalpy, ΔH_m, is proportional to the Flory-Huggins parameter, χ_{AB}, and reflects the variation of the interaction energy when bringing two incompatible repeating units (A and B) into contact and is expressed as follows:

$$\chi_{AB} = \frac{z}{k_B T} \left(\varepsilon_{AB} - \frac{1}{2} \left(\varepsilon_{AA} + \varepsilon_{BB}\right)\right) \quad \textbf{(eq. 1-4)}$$

where z is the coordination number and ε_{XY} is the interaction energy between the X and Y repeating units.

However, it has been experimentally noticed that χ appears to be realistically represented by an excess of free energy of mixing ΔG_m^{ex}. Thus χ exhibits not only an enthalpy contribution but also an entropic one [45]. For this reason, it is common to describe the Flory-Huggins parameter as a function of the temperature following the expression:

$$\chi_{AB} = A + \frac{B}{T} \quad \textbf{(eq. 1-5)}$$

where A and B are the entropy and enthalpy contributions, respectively.

If there is a high degree of incompatibility between the blocks (or at low temperature), the value of χ_{AB} is high and will favour BCP microphase separation. Conversely, if χ_{AB} and N ($N \sim N_A + N_B$) are sufficiently low, the entropy term will be dominant and will lead to a disordered phase. Consequently, the product $\chi_{AB}N$ can be seen as the segregation strength of the system: the microphase separation will be more defined as the product $\chi_{AB}N$ will be large as shown in Figure 1-9.

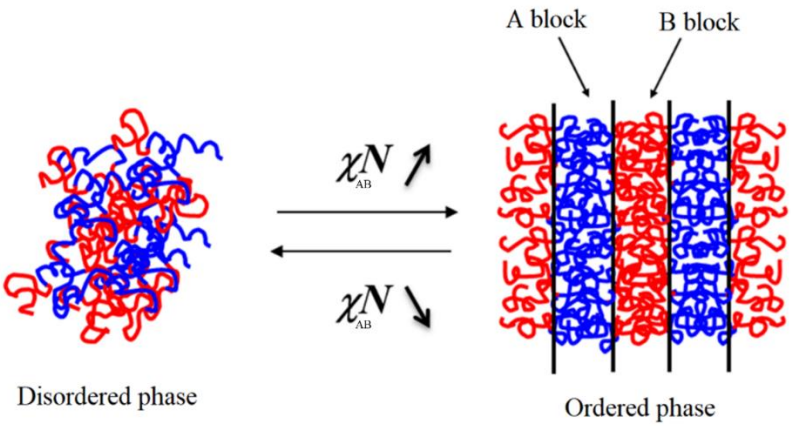

Figure 1-9: Transition between the disordered and ordered phases as a function of the product $\chi_{AB}N$ for a symmetric diblock copolymer [46].

(2) Segregation regimes

It is possible to describe the change of BCP physical behaviour with respect to the segregation strength. With the use of Figure 1-10 [47], we will discuss the different segregation regimes for a symmetric diblock copolymer.

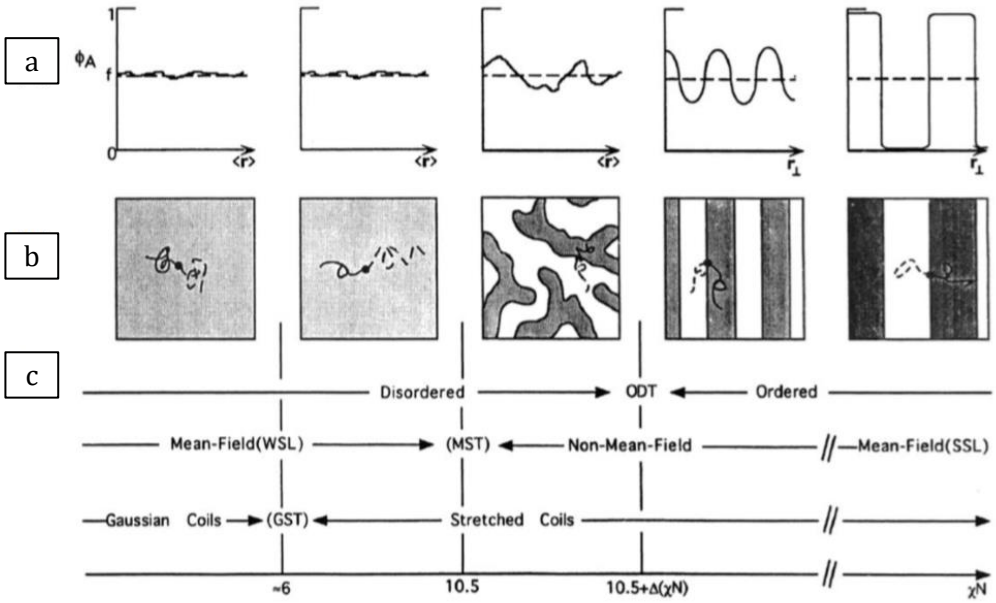

Figure 1-10: Illustration of the 5 segregation regimes of a symmetric diblock copolymer [47].
(a) Profile of the local composition of the block A, Φ_A, along the radial direction <r> of the nanodomains for each segregation regime. (b) The corresponding segregation states of the system. (c) Definition of the different regimes as a function of the product $\chi_{AB}N$.

When $\chi_{AB}N$ << 10.5, a BCP system is in a disordered state and has a uniform composition. In this regime called "Weak Segregation Limit" (WSL), the repulsion between the blocks is low (i.e. high temperature) and the chains follow the random walk model (Gaussian coils):

$$\mathbf{(eq.\ 1\text{-}6)} \quad R_g = \frac{a N^{\frac{1}{2}}}{6}$$

where R_g is the gyration radius and a is the length of the statistical segment [47].

With the increase of $\chi_{AB}N$, the chains start to stretch until undergoing microphase separation. This microphase separation transition (MST) occurs in order to minimize the contact between the blocks. Assuming that the copolymers are only weakly disrupted by the composition fluctuations at the interface between the blocks (WSL assumption), Leibler was able to locate the MST for $\chi_{AB}N$ = 10.5 (for a volume fraction of 0.5), at which a homogeneous block copolymer melt first separates [48]. The creation of organized domains is appearing at the order-disorder transition (ODT). Several theories have been proposed in order to localized this transition [49], [50]. Taking into account the composition fluctuations at the interface between the blocks having a given molecular weight, Fredrickson and Helfand demonstrated that the ODT occurs at $\chi_{AB}N = 10.5 + \Delta(\chi_{AB}N)$ (for a volume fraction of 0.5) with $\Delta(\chi_{AB}N) = 41.0\ \overline{N}^{-\frac{1}{3}}$ and $\overline{N}$, the finite molecular weight correction due to the fluctuations of composition [49]. When $\overline{N}$ tends to infinite, the Leibler's theory is retrieved ($\chi_{AB}N$ = 10.5) as the effect of the composition fluctuation is lowered with the increase of the molecular weight.

Above the ODT, the system is in an ordered state. The interface between the blocks becomes more defined with the increase of $\chi_{AB}N$. At a certain point, the interface is so sharp that the local composition, Φ, follows a rectangular function whose average value is *f* for a symmetric system (Figure 1-10(a)): this is the strong segregation limit regime (SSL). Semenov used an analytical method to estimate the free energy of the system in the case of $\chi_{AB}N$ tending to infinite; equation 1-7 and equation 1-8 are the resulting entropy and enthalpy contributions per chain, respectively [51].

$$\mathbf{(eq.\ 1\text{-}7)} \quad \frac{F_{el}}{k_B T} = \alpha \left(\frac{R}{a N^{\frac{1}{2}}} \right)^2$$

$$\frac{F_{int}}{k_B T} \sim \gamma_{AB}\sigma = \beta \frac{aN^{\frac{1}{2}}\sqrt{\chi_{AB}N}}{R} \quad \textbf{(eq. 1-8)}$$

where R is the size of a domain; α and β are pre-factors that depend on the morphology of the domains; $\gamma_{AB} \sim \frac{\sqrt{\chi_{AB}}}{a^2}$ is the interfacial tension between the blocks and $\sigma \sim \frac{Na^3}{R}$ is the area of a diblock chain.

At equilibrium, for which the free energy is zero, it is possible to extract the theoretical period R*:

$$R^* \sim a\, N^{\frac{2}{3}} \chi_{AB}{}^{\frac{1}{6}} \quad \textbf{(eq. 1-9)}$$

Due to their ability to segregate into nanometric domains, BCPs show thus a great potential for nanolithography. As described above, the self-assembly depends on the segregation strength of the BCP system. Indeed, microphase separation will occur for a $\chi_{AB}N$ product greater than 10.5 (for a symmetrical system) and the resulting structures will be more defined as the $\chi_{AB}N$ product increases. Three main regimes are used to define the segregation state of a BCP system according to the product of $\chi_{AB}N$: the WSL regime with $\chi_{AB}N < 10.5$, the intermediate segregation limit (ISL) regime with $\chi_{AB}N \approx 10.5\text{-}100$ and the SSL regime with $\chi_{AB}N \geq 100$. These regimes are crucial because they will determine the sharpness of the interface between the nanodomains. Indeed, the highest the $\chi_{AB}N$ product is, the highest the segregation strength of the BCP system is. The chains will therefore be further stretched at the junction point between the blocks. Consequently, there will be a clear and sharp interface between the domains (see Figure 1-10(a)). As the use of the BCP for nanolithography requires the removal of one of the domains, it is necessary to have a well-defined interface to have the best removal and limit the roughness of the patterns.

(3) Phase diagram

The microphase separation of a diblock copolymer is determined by three experimental factors (at a given temperature): the overall degree of polymerization *N*, the volume fraction *f* and the Flory-Huggins parameter χ_{AB}. By tuning the product $\chi_{AB}N$, it is possible to bring a BCP system towards the segregated regime enabling microphase separation with well-defined nanodomains. The χ_{AB} parameter is determined by the choice of the starting material (i.e. the monomers) while N depends on the polymerization procedure. Once the segregation strength is high enough (i.e. $\chi_{AB}N >> 10.5$), the resulting self-assembled structures are dictated by the minimization of the free energy which strongly depends on the volume fraction *f*. Figure 1-11 illustrates the different structures that can be obtained with a diblock copolymer architecture.

For *f* below 0.12, the system adopts a spherical structure with spheres of the minor phase forming a body-centered cubic lattice in the matrix of the major phase. From 0.12 to 0.33, the system self-assembles into a hexagonally packed structure of cylinders of the minor phase into the matrix of the major phase. Around *f* = 0.35, the system forms a 3D bicontinuous network called gyroid. Finally, for *f* comprised between 0.38 and 0.5, the BCP exhibits a lamellar structure.

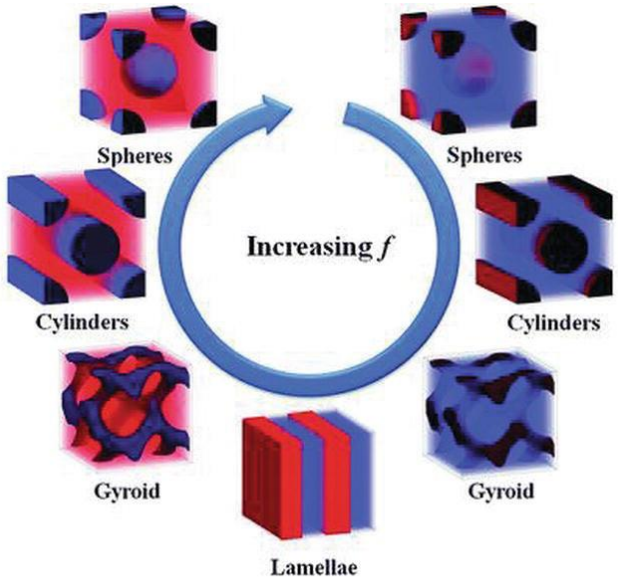

Figure 1-11: Nanostructures formed by the self-assembly of BCPs. *f* indicates the volume fraction of the red block [52].

Several groups have reported theoretical studies in order to establish the phase behaviour of BCPs. Such works have provided a guide to access unique BCP architectures (i.e. given χ_{AB}, N and f). In 1980, Leibler established the theoretical phase diagram of a diblock copolymer melt near the ODT (WSL) with the disordered, lamellar, cylindrical and spherical phases [48]. The Leibler's theory predicts a critical point at $\chi_{AB}N$ = 10.5 (localized at f = 0.5), where a symmetric diblock undergo a second-order phase transition from the disordered to the lamellar phase. A few years later, Matsen *et al.* used the Self-Consistent Field Theory (SCFT) to propose a more complex phase diagram [53], [54](see in the Figure 1-12).

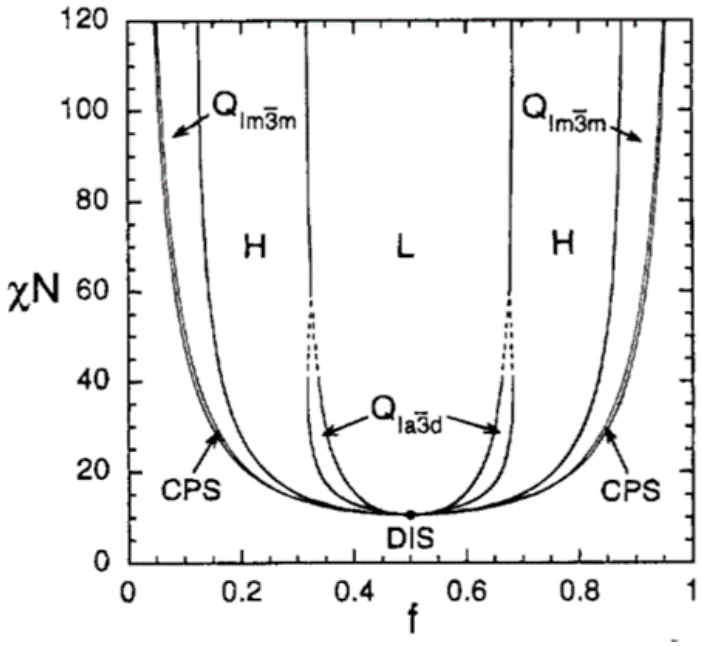

Figure 1-12: **Theoretical phase diagram for a diblock copolymer obtained using SCFT [54].**
The phase are labeled: L for lamellae, H for hexagonal cylinders, $Q_{Ia\bar{3}d}$ for the bicontinuous $Ia\bar{3}d$ cubic structure, $Q_{Im\bar{3}m}$ for BCC spheres, CPS for close-packed spheres and DIS for the disordered phase. Dashed lines denote extrapolated phase boundaries, and the dot denotes the mean-field critical point.

The phase diagram includes a new phase called gyroid ($Q_{Ia\bar{3}d}$ in the diagram) in addition to former theoretical phase diagrams [48], [49]. This bicontinuous phase consists of two interwoven continuous networks of the minority phase embedded in a matrix phase of the majority block. In 1994, Hajduk and Schulz groups independently identified this gyroid phase in diblock copolymers [55], [56]. Other complex structures in the di-BCP phase diagram were experimentally reported such as the double-diamond phase (OBDD) [57]–[59], the hexagonally perforated layers (HPL)

[60] and the orthorhombic (O^{70}) structure [61]. The HPL and OBDD phases are considered as metastable while the O^{70} was recently established as a thermodynamically stable phase between the lamellar and gyroid structures [62].

Experimental BCP phase diagrams were also reported by a number of groups [63]–[65]. As example, Khandpur *et al.* studied the poly(isoprene)-*b*-poly(styrene) (PS-*b*-PI) BCP system and managed to obtain a phase diagram using ten diblock copolymers with PI volume fractions ranging from 0.24 to 0.82 [63]. As shown in Figure 1-13, they observed spheres, lamellae, hexagonally perforated lamellae, cylinders and gyroid structures. We can once again notice that the $(\chi_{AB}N)_{ODT}$ obtained values were found to be higher than the Leibler's prediction (dash-dot curve) suggesting that finite molecular weight effects influence the experimental phase behaviour.

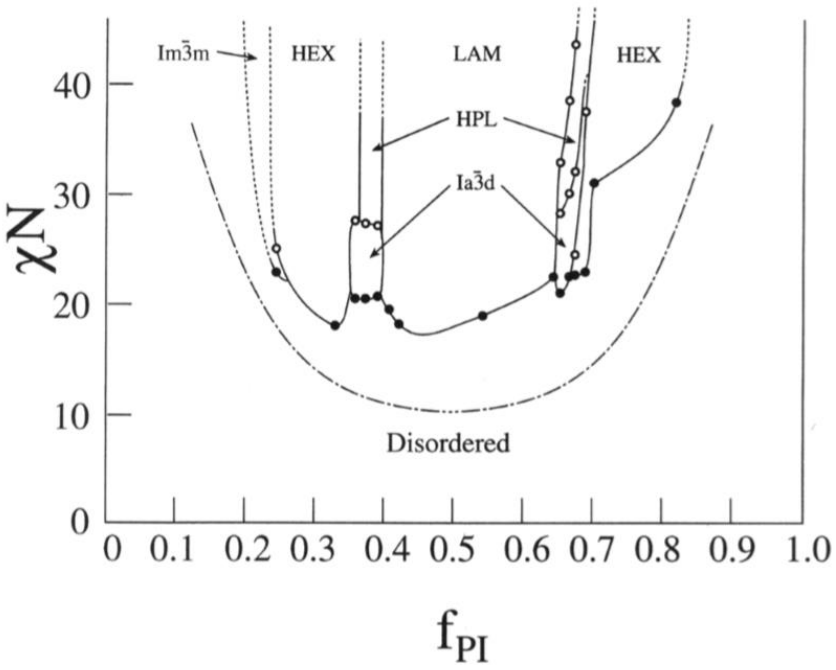

Figure 1-13: Experimental phase diagram of the poly(isoprene)-*b*-poly(styrene) system [63].
Open and filled circles represent the order-order and order-disorder transitions, respectively. The dash-dot curve is the mean field prediction for the ODT while the solid curves have been drawn from the experiments.

b) In thin film

When transitioning from bulk to thin film, the morphology of a BCP is influenced by additional factors such as the geometric confinement and the interactions between the BCP film and the interfaces (substrate and air). These interactions depend on the affinity of the blocks for either the substrate or the air interfaces and can lead to a preferential wetting of the BCP domains for one or both surfaces. In the case of structures for which the nanodomains are anisotropic, this preferential wetting results in an orientation of the BCP structure as regards to the interfaces. These phenomena are briefly exposed below for the most common phases.

(1) Lamellar phase

For lamellar-forming BCPs, the orientation of the domains strongly depends on the interactions of the blocks for either the substrate or the air interfaces as well as on the commensurability between the thickness of the film and the BCP periodicity, L_0, as illustrated in the Figure 1-14.

Indeed, when there is a preferential interaction at an interface with one of the blocks, different scenarios are possible:

(i) When the initial thickness of the film is higher than the BCP periodicity, L_0:

(a) if one of the blocks interacts with both surfaces (substrate and air), the thickness of the film will be an integer number of the equilibrium periodicity: nL_0. Moreover, the thickness of the wetting lamellae will be thinner at the interfaces due to the surface tension between the block and the interface (Figure 1-14(a))

(b) if each interface has a specific interaction with one of the blocks, the film thickness will be $(n+1/2)L_0$: this is the asymmetric wetting (Figure 1-14(c)).

(ii) When the thickness of the film is not commensurate with the BCP periodicity, islands and holes with nL_0 step height, called terraces, form as shown in the Figure II 6(b) and (c). Indeed, the energy expenditure to create a surface is lower than the penalty

induced (i) by the alteration of the domain periodicity or (ii) by the contact between a BCP domain and an interface for which it has no affinity.

(iii) Finally, when the thickness of the film is lower than L_0, obtaining parallel lamellae would lead to a compression of the polymer chains. In this configuration, it is thus possible to obtain perpendicular lamellae that are less energy consuming for the system.

In contrast, if no preferential interactions exist, it is possible to obtain out-of-plane lamellae whatever the film thickness is (Figure 1-14(e)). However, if the blocks have no affinity for the substrate but there is a preferential wetting of one of the blocks for the top interface, there will be a perpendicular orientation of the lamellae at the bottom of the film and in-plane lamellae at the top of the film as shown in Figure 1-14(f) [66].

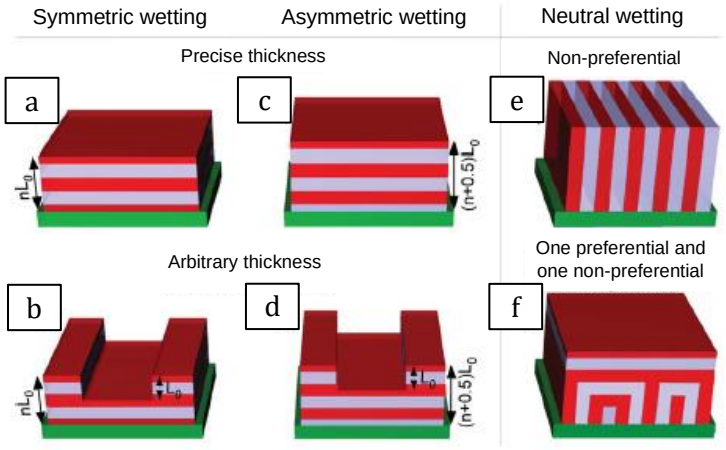

Figure 1-14: Orientation of the BCP domains regarding the commensurability of L_0 with the film thickness and the affinity of the blocks for the interfaces [66].
Lamellae with in-plane orientation are observed in case of symmetric (a and b) and asymmetric (c and d) wetting conditions while out-of-plane lamellae are observed with neutral wetting conditions (e and f). Terraces form when the average film thickness is not commensurate with the natural periodicity, L_0, of the BCP (b and d).

To highlight these different behaviours, Kim *et al.* studied the self-assembly of two lamellar-forming BCPs: poly(styrene)-*b*-poly(isoprene) (PS-*b*-PI) and partially epoxidized poly(styrene)-*b*-poly(isoprene) (PS-*b*-PEI) with L_0 = 19 nm [67]. For this purpose, they performed the self-assembly of the BCPs on PS brush for several film thicknesses. As expected, they observed a film split into islands and holes of PS-*b*-PI BCP film for a film thickness of $2.3L_0$, which is

consistent with an asymmetric wetting where the PI block wets the free surface and the PS block wets the substrate (due to the PS brush) as shown the Figure 1-15(a). Interestingly, for the same condition, PS-*b*-PEI terraces with $0.5L_0$ step heights were observed as shown the Figure 1-15(b). It is assumed that this unusual step height is due to a configuration where the PS block wets the substrate (due to the PS brush) and where both blocks are present at the top surface as shown the scheme in Figure 1-15(c). This work offers thus an additional methodology to determine the affinity of the blocks for an interface by measuring the step heights of the BCP thin film.

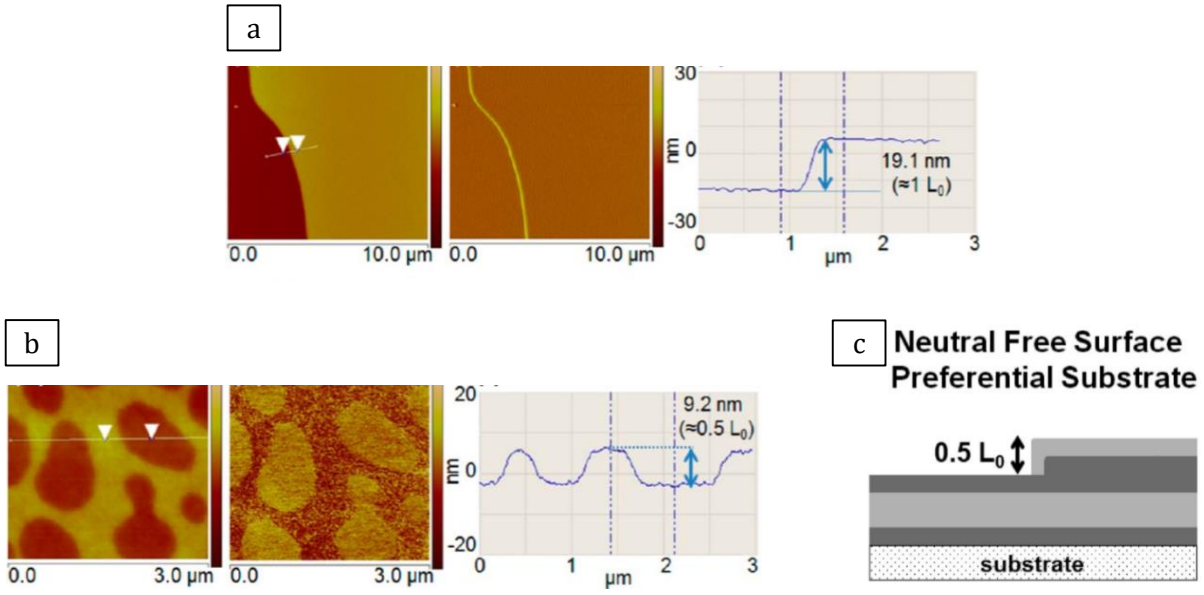

Figure 1-15: (a) is the atomic force microscopy (AFM) images (right is height and left is phase) and respective height profile of PS-*b*-PI thin films thermally-annealed on PS brush for a film thickness of 2.3 L_0. (b) is the AFM images and respective height profile of PS-*b*-PEI thin films thermally-annealed on PS brush for a film thickness of 2.3 L_0. (c) is the scheme of explaining the topography of the PS-*b*-PEI where the two blocks are present at the upper interface and the substrate has preferential interaction with one of the blocks [67].

(2) Cylindrical phase

The behaviour of the cylindrical phase is similar to the one of the lamellar phase since the affinity of one block for the air and/or the substrate will lead to a parallel orientation of the cylinders. Moreover, if the minority block has an affinity for one of the interfaces, a brush-like wetting layer will form at the film/surface. However, as the structure is asymmetric, the preferential affinity of this block for one of the surfaces can lead to a modification of the morphology and even lead to the stabilization of a metastable structure *via* surface reconstruction. Kim *et al.* illustrated this phenomenon by studying the structure of cylinder-forming PS-*b*-PMMA

thin films [68]. For this purpose, they thermally-annealed ~1L_0 thick PS-*b*-PMMA films for different times. Starting with a smooth film for low annealing time, they interestingly observed the appearance of 1L_0 step height islands with a PS-wetting layer after 24h of annealing (as shown the Figure 1-16). Indeed, the interaction of the PMMA (minor block) with the substrate leads to the formation of a $L_0/2$ thick brush adsorbed to the substrate. There is consequently only a $L_0/2$ thickness left on top the PMMA brush, which leads to the formation of a single layer of parallel in-plane PMMA cylinders. On the other hand, the PS-wetting layer is explained by the surface energy of the PS that is slightly lower than the one of the PMMA.

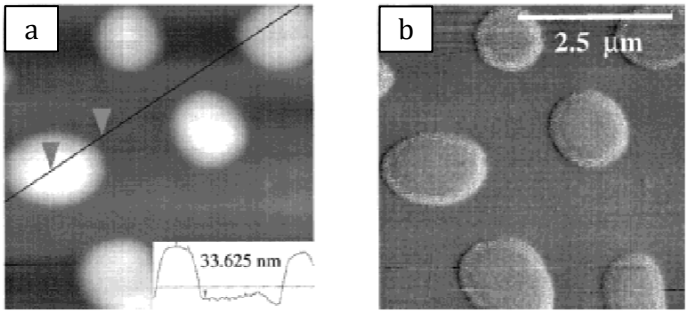

Figure 1-16: (a) and (b) are the AFM height and phase images of a PS-*b*-PMMA thin film thermally-annealed at 160 °C for 24 h, respectively. The inset in (a) corresponds to the height profile along the line. The surface of the film is entirely covered by the PS-wetting layer that appears darker on the AFM phase (b) [68].

This work highlights the fact that the wetting behaviour of the blocks can have a significant impact on the thin film nanostructure even when commensurability conditions are achieved.

Moreover, for non-commensurate film thickness, the behaviour of the cylindrical phase is similar to the lamellar phase with a splitting of the film into terraces as discussed above. As example, Dijk *et al.* reported the formation of terraces in a poly(styrene)-*b*-poly(butadiene)-*b*-poly(styrene) copolymers films for a non-commensurate film thickness [69]. After a long annealing time, they observed a splitting of the film into terraces such that in the higher regions the thickness is equal to an integer number of L_0 (Figure 1-17(a)). Moreover, out-of-plane cylinders were observed in the lower part of the terraces, while in-plane cylinders were observed in the upper part as shown in Figure 1-17(b). Indeed, in the thinnest regions, obtaining a parallel orientation of the cylinders

would constrain the polymer chains, which thus favoured a perpendicular orientation of the cylinders.

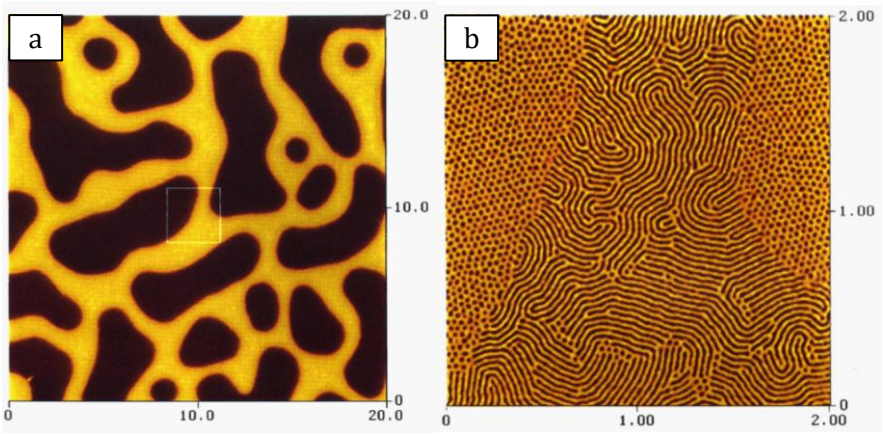

Figure 1-17: (a) and (b) are the AFM height images of a PS-*b*-PB-*b*-PS thin film thermally-annealed at 115°C for 96h. (b) is a zoom image of (a) highlighting the perpendicular and parallel orientations of the cylinders in the hills and in the valleys, respectively [69].

(3) Spherical phase

For sphere-forming diblock copolymers, brush-like wetting layers can also form if the minority block wets the surface. Mansky et *al.* studied the effect of the preferential interaction of a polybutadiene (PB) block at the interfaces for a poly(styrene)-*b*-poly(butadiene) system (PS-*b*-PB) [70]. They synthesized two BCPs; one with a majority PB block and one with a minority PB block to form spheres of PS in a matrix of PB and spheres of PB in a matrix of PS, respectively. A monolayer of PB spheres in a hexagonal lattice was obtained for the BCP with a majority of PS while an ill-defined segregated structure was obtained from the BCP with a majority of PB (Figure 1-18(a) and (b)). In the first case, the PB block wets both interfaces due to its preferential wetting with the interfaces and is thus forming a brush-like wetting layer as shown in the Figure 1-18(d). The PB chains forming the spheres within the PS matrix are thus free to diffuse without interaction with the surface or the substrate during the annealing treatment, leading to a well-ordered self-assembled structure. In the second case, the PS spheres are surrounded by the PB block. In this configuration, some of the PB chains are highly constrained due to the preferential interactions at the interfaces and the overall degree of freedom of the BCP chains is limited during the annealing step leading to an ill-defined self-assembled structure (Figure 1-18(b) and (d)).

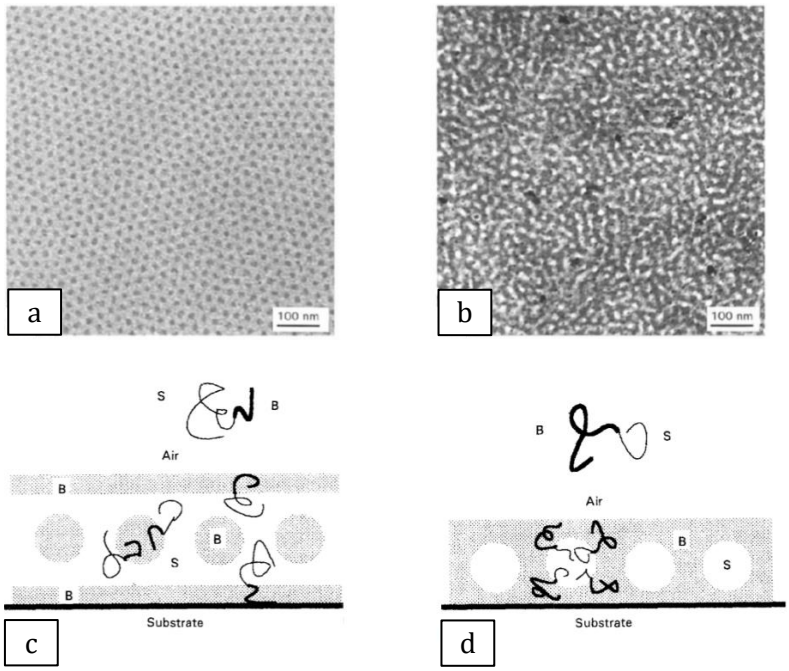

Figure 1-18: Bright-field transmission electron micrographs of nanostructured PS-*b*-PB films (a) with the majority PS block and (b) with the majority PB block. (c) and (d) are the corresponding schemes explaining the self-assembly behaviour as regards to the interactions of the block with the interfaces [70].

Interestingly, we observed in this example that the spheres packing into a body centered cubic lattice (BCC) in bulk, tend to assemble into a close packed configuration in thin film. This structure might be seen as a deformed (110) plane of the BCC structure as there are no more neighbouring layers to break the in-plane symmetry. Stein *et al.* investigated this structural change of the sphere packing when passing from film to bulk configuration for a poly(styrene)-*b*-poly(2-vinylpyridine) (PS-*b*-P2VP) system. For this purpose, they studied the spherical morphology as a function of the film thickness and highlighted a hexagonal close-packed (HCP) structure for the first three layers of spheres followed by an intermediate face-centered orthorhombic (FCO) packing before retrieving the BCC structure with the increase of the number of the layers. The symmetries observed for a low number of layers are attributed to a minimization of the packing frustration in a 2D configuration [71], [72].

2. Use of block copolymers as mask for nanolithography

a) Concept of BCP lithography

As stated in the Introduction part, the main interest in using BCP materials for nanolithography is their ability to self-assemble into nanostructures with dimensions and spacings that are very difficult to obtain with other techniques or not possible to achieve considering the expensive cost of the machines and/or of the processes. BCP lithography is based on the use of these materials in thin films whose the nanostructures are able to provide a mask that can be used, *inter alia*, for pattern transfer. Indeed, it could be possible to obtain (i) parallel line arrays from perpendicular lamellae or parallel cylindrical structures or (ii) hexagonal/square dot arrays from perpendicular cylindrical or spherical structures, respectively. Their use at industrial scale requires the precise positioning or registration of the BCP nanostructures arranged within a highly-ordered nanoscale array. However, a polygrain BCP structure is generally observed in thin film as shown in Figure 1-19. For this reason, optimization of the processing conditions and DSA strategies are currently developed to provide a long-range ordering of the BCP nanodomains that could be further used for pattern transfer in nanolithography applications (Figure 1-19).

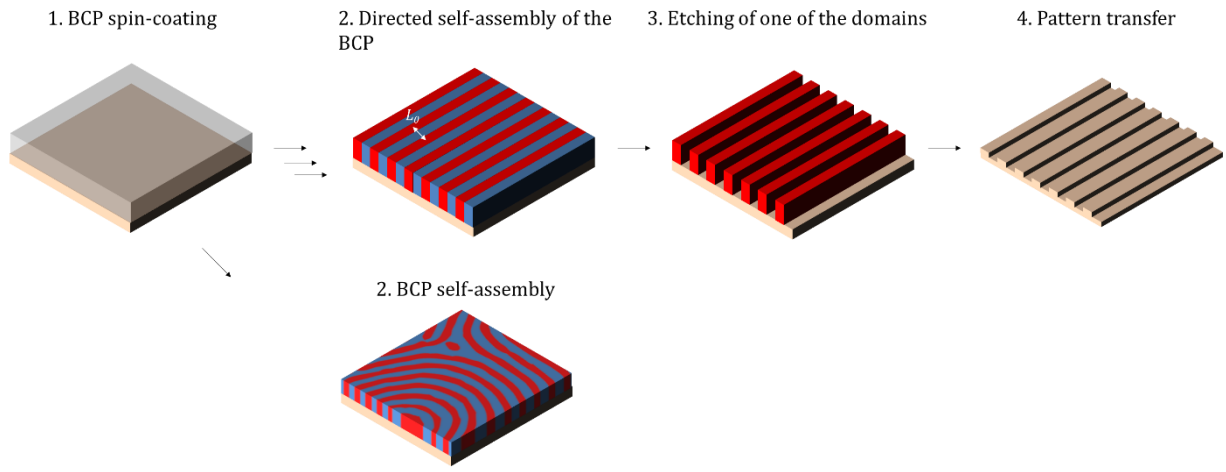

Figure 1-19 : Scheme of the general principle of BCP lithography.

The choice of the BCP system is of great importance for the targeted dimensions and applications. Indeed, the choice of the monomer will define the χ of the system and thus the accessible dimensions (step 2 of Figure 1-19). Moreover, the nature of the blocks has to be compatible with the targeting application. For instance, in lithography applications, the blocks should have a good etching contrast in order to easily remove one of the domains by dry or wet etching (step 3 of Figure 1-19). Afterward, the remaining mask should have enough mechanical and etching resistance to serve as a mask for the transfer of the pattern in the underlying substrate (step 4 of Figure 1-19). The following part is consequently devoted to a discussion on the different BCPs systems reported in the literature for nanolithography applications with an emphasis on sub-20 nm lamellar- and cylinder-forming BCPs.

After designing the BCP system, the control of the organisation and alignment is a key issue to make BCP lithography viable at industrial scale. We have already discussed the effect of thin film confinement on the BCP nanostructures. However, an enhancement of the BCP organisation and a control of the orientation at short and long range are possible using several strategies (implemented in the step 2 of Figure 1-19) that will be exposed in the following sections.

b) Choice of the materials

The most studied BCP for the fabrication of masks for nanolithography is the poly(styrene)-*b*-poly(methyl methacrylate) (PS-*b*-PMMA) system as its synthesis at large-scale is well-controlled [46]. However, the achievable critical dimension for this particular system is higher than 22 nm because of a low Flory-Huggins parameter: $\chi = 0.03$ at room temperature (RT) [74]. Increasing χ would allow to observe a microphase separation for smaller degree of polymerization and therefore decrease the critical dimensions of the domains. That is why the self-assembly of high-χ BCP is a challenge to date in order to reduce the characteristic dimensions of structures below 20 nm or even 10 nm. For this purpose, it requires an increase of the incompatibility between the blocks by, for example, (i) incorporating inorganic atoms into one of the blocks, (ii) increasing the hydrophobicity/hydrophilicity balance of the blocks, or (iii) inducing crystallinity [75]–[77]. Table 1-1 lists some of the diblock copolymers systems that were

studied in the literature, as well as their morphology, characteristic size and Flory-Huggins parameter.

It is possible to see the effect of the addition of an inorganic atom on the interaction parameter. For example, by replacing the PMMA block with an inorganic block (such as poly(1,1-dimethylsiloxane) (PDMS)), the Flory-Huggins parameter increases from 0.03 for PS-*b*-PMMA to 0.26 for PS-*b*-PDMS (at RT) (see Table 1-1). Moreover, the advantage of a Si-containing block is that it can form silicon oxides after an oxygen plasma treatment enhancing the etching contrast as regards to all-organic BCPs: one could therefore have a robust silicon oxide mask more suitable for further pattern transfer than a fragile organic mask. As example, one can cite the work of Lee et *al*. in which they obtained PDMS cylinders with 8.5 nm diameter and 17.7 nm periodicity from a 16 kg.mol^{-1} PS-*b*-PDMS as shown in Figure 1-20. An oxygen/fluorine plasma was performed in order to remove the PS cylinders while leaving a mask of the oxidized PDMS matrix [78].

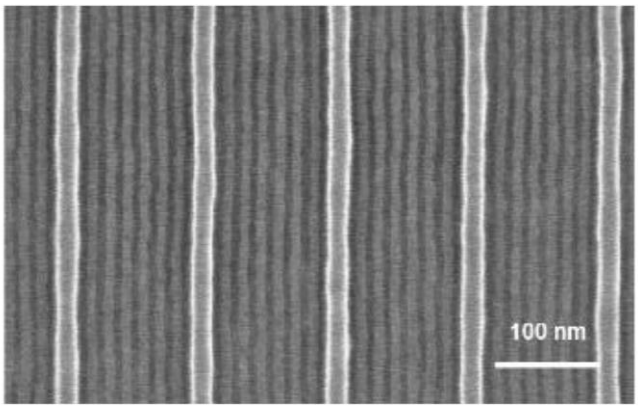

Figure 1-20: Transmission electron microscopy (TEM) image of cylinder-forming PS-*b*-PDMS in thin film. The long-range ordering is obtained using the graphoepitaxy technique [78].

Similarly, the use of an inorganic derivative of PS such as poly(trimethylsilylstyrene) (PTMSS), allows to increase threefold the poly(styrene)-*b*-poly(D,L-lactide) (PS-*b*-PLA) interaction parameter (see in Table 1-1). Figure 1-21 is an AFM image of PTMSS-*b*-PLA lamellae with a periodicity of 13 nm obtained by Cushen et *al*. [80]. Thanks to the strong etching contrast between the two blocks, an oxygen plasma was able to remove the PLA domains (degradation rate of the PLA 12 times higher than that of the PTMSS) [79].

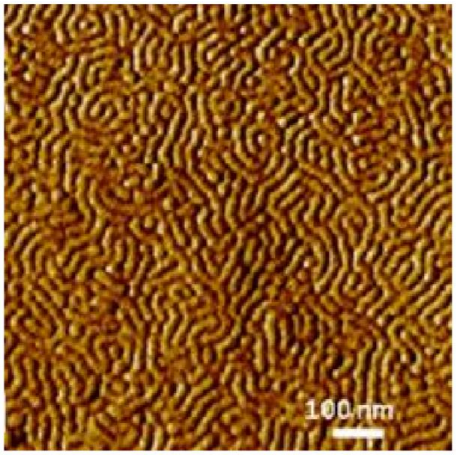

Figure 1-21: AFM phase image (1 µm x 1 µm) of lamellar-forming PTMSS-*b*-PLA BCP in thin film after a solvent annealing treatment (L_0 = 13 nm) [80].

The use of a Si-containing semi-crystalline block also provides an increase of the Flory-Huggins parameter and a good etching contrast. Hirai et *al.* associated polyhedral oligomeric silsesquioxane (POSS) semi-crystalline molecules to PS and PMMA, respectively, to obtain out-of-plane lamellae [80]. Aissou et *al.* also used a PDMSB-*b*-PMMA BCP to obtain sub-20 nm features and proposed that the crystallinity of the PDMSB block acts as an additional driving force of the microphase separation [76], [77].

As said previously, it is also possible to modulate the χ parameter by increasing the hydrophobicity of one of the blocks. The use of a poly(4-*tert*-butylstyrene) (PtBS) block instead of a PS block has been shown to drastically increase the χ parameter of modified PS-*b*-P2VP and PS-*b*-PMMA systems: the χ of the PS-*b*-P2VP was indeed multiplied by 1.5 (Table 1-1) [81] while the χ of the PS-*b*-PMMA was multiplied by 3 with $\chi_{PtBS\text{-}b\text{-}PMMA}$= 0.09 at RT [82]. Similarly, by replacing the PS block in the archetypical PS-*b*-PMMA system with a more hydrophobic block, i.e. poly(cyclohexylethylene) (PCHE), an increase of the Flory-Huggins parameter was observed as well (0.32 at RT [73]). Kennemur et *al.* were thus able to produce out-of-plane lamellae with a periodicity of 15 nm as shown in the Figure 1-22 [73].

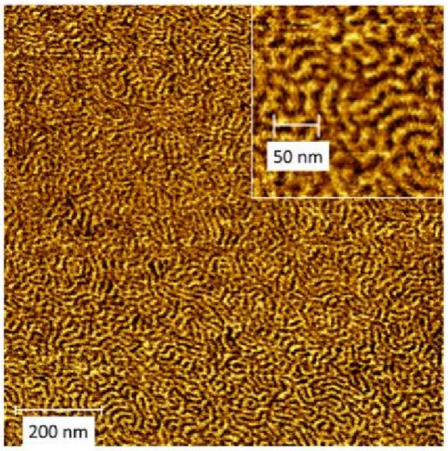

Figure 1-22: **AFM phase image (1 µm x 1 µm) of lamellar-forming PCHE-*b*-PMMA BCP in thin film after a solvent annealing treatment (L_0 = 15 nm) [73].**

Table 1-1: Non-exhaustive list of the high-χ BCPs studied in the literature. The two last columns refer to the methods used to control the self-assembly; these methods will be presented in the next sections. The abbreviations of the polymers can be found at the beginning of the manuscript (see section List of abbreviations).

BCP system	Structure	χ	Morphology	Periodicity (nm)	Orientation	Method used for orientation control	Annealing method
PCHE-*b*-PLA	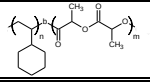	~ 0.306 at 187°C [83]	Cylinders [84]	16	Perpendicular	Nothing	SVA [2]
PTMSS-*b*-PLA	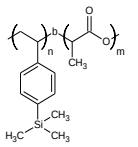	0.4 at 140°C [79]	Lamellae [85]	19	Perpendicular	X-linked [3] copolymer mat + top-coat	TA [4]
			Lamellae [79]	13	Perpendicular	Nothing	SVA
			Cylinders [79]	13	Perpendicular	Nothing	SVA
			Cylinders [86]	13.5	In-plane	Nothing	SVA
			Lamellae [86]	18.7	Perpendicular	X-linked copolymer mat	SVA
PS-*b*-PLA	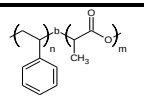	~ 0.219 at RT [87] ~ 0.13 at 140°C [79], [88]	Lamellae [87]	32.5	Perpendicular	Nothing	STVA [5]
PS-*b*-PDMS	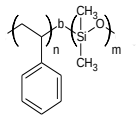	0.26 at RT [89], [74], [85]	Cylinders [78]	17.7	In-plane	Homobrush	SVA
			Cylinders [90]	18.4		Nothing	SVA
			Cylinders [91]	18.2	Perpendicular	Top-coat	SVA
			Lamellae [92]	35		Homobrush	SVA
PS-*b*-PEO	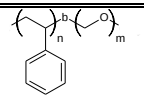	~0.049 at 140°C [79] ~ 0.08 at RT [74]	Lamellae [93]	15	Perpendicular	Nothing	STVA

[2] Solvent annealing
[3] Crosslinked
[4] Thermal annealing
[5] Solvo-thermal annealing

PS-*b*-PMAPOSS	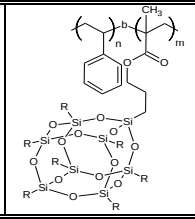	N.A[6]	Lamellae [80]	38	Perpendicular	Nothing	SVA
PS-*b*-PMA	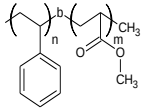	~0.068 at 150°C [94]	Lamellae [94]	13.9	Perpendicular	-	TA
PS-*b*-PLGA	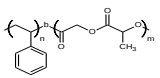	~0.098 at 200°C [95]	Lamellae [95]	27	Perpendicular	-	TA
PMMA-*b*-PMAPOSS	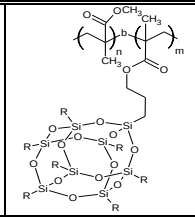	N.A	Cylinders [80]	20	Perpendicular	Nothing	SVA
PS-*b*-PTMSS	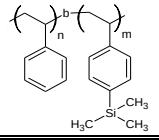	N.A	Lamellae [96]	18	Perpendicular	X-linked copolymer mat + top-coat	TA
PS-*b*-PTMC-Me	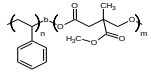	N.A	Lamellae [97]	19	Perpendicular	Homobrush + additives	TA
PS-*b*-P4VP	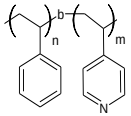	N.A	Cylinders [98]	25	Perpendicular	Homobrush	SVA
PS-*b*-P2VP	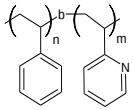	~ 0.18 at RT [99]	Cylinders [100]	37	Perpendicular	Nothing	SVA
			Lamellae [101]	28		Brush + additives	TA

[6] Not attributed

PtBS-*b*-P2VP	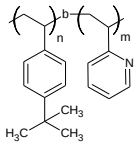	~ 0.11 at 150°C [81]	Cylinders [81]	Diameter ~ 9 nm	In-plane	Nothing	TA
PS-*b*-PMMA	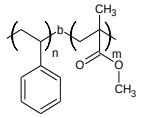	~ 0.03 at RT [82]	Cylinders [102]	60	In-plane	Nothing	TA
			Lamellae [103]	27	Perpendicular	Random copolymer brush	TA
			Lamellae [104]	14	Perpendicular	Random copolymer brush	TA
PCHE-*b*-PMMA	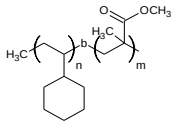	~ 0.32 at RT [73]	Lamellae [73]	14	Perpendicular	HMDS[7] surface treatment	SVA
PDMSB-*b*-PMMA	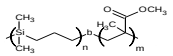	~ 0.20 at RT [8]	Cylinders [77]	16.5	In-plane	Nothing	TA
			Cylinders [76]	9.7	In-plane	Nothing	TA
PVBD-*b*-PDSS	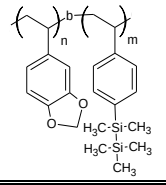	N.A	Lamellae [96]	10	Perpendicular	X-linked copolymer mat + TC	TA

[7] Hexamethyldisilazane

[8] $\chi = (34.16)/T + 0.0855$ experimentally determined by Fleury G. *et al*. (LCPO)

c) Control of the organization of the BCP domains

In thin film configuration, the BCP chains undergo constraints that can kinetically trap the segregated structure into an out-of-equilibrium state with poor order. To reorganize the BCP structure into well-ordered nanodomains, the chains must have sufficient mobility. Moreover, the domains generally adopt a random orientation, generally an in-plane orientation in the case of cylinders and lamellae, which is detrimental for most technological applications (it prevents the further removal of the domains during the etching step). This is especially true for the high-χ BCPs because of their very large difference in surface energies [91]. The challenge was thus to develop methodologies allowing to control the ordering as well as the orientation of the BCP domains in nanostructured BCP thin films.

(1) Thermal annealing

Thermal annealing consists of heating the BCP chains above their glass transition in order to give mobility to the chains and promote the self-assembly. The film is then cooled down to quench the final ordered structure. The thermal annealing process remains the most widely used technique to date thanks to its simplicity and ease of application at industrial scale. Thermal annealing has been used by many research groups to organize in-plane [102] and out-of-plane cylinders [105] of PMMA in a PS matrix or to obtain out-of-plane PS and PMMA lamellar domains [103], [104].

However, the thermal annealing process has some limitations since the thermal energy alone is not generally enough to give sufficient mobility to the chains or requires high temperatures and long annealing times that can lead to the dewetting of the BCP thin films [105], [88]. For instance, the PS-*b*-PMMA cylindrical or lamellar structures presented in Table 1-1 were annealed at approximately 250°C for two hours due to their high molar mass (higher than 40 kg.mol^{-1}) [102]–[104]. The increase in annealing temperature appears to be an interesting solution to self-assemble high molar mass (and low χ) BCPs and to overcome the activation barriers in order to reduce the number of defects [95]. However, in the case of high-χ BCPs, it is more complicated to

use thermal annealing. Indeed, the chain diffusion is low for a high χ system (at given N) which generally hinders the thermal annealing efficiency [78], [106]. To overcome these limitations, solvent vapour annealing is increasingly used and will be the purpose of the following section.

(2) Solvent vapour annealing

Solvent annealing involves putting the polymer film in contact with solvent vapours to promote mobility and induce the organization of the polymer chains [86], [107]. Several protocols have been reported to expose the film to a vapour of solvent, the most common being to (i) put the film in a desiccator containing a vial of the given solvent (static annealing), (ii) expose the film to a continuous flow of solvent vapours controlled with a carrier gas (dynamic annealing) [108], [107]. Solvent vapour annealing is generally carried out at RT allowing mild application conditions as opposed to thermal annealing which requires high temperatures [107].

As a demonstration, Hirai et *al.* used this technique to self-assemble a PMMA-*b*-PMAPOSS BCP chains into out-of-plane cylinders as shown in the Figure 1-23. The PMMA domains were removed using a O_2 etching treatment leading to a PMAPOSS mask [80].

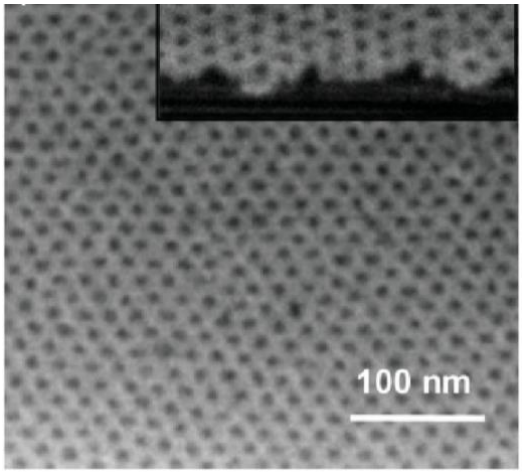

Figure 1-23: **AFM images of cylinder-forming PMMA-*b*-PMAPOSS in thin film after the removal of the PMMA domains [80].**

It is possible to distinguish two main steps in the solvent annealing process. The first step consists in putting into contact the film with the solvent vapours, which is accompanied by a swelling of the film (in the case of the use of a good solvent) because of the solvent adsorption and of the

diffusion of the solvent within the film. The second step is the removal of the film from the solvent-saturated atmosphere. When this step is quickly carried out (out-of-equilibrium), the BCP structure is frozen into the state it had in the swelled state [86].

Using a selective solvent to one of the two blocks will lead to an unequal partition of the solvent molecules within the domains. This swelling of the block(s) will give to the chains sufficient mobility to self-organize [86]. In order to have an insight of the interactions between the blocks in the swollen state, it is usual to define the effective Flory-Huggins interaction parameter, χ_{eff}. This parameter reflects the presence of the solvent in the system during the solvent annealing [78]. For example, the preferential swelling of one of the blocks will increase the incompatibility of the blocks resulting in an increase of χ_{eff} [107]. In the case of a non-selective solvent, the homogeneous repartition of the fluid within the blocks will lead to a disorder polymer state (decrease of χ_{eff}) contrary to a selective solvent [109].

As a preferential swelling can lead to a change in the volume fraction of the block, it can thus lead to a change in morphology. As example, Borsworth et *al.* observed an order-order transition during the annealing of poly(α-methylstyrene)-*b*-poly(4-hydrostyrene) by acetone vapour (selective to the 4-hydrostyrene block) with a transition from a cylindrical to spherical morphology [109], [107]. Paik et *al.* studied using grazing-incident small angle X-ray scattering (GISAXS) the organization of the same copolymer and also found that order-order transitions can occur depending on the annealing conditions. Indeed, spheres were obtained after the solvent annealing of the film with acetone (selective to the 4-hydrostyrene block), while a solvent annealing process with tetrahydrofurane (THF) (solvent with a low selectivity) led to in-plane cylinders. Finally, they showed that by alternating these two solvents during the annealing process (THF and acetone), it was possible to switch from one morphology to the other in a reversible way (Figure 1-24) [110].

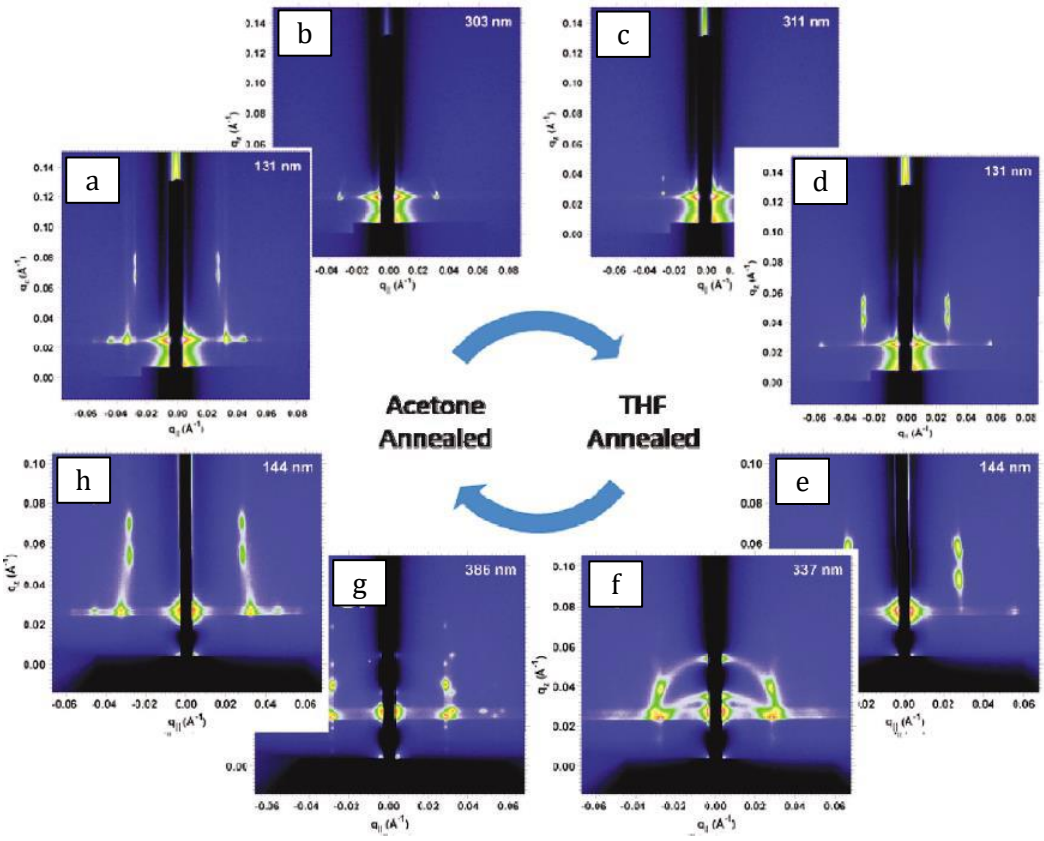

Figure 1-24: **Control of the morphology of the poly(α-methylstyrene)-*b*-poly(4-hydrostyrene) with the solvent used for the annealing treatment. The morphological change was monitored by GISAXS which shows the characteristic pattern (a) of a spherical morphology when using acetone vapours, followed by the one (d) of the cylindrical morphology when using THF vapours and finally, the recovery (h) of the spherical morphology when back to acetone vapours [110].**

These works highlighted the importance of the choice of the solvent to ensure the organization of the BCP domains into the desired morphology. It is consequently common to use a mixture of solvents to avoid morphological transition to occur; each solvent having an affinity for each block. By controlling the degree of swelling of each block (*via* the control of the solvent vapour flow rate), it is then possible to swell the two blocks in the same way and thus retain the volume fractions of the blocks [86], [100], [107]. Moreover, a mixture of solvent can be very effective because it will decrease the miscibility of the blocks increasing thus the effective interaction parameter so that is possible to organize BCP systems whose the product $\chi_{AB}N$ is not sufficiently high [86]. Conversely, the use of a non-selective solvent will result in an increase of the miscibility of the domains (= decrease of the effective interaction parameter) and thus a decrease of their periodicity [107], [111]. These variations can be preserved after a quick drying, the structure remaining frozen in its current swollen state.

Apart from the block selectivity, a key criterion for choosing the solvent is the vapour pressure. The vapour pressure can be defined as the pressure at which the phase gas of a substance is in equilibrium with its liquid or solid phase at a given temperature in a closed system. Thus, the vapour pressure of a solvent will dictate the ease with which the molecules passed from the liquid phase to the gaseous phase. The highest is this pressure, the fastest the solvent molecules will move to the vapour phase to achieve the equilibrium pressure (= high evaporation rate). As one needs to provide sufficient mobility to the chains, the solvent molecules must remain long enough in the polymer film and therefore the evaporation rate of the solvent has to be slower than the characteristic diffusion time of the chains. For this reason, lower vapour pressure solvents such as toluene or chlorobenzene (21 mmHg and 87 mmHg at 20°C, respectively) are preferred to high vapour pressure solvents such as tetrahydrofuran (144 mmHg at 20°C) or dichloromethane (355 mmHg at 20°C) [108]. Moreover, Kim et *al.* reported that the residence time of the solvent in the film is crucial to avoid the appearance of structural defects [114] which is linked to the solvent vapour pressure and its affinity for the blocks.

Several theories are currently being discussed to describe the mechanisms taking place during the second stage of drying. The most frequently reported is considering a solvent front inducing a solvent concentration gradient in the BCP film that further generates both the organization and the orientation of the nanodomains as shown in the Figure 1-25 [79], [88], [91], [107], [112].

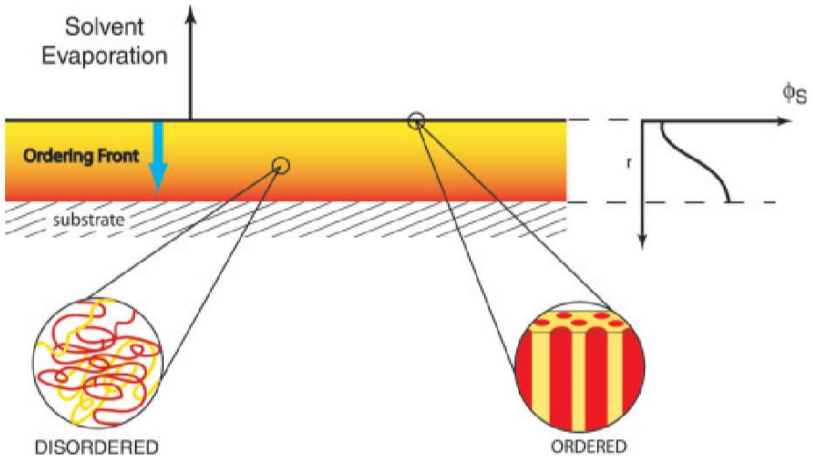

Figure 1-25: Scheme of the mechanism proposed in order to explain the orientation and the organization of the BCP domains during the solvent annealing treatment : the orientation of the domains is perpendicular to the evaporation front. Φs is the volume fraction of the solvent and r is the film thickness.

To summarize, the efficiency of the solvent vapour annealing techniques lies on the numerous parameters allowing the fine tuning of the self-assembly thermodynamics and kinetics. Thanks to this wide range of parameters, it is thus possible to drive the organization of the nanodomains into a highly ordered structure which is difficult to obtain with thermal annealing. As an example, Figure 1-26 shows the long-range ordering that Park et *al.* were able to achieve with poly(styrene)-*b*-poly(4-vinylpyridine) (PS-*b*-P4VP) by using an ethanol vapour annealing [98].

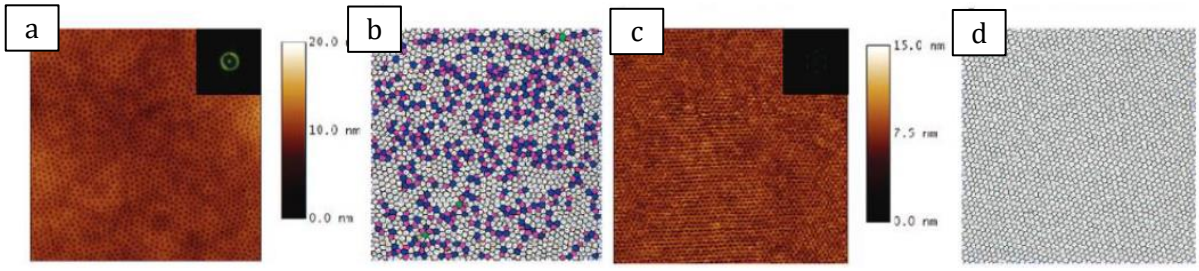

Figure 1-26: AFM phase images (2 µm x 2 µm) of a cylinder-forming PS-*b*-P4VP in thin film before ((a) and (b)) and after ((c) and (d)) the solvent annealing treatment. A Fourier transform and a program based on the Voronoï construction diagram were used to highlight the degree of ordering obtained by the annealing treatment [98].

One can also cite the work of Cushen et *al.* that used solvent vapour annealing to organize PLA cylinders with 8.8 nm diameter in a PTMSS matrix [79]. Figure 1-27 shows the AFM images of the cylinders they obtained before (Figure 1-27(a)) and after thermal annealing (Figure 1-27(b)) and solvent annealing (Figure 1-27(c)). It shows the ability of solvent annealing to obtain better organization of the nanostructure with a controlled orientation as compared to thermal annealing process.

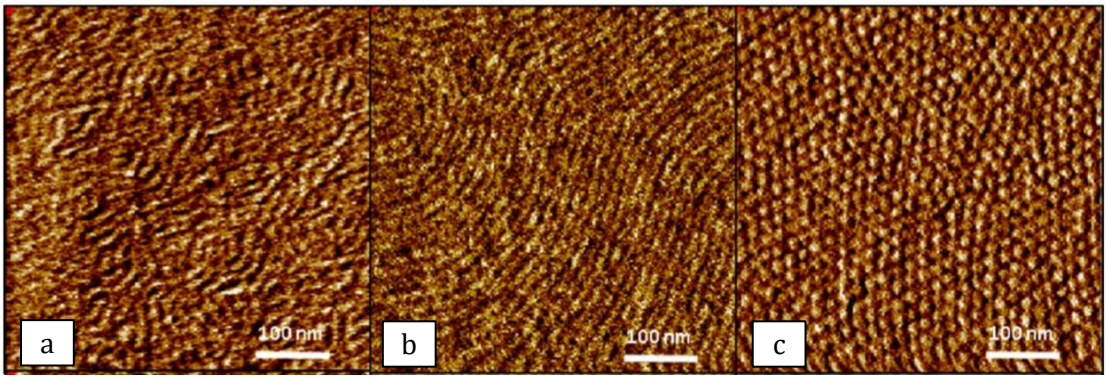

Figure 1-27: AFM phase images (1 µm x 1 µm) of cylinder-forming PTMSS-*b*-PLA thin films: (a) as-cast, (b) after thermal annealing and (c) after the solvent annealing [79].

d) Control of the orientation

(1) Self-assembled monolayer (SAM)

Historically, the method used to control the substrate affinity as regards to the BCP domains is based on the use of self-assembled monolayers called "SAM". SAMs are composed of two functional groups: a head group having an affinity for the surface (typically thiol, silane or phosphate) and a "body" group (generally a long alkyl chain). In the case of sulphur terminated SAMs, a gold surface is the common substrate as the SAM molecules can easily adsorb *via* a strong gold-sulphur interaction to form ordered and oriented monolayers [113], [114]. For silicon substrates, SAMs of alkylsiloxanes are commonly used [115]. The main advantage of the SAMs is their crystalline structure allowing to form a flat and impenetrable film [114], [116]. Moreover, the surface chemistry of the SAMs can be modified by exposure to X-rays in order to tune its surface energy [117]-[120].

In 1997, Heir et *al.* were the first to study the wetting behaviour of BCPs on alkanethiols functionalized SAMs. They obtained out-of-plane lamellae of PS-*b*-P2VP using a -CH_3 terminated SAM while in-plane lamellae were obtained with a -OH terminated SAM [117]. Following this work, Nealey's group worked on the effect of a X-ray chemically-modified SAM of octadecyltrichlorosilane on the self-assembly of PS-*b*-PMMA BCPs [115], [118]. They observed a transition from symmetric to neutral to asymmetric wetting with the increasing of the X-ray dose due to an increase of the hydrogen and dipole-dipole interactions between the surface and the PMMA block. Other examples of the use of SAMs can be found elsewhere and have demonstrated the ability of SAMs to control the self-assembly of BCPs in thin films [119]–[122].

(2) Grafting of random copolymers

Nowadays, the grafting of random copolymers is the most conventional technique for substrate neutralization. The principle is to modify the substrate with a random copolymer brush with a finely tuned composition in A and B monomers so that none of the A and B blocks have a preferential interaction with the substrate. Mansky et *al.* were the first to demonstrate the grafting

of a random copolymer to neutralize a silicon substrate [123]. For this purpose, a hydroxyl-terminated PS-*r*-PMMA was grafted by dehydration at 140°C for 2 days with f_{PS} = 0.57, which was found to be the neutral composition for the lamellar PS-*b*-PMMA used in this study [123]. Han et *al.* studied the evolution of the orientation of cylinder-forming and lamellar-forming PS-*b*-PMMA by varying the PS-*r*-PMMA composition from f_{PS} = 0.45 to f_{PS} = 0.72 [124]. The Figure 1-28 presents the scanning electron microscope (SEM) images of lamellar-forming PS-*b*-PMMA after their self-assembly on the grafted PS-*r*-PMMA copolymers. For $f_{PS} \leq 0.50$, the brush has a slight affinity for the PMMA block. However, the lamellar structure is not strongly affected as out-of-plane lamellae are still observed although a large number of defects is present reflecting the non-optimal self-assembly. When the fraction of PS increases, the BCP domains orient perpendicular over the entire surface. Beyond f_{PS}= 0.52, a mixed orientation of the BCP domains is obtained as the grafted layer is PS-affine.

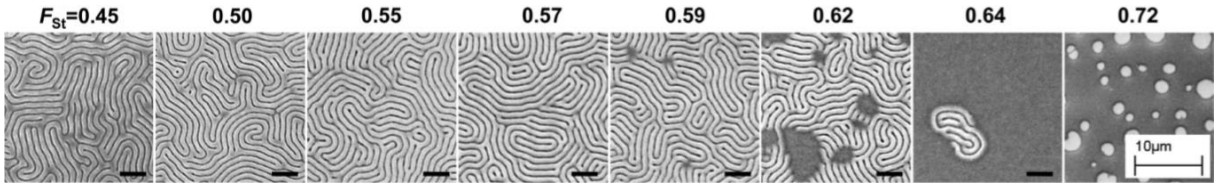

Figure 1-28: SEM images of a lamellar-forming PS-*b*-PMMA BCPs on PS-*r*-PMMA brushes of different compositions starting from f_{PS} = 0.45 to f_{PS} = 0.72 where f_{PS} is the fraction of styrene in the random copolymer [124].

Moreover, in order to reach a perfect out-of-plane orientation of the domains, the total molecular weight and the grafting density of the random copolymer are also key parameters. Indeed, insufficient molecular weight or grafting density lead to a bad coverage of the substrate resulting in parallel or mixed orientations of the BCP domains. Sparnacci et *al.* highlighted these effects on cylinder-forming PS-*b*-PMMA. As shown in the Figure 1-29, out-of-plane cylinders are obtained using high molecular weight grafted polymer (M_n > 8700 g.mol^{-1}) with a grafting density greater than 0.34 chains.nm^{-2} [125].

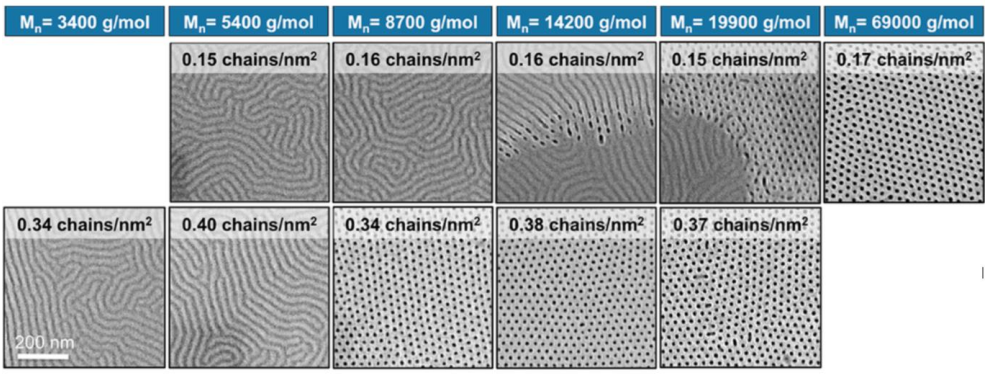

Figure 1-29: **SEM images of a cylinder-forming PS-*b*-PMMA BCP on PS-*r*-PMMA brushes of different molecular weight and grafting density [125].**

PS-*r*-PMMA brushes were used by many groups over the past years including the work of Chevalier et *al.* and Borah et *al.* in 2013 to obtain out-of-plane PS-*b*-PMMA lamellae [126], [127]. In et *al.* demonstrated that it was also possible to graft a polymer chain *via* their pendant groups using hydroxyethyl methacrylate (HEMA) as a third co-monomer as shown in the Figure 1-30. The pendant hydroxyl group is able to undergo a dehydration reaction with the substrate for a shorter processing time (≈ 4 h at 140 °C) [128].

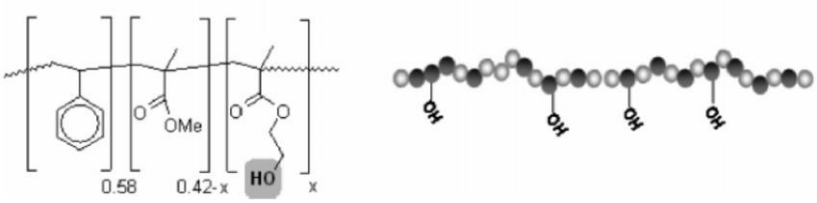

Figure 1-30: **Structure of the random PS-*r*-PMMA BCP modified with a small fraction of HEMA [128].**

(3) Grafting of homopolymer or BCP

The main drawback of the random copolymer approach is its lack of versatility. Indeed, it implies to have monomers that can be randomly polymerized, thus having similar reactivity ratios. However, it is difficult to obtain random copolymer brushes for high-χ BCPs, as the monomers constituting the BCPs have very different polymerization abilities, thus limiting the use of random copolymers to particular BCP systems. That is the reason why the grafting of homopolymers and BCPs has been utilized as an alternative method to obtain perpendicular microdomains.

In this way, homopolymers can also be grafted allowing the neutralization of the substrate. For example, Guo et *al.* played on the grafting density of PS-OH brushes with the respect to thickness commensurability in order to obtain out-of-plane lamellae and out-of-plane cylinders. It was assumed that the PS brush induced surface heterogeneity directing the microdomain orientation [129]. Another example was provided by Ji et *al.* by using a mixture of PS-OH, PMMA-OH and a short PS-*b*-PMMA as underlayer. Indeed, the short PS-*b*-PMMA ($M_{n,PMMA}$ = 5000 g.mol^{-1} and $M_{n,PS}$ = 5000 g.mol^{-1}) plays the role of compatibilizer in order to graft homogeneously the homopolymers onto the substrate. This method allows to obtain out-of-plane lamellae for a symmetrical PS-*b*-PMMA BCP [130]. Similarly, Gu et *al.* grafted a hydroxyl-terminated PS-*b*-PEO BCP onto a silicon substrate [131], and demonstrated its ability to neutralize the surface for PS-*b*-PEO BCPs having similar compositions.

(4) Crosslinked neutral layer

Instead of grafting a neutral layer, it is also possible to crosslink a polymer layer to allow the subsequent deposition of a BCP thin film. The main advantage of this approach is the production of neutral surfaces independently of the substrate surface chemistry. Indeed, the dehydration of hydroxyl-groups leading to grafted underlayers requires substrates presenting oxidized surfaces. There are also other grafting chemistries such as thiol-gold interactions [132], azide-alkyne cycloaddition [133] or thiol-ene click [134], but they are still limited to a particular type of substrates. The use of a crosslinked polymer layers could thus provide an alternative way for substrate independency as the crosslinking reaction should not be affected by the underlying substrate [135].

In 2005, Ryu et *al.* were the first to demonstrate the use of heat-induced crosslinked polymers as neutral layer. They randomly incorporated 2% of reactive benzocyclobutene functionality along the backbone of a random PS-*r*-PMMA copolymer to form an insoluble neutral film applicable to Au, Al, Si_3N_4, and Kapton substrates [136]. Jung et *al.* incorporated azide groups in the PS block of a cylinder-forming PS-*b*-PMMA BCP. The self-assembled BCP was then crosslinked allowing the spin-coating and the further self-assembly of a lamellae-forming PS-*b*-PMMA BCP. Interestingly,

the perpendicular lamellae are registered onto the underlying perpendicular cylinders as shown in Figure 1-31 [137]. One can also cite the recent work of Pang et *al.* on the thermal crosslinking of PMMA by introducing small amount of glycidyl methacrylate moieties [138].

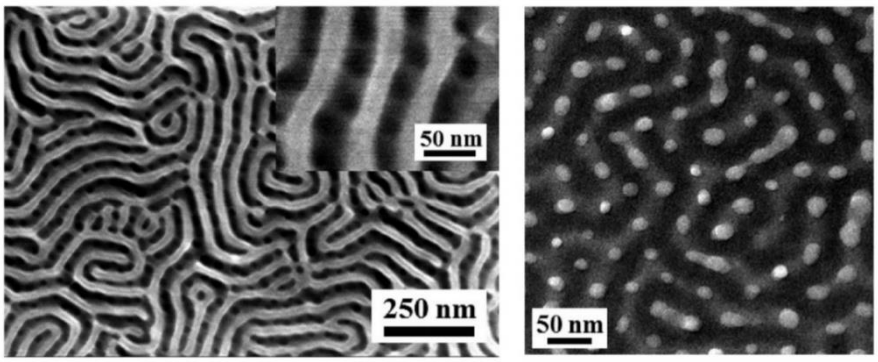

Figure 1-31: SEM (left) and TEM (right) images of a lamellae-forming PS-*b*-PMMA BCP on a crosslinked underlayer of cylinder-forming PS-*b*-PMMA [137].

It is also possible to induce the crosslinking reaction using UV radiation instead of heat. Indeed, Bang et *al.* used the azide chemistry to UV-induced the crosslinking of a random copolymer avoiding thus a high temperature process. They were also able to photo-pattern the neutral layer resulting in well-defined areas of in-plane and out-of-plane orientations for both lamellar- and cylinder-forming PS-*b*-PMMA BCPs [139]. Han et *al.* demonstrated the use of several photo-crosslinkable random copolymers using alternative functional groups such as acryloyl and epoxy in the presence of a photoinitiator and a photoacid generator, respectively [105], [140]. As example of UV-crosslinked homopolymer, one can cite the work of Cheng et *al.* as they used UV-crosslinked PS homopolymers to obtain an out-of-plane orientation of cylinder-forming brominated poly(styrene)-*b*-poly(methyl methacrylate) (PBrS-*b*-PMMA) BCPs.

Both thermal- and UV-crosslinking reactions used in order to obtain a neutral layer are all following a two-step procedure: a spin-coating step and a subsequent crosslinking. Moni et *al.* reported the only study describing an one-step process to produce a crosslinked underlayer of poly(divinyl benzene) (PDVB) using iCVD (Initiated Chemical Vapour Deposition) [141]. The mechanism of formation of the PDVB layer will be discuss in the 3rd chapter as they further used this methodology to deposit a neutral top-coat layer.

3. Methods for directed self-assembly

One of the challenges for the integration of the BCPs in the microelectronics industry is the lack of long-range ordering of the BCP structures. Indeed, most of the applications required the precise positioning or registration of the BCP domains; however, a polygrain BCP structure is experimentally observed in thin film due to slow coarsening kinetics, even if the equilibrium energy state of a BCP nanostructured film is a single grain of well-ordered domains. This weak thermodynamic driving force led scientists to develop DSA methods providing means to control domain alignment and orientation while inducing defect annihilation at grain boundaries. The most developed methods of alignment are graphoepitaxy, which is based on the use of topographical constraints to guide the BCP self-assembly, and chemoepitaxy, which used chemical affinity to drive the self-assembly process.

a) Graphoepitaxy

The graphoepitaxy technique consists of depositing a BCP into topographical patterns (generally trenches) obtained by optical lithography. The pattern will act as a physical guide for the BCP nanostructure to align during the annealing process. Indeed, the BCP domains will be constrained by both side walls, which will lead to an orientational field inducing the long-range ordering of the BCP structure. Moreover, this lateral ordering is generally enforced by inducing a selective wetting of one of the block at the side walls by grafting homopolymer brushes for example [142], [143]. Figure 1-32 shows the principle of the technique for the alignment of a lamellar-forming BCP [143].

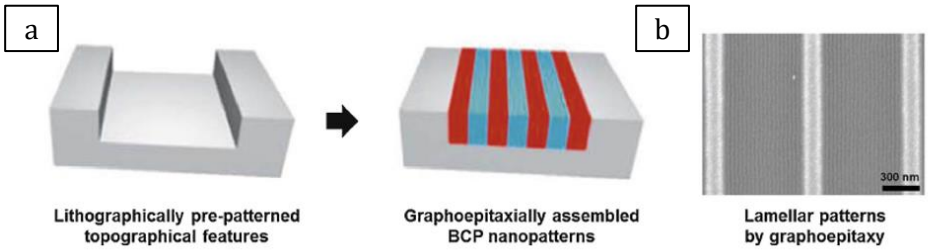

Figure 1-32: (a) Scheme of the graphoepitaxy method utilizing topographic pattern to direct BCP assembly and (b) SEM image showing long-range ordered lamellae of PS-*b*-PMMA obtained by graphoepitaxy [143].

Graphoexpitaxy implies the use of photosensitive resins to fabricate the guiding patterns. However, the self-assembly of the BCP often requires the use of solvents and high annealing temperatures (200-250°C) that might damage most of the commercially available resins. Some studies highlight the use of silica-based inorganic resins or the chemical modification of conventional resins to address this problem [144]. Another solution is to use the resin as a sacrificial layer: the pattern of the resin is transferred into a hard material in order to obtain a topographical feature that is resistant to the BCP self-assembly conditions.

The dimensions of the guiding pattern are also a key parameter for the control of the BCP ordering. The periodicity of the template should be an integer number of the periodicity of the self-assembled BCP in order not to distort the BCP chains [146], [149], [150], [151]. Figure 1-33 highlights the commensurability conditions for the alignment of spheres, lamellae or cylinder-forming BCPs [145].

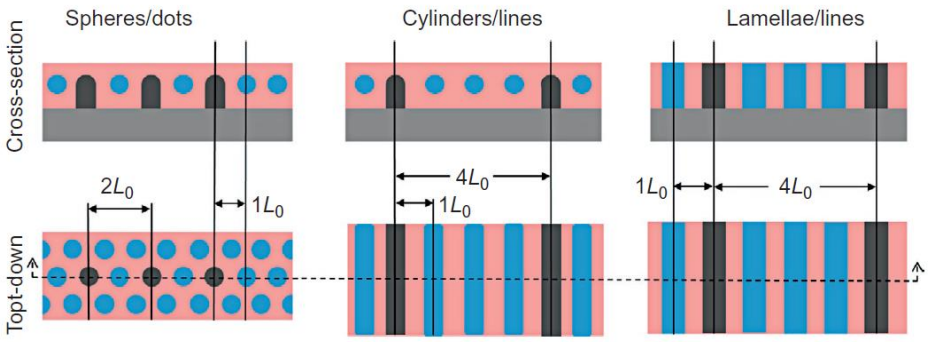

Figure 1-33 : Schematic diagrams of the commensurability conditions for the alignment of spheres, cylinders and lamellae. The templating features are at integer number of the BCP periodicity [145].

The width of the pattern is also crucial for the alignment of the BCP domains as the alignment of the BCP is mostly induced by the walls of the topographical pattern. In the case of trenches, the alignment quality can be lost in the center of the pattern if the trench width exceeds a certain threshold value [146], [147].

b) Chemoepitaxy

The chemoepitaxy consists of depositing the BCP chains on a chemically patterned surface having an affinity with one of the blocks in order to promote the alignment of the BCP domains as shown in the Figure 1-34 [143], [147].

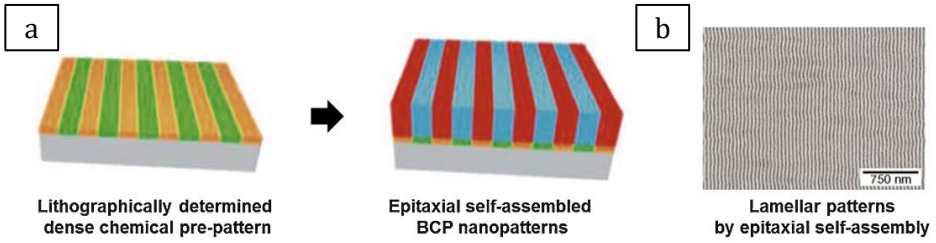

Figure 1-34: **(a) Scheme of the epitaxy method utilizing a chemical pattern to direct the BCP assembly. The green lines are affine to the blue block so that the blue domains follow the affine lines and induce the long-range ordering. (b) SEM image showing long-range ordered lamellae of PS-*b*-PMMA obtained by chemoepitaxy [145].**

This BCP alignment method has been the most actively researched area following the pioneering works of Nealey and co-workers, which developed a process for the alignment of lamellar-forming PS-*b*-PMMA. This is as today the accepted process flow for the integration of BCP self-assembly into integrated circuit manufacturing with a patented process known as the Liu–Nealey (LiNe) process [148].

Figure 1-35(a) shows the different steps of the process. To obtain the chemically patterned substrate, they first deposited and crosslinked a PS layer (step A in the Figure 1-35(a)). Then, they deposited a photosensitive resin in order to define a pattern using immersion lithography or electron-beam lithography (step B). The periodicity of the lines has to be n times the periodicity of the lamellae in order to match the affine PS lines with the PS domains (see the step F). Moreover, to control more precisely the width of the patterned lines (to be equal to the selected BCP domain size), the resin is etched (see step C, the term “trimming” is commonly used). The crosslinked PS that is not covered by the resin is then removed by a dry etching process (step D) followed by the removal of the resin (the term “stripping” is commonly used) resulting in a patterned substrate with crosslinked PS lines. A PS-*r*-PMMA brush is then deposited and grafted in between the PS

lines, which result in a surface alternating PS-affine lines and neutral areas (step E). Finally, the PS-*b*-PMMA is deposited and annealed in such way that the PS domains follow the crosslinked PS lines in order to obtain a long-range ordering of out-of-plane lamellae.

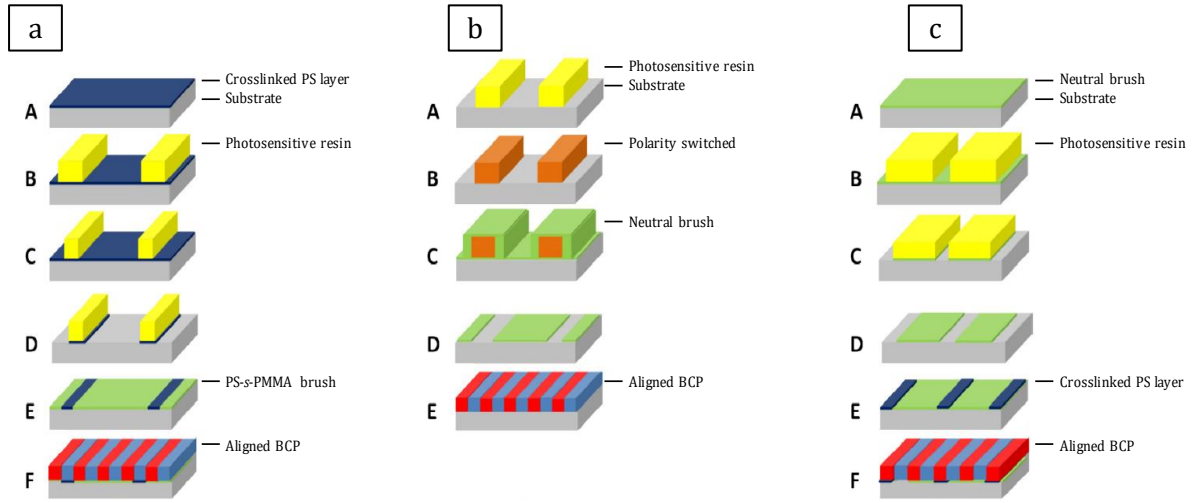

Figure 1-35: Process flows for chemoepitaxy of block copolymer patterns. (a) is the LiNe process, (b) is the IBM lift-off process and (c) is the process flow from AZ Electronic Materials scientists [143].

Researchers at IBM have extended the Nealey process and proposed a process called "lift-off" (see Figure 1-35(b) [152], [154]). The main innovation is the use of a photosensitive resin that can be "switched" from positive to negative polarity. Indeed, a chemically amplified 193 nm positive resin (CAR) is deposited and exposed using immersion lithography (step A). As stated in the previous section, the exposed part of the resin can then be removed using an alkaline solution (tetramethylammonium hydroxide - TMAH) due to the acidolysis of the pendant tertiary ester groups to produce carboxylic acid groups. The lines are further exposed to deep-UV irradiations in order to catalyse the deprotection of the remaining protecting groups (ester groups) (step B). A neutral brush is then deposited and grafted (step C). The resin is removed with TMAH (lift-off) carrying with it the non-grafted chains of the neutral brush (step D). Finally, a PS-*b*-PMMA is deposited and annealed in such way that the PMMA domains follow the lines non-covered by the neutral brush leading to a long-range ordering of out-of-plane lamellae. Scientists at AZ Electronic Materials designed a similar method than the LiNe process, the only difference being that they start with the deposition of the neutral layer (see Figure 1-35(c)) [149].

III. Conclusion

In this chapter, the concept of DSA lithography based on BCP self-assembly has been introduced. We have shown that BCP self-assembly is a good alternative to address the limitations of conventional lithography methods since it allows to produce spontaneously self-assembled structures with nanometric length scale. However, some challenges remain to be tackled in order to assert the viability of this bottom-up approach at an industrial scale. The achievement of smaller features requires high-χ BCP systems whose the design and development are tedious. Indeed, these systems have to meet several specifications which can be identified as: (i) possess a high Flory-Huggins parameter, (ii) allow the easy selective removal of one the domains to obtain a mask and (iii) have a good etching resistance in order to transfer the pattern into an underlying substrate. Moreover, the control of the organization and of the orientation at a long-range using an industrially-friendly process is needed.

The objective of our work is to demonstrate the potential of the semi-crystalline PDMSB-*b*-PS BCP for nanolithography applications considering the specifications that were highlighted in this state-of-the-art. The following chapter will be dedicated to a fundamental study of the self-assembly behaviour of the polymer in bulk and in thin film in order to evaluate its ability to segregate into various nanostructures using industrially-friendly processes.

The next chapters will subsequently present a new methodology to control the orientation of lamellar-forming PDMSB-*b*-PS BCP, morphology of interest for the line/space arrays. This control was achieved with a crosslinkable top-coat material and that allows us to build complex nanostructures of the film.

IV. References

[1] D. P. Sanders, "Advances in Patterning Materials for 193 nm Immersion Lithography", *Chem. Rev.*, vol. 110, nº 1, p. 321-360, janv. 2010.

[2] R. F. Pease and S. Y. Chou, "Lithography and Other Patterning Techniques for Future Electronics", *Proceedings of the IEEE*, vol. 96, nº 2, p. 248-270, févr. 2008.

[3] S. G. Kaplan and J. H. Burnett, "Optical properties of fluids for 248 and 193 nm immersion photolithography", *Appl Opt*, vol. 45, nº 8, p. 1721-1724, mars 2006.

[4] B. Smith, "Under Water", *SPIE's OEMagazine July*, p. 22–25, 2004.

[5] B. Hoefflinger, "The International Technology Roadmap for Semiconductors", 2011.

[6] S.-Y. Moon and J.-M. Kim, "Chemistry of photolithographic imaging materials based on the chemical amplification concept", *Journal of Photochemistry and Photobiology C: Photochemistry Reviews*, vol. 8, nº 4, p. 157-173, déc. 2007.

[7] A. Furuta and M. Hanabata, "Novolak Structures Suitable for High Resolution Positive Photoresists and Application", *J. Photopol. Sci. Technol.*, vol. 2, nº 3, p. 383-390, 1989.

[8] T. Nakayama and M. Ueda, "A new positive-type photoresist based on mono-substituted hydroquinone calixarene and diazonaphthoquinone", *J. Mater. Chem.*, vol. 9, nº 3, p. 697-702, janv. 1999.

[9] K. Tanigaki, "Characteristics of diazonaphthoquinone-4- and -5-sulfonate derivatives as sensitizers for electron-beam positive resists", *Journal of Vacuum Science & Technology B: Microelectronics Processing and Phenomena*, vol. 6, nº 1, p. 91-94, janv. 1988.

[10] A. Soyano, "Application of Polymers to Photoresist Materials", *Nippon Gomu Kyokaishi*, vol. 85, nº 2, p. 33-39, 2012.

[11] S. Takei and M. Hanabata, "Sub-70 nm resolution patterning of high etch-resistant epoxy novolac resins using gas permeable templates in ultraviolet nanoimprint lithography", *Applied Physics Express*, vol. 9, nº 5, p. 056501, mai 2016.

[12] H. Ito and C. G. Willson, "Chemical amplification in the design of dry developing resist materials", *Polymer Engineering and Science*, vol. 23, nº 18, p. 1012-1018, déc. 1983.

[13] S. A. MacDonald, H. Ito, and C. G. Willson, "Advances in the design of organic resist materials", *Microelectronic Engineering*, vol. 1, nº 4, p. 269-293, déc. 1983.

[14] C. G. Willson, H. Ito, J. M. J. Fréchet, T. G. Tessier, and F. M. Houlihan, "Approaches to the Design of Radiation-Sensitive Polymeric Imaging Systems with Improved Sensitivity and Resolution", *J. Electrochem. Soc.*, vol. 133, nº 1, p. 181-187, janv. 1986.

[15] H. Ito, M. Ueda, and R. Schwalm, "Highly sensitive thermally developable positive resist systems", *Journal of Vacuum Science & Technology B: Microelectronics Processing and Phenomena*, vol. 6, nº 6, p. 2259-2263, nov. 1988.

[16] H. Ito, C. G. Willson, J. M. J. Frechet, M. J. Farrall, and E. Eichler, "Synthesis of poly(p-hydroxy-α-methylstyrene) by cationic polymerization and chemical modification", *Macromolecules*, vol. 16, nº 4, p. 510-517, avr. 1983.

[17] K. Yamashita, "Performance of 0.2 μm optical lithography using KrF and ArF excimer laser sources", *Journal of Vacuum Science & Technology B: Microelectronics and Nanometer Structures*, vol. 11, nº 6, p. 2692, nov. 1993.

[18] E. Reichmanis, S. A. MacDonald and T. Iwayanagi, Éd, *Polymers in microlithography: materials and processes*. Washington, DC: American Chemical Society, 1989.

[19] R. D. Allen, I. Y. Wan, G. M. Wallraff, R. A. Dipietro, D. C. Hofer, and R. R. Kunz, "Resolution and etch resistance of a family of 193nm positive resists", *Journal of Photopolymer Science and Technology*, vol. 8, nº 4, p. 623-626, 1995.

[20] G. M. Wallraff, "Single-layer chemically amplified photoresists for 193-nm lithography", *Journal of Vacuum Science & Technology B: Microelectronics and Nanometer Structures*, vol. 11, nº 6, p. 2783, nov. 1993.

[21] T. Davidson, Éd., *Polymers in Electronics*, vol. 242. Washington, D.C.: American Chemical Society, 1984.

[22] S. I. Schlesinger, "Epoxy photopolymers in photoimaging and photofabrication", *Polym Eng Sci*, vol. 14, nº 7, p. 513-515, juill. 1974.

[23] K. J. Stewart, M. Hatzakis, J. M. Shaw, D. E. Seeger, and E. Neumann, “Simple negative resist for deep ultraviolet, electron beam, and x-ray lithography”, *Journal of Vacuum Science & Technology B: Microelectronics Processing and Phenomena*, vol. 7, nº 6, p. 1734-1739, nov. 1989.
[24] B. Stapp, L. Schön, H. Bayer, and M. Hoffmann, “Photo- and thermoinitiated curing of epoxy resins by sulfonium salts”, *Angew. Makromol. Chem.*, vol. 209, nº 1, p. 197-212, juill. 1993.
[25] “Dissolution inhibition mechanism of ANR photoresists: crosslinking vs. -OH site consumption”. [En ligne]. Disponible sur: https://www.spiedigitallibrary.org/conference-proceedings-of-spie/1466/0000/Dissolution-inhibition-mechanism-of-ANR-photoresists--crosslinking-vs/10.1117/12.46357.short?SSO=1. [Consulté le: 11-janv-2018].
[26] F. M. Houlihan, A. Shugard, R. Gooden, and E. Reichmanis, “An Evaluation Of Nitrobenzyl Ester Chemistry For Chemical Amplification Resists”, présenté à 1988 Microlithography Conferences, Santa Clara, CA, United States, 1988, p. 67.
[27] F. M. Houlihan *et al.*, “Chemically amplified resists: The chemistry and lithographic characteristics of nitrobenzyl benzenesulfonate derivatives.”, *Journal of Photopolymer Science and Technology*, vol. 3, nº 3, p. 259-273, 1990.
[28] T. X. Neenan, F. M. Houlihan, E. Reichmanis, J. M. Kometani, B. J. Bachman, and L. F. Thompson, “Chemically Amplified Resists: A Lithographic Comparison of Acid Generating Species.”, présenté à 1989 Microlithography Conferences, San Jose, CA, 1989, p. 2.
[29] F. M. Houlihan, T. X. Neenan, E. Reichmanis, J. M. Kometani, and T. Chin, “Design, synthesis, characterization, and use of all-organic, nonionic photogenerators of acid”, *Chemistry of Materials*, vol. 3, nº 3, p. 462-471, mai 1991.
[30] F. M. Houlihan, A. Shugard, R. Gooden, and E. Reichmanis, “Nitrobenzyl ester chemistry for polymer processes involving chemical amplification”, *Macromolecules*, vol. 21, nº 7, p. 2001-2006, juill. 1988.
[31] T. X. Neenan, F. M. Houlihan, E. Reichmanis, J. M. Kometani, B. J. Bachman, and L. F. Thompson, “Photo- and thermochemistry of select 2,6-dinitrobenzyl esters in polymer matrixes: studies pertaining to chemical amplification and imaging”, *Macromolecules*, vol. 23, nº 1, p. 145-150, janv. 1990.
[32] T. X. Neenan, F. M. Houlihan, E. Chin, E. Reichmanis, and J. M. Kometani, “The synthesis, characterization and lithographic behavior of acid photogenerating systems based upon 2-nitrobenzyl ester derivatives.”, *Journal of Photopolymer Science and Technology*, vol. 4, nº 3, p. 341-355, 1991.
[33] G. Pohlers, J. C. Scaiano, and R. Sinta, “A Novel Photometric Method for the Determination of Photoacid Generation Efficiencies Using Benzothiazole and Xanthene Dyes as Acid Sensors”, *Chemistry of Materials*, vol. 9, nº 12, p. 3222-3230, déc. 1997.
[34] J. F. Bohland *et al.*, “Some resists based on chemically-amplified crosslinking of phenolic polymers.”, *Journal of Photopolymer Science and Technology*, vol. 3, nº 3, p. 355-373, 1990.
[35] C. J. Martin, G. Rapenne, T. Nakashima, and T. Kawai, “Recent progress in development of photoacid generators”, *Journal of Photochemistry and Photobiology C: Photochemistry Reviews*, vol. 34, p. 41-51, mars 2018.
[36] H. Kinoshita, “History of extreme ultraviolet lithography”, *Journal of Vacuum Science & Technology B: Microelectronics and Nanometer Structures*, vol. 23, nº 6, p. 2584, 2005.
[37] D. De Simone, Y. Vesters, and G. Vandenberghe, “Photoresists in extreme ultraviolet lithography (EUVL)”, *Advanced Optical Technologies*, vol. 6, nº 3-4, janv. 2017.
[38] “ASML Integrated Report 2017”. 2017.
[39] “ASML Integrated Report 2018”. 2018.
[40] M. S. M. Saifullah, T. Ondar uhu, D. K. Koltsov, C. Joachim, and M. E. Welland, “A reliable scheme for fabricating sub-5 nm co-planar junctions for single-molecule electronics”, *Nanotechnology*, vol. 13, nº 5, p. 659-662, oct. 2002.
[41] M. Altissimo, “E-beam lithography for micro-/nanofabrication”, *Biomicrofluidics*, vol. 4, nº 2, p. 026503, juin 2010.
[42] A. Pimpin and W. Srituravanich, “Review on Micro- and Nanolithography Techniques and their Applications”, *Engineering Journal*, vol. 16, nº 1, p. 37-56, janv. 2012.
[43] S. Y. Chou, P. R. Krauss, and P. J. Renstrom, “Imprint of sub-25 nm vias and trenches in polymers”, *Applied Physics Letters*, vol. 67, nº 21, p. 3114-3116, nov. 1995.

[44] P. Voisin, “Lithographie de nouvelle génération par nanoimpression assistée par UV: étude et développement de matériaux et procédés pour l’application microélectronique”, p. 172.
[45] F. S. Bates, M. A. Hillmyer, T. P. Lodge, C. M. Bates, K. T. Delaney, and G. H. Fredrickson, “Multiblock Polymers: Panacea or Pandora’s Box?”, *Science*, vol. 336, nº 6080, p. 434-440, avr. 2012.
[46] C. Reboul, “Auto-assemblage de copolymères à blocs à haute force de ségrégation dans une configuration de film mince”, Université Sciences et Technologies-Bordeaux I, 2013.
[47] J. H. Rosedale, F. S. Bates, K. Almdal, K. Mortensen, and G. D. Wignall, “Order and Disorder in Symmetric Diblock Copolymer Melts”, *Macromolecules*, vol. 28, nº 5, p. 1429-1443, sept. 1995.
[48] L. Leibler, “Theory of Microphase Separation in Block Copolymers”, *Macromolecules*, vol. 13, nº 6, p. 1602-1617, nov. 1980.
[49] G. H. Fredrickson and E. Helfand, “Fluctuation effects in the theory of microphase separation in block copolymers”, *The Journal of Chemical Physics*, vol. 87, nº 1, p. 697-705, juill. 1987.
[50] T. M. Gillard, P. Medapuram, D. C. Morse, and F. S. Bates, “Fluctuations, Phase Transitions, and Latent Heat in Short Diblock Copolymers: Comparison of Experiment, Simulation, and Theory”, *Macromolecules*, vol. 48, nº 8, p. 2801-2811, avr. 2015.
[51] A. N. Semenov, “Contribution to the theory of microphase layering in block-copolymer melts”, vol. 61, nº 4, p. 733, 1985.
[52] K. Koo, H. Ahn, S.-W. Kim, D. Y. Ryu, and T. P. Russell, “Directed self-assembly of block copolymers in the extreme: guiding microdomains from the small to the large”, *Soft Matter*, vol. 9, nº 38, p. 9059, 2013.
[53] M. W. Matsen and M. Schick, “Stable and unstable phases of a diblock copolymer melt”, *Physical Review Letters*, vol. 72, nº 16, p. 2660-2663, avr. 1994.
[54] M. W. Matsen and F. S. Bates, “Unifying Weak- and Strong-Segregation Block Copolymer Theories”, *Macromolecules*, vol. 29, nº 4, p. 1091-1098, janv. 1996.
[55] D. A. Hajduk *et al.*, “The Gyroid: A New Equilibrium Morphology in Weakly Segregated Diblock Copolymers”, *Macromolecules*, vol. 27, nº 15, p. 4063-4075, juill. 1994.
[56] M. F. Schulz, F. S. Bates, K. Almdal, and K. Mortensen, “Epitaxial Relationship for Hexagonal-to-Cubic Phase Transition in a Book Copolymer Mixture”, *Physical Review Letters*, vol. 73, nº 1, p. 86-89, juill. 1994.
[57] D. B. Alward, D. J. Kinning, E. L. Thomas, and L. J. Fetters, “Effect of arm number and arm molecular weight on the solid-state morphology of poly(styrene-isoprene) star block copolymers”, *Macromolecules*, vol. 19, nº 1, p. 215-224, janv. 1986.
[58] E. L. Thomas, D. B. Alward, D. J. Kinning, D. C. Martin, D. L. Handlin, and L. J. Fetters, “Ordered bicontinuous double-diamond structure of star block copolymers: a new equilibrium microdomain morphology”, *Macromolecules*, vol. 19, nº 8, p. 2197-2202, août 1986.
[59] A. J. Meuler, M. A. Hillmyer, and F. S. Bates, “Ordered Network Mesostructures in Block Polymer Materials”, *Macromolecules*, vol. 42, nº 19, p. 7221-7250, oct. 2009.
[60] E. L. Thomas, D. M. Anderson, C. S. Henkee, and D. Hoffman, “Periodic area-minimizing surfaces in block copolymers”, *Nature*, vol. 334, nº 6183, p. 598-601, août 1988.
[61] M. Takenaka *et al.*, “Orthorhombic *Fddd* Network in Diblock Copolymer Melts”, *Macromolecules*, vol. 40, nº 13, p. 4399-4402, juin 2007.
[62] M. I. Kim *et al.*, “Stability of the *Fddd* Phase in Diblock Copolymer Melts”, *Macromolecules*, vol. 41, nº 20, p. 7667-7670, oct. 2008.
[63] A. K. Khandpur *et al.*, “Polyisoprene-Polystyrene Diblock Copolymer Phase Diagram near the Order-Disorder Transition”, *Macromolecules*, vol. 28, nº 26, p. 8796-8806, déc. 1995.
[64] J. Zhao *et al.*, “Phase Behavior of Pure Diblocks and Binary Diblock Blends of Poly(ethylene)−Poly(ethylethylene)”, *Macromolecules*, vol. 29, nº 4, p. 1204-1215, janv. 1996.
[65] M. F. Schulz *et al.*, “Phase Behavior of Polystyrene−Poly(2-vinylpyridine) Diblock Copolymers”, *Macromolecules*, vol. 29, nº 8, p. 2857-2867, janv. 1996.
[66] H. Hu, M. Gopinadhan, and C. O. Osuji, “Directed self-assembly of block copolymers: a tutorial review of strategies for enabling nanotechnology with soft matter”, *Soft Matter*, vol. 10, nº 22, p. 3867, 2014.
[67] S. Kim *et al.*, “Consequences of Surface Neutralization in Diblock Copolymer Thin Films”, *ACS Nano*, vol. 7, nº 11, p. 9905-9919, nov. 2013.

[68] H.-C. Kim and T. P. Russell, "Ordering in thin films of asymmetric diblock copolymers", *Journal of Polymer Science Part B: Polymer Physics*, vol. 39, nº 6, p. 663-668, mars 2001.
[69] M. A. van Dijk and R. van den Berg, "Ordering Phenomena in Thin Block Copolymer Films Studied Using Atomic Force Microscopy", *Macromolecules*, vol. 28, nº 20, p. 6773-6778, sept. 1995.
[70] P. Mansky, P. Haikin, and E. L. Thomas, "Monolayer films of diblock copolymer microdomains for nanolithographic applications", *Journal of Materials Science*, vol. 30, nº 8, p. 1987-1992, 1995.
[71] G. E. Stein *et al.*, "Symmetry Breaking of In-Plane Order in Confined Copolymer Mesophases", *Physical Review Letters*, vol. 98, nº 15, avr. 2007.
[72] G. E. Stein, E. J. Kramer, X. Li, and J. Wang, "Layering Transitions in Thin Films of Spherical-Domain Block Copolymers", *Macromolecules*, vol. 40, nº 7, p. 2453-2460, avr. 2007.
[73] J. G. Kennemur, L. Yao, F. S. Bates, and M. A. Hillmyer, "Sub-5 nm Domains in Ordered Poly(cyclohexylethylene)-*block*-poly(methyl methacrylate) Block Polymers for Lithography", *Macromolecules*, vol. 47, nº 4, p. 1411-1418, févr. 2014.
[74] Y. S. Jung and C. A. Ross, "Orientation-Controlled Self-Assembled Nanolithography Using a Polystyrene−Polydimethylsiloxane Block Copolymer", *Nano Letters*, vol. 7, nº 7, p. 2046-2050, juill. 2007.
[75] A. Nunns, J. Gwyther, and I. Manners, "Inorganic block copolymer lithography", *Polymer*, vol. 54, nº 4, p. 1269-1284, févr. 2013.
[76] K. Aissou, M. Mumtaz, G. Fleury *et al.*, "Sub-10 nm Features Obtained from Directed Self-Assembly of Semicrystalline Polycarbosilane-Based Block Copolymer Thin Films", *Adv. Mater.*, vol. 27, nº 2, p. 261-265, janv. 2015.
[77] G. Fleury, K. Aissou, M. Mumtaz *et al.*, "Development and integration of systems with enhanced resolutions based on Si-containing block copolymers for line space applications", 2015, p. 94250Z.
[78] J. H. Lee, Y. Kim, J. Y. Cho *et al.*, "In Situ Nanolithography with Sub-10 nm Resolution Realized by Thermally Assisted Spin-Casting of a Self-Assembling Polymer", *Advanced Materials*, vol. 27, nº 33, p. 4814-4822, sept. 2015.
[79] J. D. Cushen, C. Bates, E. L. Rausch *et al.*, "Thin film self-assembly of poly(trimethylsilylstyrene-*b*-d, l-lactide) with sub-10 nm domains", *Macromolecules*, vol. 45, nº 21, p. 8722-8728, 2012.
[80] T. Hirai *et al.*, "One-Step Direct-Patterning Template Utilizing Self-Assembly of POSS-Containing Block Copolymers", *Advanced Materials*, vol. 21, nº 43, p. 4334-4338, nov. 2009.
[81] J. W. Choi, Z. Li, C. T. Black, D. P. Sweat, X. Wang, and P. Gopalan, "Patterning at the 10 nanometer length scale using a strongly segregating block copolymer thin film and vapor phase infiltration of inorganic precursors", *Nanoscale*, vol. 8, nº 22, p. 11595-11601, 2016.
[82] J. G. Kennemur, M. A. Hillmyer, and F. S. Bates, "Synthesis, Thermodynamics, and Dynamics of Poly(4-tert-butylstyrene-*b*-methyl methacrylate)", *Macromolecules*, vol. 45, nº 17, p. 7228-7236, sept. 2012.
[83] J. H. Wolf and M. A. Hillmyer, "Ordered Nanoporous Poly(cyclohexylethylene) †", *Langmuir*, vol. 19, nº 16, p. 6553-6560, août 2003.
[84] L. Yao, L. E. Oquendo, M. W. Schulze, R. M. Lewis, W. L. Gladfelter, and M. A. Hillmyer, "Poly(cyclohexylethylene)- *block* -Poly(lactide) Oligomers for Ultrasmall Nanopatterning Using Atomic Layer Deposition", *ACS Applied Materials & Interfaces*, vol. 8, nº 11, p. 7431-7439, mars 2016.
[85] C. M. Bates *et al.*, "Polarity-Switching Top Coats Enable Orientation of Sub-10-nm Block Copolymer Domains", *Science*, vol. 338, nº 6108, p. 775-779, nov. 2012.
[86] J. D. Cushen *et al.*, "Ordering poly(trimethylsilyl styrene-*block*-D,L-lactide) block copolymers in thin films by solvent annealing using a mixture of domain-selective solvents", *Journal of Polymer Science Part B: Polymer Physics*, vol. 52, nº 1, p. 36-45, janv. 2014.
[87] C. Cummins, P. Mokarian-Tabari, P. Andreazza, C. Sinturel, and M. A. Morris, "Solvothermal Vapor Annealing of Lamellar Poly(styrene)-*block*-poly(D,L-lactide) Block Copolymer Thin Films for Directed Self-Assembly Application", *ACS Applied Materials & Interfaces*, vol. 8, nº 12, p. 8295-8304, mars 2016.

[88] C. Sinturel *et al.*, “Structural Transitions in Asymmetric Poly(styrene)-*block*-Poly(lactide) Thin Films Induced by Solvent Vapor Exposure”, *ACS Appl. Mater. Interfaces*, vol. 6, nº 15, p. 12146-12152, août 2014.

[89] T. P. Russell, R. P. Hjelm Jr, and P. A. Seeger, “Temperature dependence of the interaction parameter of polystyrene and poly (methyl methacrylate)”, *Macromolecules*, vol. 23, nº 3, p. 890–893, 1990.

[90] B. M. D. O’Driscoll *et al.*, “Achieving structural control with thin polystyrene-b-polydimethylsiloxane block copolymer films: The complex relationship of interface chemistry, annealing methodology and process conditions”, *European Polymer Journal*, vol. 49, nº 11, p. 3445-3454, nov. 2013.

[91] E. Kim, W. Kim, K. H. Lee, C. A. Ross, and J. G. Son, “A Top Coat with Solvent Annealing Enables Perpendicular Orientation of Sub-10 nm Microdomains in Si-Containing Block Copolymer Thin Films”, *Advanced Functional Materials*, vol. 24, nº 44, p. 6981-6988, nov. 2014.

[92] D. Borah *et al.*, “Nanopatterning via Self-Assembly of a Lamellar-Forming Polystyrene-block-Poly(dimethylsiloxane) Diblock Copolymer on Topographical Substrates Fabricated by Nanoimprint Lithography”, *Nanomaterials*, vol. 8, nº 1, p. 32, janv. 2018.

[93] T. Ghoshal, C. Ntaras, J. O'Connell *et al.*, “Fabrication of ultra-dense sub-10 nm in-plane Si nanowire arrays by using a novel block copolymer method: optical properties”, *Nanoscale*, vol. 8, nº 4, p. 2177-2187, 2016.

[94] Y. Pang, X. Jin, G. Huang, L. Wan, and S. Ji, “Directed Self-Assembly of Styrene-Methyl Acrylate Block Copolymers with Sub-7 nm Features via Thermal Annealing”, *Macromolecules*, vol. 52, nº 8, p. 2987-2994, avr. 2019.

[95] X. Zhang, Q. He, Q. Chen, P. F. Nealey, and S. Ji, “Directed Self-Assembly of High χ Poly(styrene-*b* -(lactic acid- *alt* -glycolic acid)) Block Copolymers on Chemical Patterns via Thermal Annealing”, *ACS Macro Letters*, vol. 7, nº 6, p. 751-756, juin 2018.

[96] M. J. Maher, C. M. Bates, G. Blachut *et al.*, “Interfacial Design for Block Copolymer Thin Films”, *Chem. Mater.*, vol. 26, nº 3, p. 1471-1479, févr. 2014.

[97] A. Vora, K. Smidt, G. Alva *et al.*, “Orientation Control of Block Copolymers Using Surface Active, Phase-Preferential Additives”, *ACS Appl. Mater. Interfaces*, vol. 8, nº 43, p. 29808-29817, nov. 2016.

[98] S. Park, J.-Y. Wang, B. Kim, J. Xu, and T. P. Russell, “A Simple Route to Highly Oriented and Ordered Nanoporous Block Copolymer Templates”, *ACS Nano*, vol. 2, nº 4, p. 766-772, avr. 2008.

[99] C. Cummins, T. Ghoshal, J. D. Holmes, and M. A. Morris, “Strategies for Inorganic Incorporation using Neat Block Copolymer Thin Films for Etch Mask Function and Nanotechnological Application”, *Advanced Materials*, vol. 28, nº 27, p. 5586-5618, juill. 2016.

[100] J. Yin, X. Yao, J.-Y. Liou, W. Sun, Y.-S. Sun, and Y. Wang, “Membranes with Highly Ordered Straight Nanopores by Selective Swelling of Fast Perpendicularly Aligned Block Copolymers”, *ACS Nano*, vol. 7, nº 11, p. 9961-9974, nov. 2013.

[101] J. Zhang, M. B. Clark, C. Wu, M. Li, P. Trefonas, and P. D. Hustad, “Orientation Control in Thin Films of a High-χ Block Copolymer with a Surface Active Embedded Neutral Layer”, *Nano Lett.*, vol. 16, nº 1, p. 728-735, janv. 2016.

[102] Q. Peng, Y.-C. Tseng, S. B. Darling, and J. W. Elam, “Nanoscopic Patterned Materials with Tunable Dimensions via Atomic Layer Deposition on Block Copolymers”, *Advanced Materials*, vol. 22, nº 45, p. 5129-5133, déc. 2010.

[103] R. Ruiz, L. Wan, J. Lille *et al.*, “Image quality and pattern transfer in directed self assembly with block-selective atomic layer deposition”, *Journal of Vacuum Science & Technology B: Microelectronics and Nanometer Structures*, vol. 30, nº 6, p. 06F202, 2012.

[104] H.-S. Moon, J. Y. Kim, H. M. Jin *et al.*, “Atomic Layer Deposition Assisted Pattern Multiplication of Block Copolymer Lithography for 5 nm Scale Nanopatterning”, *Advanced Functional Materials*, vol. 24, nº 27, p. 4343-4348, juill. 2014.

[105] E. Han, K. O. Stuen, M. Leolukman, C.-C. Liu, P. F. Nealey, and P. Gopalan, “Perpendicular orientation of domains in cylinder-forming block copolymer thick films by controlled interfacial interactions”, *Macromolecules*, vol. 42, nº 13, p. 4896–4901, 2009.

[106] T. P. Lodge and M. C. Dalvi, “Mechanisms of Chain Diffusion in Lamellar Block Copolymers”, *Physical Review Letters*, vol. 75, nº 4, p. 657-660, juill. 1995.

[107] C. Sinturel, M. Vayer, M. Morris, and M. A. Hillmyer, "Solvent Vapor Annealing of Block Polymer Thin Films", *Macromolecules*, vol. 46, nº 14, p. 5399-5415, juill. 2013.
[108] K. W. Gotrik, A. F. Hannon, J. G. Son, B. Keller, A. Alexander-Katz, and C. A. Ross, "Morphology control in block copolymer films using mixed solvent vapors", *ACS Nano*, vol. 6, nº 9, p. 8052-8059, sept. 2012.
[109] J. K. Bosworth, M. Y. Paik, R. Ruiz *et al.*, "Control of self-assembly of lithographically patternable block copolymer films", *ACS Nano*, vol. 2, nº 7, p. 1396-1402, juill. 2008.
[110] M. Y. Paik, J. K. Bosworth, D.-M. Smilges, E. L. Schwartz, X. Andre, and C. K. Ober, "Reversible Morphology Control in Block Copolymer Films via Solvent Vapor Processing: An in Situ GISAXS Study", *Macromolecules*, vol. 43, nº 9, p. 4253-4260, mai 2010.
[111] T. P. Russell, G. Coulon, V. R. Deline, and D. C. Miller, "Characteristics of the surface-induced orientation for symmetric diblock PS/PMMA copolymers", *Macromolecules*, vol. 22, nº 12, p. 4600-4606, déc. 1989.
[112] S. H. Kim, M. J. Misner, T. Xu, M. Kimura, and T. P. Russell, "Highly Oriented and Ordered Arrays from Block Copolymers via Solvent Evaporation", *Adv. Mater.*, vol. 16, nº 3, p. 226-231, févr. 2004.
[113] A. Cossaro, R. Mazzarello, R. Rousseau *et al.*, "X-ray Diffraction and Computation Yield the Structure of Alkanethiols on Gold(111)", *Science*, vol. 321, nº 5891, p. 943-946, août 2008.
[114] C. D. Bain, H. A. Biebuyck, and G. M. Whitesides, "Comparison of self-assembled monolayers on gold: coadsorption of thiols and disulfides", *Langmuir*, vol. 5, nº 3, p. 723-727, mai 1989.
[115] R. D. Peters, X. M. Yang, T. K. Kim, B. H. Sohn, and P. F. Nealey, "Using Self-Assembled Monolayers Exposed to X-rays To Control the Wetting Behavior of Thin Films of Diblock Copolymers", *Langmuir*, vol. 16, nº 10, p. 4625-4631, mai 2000.
[116] B. H. Sohn and S. H. Yun, "Perpendicular lamellae induced at the interface of neutral self-assembled monolayers in thin diblock copolymer films", *Polymer*, vol. 43, nº 8, p. 2507-2512, avr. 2002.
[117] J. Heier, E. J. Kramer, S. Walheim, and G. Krausch, "Thin Diblock Copolymer Films on Chemically Heterogeneous Surfaces †", *Macromolecules*, vol. 30, nº 21, p. 6610-6614, oct. 1997.
[118] T. K. Kim, X. M. Yang, R. D. Peters, B. H. Sohn, and P. F. Nealey, "Chemical Modification of Self-Assembled Monolayers by Exposure to Soft X-rays in Air", *The Journal of Physical Chemistry B*, vol. 104, nº 31, p. 7403-7410, août 2000.
[119] A. P. Smith, J. F. Douglas, J. C. Meredith, E. J. Amis, and A. Karim, "Combinatorial Study of Surface Pattern Formation in Thin Block Copolymer Films", *Physical Review Letters*, vol. 87, nº 1, juin 2001.
[120] A. Niemz, K. Bandyopadhyay, E. Tan, K. Cha, and S. M. Baker, "Fabrication of Nanoporous Templates from Diblock Copolymer Thin Films on Alkylchlorosilane-Neutralized Surfaces", *Langmuir*, vol. 22, nº 26, p. 11092-11096, déc. 2006.
[121] T. H. Epps, D. M. DeLongchamp, M. J. Fasolka, D. A. Fischer, and E. L. Jablonski, "Substrate Surface Energy Dependent Morphology and Dewetting in an ABC Triblock Copolymer Film", *Langmuir*, vol. 23, nº 6, p. 3355-3362, mars 2007.
[122] P.-H. Liu, P. Thébault, P. Guenoun, and J. Daillant, "Easy Orientation of Diblock Copolymers on Self-Assembled Monolayers Using UV Irradiation", *Macromolecules*, vol. 42, nº 24, p. 9609-9612, déc. 2009.
[123] P. Mansky, Y. Liu, E. Huang, T. P. Russell and C. Hawker, "Controlling Polymer-Surface Interactions with Random Copolymer Brushes", *Science*, vol. 275, nº 5305, p. 1458-1460, mars 1997.
[124] E. Han, K. O. Stuen, Y.-H. La, P. F. Nealey, and P. Gopalan, "Effect of Composition of Substrate-Modifying Random Copolymers on the Orientation of Symmetric and Asymmetric Diblock Copolymer Domains", *Macromolecules*, vol. 41, nº 23, p. 9090-9097, déc. 2008.
[125] K. Sparnacci, D. Antonioli, V. Gianotti *et al.*, "Ultrathin Random Copolymer-Grafted Layers for Block Copolymer Self-Assembly", *ACS Applied Materials & Interfaces*, vol. 7, nº 20, p. 10944-10951, mai 2015.
[126] X. Chevalier, C. Nicolet, R. Tiron, A. Gharbi *et al.*, "Scaling-down lithographic dimensions with block-copolymer materials: 10nm sized features with PS- *b* -PMMA", 2013, p. 868006.
[127] D. Borah, S. Rasappa, R. Senthamaraikannan, M. T. Shaw, J. D. Holmes, and M. A. Morris, "The sensitivity of random polymer brush-lamellar polystyrene-b-polymethylmethacrylate block

copolymer systems to process conditions", *Journal of Colloid and Interface Science*, vol. 393, p. 192-202, mars 2013.
[128] I. In, Y.-H. La, S.-M. Park, P. F. Nealey, and P. Gopalan, "Side-Chain-Grafted Random Copolymer Brushes as Neutral Surfaces for Controlling the Orientation of Block Copolymer Microdomains in Thin Films", *Langmuir*, vol. 22, nº 18, p. 7855-7860, août 2006.
[129] R. Guo, E. Kim, J. Gong, S. Choi, *et al*,, "Perpendicular orientation of microdomains in PS-b-PMMA thin films on the PS brushed substrates", *Soft Matter*, vol. 7, nº 15, p. 6920, 2011.
[130] S. Ji, G. Liu, F. Zheng, G. S. W. Craig, *et al.*, "Preparation of Neutral Wetting Brushes for Block Copolymer Films from Homopolymer Blends", *Advanced Materials*, vol. 20, nº 16, p. 3054-3060, août 2008.
[131] W. Gu, S. W. Hong, and T. P. Russell, "Orienting Block Copolymer Microdomains with Block Copolymer Brushes", *ACS Nano*, vol. 6, nº 11, p. 10250-10257, nov. 2012.
[132] M. Kim, S. Schmitt, J. Choi, J. Krutty, and P. Gopalan, "From Self-Assembled Monolayers to Coatings: Advances in the Synthesis and Nanobio Applications of Polymer Brushes", *Polymers*, vol. 7, nº 7, p. 1346-1378, juill. 2015.
[133] R.-V. Ostaci *et al.*, "Polymer Brushes Grafted to "Passivated" Silicon Substrates Using Click Chemistry", *Langmuir*, vol. 24, nº 6, p. 2732-2739, mars 2008.
[134] C. I. Biggs, M. Walker, and M. I. Gibson, "Grafting to" of RAFTed Responsive Polymers to Glass Substrates by Thiol–Ene and Critical Comparison to Thiol–Gold Coupling", *Biomacromolecules*, vol. 17, nº 8, p. 2626-2633, août 2016.
[135] H. S. Wang, K. H. Kim, and J. Bang, "Thermal Approaches to Perpendicular Block Copolymer Microdomains in Thin Films: A Review and Appraisal", *Macromolecular Rapid Communications*, vol. 40, nº 4, p. 1800728, févr. 2019.
[136] D. Y. Ryu, "A Generalized Approach to the Modification of Solid Surfaces", *Science*, vol. 308, nº 5719, p. 236-239, avr. 2005.
[137] H. Jung, D. Hwang, E. Kim *et al.*, "Three-Dimensional Multilayered Nanostructures with Controlled Orientation of Microdomains from Cross-Linkable Block Copolymers", *ACS Nano*, vol. 5, nº 8, p. 6164-6173, août 2011.
[138] Y. Pang, L. Wan, G. Huang *et al.*, "Controlling Block Copolymer–Substrate Interactions by Homopolymer Brushes/Mats", *Macromolecules*, vol. 50, nº 17, p. 6733-6741, sept. 2017.
[139] J. Bang, J. Bae, P. Löwenhielm *et al.*, "Facile Routes to Patterned Surface Neutralization Layers for Block Copolymer Lithography", *Advanced Materials*, vol. 19, nº 24, p. 4552-4557, déc. 2007.
[140] E. Han, I. In, S.M. Park *et al.*, "Photopatternable Imaging Layers for Controlling Block Copolymer Microdomain Orientation", *Advanced Materials*, vol. 19, nº 24, p. 4448-4452, déc. 2007.
[141] P. Moni, H.S. Suh *et al.*, "Ultrathin and Conformal Initiated Chemical-Vapor-Deposited Layers of Systematically Varied Surface Energy for Controlling the Directed Self-Assembly of Block CoPolymers", *Langmuir*, vol. 34, nº 15, p. 4494-4502, avr. 2018.
[142] I. Bita, J. K. W. Yang, Y. S. Jung, C. A. Ross, E. L. Thomas, and K. K. Berggren, "Graphoepitaxy of Self-Assembled Block Copolymers on Two-Dimensional Periodic Patterned Templates", *Science*, vol. 321, nº 5891, p. 939-943, août 2008.
[143] S.-J. Jeong, J. Y. Kim, B. H. Kim, *et al*., "Directed self-assembly of block copolymers for next generation nanolithography", *Materials Today*, vol. 16, nº 12, p. 468-476, déc. 2013.
[144] X. Chevalier, R. Tiron, T. Upreti *et al.*, "Study and optimization of the parameters governing the block copolymer self-assembly: toward a future integration in lithographic process", présenté à SPIE Advanced Lithography, San Jose, California, USA, 2011, p. 79700Q.
[145] S. M. Nicaise, K. G. Amir Tavakkoli, and K. K. Berggren, "Self-assembly of block copolymers by graphoepitaxy", in *Directed Self-assembly of Block Co-polymers for Nano-manufacturing*, Elsevier, 2015, p. 199-232.
[146] R. A. Segalman, H. Yokoyama, and E. J. Kramer, "Graphoepitaxy of Spherical Domain Block Copolymer Films", *Advanced Materials*, vol. 13, nº 15, p. 1152-1155, août 2001.
[147] M. A. Morris, "Directed self-assembly of block copolymers for nanocircuitry fabrication", *Microelectronic Engineering*, vol. 132, p. 207-217, janv. 2015.
[148] C.-C. Liu, E. Han, M.S. Onses *et al.*, "Fabrication of Lithographically Defined Chemically Patterned Polymer Brushes and Mats", *Macromolecules*, vol. 44, nº 7, p. 1876-1885, avr. 2011.
[149] J. Kim, J. Wan, S. Miyazaki *et al.*, "The SMARTTM Process for Directed Block Co-Polymer Self-Assembly", *Journal of Photopolymer Science and Technology*, vol. 26, nº 5, p. 573-579, 2013.

CHAPTER 2: Phase diagram of PDMSB-*b*-PS BCPs

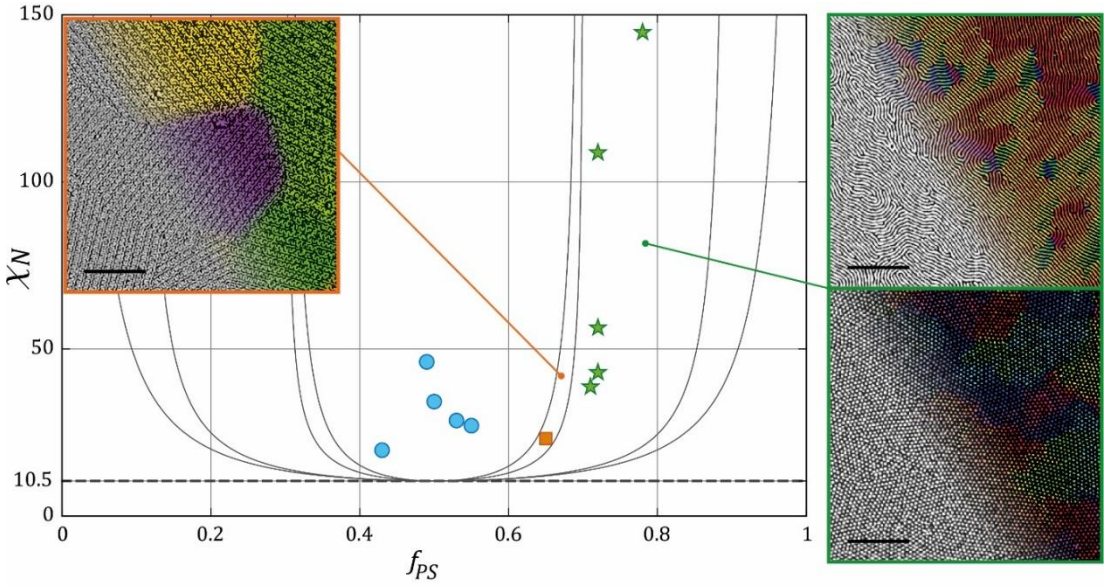

In this chapter, we highlight the potential of PDMSB-*b*-PS BCP for nanolithography applications. The Flory-Huggins interaction parameter of the PDMSB-*b*-PS system was found to be 0.13 ± 0.06 at RT, which is four times the value of the conventional PS-*b*-PMMA. We demonstrate the ability of our system to self-assemble into various nanostructures in bulk which led us to establish an experimental phase diagram for the PDMSB-*b*-PS BCP. Moreover, we perform the self-assembly of cylinder- and gyroid-forming PDSMB-*b*-PS in thin film using industrially-friendly processes and provide an understanding of the parameters that have to be taken into account for the control of the organisation and orientation of the nanostructures.

I. Introduction

Numerous studies have been performed to develop high-χ BCPs in order to decrease the characteristic dimension of the self-assembled nanostructures below 20 nm. Several strategies were highlighted in the last chapter such as the increase of the incompatibility between the blocks by incorporating inorganic atoms or by inducing crystallinity in one of the domains [1]–[3].

In this work, we decided to focus on the poly(1,1-dimethylsilacyclobutane)-*b*-poly(styrene) (PDMSB-*b*-PS) system which answers the specifications of a BCP system for lithography (Figure 2-1). Indeed, preliminary studies have shown the potential of this system to provide sub-20 nm features thanks to the Si-containing semi-crystalline block [2], [4], [5]. Moreover, this Si-containing block provides the etching contrast between the BCP domains during subsequent pattern transfer, allowing thus the removal of the PS domains while keeping the oxidized PDMSB domains as mask [5].

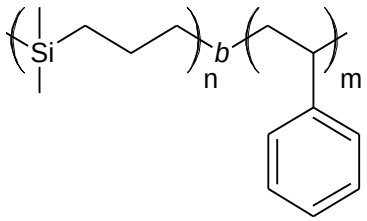

Figure 2-1: Chemical structure of the PDMSB-*b*-PS BCP.

A series of PDMSB-*b*-PS BCPs was synthetized during a former study *via* sequential anionic polymerization of (1,1-dimethyl silacyclobutane) and styrene (Figure 2-2) with various molecular weights and compositions. Table 2-1 summarizes the macromolecular characteristics of the BCPs. The molecular weight of the BCPs was determined using a combination of size-exclusion chromatography (SEC) and ^{1}H NMR spectroscopy while the volume fraction of the PDMSB block was estimated from ^{1}H NMR spectra. The glass transitions (T_g) were determined using differential scanning calorimetry (DSC) on a TA Instruments Q100. The samples were first heated to 150°C and cooled to -160°C at 10°C.min^{-1}. A second heating run was then performed to 150°C at 10°C.min^{-1} to evaluate the T_g. As shown the Figure 2-3, it is possible to see two glass transitions

around -70°C and 90°C corresponding to the ones of the PDMSB and PS blocks, respectively [6], [7]: the appearance of two glass transitions on the DSC traces hints a segregated state of the BCPs. Moreover, an endothermic peak corresponding to the melting of the semi-crystalline PDMSB block can be seen on the DSC traces, confirming the potential interplay between crystallization and chemical phase separation in this particular system.

For the determination of the Flory-Huggins parameter (see in section II), we used the overall Flory degree of polymerization, N_{Flory}, which was calculated using the density values of PDMSB (0.895 g.cm^{-3}) and PS (0.969 g.cm^{-3}) at 140°C and using a reference volume, v_0, of 118 Å^3 [8]. In the following parts, the polymers will be denoted as $PDMSB_n$-*b*-PS_m with *n* and *m* the Flory degree of polymerization of the PDMSB and PS blocks, respectively.

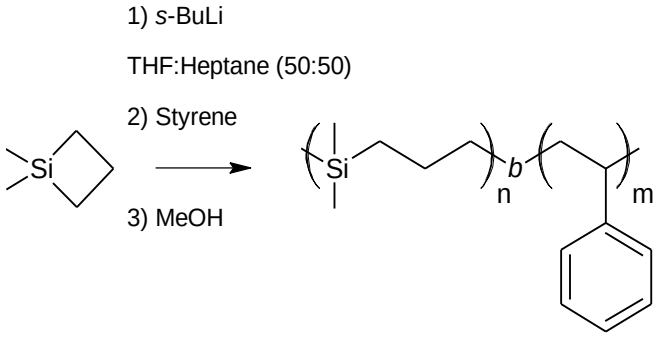

Figure 2-2: Synthesis of PDMSB-*b*-PS BCPs via sequential anionic polymerization by the subsequent addition of styrene to living PDMSB chains. The polymerization was performed in a THF/heptane mixture (50:50 volume ratio) at -50°C using sec-BuLi (*s*-BuLi) as initiator. The reaction was terminated with methanol.

Table 2-1: Macromolecular characteristics of the set of synthetized PDMSB-*b*-PS BCPs.

Materials	M_n (g.mol^{-1})[a]	PDI[b]	f_{PDMSB}[c]	N[d]	N_{Flory}[e]	Expected morphology	$T_{g,PS}$ (°C)[f]	$T_{g,PDMSB}$ (°C)[g]
$PDMSB_{79}$-*b*-PS_{76}	9850	1.13	0.57	98	155	Lam	62	- 65
$PDMSB_{84}$-*b*-PS_{123}	13600	1.13	0.45	133	207	Lam	83	- 65
$PDMSB_{94}$-*b*-PS_{125}	14350	1.1	0.47	140	219	Lam	83	- 64
$PDMSB_{120}$-*b*-PS_{143}	17140	1.1	0.5	168	263	Lam	88	- 62
$PDMSB_{165}$-*b*-PS_{195}	23000	1.08	0.51	230	360	Lam	89	- 60
$PDMSB_{74}$-*b*-PS_{224}	19350	1.08	0.29	193	298	Cyl	94	-73
$PDMSB_{79}$-*b*-PS_{251}	21500	1.08	0.28	215	331	Cyl	96	-74
$PDMSB_{102}$-*b*-PS_{245}	22500	1.06	0.34	225	348	Cyl	92	-71
$PDMSB_{104}$-*b*-PS_{330}	28200	1.13	0.28	282	434	Cyl	84	-77
$PDMSB_{200}$-*b*-PS_{636}	54400	1.05	0.28	543	837	Cyl	102	-74
$PDMSB_{207}$-*b*-PS_{906}	72700	1.1	0.22	726	1114	Cyl	101	-78
$PDMSB_{54}$-*b*-PS_{124}	11500	1.12	0.35	115	178	Gyr	83	-71

a: Molecular weight determined by SEC using PS standards
b: Dispersity determined by SEC analysis
c: PDMSB volume fraction determined by ^{1}H NMR
d: Overall degree of polymerization
e: Overall Flory degree of polymerization based on the reference volume (v_0)
f & g: T_gs determined on the second heating run: from −160 to 150°C at 10°C.min^{-1}.

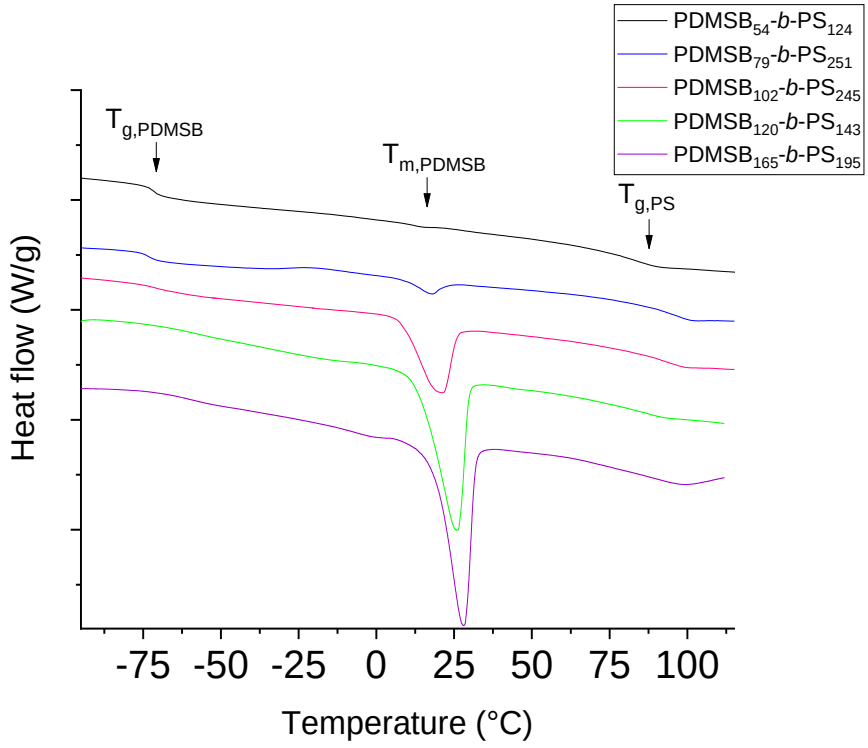

Figure 2-3: DSC traces of selected PDMSB-*b*-PS BCPs: $PDMSB_{54}$-*b*-PS_{124}, $PDMSB_{79}$-*b*-PS_{251}, $PDMSB_{102}$-*b*-PS_{245}, $PDMSB_{120}$-*b*-PS_{143} and $PDMSB_{165}$-*b*-PS_{195}.

II. Characterization of PDMSB-*b*-PS in bulk

1. Lamellar-forming PDMSB-*b*-PS BCP

Small-angle X-ray scattering (SAXS) was performed in order to confirm the lamellar structure in bulk of the $PDMSB_{79}$-*b*-PS_{76}, $PDMSB_{84}$-*b*-PS_{123}, $PDMSB_{94}$-*b*-PS_{125} and $PDMSB_{120}$-*b*-PS_{143} with near to symmetric composition. Figure 2-4 shows the intensity profile of the BCPs at 140°C. The SAXS reflections are consistent with a lamellar structure with well-defined peaks with q/q^* ratios of 1, 2, 3, 4 and 5, where q^* is the wavevector of the first peak. The values of the interdomain spacing, d, were calculated from the first order peak position, q^*, using the following equation: $d = \frac{2\pi}{q^*}$ [9]. The d-spacing corresponds to the lamellar spacing, L_0, and was found to be 13 nm, 15.4 nm, 15.5 nm and 18.2 nm for the $PDMSB_{79}$-*b*-PS_{76}, $PDMSB_{84}$-*b*-PS_{123}, $PDMSB_{94}$-*b*-PS_{125} and $PDMSB_{120}$-*b*-PS_{143}, respectively (see in Table 2-2). The secondary scattering peak located at $2q^*$ is not visible for the $PDMSB_{120}$-*b*-PS_{143} which is consistent with an extinction of the form factor for lamellar morphologies having a symmetric composition (see Annex).

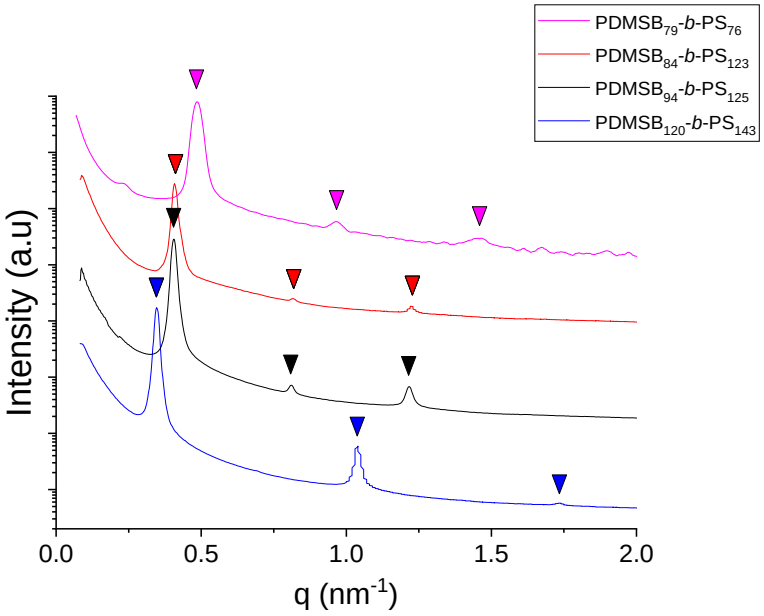

Figure 2-4: SAXS profiles of the $PDMSB_{79}$-*b*-PS_{76}, $PDMSB_{84}$-*b*-PS_{123}, $PDMSB_{94}$-*b*-PS_{125} and $PDMSB_{120}$-*b*-PS_{143} at 140°C highlighting a lamellar phase.

Table 2-2: **Macromolecular characteristics of the lamellar-forming PDMSB-*b*-PS.**

Material	M_n (g.mol^{-1}) [a]	f_{PDMSB} [b]	d (nm) [c]
PDMSB$_{79}$-*b*-PS$_{76}$	9850	0.57	13
PDMSB$_{84}$-*b*-PS$_{123}$	13600	0.45	15.4
PDMSB$_{94}$-*b*-PS$_{125}$	14350	0.47	15.5
PDMSB$_{120}$-*b*-PS$_{143}$	17140	0.5	18.2

a: Molecular weight determined by SEC
b: PDMSB volume fraction determined by ^{1}H NMR
c: *d*-spacing calculated using the first order diffraction peak

Moreover, the experimental results for this series of PDMSB-*b*-PS with a nearly constant composition exhibit a linear dependence of ln(*d)* with ln(*N)* (see in the Figure 2-5) in agreement with an intermediate segregation behaviour (i.e. $d \sim N^{0.72}$)[10].

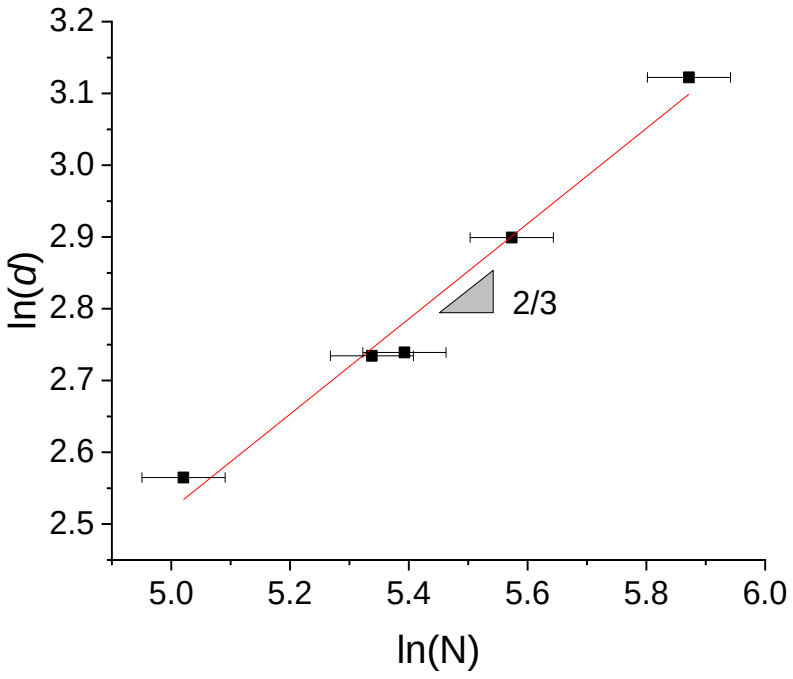

Figure 2-5: **Dependance of the domain spacing with the overall degree of polymerization *N* for a series of lamellar-forming PDMSB-*b*-PS. The *d*-spacing scales as $d \sim N^{2/3}$ (slope = 0.66 ± 0.05) in accordance with the strong segregation theory.**

2. Determination of the Flory-Huggins interaction parameter

We have determined the Flory-Huggins parameter of the PDMSB-*b*-PS using our set of lamellar-forming BCPs (see in Table 2-1). Indeed, as discussed in the previous chapter, the Flory-Huggins parameter can be expressed as a linear relationship with the inverse of temperature [11]:

$$\chi_{AB} = A + \frac{B}{T} \quad \textbf{(eq. 2-1)}$$

For a symmetric diblock copolymer**,** the order-disorder transition takes place in first approximation at:

$$(\chi_{AB}N)_{ODT} = 10.5 \quad \textbf{(eq. 2-2)}$$

Consequently, by measuring the order-disorder temperature for BCPs having different degree of polymerization, it is possible to determine the $\chi(T)$ of a BCP system. For this purpose, the T_{ODT} values were measured using an Anton Paar MCR302 rheometer with a plane-plane geometry (8 mm diameter). Samples of each BCP were prepared by melt pressing the polymer within circular molds at 180°C for 10 min. The measurement of the dynamic elastic modulus (G') was performed as a function of the temperature (heating rate of 2.5°C.min^{-1}) at a frequency of 1 rad.s^{-1} in the linear viscoelastic domain (strain, γ = 1%). Upon heating, the order to disorder transition is accompanied with a sudden drop of G' (see Figure 2-6). The T_{ODT} was taken at the onset of the drop using a tangent method. For each polymer, it is finally possible to calculate the χ_{ODT} using the equation 2-2. Finally, by plotting the χ_{ODT} as a function of the $1/T_{ODT}$ (Figure 2-7), we can draw a linear regression line from which the slope and intercept provide the temperature dependence of the Flory-Huggins parameter of the PDMSB-*b*-PS: $\chi(T) = \frac{51.25 \pm 8.6}{T} - (0.046 \pm 0.015)$.

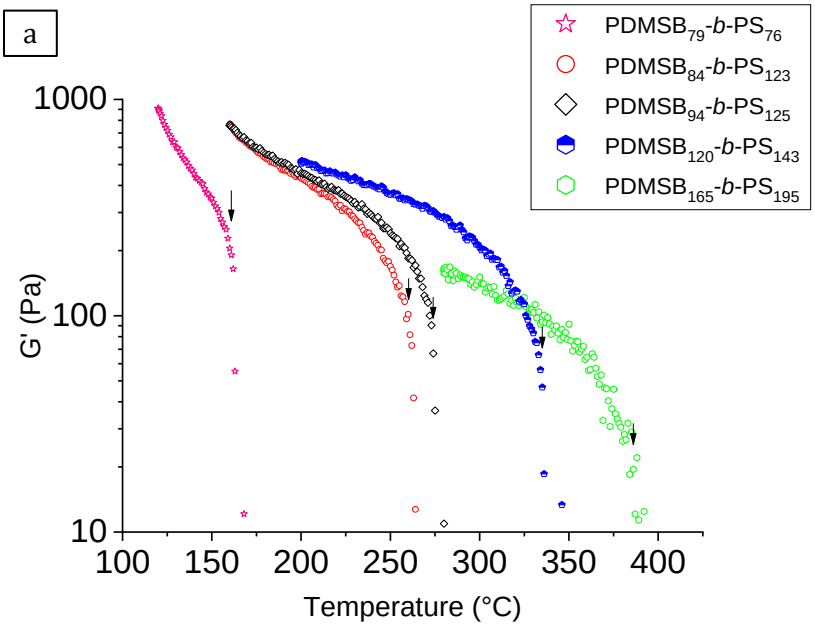

b

Material	T_{ODT} (°C)
PDMSB$_{79}$-*b*-PS$_{76}$	162
PDMSB$_{84}$-*b*-PS$_{123}$	260
PDMSB$_{94}$-*b*-PS$_{125}$	274
PDMSB$_{120}$-*b*-PS$_{143}$	342
PDMSB$_{165}$-*b*-PS$_{195}$	389

Figure 2-6: Plot of the elastic modulus, G′, as a function of temperature for lamellar-forming PDMSB-*b*-PS (a). The order−disorder transition is observed with the fast decrease of G′. Pulsation: ω = 1 rad.s^{-1}, strain: γ = 1 % and heating rate: 2.5°C.min^{-1}. The arrows indicate the onset of the drop used to estimate the T_{ODT}. (b) Table of the order-disorder temperatures measured for the BCPs with an instrumental error of ± 2.5°C.

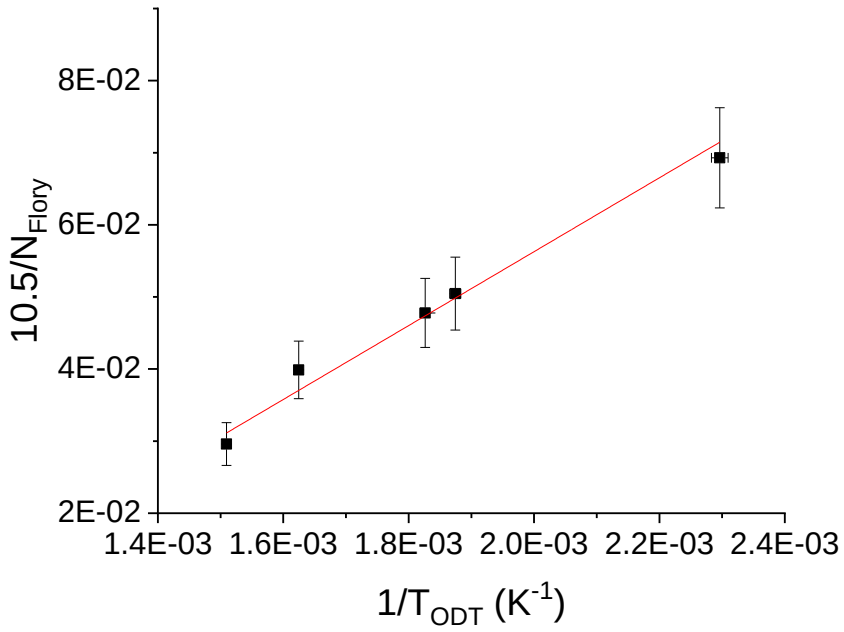

Figure 2-7: Linear dependence of χ as a function of inverse of T_{ODT}.

The Flory-Huggins interaction parameter of the PDMSB-*b*-PS was thus estimated to be 0.13 ± 0.06 at RT. This value is four times the value of the conventional PS-*b*-PMMA system ($\chi_{PS\text{-}b\text{-}PMMA}$ = 0.03 at RT [12]) which confirms the interest of using the PDMSB-*b*-PS architecture for the definition of sub-20 nm features.

3. Cylinder-forming PDMSB-*b*-PS BCP

SAXS experiments were also performed on PDMSB-*b*-PS BPCs having a ~30% volume fraction of PDMSB. Figure 2-8 shows the intensity profile of six PDMSB-*b*-PS at 140°C. The SAXS reflections are consistent with a cylindrical structure with defined peaks at q/q* ratios of 1, $\sqrt{3}$, 2, $\sqrt{7}$, 3 and $\sqrt{12}$. One can note a shift of the first order peak to lower q values from $PDMSB_{74}$-*b*-PS_{224} to $PDMSB_{207}$-*b*-PS_{906} which is consistent with the increase of molecular weights. From the first order peak, it is possible to determine the interdomain spacing, *d,* of the cylinder-forming BCPs that corresponds to the spacing between the (10) planes of the hexagonal lattice (see Table 2-3).

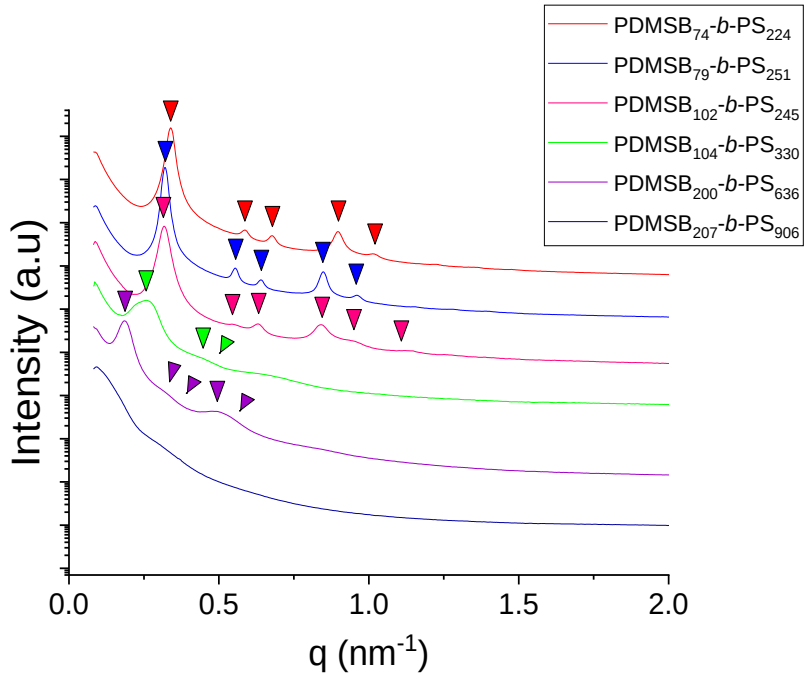

Figure 2-8: SAXS profiles of the cylinder-forming BCPs at 140°C.

Table 2-3: Macromolecular characteristics of the cylinder-forming PDMSB-*b*-PS BCPs.

Material	M_n (g.mol^{-1}) [a]	f_{PDMSB} [b]	*d*(nm)[c]
$PDMSB_{74}$-*b*-PS_{224}	19350	0.29	18.5
$PDMSB_{79}$-*b*-PS_{251}	21500	0.28	19.6
$PDMSB_{102}$-*b*-PS_{245}	22500	0.34	19.7
$PDMSB_{104}$-*b*-PS_{330}	28200	0.28	24.3
$PDMSB_{200}$-*b*-PS_{636}	54400	0.28	33.8
$PDMSB_{207}$-*b*-PS_{906}	72700	0.22	-

a: Molecular weight determined by SEC using PS standards
b: PDMSB volume fraction determined by ^{1}H NMR
c: *d*-spacing calculated using the first order diffraction peak

4. Gyroid-forming PDMSB-*b*-PS BCP

Finally, SAXS experiments were performed on the $PDMSB_{54}$-*b*-PS_{124} in order to determine the structure in bulk. Figure 2-9 shows the intensity profile of the $PDMSB_{54}$-*b*-PS_{124} at 200°C. The SAXS reflections are consistent with a double gyroid structure with well-defined peaks at q/q* ratios of $\sqrt{6}$, $\sqrt{8}$, $\sqrt{14}$, $\sqrt{16}$, $\sqrt{20}$.... The first order peak is centered at a q value of 0.419 nm^{-1} corresponding to a unit cell dimension, a_G, of 35 nm (see in Table 2-4).

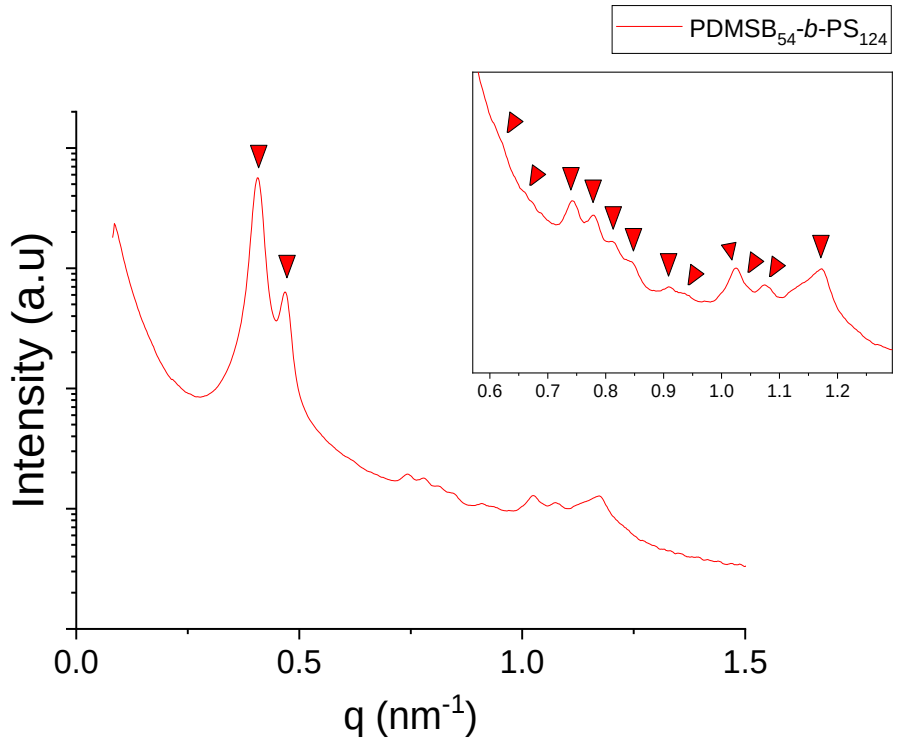

Figure 2-9: SAXS profile of the $PDMSB_{54}$-*b*-PS_{124} at 200°C highlighting a gyroid structure. The inset shows the peaks between 0.6 and 1.3 nm^{-1} underlining the long-range ordering of the structure.

Table 2-4: Macromolecular characteristics of the gyroid-forming PDMSB-*b*-PS.

Material	M_n (g.mol^{-1}) [a]	f_{PDMSB} [b]	d (nm) [c]	a_G (nm) [d]
$PDMSB_{54}$-*b*-PS_{124}	11500	0.35	15.8	35

a: Molecular weight determined by SEC using PS standards
b: PDMSB volume fraction determined by ^1H NMR
c & d: *d*-spacing and unit-cell dimension (a_G) were calculated using the first order diffraction peak

In conclusion, we highlighted the potential of the PDMSB-*b*-PS BCPs for the definition of self-assembled nanostructures of various morphologies and sizes in bulk. Additionally, we have determined the temperature-dependent Flory-Huggins parameter for this system, expressed as $\chi(T) = \frac{51.25 \pm 8.6}{T} - (0.046 \pm 0.015)$, which is higher than the one of the archetypical PS-*b*-PMMA system: $\chi_{\text{PDMSB-}b\text{-PS}}$ 0.13 ± 0.06 *vs* $\chi_{\text{PS-}b\text{-PMMA}}$ = 0.03 at RT [12]. This study led us to establish an experimental phase diagram for the PDMSB-*b*-PS system. As shown the Figure 2-10, our set of data matches well with the theoretical phase diagram.

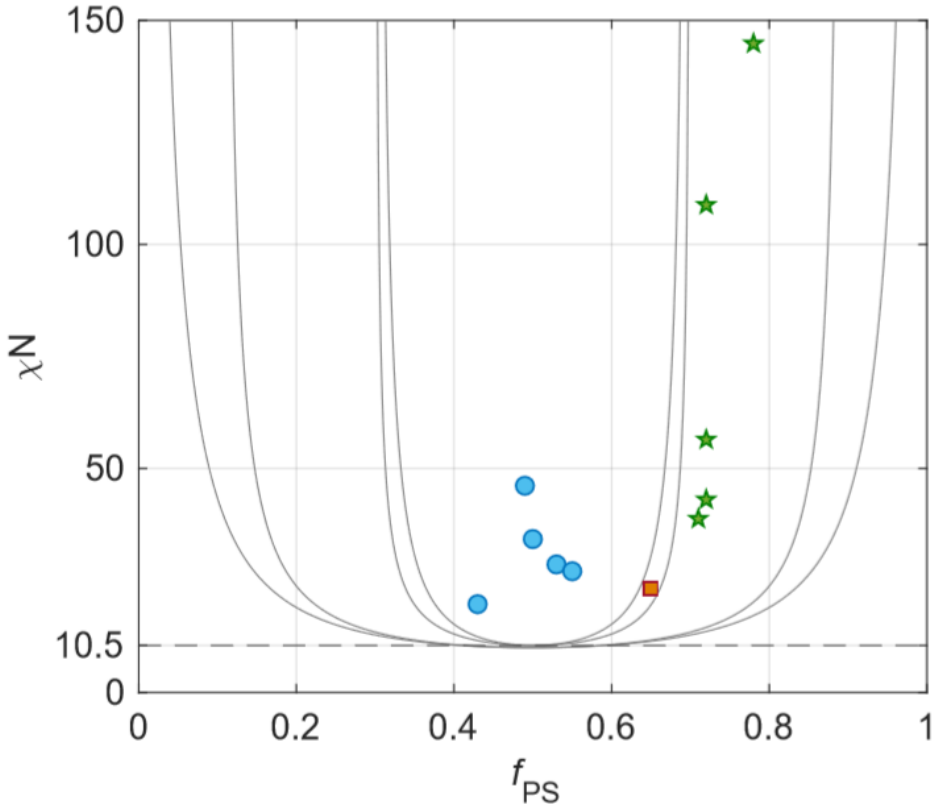

Figure 2-10: Phase diagram of the PDMSB-*b*-PS BCPs used in the study. The filled circles, filled square and filled stars correspond to the lamellar-forming, gyroid-forming and cylinder-forming PDMSB-*b*-PS BCPs, respectively. The curve corresponds to the SCFT simulation of the theoretical phase diagram.

III. Self-assembly of the PDMSB-*b*-PS in thin film

1. Cylinder-forming PDMSB-*b*-PS BCP

In this section, we perform the self-assembly of cylinder-forming PDMSB-*b*-PS BCPs in thin film using a thermal annealing process. We highlight the experimental parameters that have to be taken into account in order to control the self-assembly and the orientation of PDMSB cylinders in thin films. Several strategies have been proposed in the literature in order to have a control of the morphology and its orientation, i.e. thermal annealing and variation of the BCP film thickness. In a preliminary study, we consequently have explored these different methods in order to optimize the BCP structure. Moreover, we introduce a new parameter to control the orientation of the cylinders in thin film, the crystallinity.

For this purpose, 2% wt. solution of $PDMSB_{74}$-*b*-PS_{224} was prepared in methyl isobutyl ketone. The solution was spin-coated onto silicon substrates at either 2000 rpm or 4000 rpm in order to reach film thicknesses of 42 nm and 35 nm, respectively. The BCP film was then thermally-annealed at 180°C for 5 min. The AFM characterization of this BCP layer did not reveal any self-assembled structure. To understand this phenomenon, the estimation of the surface energy of PDMSB and PS was performed by measuring the contact angle of three typical liquids (water, diiodomethane and ethylene glycol) on PDMSB-OH and PS-OH brushes grafted on silicon substrates at 200°C for 75 s. The angles were determined with a Drop Shape Analyzer – DSA100 (KRÜSS) and the surface energy was estimated using the Owens, Wendt, Rabel and Kaelble (OWRK) method. As shown in the Table 2-5, PDMSB has a low surface energy consistent with the formation of a PDMSB-wetting layer on top of the PDMSB-*b*-PS self-assembled structure.

Table 2-5: Surface energies of PDMSB and PS using contact angle measurements and the OWRK model.

Material	Total surface energy ($mN.m^{-1}$)	Dispersive component ($mN.m^{-1}$)	Polar component ($mN.m^{-1}$)
PS-OH	43.5	42.1	1.4
PDMSB-OH	27.3	25.1	2.2

We consequently performed a CF_4/O_2 (17 sccm of CF_4, 3 sccm of O_2, 40W and 45 s) reactive ion etch (RIE) treatment in PE-100 chamber (RIE, Plasma Etch) to remove this PDMSB wetting layer and Figure 2-11 shows AFM images of the $PDMSB_{74}$-*b*-PS_{224} films after this etching step. As expected, the affinity of the PDMSB block for the free interface led to a parallel orientation of the PDMSB cylinders. The interdomain spacing, L_0, of the PDMSB cylinders was found to be ~21 nm for both thicknesses. L_0 was determined using the 2D-Fast Fourier Transform (FFT) of the topographical images. There is consequently a factor of $2/\sqrt{3}$ between this value and the *d*-spacing deduced from the SAXS data which corresponds from the spacing between the (10) planes of the hexagonal lattice.

For a film thickness of 42 nm (corresponding to ~ $2L_0$), a smooth film is obtained (Figure 2-11(a)) while terraces of ~$1/2L_0$ and ~L_0 are formed for a film thickness of 35 nm (Figure 2-11(b) and (c)). This is consistent with an asymmetric wetting of the blocks and confirms previous findings in the literature reporting the formation of terraces when the film thickness is not commensurate with the periodicity of the domains [13]–[15].

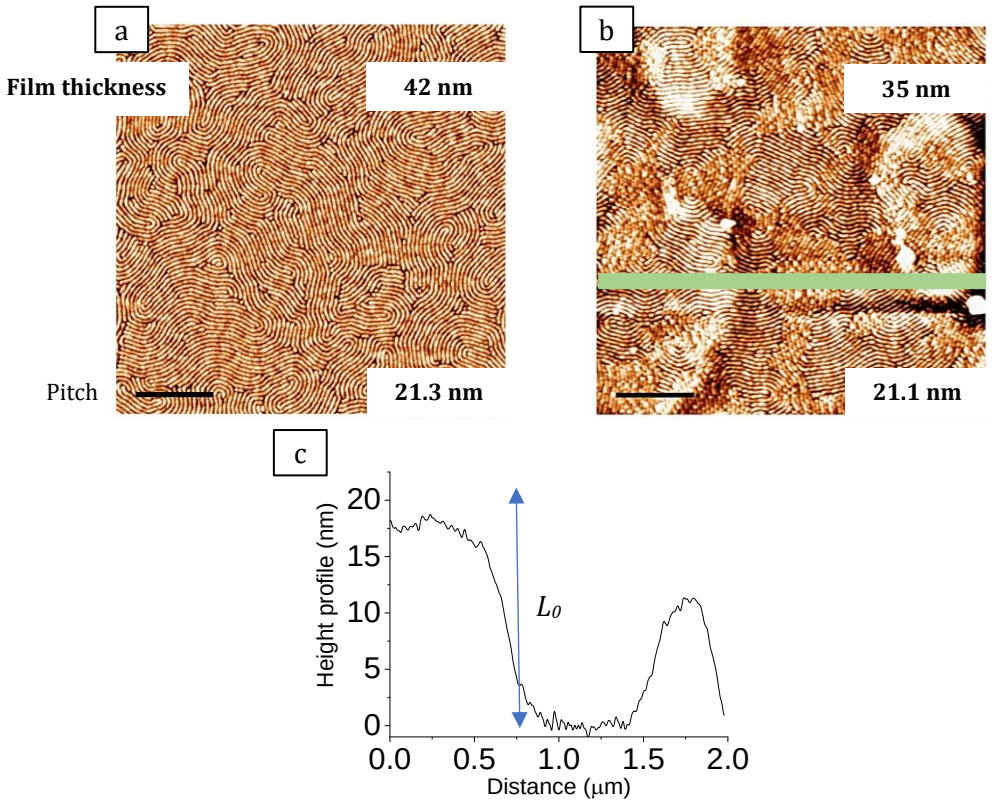

Figure 2-11: Self-assembly of cylinder-forming $PDMSB_{74}$-*b*-PS_{224} in thin film. (2 µm x 2 µm) AFM images (height) of (a) 42-nm thick and (b) 35-nm thick films of $PDMSB_{74}$-*b*-PS_{224}. (c) is the corresponding height profile obtained from the green line in (b).

Using a film thickness that is commensurate with L_0, it is possible to obtain a smooth film of in-plane PDMSB cylinders. In order to further improve the grain size of the cylinders, it is common to increase either the temperature or the time of the thermal annealing process in order to kinetically annihilate trapped defects at the grain boundaries [16]–[18]. To this end, we performed the self-assembly of the PDMSB$_{74}$-*b*-PS$_{224}$ at the given thickness of 42 nm and we increased the thermal annealing time from 2 min to 45 min. As expected, we are able to improve the ordering of the self-assembled nanostructures (Figure 2-12).

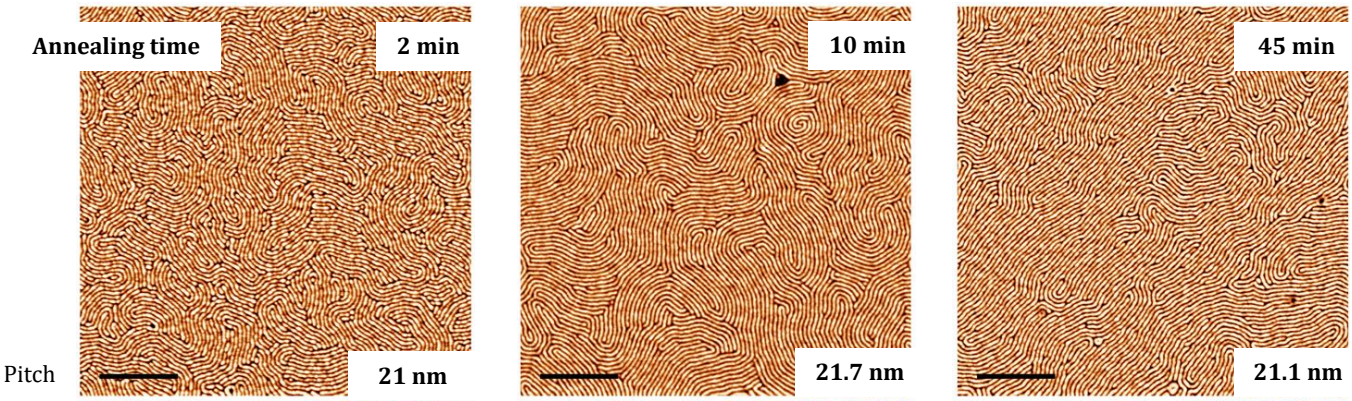

Figure 2-12: (2 µm x 2 µm) AFM images (height) of self-assembled cylinder-forming PDMSB$_{74}$-*b*-PS$_{224}$ in thin film as a function of the annealing time.

We used an image analysis tool developed by Murphy et *al.* [19] in order to highlight the relationship between the improvement of the ordering and the annealing time. This tool is an available macro that can be uploaded on the Image J software to evaluate the characteristics (such as the density of defects or the correlation length) of in-plane cylinder- or lamellar-forming nanostructures. The correlation length is related to the degree of ordering of the nanostructured film. It describes the average distance over which the orientational order is maintained. Figure 2-13 shows orientationally colour-mapped images corresponding to the PDMSB$_{74}$-*b*-PS$_{224}$ films presented in Figure 2-12. The coloured grains correspond to ordered domains of in-plane cylinders, aligned in a given direction. As shown in the Figure 2-13, the increase of the annealing time is correlated with an increase of the grain size up to a correlation length value of 433 nm.

This analysis is thus in agreement with an enhanced diffusion of the polymer chains with the increase of the thermal budget as reported in the literature [20]–[22].

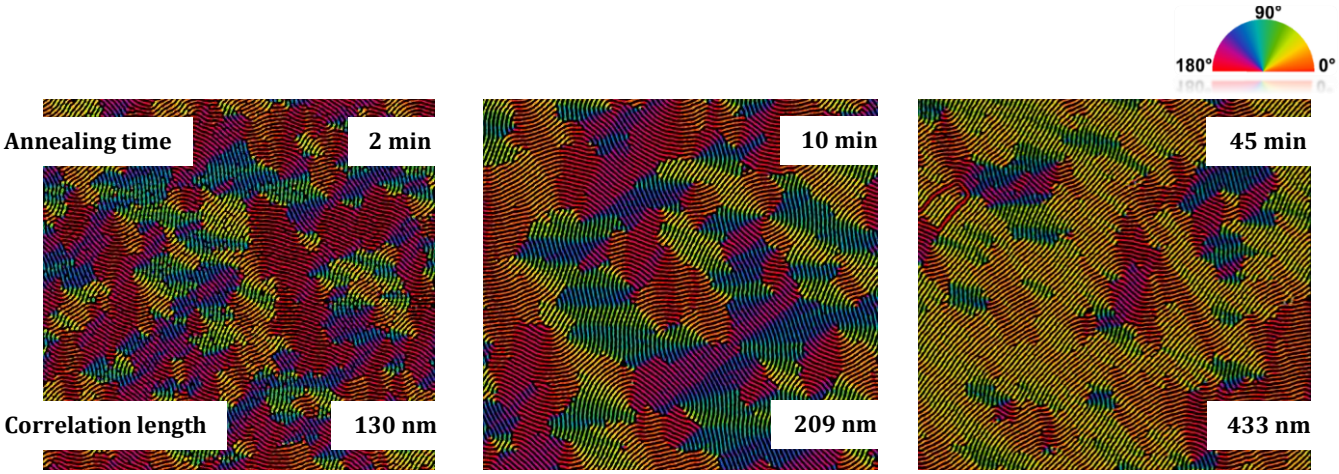

Figure 2-13: Correlation between the annealing time and the grain size in self-assembled cylinder-forming PDMSB$_{74}$-*b*-PS$_{224}$ films.

We decided to perform the self-assembly of the other cylinder-forming PDMSB-*b*-PS in thin film following the procedure:

i. spin-coating of the BCP film at 2000 rpm,
ii. thermal annealing of the BCP at 180°C for 5 min,
iii. and removal of the wetting PDMSB layer by plasma etching.

As shown the Figure 2-14, well-defined PDMSB cylinders are obtained in ~42 nm thick film after the removal of the PDMSB wetting layer. The periodicity of the domains varies from 21.7 nm to 41.6 nm which is consistent with the increase of the BCP molecular weight. Surprisingly, in-plane cylinders were observed for PDMSB$_{74}$-*b*-PS$_{224}$ and PDMSB$_{79}$-*b*-PS$_{251}$ while out-of-plane cylinders are observed for PDMSB$_{102}$-*b*-PS$_{245}$, PDMSB$_{104}$-*b*-PS$_{330}$, PDMSB$_{200}$-*b*-PS$_{636}$, PDMSB$_{207}$-*b*-PS$_{906}$ for this given thickness.

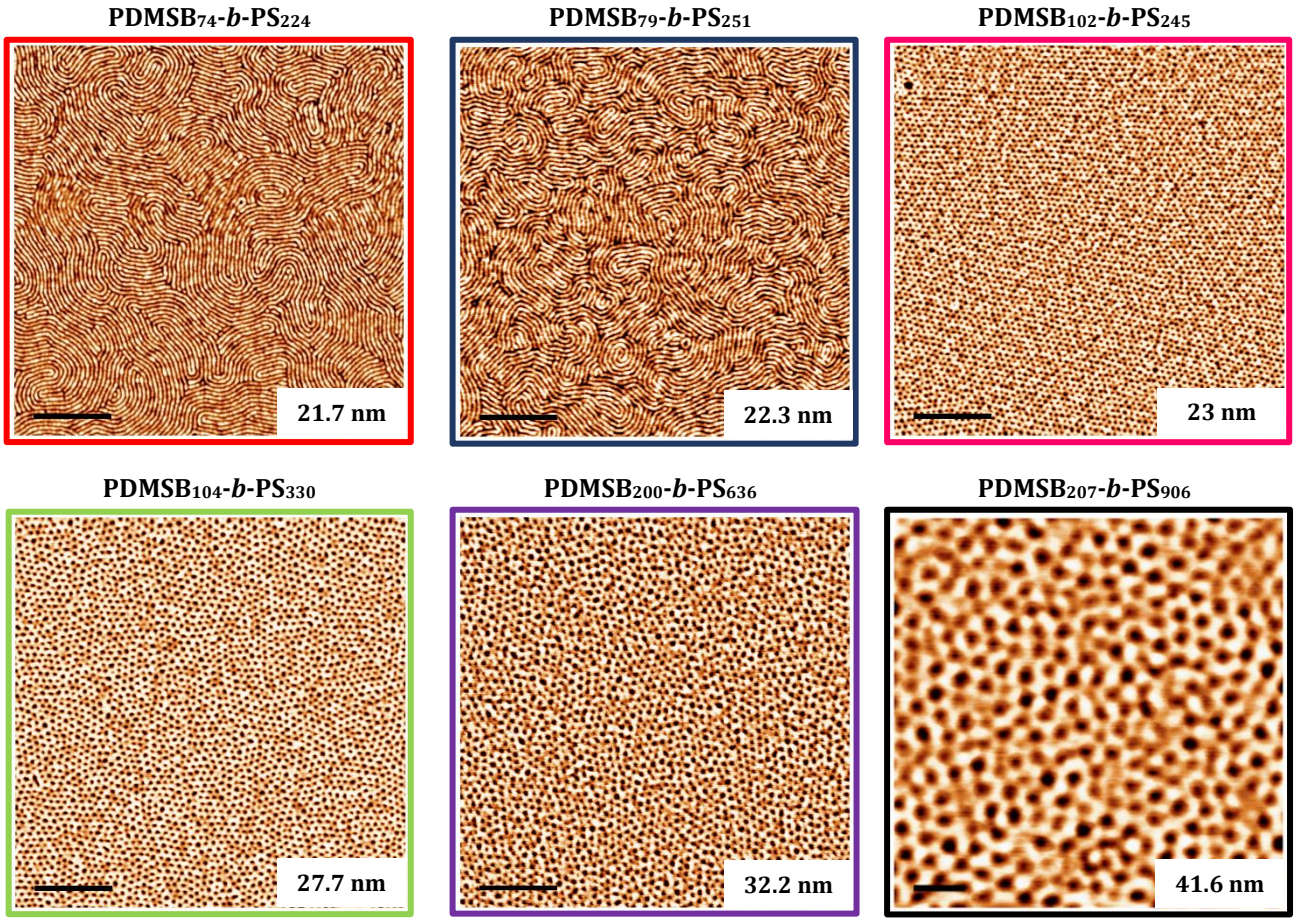

Figure 2-14: AFM images (height) of self-assembled cylinder-forming PDMSB-*b*-PS of various molecular weights. Scale bar: 200 nm except for the PDMSB$_{207}$-*b*-PS$_{906}$ for which the scale bar is 100 nm.

To understand this behaviour, we looked at the DSC thermograms of the polymers (Figure 2-15). As the molecular weight of the polymer increased, the size of the PDMSB domains concurrently increased (for nearly constant composition) leading to an increase of the stacking of folded chains. As the $T_{m,\,PDMSB}$ is related to the thickness of the crystalline lamellar stack, there is thus a shift of the $T_{m,\,PDMSB}$ to higher temperatures [23].

Consequently, we can access a range of melting temperatures around the RT, with the small molecular weight PDMSB-*b*-PS having a melting temperature below RT, while the higher molecular weight ones having a melting temperature above this threshold value. Consequently, it appears that a correlation exists between the orientation of the cylinders and the $T_{m,\,PDMSB}$ with the respect to the RT: in-plane cylinders are obtained for the BCPs having a melting temperature

below RT while out-of-plane cylinders are obtained for the ones having a melting temperature above RT as shown the Table 2-6.

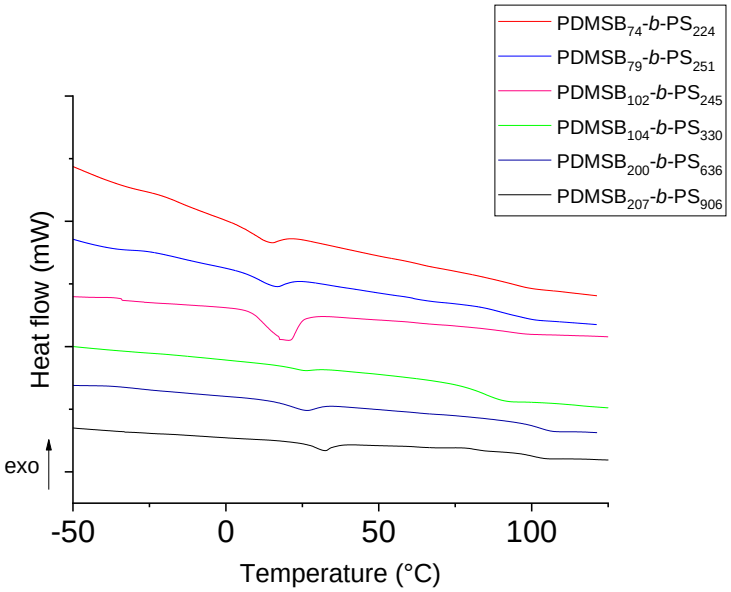

Figure 2-15: DSC traces of cylinder-forming PDMSB$_{74}$-*b*-PS$_{224}$, PDMSB$_{79}$-*b*-PS$_{251}$, PDMSB$_{102}$-*b*-PS$_{245}$, PDMSB$_{104}$-*b*-PS$_{330}$, PDMSB$_{200}$-*b*-PS$_{636}$ and PDMSB$_{207}$-*b*-PS$_{906}$. Heating rate: 10°C.min^{-1}.

Table 2-6: Macromolecular characteristics of the cylinder-forming PDMSB-*b*-PS and correlation between the PDMSB melting temperature and the orientation of the cylinders in thin film.

Material	M_n (g.mol^{-1})	f_{PDMSB}	$T_{g,\,PS}$ (°C)	$T_{m,\,PDMSB}$ (°C)	Cylinders orientation
PDMSB$_{74}$-*b*-PS$_{224}$	19350	0.29	94	15.2	In-plane
PDMSB$_{79}$-*b*-PS$_{251}$	21500	0.28	96	17	In-plane
PDMSB$_{102}$-*b*-PS$_{245}$	22500	0.34	92	20.5	Out-of-plane
PDMSB$_{104}$-*b*-PS$_{330}$	28200	0.28	84	25.5	Out-of-plane
PDMSB$_{200}$-*b*-PS$_{636}$	54400	0.28	102	26.2	Out-of-plane
PDMSB$_{207}$-*b*-PS$_{906}$	72700	0.22	101	32.5	Out-of-plane

As discussed in the Introduction part, the segregation strength of a given BCP system increases with the degree of polymerization. Consequently, we can assume that the increase of the segregation strength in higher molecular weight PDMSB-*b*-PS and the underlying crystallization prevent the conformational adjustment of the blocks in thin films leading to kinetically trapped perpendicular structure. On the other hand, in the case of smaller molecular weight for which $T_{m,}$

$_{PDMSB}$ is below RT, the surface free energy dominates the orientation of the cylinders: as the surface energy of the PDMSB is lower than the one of the PS, in-plane PDMSB cylinders are obtained.

In order to further investigate the effect of the $T_{m,\ PDMSB}$ on the cylinder orientation, blends of PDMSB$_{74}$-*b*-PS$_{224}$ and PDMSB$_{104}$-*b*-PS$_{330}$ were prepared at different weight fraction: 70:30, 55:45, 50:50, 30:70. The blends were characterized by DSC as shown in the Figure 2-16. One can see that there is a relationship of the characteristic temperatures, $T_{g,\ PS}$ and $T_{m,\ PDMSB}$ with the PDMSB$_{74}$-*b*-PS$_{224}$ content (Figure 2-17(a)). The $T_{g,\ PS}$ in the different mixtures can be predicted using the Fox equation: $\frac{1}{T_{g,PS}} = \frac{w_1}{T_{g1,PS}} + \frac{w_2}{T_{g2,PS}}$ where $T_{g,\ PS}$ is the glass transition temperature of the PS block in the blend, $T_{gx,\ PS}$ and w_x the glass transition temperature and weight fraction of the block *x*. It is thus consistent with a homogeneous and miscible mixture of the two PS blocks in the blend (Figure 2-17(b)). Additionally, by varying the PDMSB$_{74}$-*b*-PS$_{224}$:PDMSB$_{104}$-*b*-PS$_{330}$ ratio, it is possible to access a continuous range of PDMSB melting temperature comprised between the ones of the PDMSB$_{74}$-*b*-PS$_{224}$ and PDMSB$_{104}$-*b*-PS$_{330}$.

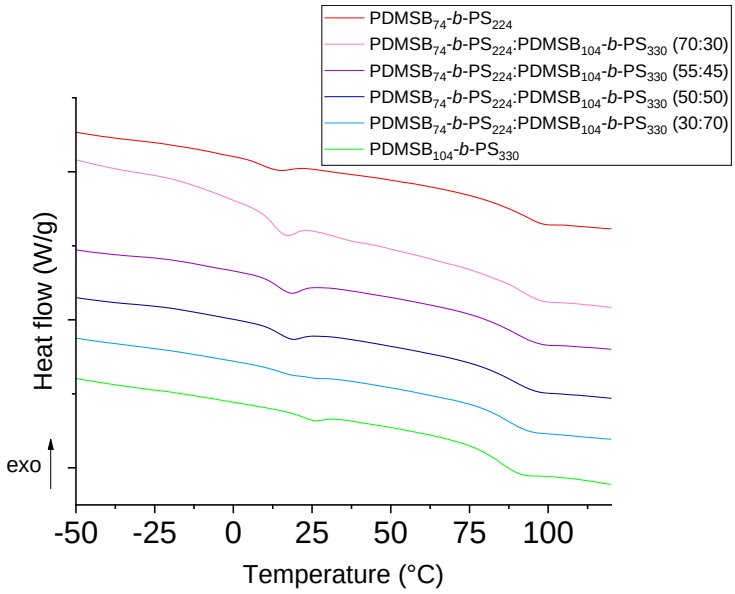

Figure 2-16: DSC traces of PDMSB$_{74}$-*b*-PS$_{224}$ and PDMSB$_{104}$-*b*-PS$_{330}$ mixed at different weight fraction. Heating rate: 10°C.min^{-1}.

a

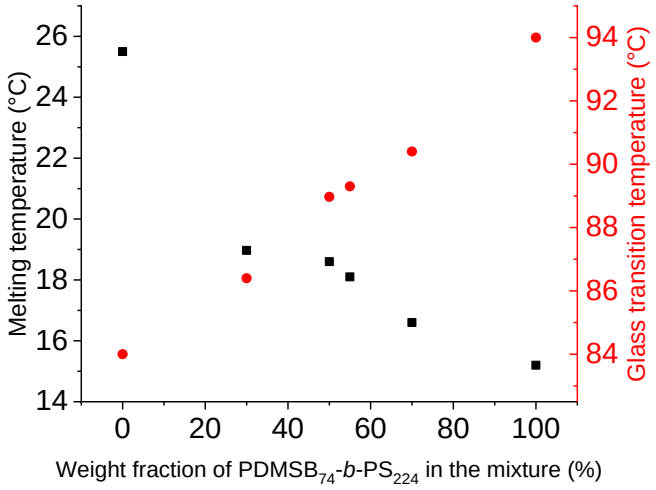

b

PDMSB$_{74}$-*b*-PS$_{224}$ (% wt.)	$T_{g,\,PS}$ Exp. (°C)	$T_{g,\,PS}$ Fox (°C)	$T_{m,\,PDMSB}$ (°C)
0	84	84	25.5
30	86.4	86.8	19
50	88.9	88.7	18.6
55	89.3	89.2	18.1
70	90.4	90.8	16.6
100	94	94	15.2

Figure 2-17: Melting and glass transition temperatures of the polymer mixtures as a function of the PDMSB$_{74}$-*b*-PS$_{224}$ weight fraction.

The self-assembly of the PDMSB$_{74}$-*b*-PS$_{224}$:PDMSB$_{104}$-*b*-PS$_{330}$ mixtures was performed by preparing 2% wt. solution of three blends (70:30, 50:50, 30:70) in methyl isobutyl ketone. The solutions were spin-coated onto silicon substrates at various speeds in order to reach films with thicknesses of 15 nm, 65 nm and 140 nm. A thermal annealing was then performed at 180°C for 5 min followed by a CF_4/O_2 plasma for 45 s to remove the PDMSB wetting layer.

Interestingly, the 15-nm thick film with 70% of PDMSB$_{74}$-*b*-PS$_{224}$ is split into 15 nm-depth terraces with out-of-plane cylinders in the lower part while in-plane cylinders are observed in the upper part (see in the Figure 2-18(a) and (d)). This is due to the non-commensurability of the film thickness with the periodicity of the cylinders. Indeed, as the average film thickness is less than a repeating distance (21.9 nm), hills and valleys are formed such that in higher regions the thickness is equal to an integer number of repeat distances [13]. For the thin film containing 50% of PDMSB$_{74}$-*b*-PS$_{224}$, a smoother film is obtained with a mixed orientation consisting of out-of-plane cylinders and ill-defined in-plane cylinders (see in the Figure 2-18(b)). We can note, however, the presence of small hills of 15 nm-depth with a majority of out-of-plane cylinders (see bottom-right of the AFM image, Figure 2-18(b)). Finally, for the film having 30% of PDMSB$_{74}$-*b*-PS$_{224}$, a smooth film is obtained with poorly organized out-of-plane cylinders (see in the Figure 2-18(c)). Consequently, it seems that there is a competition between the thermodynamic and an underlying

crystallization mechanism. Indeed, for high PDMSB$_{74}$-*b*-PS$_{224}$ content (i.e. $T_{m,\ PDMSB}$ below RT), the surface free energy is dominating such that terraces are formed. When the PDMSB$_{74}$-*b*-PS$_{224}$ content in the blend decreases (i.e. $T_{m,\ PDMSB}$ above RT), the formation of terraces is inhibited until reaching a smooth film of kinetically frozen out-of-plane cylinders.

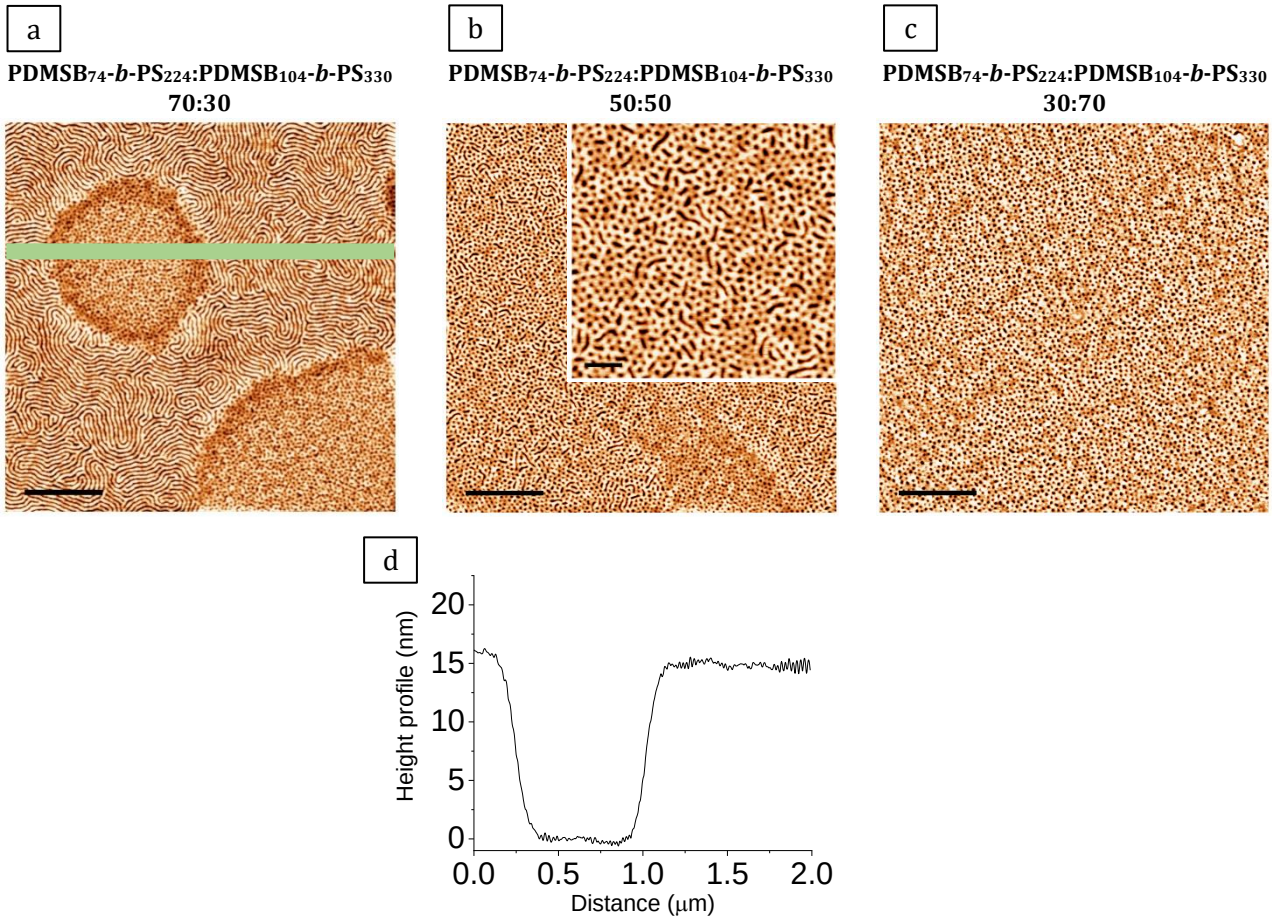

Figure 2-18: **(2 µm x 2 µm) AFM images (height) of self-assembled PDMSB$_{74}$-*b*-PS$_{224}$:PDMSB$_{104}$-*b*-PS$_{330}$ mixtures in thin film with (a) 70%, (b) 50% and (c) 30% of PDMSB$_{74}$-*b*-PS$_{224}$. The scale bar of the inset is 100 nm. (d) is the corresponding height profile of the film with 70% of PDMSB$_{74}$-*b*-PS$_{224}$. The film thickness is 15 nm.**

If we increase the thickness of the films, the in-plane orientation is favoured over the out-of-plane orientation for the 70:30 and 50:50 PDMSB$_{74}$-*b*-PS$_{224}$:PDMSB$_{104}$-*b*-PS$_{330}$ blends (Figure 2-19). For the 30:70 PDMSB$_{74}$-*b*-PS$_{224}$:PDMSB$_{104}$-*b*-PS$_{330}$ blend, the out-of-plane orientation is maintained with a decrease of the density of defects and an improvement of the long-range ordering as shown in the Figure 2-20. The correlation length was indeed found to be 49 nm, 178 nm and 210 nm for film thicknesses of 15 nm, 65 nm and 140 nm, respectively.

This out-of-plane orientation is obtained for the blend having a $T_{m,\,PDMSB}$ close to 20°C, which is in agreement with our hypothesis of an underlying crystallization that kinetically trapped the perpendicular structure. Moreover, the persistence of the out-of-plane cylinders regardless of the film thickness allows thus to decorrelate this orientation from an effect related to the commensurability between the thickness and the periodicity of the domains.

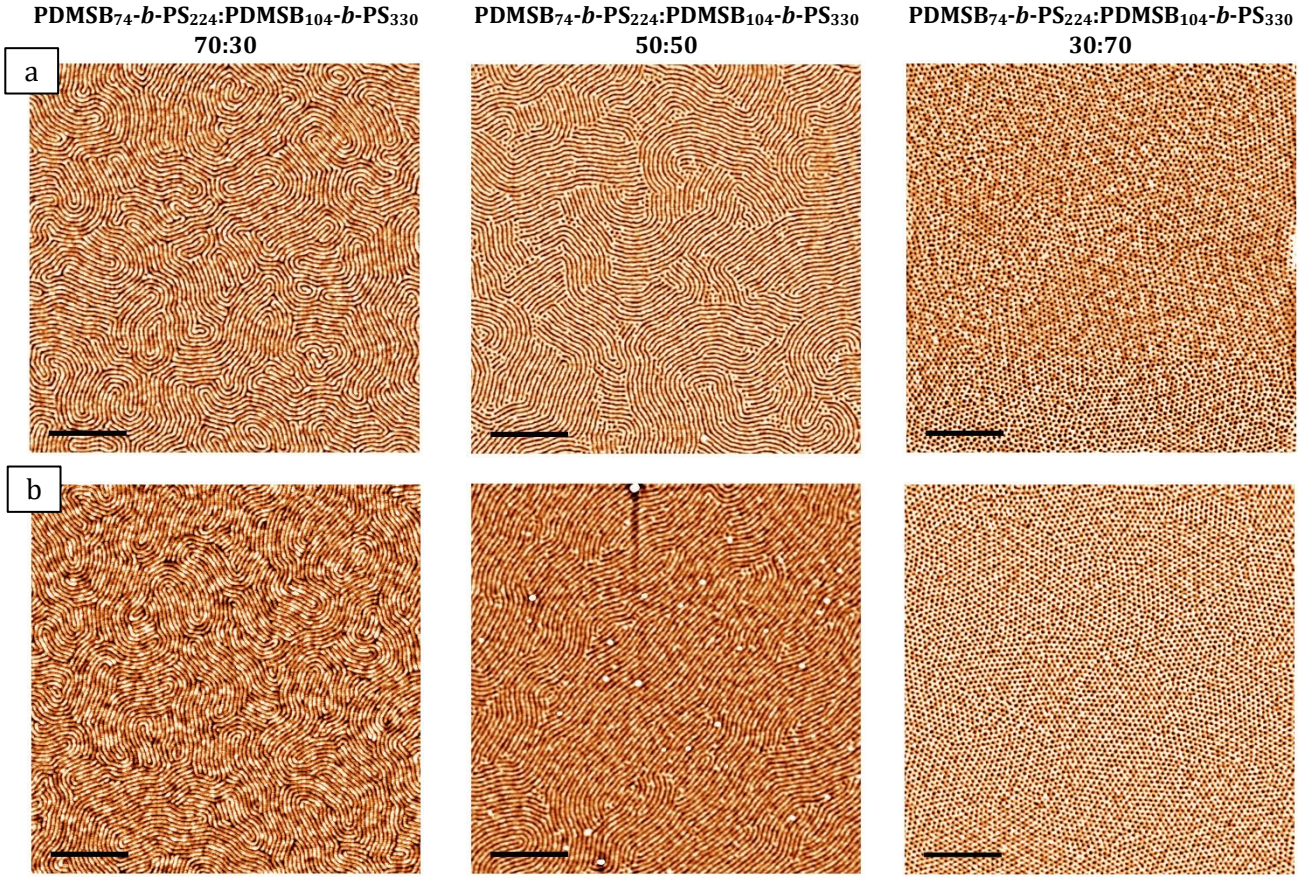

Figure 2-19: **(2 µm x 2 µm) (a) AFM images (height) of self-assembled PDMSB$_{74}$-*b*-PS$_{224}$:PDMSB$_{104}$-*b*-PS$_{330}$ blends in thin film with 70%, 50% and 30% of PDMSB$_{74}$-*b*-PS$_{224}$. The film thickness is (a) 65 nm and (b) 140 nm.**

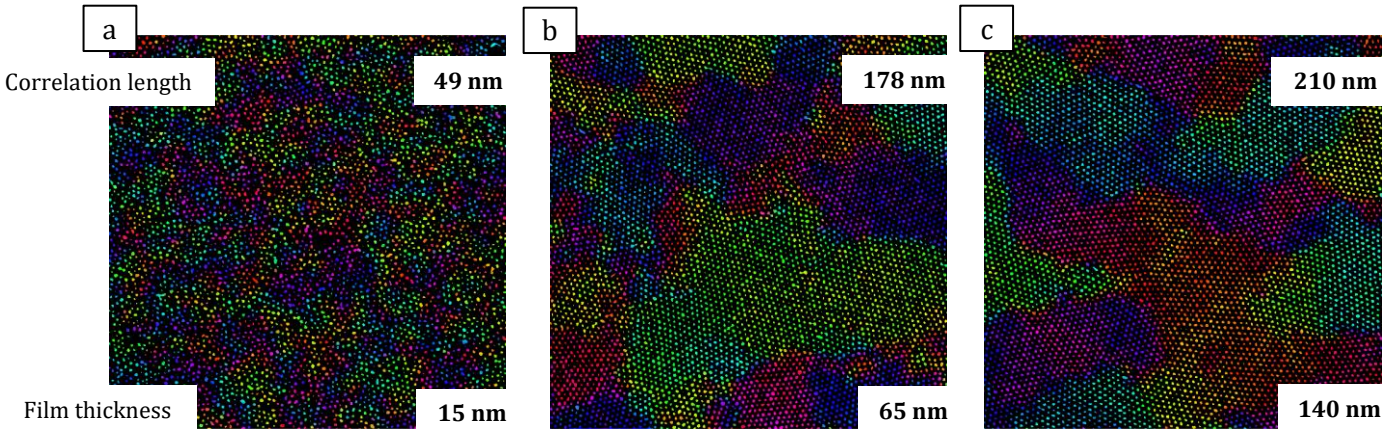

Figure 2-20: **Correlation between the film thickness and the long-range ordering in the thin film containing 30% of PDMSB$_{74}$-*b*-PS$_{224}$.**

The self-assembly of cylinder-forming PDMSB-*b*-PS was performed in thin film using a thermal annealing process. We studied some of the main parameters that have been proposed in the literature for the formation of well-defined nanostructures that are the thermal annealing time and the variation of the BCP film thickness. In the case of our semi-crystalline system, we also hilighted the effect of the cristallinity on the orientation of the cylinders in the film. Indeed, by playing with the melting temperature of the PDMSB block with the respect to RT, it is possible to balance the thermodynamic with a fast crystallization to kinetically trapped the perpendicular orientation. Consequently, it is possible to obtain well-defined out-of-plane cylinders for different film thicknesses without using neutral layers.

2. Gyroid-forming PDMSB-*b*-PS BCP

Among the wide range of accessible BCP self-assembled structures, the three-dimensional double gyroid (DG) phase is of particular interest because of its bicontinuous structure. As noted in the Introduction section, this bicontinuous phase consists of two interwoven continuous networks of the minority polymer block held in a matrix phase of the majority block. The gyroid phase has been observed in bulk for diblock copolymers [24], [25], blends of two diblock copolymers [26], blends of diblocks with homopolymers [27], [28] and small plasticizing molecules [29]. Although many studies were performed on the phase behaviour of the DG phase in bulk, only few studies on BCP forming DG in thin films were reported [4], [30]–[35]. The first reason is that the DG structure is located in a narrow window of the phase diagram which makes difficult to target the required macromolecular characteristics. When having the appropriated BCP system, the formation of this 3D structure in thin film is another challenge. Indeed, the stability of the DG phase is influenced by many parameters such as the commensurability between the film thickness and the unit cell lattice, the interactions between the film and the surface leading in some cases to the suppression of the structure or to order-order transitions [34], [36]. Moreover, all the reported self-assembled nanostructures were obtained using a solvent annealing [4], [32]–[35] or long thermal-annealing [30], [31] processes. For these reasons, we decided to study the self-assembly of the gyroid-forming $PDMSB_{54}$-*b*-PS_{124} in thin film using a

thermal annealing process. We have explored the parameters that are inherent to the formation and stabilization of the structure in thin film, i.e the thermal annealing temperature and the film thickness.

For this purpose, 3% wt. of $PDMSB_{54}$-*b*-PS_{124} in a mixture of THF and propylene glycol methyl ether acetate (PGMEA) (70:30) were spin-coated on silicon substrate at 1000 rpm to reach a 200 nm thickness (thus above the DG unit cell determined by SAXS, a_G = 35 nm). The self-assembly of $PDMSB_{54}$-*b*-PS_{124} thin film was achieved with a thermal annealing at 180°C for 5 min. The CF_4/O_2 RIE treatment was then applied to preferentially remove the PDMSB phase.

Figure 2-21 shows the AFM images (phase) of the $PDMSB_{54}$-*b*-PS_{124} thin film after the RIE treatment. This structure corresponds to a (211) DG plane oriented parallel to the air surface in accordance with the simulation of this particular plane (see inset in the Figure 2-21). Indeed, this pattern is the characteristic "double-wave" as it is made of small- and large-amplitude oscillations of the minority domains. The period of the (211) DG plane was estimated to be around 15.8 nm using the 2D-FFT of the topographical image which is consistent with the SAXS data (see Figure 2-9).

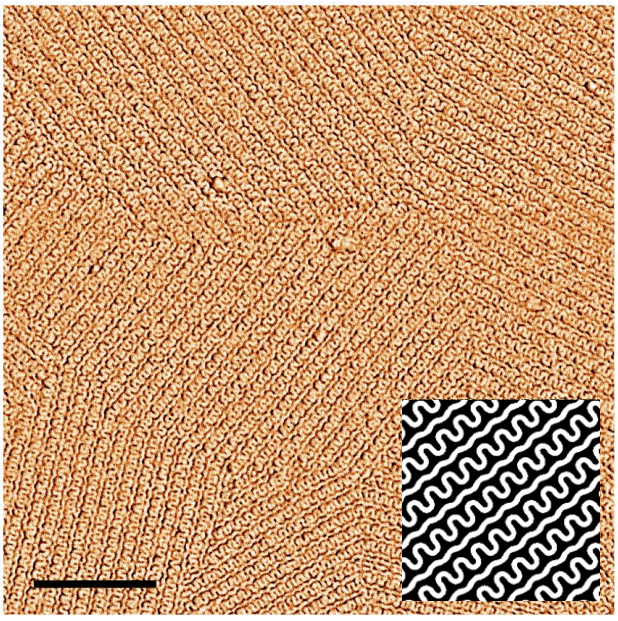

Figure 2-21: (2 µm x 2 µm) AFM phase image of self-assembled gyroid-forming PDMSB-*b*-PS in thin film. The inset corresponds to the SCFT simulation of the DG structure with the (211) plane parallel to the air surface. Scale bar: 400 nm.

The structure and its orientation were also confirmed by GISAXS. As shown in the Figure 2-22, the GISAXS experimental data matches the simulated pattern obtained for a $Ia\bar{3}d$ cubic structure with the (211) DG plane parallel to the air surface. From the GISAXS results, it is also possible to extract the unit cell dimension of the structure which was found to be 36.5 nm which is in good agreement with SAXS analysis (see section II.4).

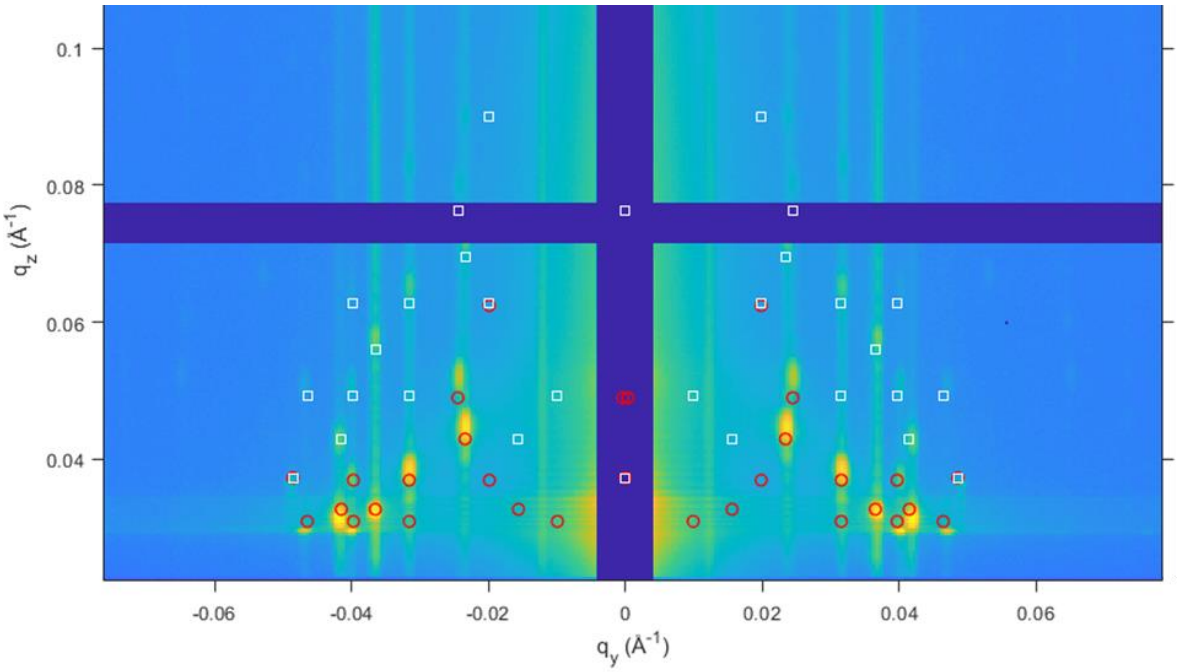

Figure 2-22: GISAXS pattern of the self-assembled PDMSB$_{54}$-*b*-PS$_{124}$ thin film which is consistent with DG structure having a (211) plane parallel to the air surface. The simulated pattern was obtained using the GIXSGUI package assuming that a (211) plane of the DG structure at the air interface.

To study the effect of the annealing temperature on the self-assembled structures, we fixed the film thicknesses at 200 nm and we thermally annealed the PDMSB-*b*-PS thin films between 140°C and 220°C for 5 min on Si substrates (Figure 2-23). As shown in the Figure 2-23(a) and (b), a 5 min annealing below 180°C does not lead to the complete formation of the DG structure. Indeed, at 140°C, we have an intermediate structure with a "dot and line" pattern from which the (211) DG structure is growing with the increase of the temperature (see Figure 2-23(a)). At 160°C, a DG grain front growth can be observed on the AFM image (see Figure 2-23(b)) which consists in small amplitude oscillations similar to the ones of the DG structure and that are commensurate with the interline distance as shown in Figure 2-24. Additionally, hints of large amplitude oscillations are

also visible (Figure 2-23(b)). In 2017, this metastable structure was experimentally observed in thin film by Aissou et *al.* in solvent annealed PDMSB-*b*-PS films for film thicknesses below the unit cell lattice and short annealing time [4]. Likewise, Matsen observed this metastable state using a SCFT study during the epitaxial cylinder-to-gyroid transition [37]. SCFT calculations were also performed by Ji et *al*. to show that lamellar-to-gyroid transition could also occur from a metastable cylinder-like phase with a similar pattern to the one we observed in Figure 2-23(a) [38]. At 180°C, the DG structure with the characteristic "double wave" pattern (Figure 2-23(c)) is retrieved.

By increasing the annealing temperature, an order-order transition from the DG structure to in-plane PDMSB cylinders was observed as it can be expected from the phase diagram (Figure 2-23(e)). Indeed, the χ parameter of the system decreases with the increase of the temperature, shifting the BCP equilibrium phase toward the cylindrical window.

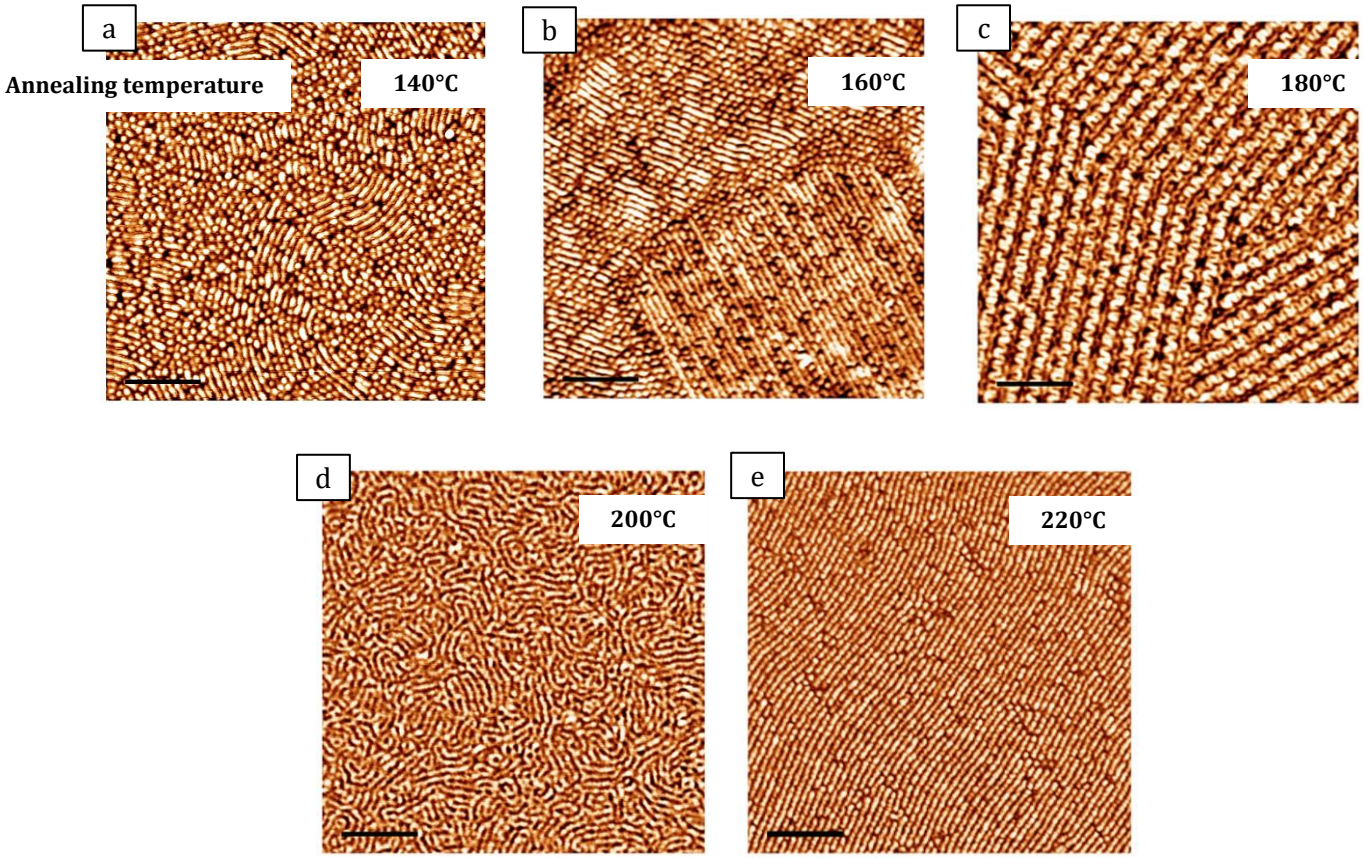

Figure 2-23: **(1 µm x 1 µm) AFM topographical images of $PDMSB_{54}$-*b*-PS_{124} thin films after a thermal annealing for 5 min at (a) 140°C, (b) 160°C, (c) 180°C, (d) 200°C and (e) 220°C. Film thickness ~200 nm. Scale bar: 200 nm.**

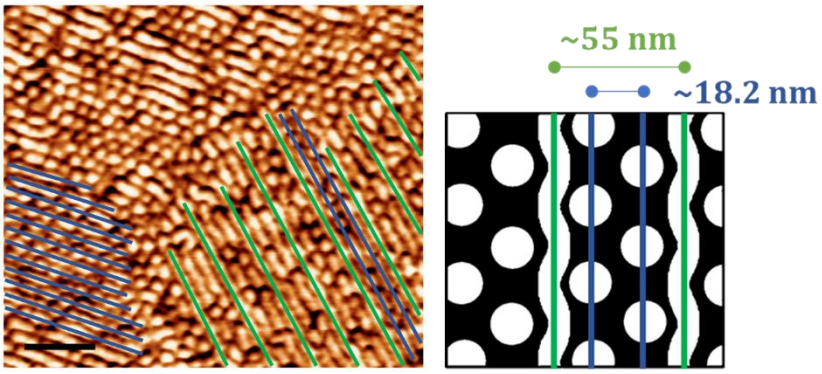

Figure 2-24: "Dot and line" pattern observed at 160°C. Commensurability between the small amplitude oscillations of the growing DG grain (highlighted with the green lines) and the interline distance (highlighted with the blue lines). Scale bar: 100 nm.

To study the effect of the film thickness, the same experiment was performed with a film thickness around 70 nm (twice the unit cell dimension). Interestingly, we were not able to stabilize the gyroid morphology. Indeed, there is a direct transition from the metastable "dot and line" pattern to in-plane PDMSB cylinders. This result is similar to the work of Aissou et *al.* where they showed that the complete formation of the gyroid requires a film thickness well above the unit cell lattice for similar annealing conditions [4]. In our case, the stabilization of the DG phase occurs for a film thickness which is four times the unit cell dimension.

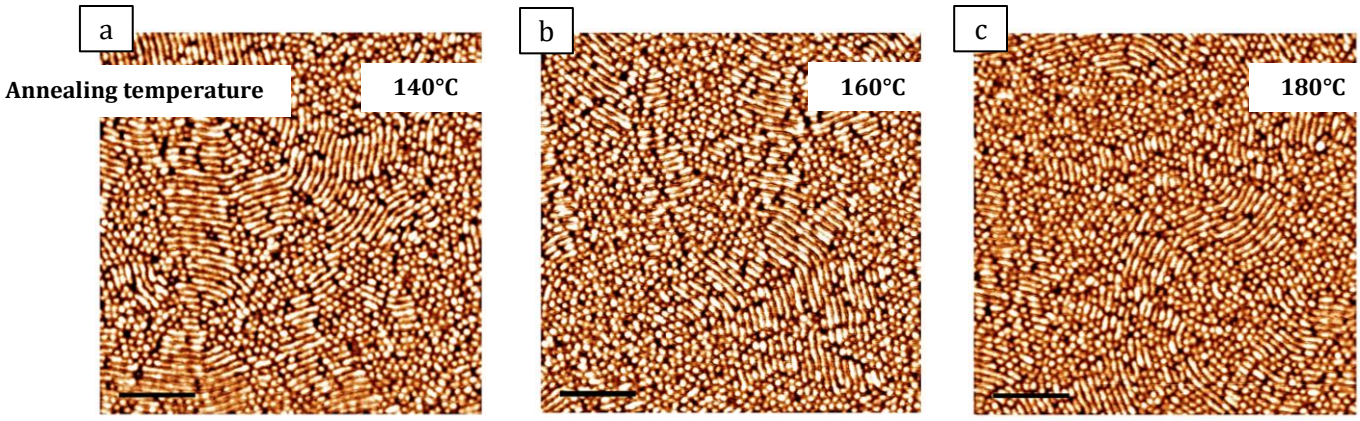

Figure 2-25: (1 µm x 1 µm) AFM images (height) of the $PDMSB_{54}$-*b*-PS_{124} after a thermal-annealing for 5 min at 160°C (a), 180°C (b) and 200°C (c). Film thickness ~70 nm. Scale bars: 200 nm.

Finally, if we keep increasing the annealing time at the same temperatures, there is a direct transition from the metastable "dot and line" pattern to in-plane PDMSB cylinders with a 18.2 nm periodicity. This structure seems thus to be the most stable structure for these conditions.

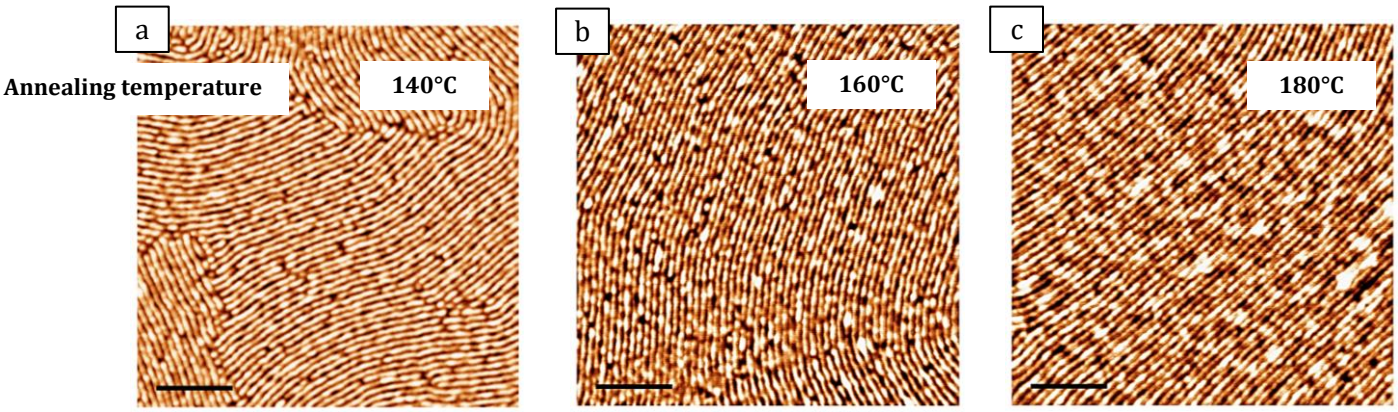

Figure 2-26: (1 µm x 1 µm) AFM images (height) of the PDMSB$_{54}$-*b*-PS$_{124}$ after a thermal-annealing for 45 min at 160°C (a), 180°C (b) and 200°C (c). Film thickness ~70 nm.

In summary, we reported the successful stabilization of a gyroid structure with the smallest unit cell reported up to date using a short thermal annealing process. We also highlighted the main parameters leading to the stabilization of this particular structure in thin film: a rapid and high temperature annealing is required to kinetically trap the DG structure in films largely thicker than the DG unit cell. Indeed, such configuration allows a decrease of the interactions between the BCP film and the interfaces (substrate and/or air) while limiting the geometric confinement due to the three-dimensional nature of the DG structure.

IV. Conclusion

To conclude, the phase behaviour of the PDMSB-*b*-PS system was deciphered in order to highlight its potential for nanolithography applications. The Flory-Huggins parameter of the PDMSB-*b*-PS system was estimated to be 0.13 ± 0.06 at RT which is four times the value of the conventional PS-*b*-PMMA BCP ($\chi_{PS\text{-}b\text{-}PMMA}$ = 0.03 at RT [12]). Moreover, we have demonstrated the ability of the PDMSB-*b*-PS to segregate into lamellae, gyroid and cylindrical nanostructures in bulk and have provided an understanding of the self-assembly behaviour of our semi-crystalline BCPs in thin film. Cylindrical and gyroid nanostructures were obtained in thin film using industrially-friendly processes (i.e. thermal annealing, compatible solvents and fast process) with an emphasis on the parameters that have to be taken into account for the control of the organisation and orientation of the nanostructures. In this context, out-of-plane and in-plane cylinders were obtained with various periodicities and the stabilization of a DG structure in thin film was demonstrated using a short thermal annealing process.

Nevertheless, the main structure of interest for BCP lithography is related to an out-of-plane lamellar morphology, which is difficult to stabilize for high-χ systems due to the important mismatch of surface energy between the BCP domains. Consequently, the next chapter will be dedicated to the methodologies allowing the formation of out-of-plane lamellae in the thin film configuration.

V. References

[1] A. Nunns, J. Gwyther and I. Manners, "Inorganic block copolymer lithography", *Polymer*, vol. 54, nº 4, p. 1269-1284, févr. 2013.

[2] K. Aissou, M. Mumtaz, G. Fleury *et al.*, "Sub-10 nm Features Obtained from Directed Self-Assembly of Semicrystalline Polycarbosilane-Based Block Copolymer Thin Films", *Adv. Mater.*, vol. 27, nº 2, p. 261-265, janv. 2015.

[3] G. Fleury, K. Aissou, M. Mumtaz *et al.*, "Development and integration of systems with enhanced resolutions based on Si-containing block copolymers for line space applications", 2015, p. 94250Z.

[4] K. Aissou, M. Mumtaz, G. Portale *et al.*, "Templated Sub-100-nm-Thick Double-Gyroid Structure from Si-Containing Block Copolymer Thin Films", *Small*, vol. 13, nº 20, p. 1603777, mai 2017.

[5] A. Legrain, G. Fleury, M. Mumtaz *et al.*, "Straightforward Integration Flow of a Silicon-Containing Block Copolymer for Line–Space Patterning", *ACS Applied Materials & Interfaces*, vol. 9, nº 49, p. 43043-43050, déc. 2017.

[6] S. Kawahara, A. Nagai, T. Kazama, A. Takano, and Y. Isono, "Preparation of Poly(1,1-dimethyl silabutane) by Anionic Polymerization and Its Crystallization", *Macromolecules*, vol. 37, nº 2, p. 315-321, janv. 2004.

[7] M. G. Abiad, M. T. Carvajal and O. H. Campanella, "A Review on Methods and Theories to Describe the Glass Transition Phenomenon: Applications in Food and Pharmaceutical Products", *Food Engineering Reviews*, vol. 1, nº 2, p. 105-132, déc. 2009.

[8] L. J. Fetters, D. J. Lohse, D. Richter, T. A. Witten and A. Zirkel, "Connection between Polymer Molecular Weight, Density, Chain Dimensions, and Melt Viscoelastic Properties", *Macromolecules*, vol. 27, nº 17, p. 4639-4647, août 1994.

[9] J. G. Kennemur, M. A. Hillmyer and F. S. Bates, "Synthesis, Thermodynamics, and Dynamics of Poly(4-tert-butylstyrene-b-methyl methacrylate)", *Macromolecules*, vol. 45, nº 17, p. 7228-7236, sept. 2012.

[10] A. N. Semenov, "Contribution to the theory of microphase layering in block-copolymer melts", *Sov. Phys. JETP*, vol. 61, nº 4, p. 733-742, 1985.

[11] F. S. Bates and G. H. Fredrickson, "Block copolymer thermodynamics: theory and experiment", *Annual Review of Physical Chemistry*, vol. 41, nº 1, p. 525–557, 1990.

[12] Y. S. Jung and C. A. Ross, "Orientation-Controlled Self-Assembled Nanolithography Using a Polystyrene−Polydimethylsiloxane Block Copolymer", *Nano Letters*, vol. 7, nº 7, p. 2046-2050, juill. 2007.

[13] M. A. van Dijk and R. van den Berg, "Ordering Phenomena in Thin Block Copolymer Films Studied Using Atomic Force Microscopy", *Macromolecules*, vol. 28, nº 20, p. 6773-6778, sept. 1995.

[14] H.-C. Kim and T. P. Russell, "Ordering in thin films of asymmetric diblock copolymers", *Journal of Polymer Science Part B: Polymer Physics*, vol. 39, nº 6, p. 663-668, mars 2001.

[15] K. Aissou, "Etude de l'auto-organisation de films minces de copolymères diblocs en vue d'applications pour la microélectronique", Laboratoire des Technologies de la Microélectronique, CNRS, 17 Rue des Martyrs (CEA-LETI), 38054 Grenoble Cedex 9, France, 10-janv-2007.

[16] Q. Peng, Y.-C. Tseng, S. B. Darling and J. W. Elam, "Nanoscopic Patterned Materials with Tunable Dimensions via Atomic Layer Deposition on Block Copolymers", *Advanced Materials*, vol. 22, nº 45, p. 5129-5133, déc. 2010.

[17] R. Ruiz, L. Wan, J. Lille *et al.*, "Image quality and pattern transfer in directed self assembly with block-selective atomic layer deposition", *Journal of Vacuum Science & Technology B: Microelectronics and Nanometer Structures*, vol. 30, nº 6, p. 06F202, 2012.

[18] H.-S. Moon, J. Y. Kim, H. M. Jin *et al.*, "Atomic Layer Deposition Assisted Pattern Multiplication of Block Copolymer Lithography for 5 nm Scale Nanopatterning", *Advanced Functional Materials*, vol. 24, nº 27, p. 4343-4348, juill. 2014.

[19] J. N. Murphy, K. D. Harris and J. M. Buriak, "Automated Defect and Correlation Length Analysis of Block Copolymer Thin Film Nanopatterns", *PLOS ONE*, vol. 10, nº 7, p. e0133088, juill. 2015.

[20] X. Gu, I. Gunkel, A. Hexemer and T. P. Russell, “Controlling Domain Spacing and Grain Size in Cylindrical Block Copolymer Thin Films by Means of Thermal and Solvent Vapour Annealing”, *Macromolecules*, vol. 49, nº 9, p. 3373-3381, mai 2016.

[21] M. Ceresoli, F.G. Volpe, G. Seguini *et al.*, “Scaling of correlation length in lamellae forming PS-b-PMMA thin films upon high temperature rapid thermal treatments”, *Journal of Materials Chemistry C*, vol. 3, nº 33, p. 8618-8624, 2015.

[22] H. Yokoyama and E. J. Kramer, “Self-Diffusion of Asymmetric Diblock Copolymers with a Spherical Domain Structure”, *Macromolecules*, vol. 31, nº 22, p. 7871-7876, nov. 1998.

[23] Z.-M. Li, S.-Q. Li and Z.-Y. Cheng, “Crystalline structure and transition behaviour of recrystallized-irradiated P(VDF-TrFE) 65⁄35 copolymer”, *Journal of Applied Physics*, vol. 97, nº 1, p. 014102, janv. 2005.

[24] G. Floudas, R. Ulrich and U. Wiesner, “Microphase separation in poly(isoprene- *b* -ethylene oxide) diblock copolymer melts. I. Phase state and kinetics of the order-to-order transitions”, *The Journal of Chemical Physics*, vol. 110, nº 1, p. 652-663, janv. 1999.

[25] L. Sun, L. Zhu, Q. Ge *et al.*, “Comparison of crystallization kinetics in various nanoconfined geometries”, *Polymer*, vol. 45, nº 9, p. 2931-2939, avr. 2004.

[26] H. Mao and M. A. Hillmyer, “Macroscopic samples of polystyrene with ordered three-dimensional nanochannels”, *Soft Matter*, vol. 2, nº 1, p. 57-59, 2006.

[27] T. Hashimoto, K. Tsutsumi and Y. Funaki, “Nanoprocessing Based on Bicontinuous Microdomains of Block Copolymers: Nanochannels Coated with Metals”, *Langmuir*, vol. 13, nº 26, p. 6869-6872, déc. 1997.

[28] A. Okumura, Y. Nishikawa and T. Hashimoto, “Nano-fabrication of double gyroid network structure via ozonolysis of matrix phase of polyisoprene in poly(2-vinylpyridine)-block-polyisoprene films”, *Polymer*, vol. 47, nº 22, p. 7805-7812, oct. 2006.

[29] S. Valkama, T. Ruotsalainen, A. Nykänen *et al.*, “Self-Assembled Structures in Diblock Copolymers with Hydrogen-Bonded Amphiphilic Plasticizing Compounds”, *Macromolecules*, vol. 39, nº 26, p. 9327-9336, déc. 2006.

[30] E. J. W. Crossland, M. Nedelcu, C. Ducati *et al.*, “Block Copolymer Morphologies in Dye-Sensitized Solar Cells: Probing the Photovoltaic Structure−Function Relation”, *Nano Letters*, vol. 9, nº 8, p. 2813-2819, août 2009.

[31] S. Salvatore, A. Demetriadou, S. Vignolini *et al.*, “Tunable 3D Extended Self-Assembled Gold Metamaterials with Enhanced Light Transmission”, *Advanced Materials*, vol. 25, nº 19, p. 2713-2716, mai 2013.

[32] M.-S. She, T.-Y. Lo and R.-M. Ho, “Controlled Ordering of Block Copolymer Gyroid Thin Films by Solvent Annealing”, *Macromolecules*, vol. 47, nº 1, p. 175-182, janv. 2014.

[33] Y.-H. Wu, T.-Y. Lo, M.-S. She and R.-M. Ho, “Morphological Evolution of Gyroid-Forming Block Copolymer Thin Films with Varying Solvent Evaporation Rate”, *ACS Appl. Mater. Interfaces*, vol. 7, nº 30, p. 16536-16547, août 2015.

[34] I. H. Ryu, Y. J. Kim, Y. S. Jung, J. S. Lim, C. A. Ross and J. G. Son, “Interfacial Energy-Controlled Top Coats for Gyroid/Cylinder Phase Transitions of Polystyrene- *block* -polydimethylsiloxane Block Copolymer Thin Films”, *ACS Applied Materials & Interfaces*, vol. 9, nº 20, p. 17427-17434, mai 2017.

[35] S. Antoine, K. Aissou, M. Mumtaz *et al.*, “Core–Shell Double Gyroid Structure Formed by Linear ABC Terpolymer Thin Films”, *Macromolecular Rapid Communications*, vol. 39, nº 9, p. 1800043, mai 2018.

[36] H.-W. Park, K. Im, B. Chung *et al.*, “Direct Observation of HPL and DG Structure in PS-b-PI Thin Film by Transmission Electron Microscopy”, *Macromolecules*, vol. 40, nº 7, p. 2603-2605, avr. 2007.

[37] M. W. Matsen, “Cylinder ↔ Gyroid Epitaxial Transitions in Complex Polymeric Liquids”, *Physical Review Letters*, vol. 80, nº 20, p. 4470-4473, mai 1998.

[38] N. Ji, P. Tang, F. Qiu and A.-C. Shi, “Kinetic Pathways of Lamellae to Gyroid Transition in Weakly Segregated Diblock Copolymers”, *Macromolecules*, vol. 48, nº 23, p. 8681-8693, déc. 2015.

CHAPTER 3: Design of crosslinkable top-coats for the controlled orientation of block copolymer structures

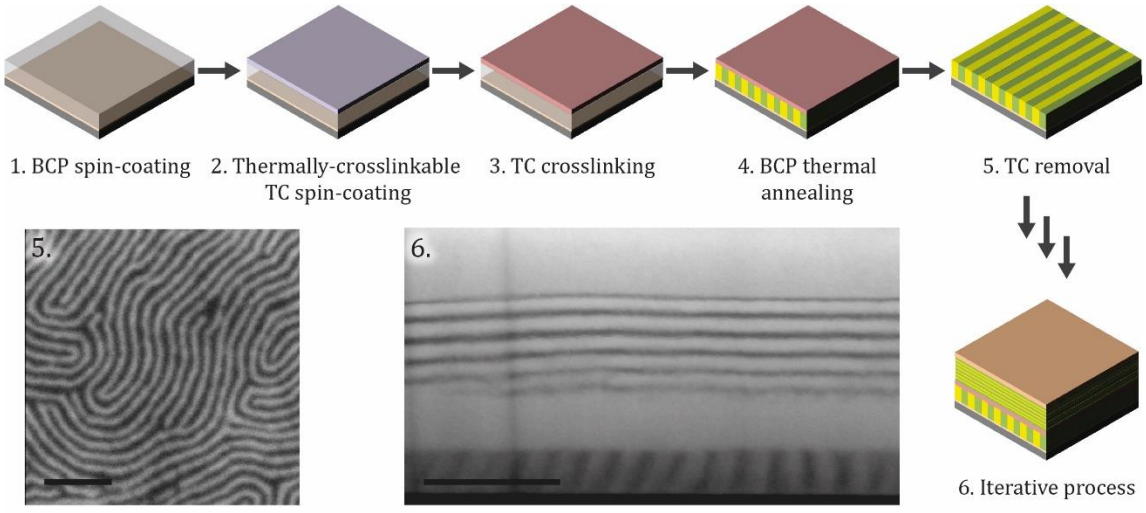

In this chapter, we propose an approach to control the orientation of lamellar-forming PDMSB-*b*-PS BCP as it is the main structure of interest for BCP lithography. The design of a TC material that provides an easy deposition of the material on top of the BCP layer, a tuning of its surface energy and a crosslinking ability is described. Crosslinking the TC using a thermal crosslinking agent is achieved in 3 min. This TC was further used for the self-assembly of three lamellar-forming PDMSB-*b*-PS BCPs leading to smooth films of out-of-plane lamellae with 14.6 nm, 17.2 nm and 22.7 nm periodicities. Finally, taking advantage of the crosslinking ability of our TC material, we use the TC as a new substrate to build multi-layers stacks with a controlled-orientation of each BCP layer.

I. Neutral top-coats: state of the art

In the case of high-χ BCPs, thermodynamics often drives the self-assembled nanostructure toward a parallel orientation as the block with the lower surface energy tends to form a wetting layer at the free interface. However, the perpendicular orientation is preferred for most applications in order to generate a topographical pattern after the selective removal of one of the domains. These patterns could indeed be used for nanolithography applications as well as for the production of hydrophobic surfaces, nanoporous membranes or low refractive index films [1]. To overcome this limitation, one has to neutralize the interfacial energy of both segregated domains with the bottom and top surfaces to induce a perpendicular orientation of the BCP structure. While the neutralization of the bottom interface by grafted polymer layers is well-documented [2]–[12], studies are currently devoted to the development of top-coats (TCs) allowing a mitigation of the surface energy effects at the polymer/air interface. A TC is a material that is generally deposited on the BCP film to control the selective wetting behaviour at the polymer/air during the annealing process in order to produce a perpendicular orientation of the BCP domains. There are several parameters that have to be taken into account to choose a TC. Firstly, the material has to be neutral for the BCP domains which limits the type of accessible material chemistry. Secondly, the deposition method has to be compatible with the underlying BCP layer in order to keep it intact while depositing the TC. For instance, if the TC is deposited by spin-coating, the solvent of the TC shall not dissolve or extensively swell the BCP layer meaning that the solvent has to be orthogonal to the BCP. However, materials that are soluble in those orthogonal solvents have different physical-chemistry properties from the ones of the targeted BCP meaning a different interfacial energy. Moreover, once an appropriate material has been chosen, one has to insure a uniform coating of the TC on the BCP film. The following section will present the different strategies that were developed in order to overcome these issues. As only a few examples were reported in the literature, each approach will be described in details and will be discussed in terms of efficiency, cost and viability at industry level.

1. Use of a top-coat in solvent vapour annealing process

Kim et *al.* used a poly(vinyl acetate)-*r*-poly(vinyl alcohol) (PVA) as a TC to control the orientation of PS-*b*-PDMS thin films [13]. The random PVA copolymers are commercially available at low cost, making it compatible for a development at the industrial level. In addition, they are soluble in polar solvents that are usually orthogonal to the majority of high-χ BCPs. Consequently, the PVA copolymers can be deposited by spin-coating without damaging the underlying BCP film. Finally, thanks to a tuneable hydrolysis degree, it is possible to access a wide range of surface energy allowing to envision the use of this random copolymer architecture for various BCP systems. Kim *et al*. used thus a partially hydrolysed PVA layer to obtain out-of-plane cylinders of PS-*b*-PDMS by acetone vapour annealing. Three TCs with different hydrolysis degree (40%, 80% and 89% denoted PVA40, PVA80 and PVA89, respectively) were studied in order to find the optimum conditions for a perpendicular alignment of the cylinders regardless of the thickness of the film.

A calculation of the interfacial energies using the Wu's method showed that PVA40 has a lower interfacial energy difference with the PS and PDMS domains. This can be explained by a Hildebrand solubility parameter (*H*) that is closer to PS and PDMS as compare to the PVA80 and PVA89 ($H_{PVA40} \approx 19.6$ MPa^{½}, $H_{PS} \approx 17.5$ MPa^{½}, $H_{PDMS} \approx 15.0$ MPa^{½} et $H_{PVA\text{-fully hydrolysed}} \approx 25.8$ MPa^{½}). This interfacial energy is even more reduced in the swollen state, due to a screening effect of the solvent molecules, which thus allows approaching a total neutrality of the TC regarding the BCP domains. Finally, PVA40 has a solubility parameter close to that of acetone ($H_{acetone} \approx 20.3$ MPa^{½}) and a high rate of acetone vapour swelling can thus be achieved providing enough mobility for the BCP chains to organize. Figure 3-1(a) and (b) show the SEM images of the out-of-plane cylinders obtained using the TC *via* the solvent vapour annealing process. However, it is important to note that the perpendicular orientation of the cylinders strongly depends on the annealing method. Indeed, as shown the Figure 3-1(c), in-plane cylinders are obtained when using a thermal annealing process regardless the use of the PVA TC. When a solvent vapour annealing process is performed in the absence of TC, out-of-plane PDMS cylinders are produced through the thickness

of the film but a wetting layer of in-plane PDMS cylinders is visible at the top interface (see Figure 3-1(d)). In addition, the thickness of the TC has to be optimized to control the solvent vapour concentration gradient in the film, which is the crucial parameter in the self-assembly process. This technique is therefore limited to one type of BCP system and studies remain to be performed in order to establish the viability of the approach at industrial scale, since the use of solvent vapour annealing could be detrimental for the industrial integration.

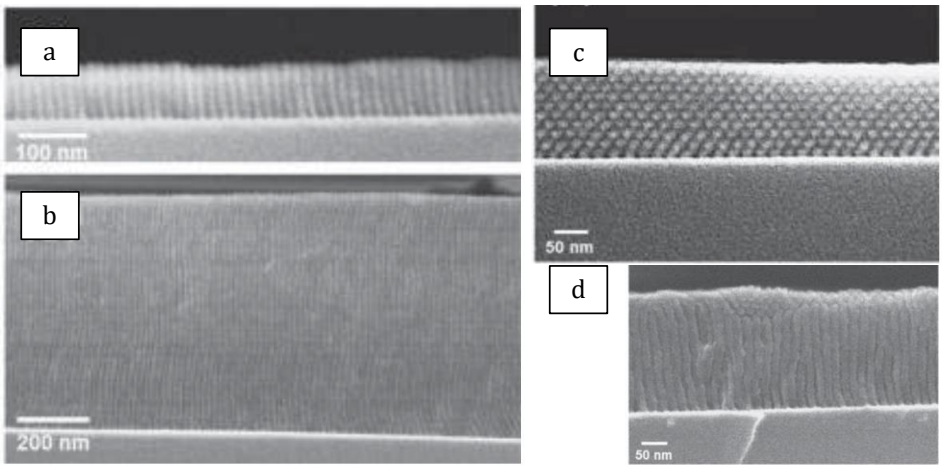

Figure 3-1: SEM images of nanostructured PS-*b*-PDMS films for various self-assembly processes. Cross-sectional images of (a) 70 nm and (b) 700 nm thick BCP films after solvent annealing and removal of the PVA40 TC. (c) Cross-sectional SEM image of a thermally-annealed 250 nm thick BCP film at 170°C for 24 h after the removal of the PVA40 TC. (d) Cross-sectional SEM image of a solvent annealed PS-*b*-PDMS film without the PVA40 TC exhibiting the in-plane cylinders wetting layer [13].

It is noteworthly that the same group obtained in 2017 a gyroid structure from a PS-*b*-PDMS/PDMS-OH blend using a PVA40/poly(vinyl acetate) blend as TC *via* solvent vapour annealing [14]. The gyroid structure is generally difficult to stabilize for thicknesses down to several hundred of nanometers due to the strong interfacial interactions that lead to order-order tansitions or metastable morphologies. By optimizing the PVA40/poly(vinyl acetate) ratio, they managed to tune the surface energy at the top interface of the PS-*b*-PDMS thin film allowing to stabilize a 125 nm-thick gyroid film with a unit cell lattice of 43.7 nm.

2. Use of a top-coat in thermal annealing process

a) Polarity switching top-coat

Bates et *al.* developed a material with switchable polarity induced by thermal annealing. The polarity-switching mechanism is based on anhydride moieties that undergo a ring-closure reaction upon heating (Figure 3-2) [15]. Indeed, a ring-opening reaction occurs while putting the polymer in an aqueous solution of ammonium hydroxide at RT. The resulting polyelectrolyte is soluble in polar solvent allowing its deposition by spin-coating on the BCP film without detrimental swelling of the BCP structure. The initial chemical structure of the TC material is then recovered during a thermal annealing at high temperature. The TC is composed of two other components (i) to increase the glass transition of the polymer reducing then dewetting phenomenon; and (ii) to adjust the surface energy of the polymer for a fine tuning of its neutrality. Thanks to the anhydride moieties, it is thus possible to obtain a polyelectrolyte highly soluble in polar solvent while incorporating hydrophobic monomers. Further use of this TC in order to orientate out-of-plane lamellae was demonstrated on poly(styrene)-*b*-poly(trimethyl silyl styrene)-*b*-poly(styrene) (PS-*b*-PTMSS-*b*-PS) and poly(trimethyl silyl styrene)-*b*-poly(D,L-lactide) (PTMSS-*b*-PLA) systems with a period of 29 nm and 19 nm, respectively (Figure 3-3) [16].

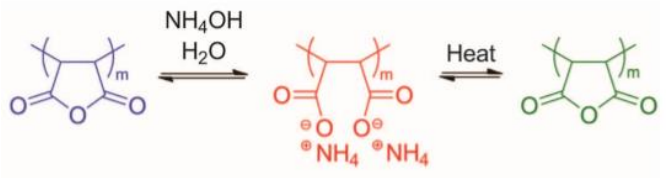

Figure 3-2: Ring-opening mechanism of the maleic anhydride unit allowing the polarity switch [15].

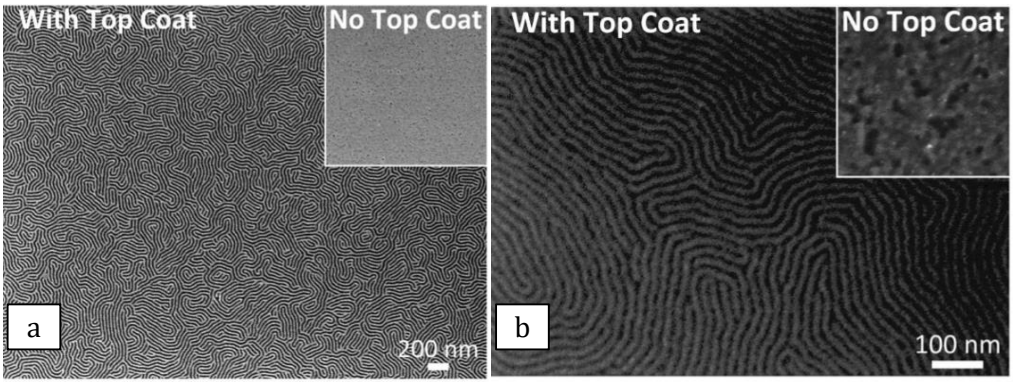

Figure 3-3: SEM images of lamellar-forming (a) PTMSS-*b*-PLA and (b) PS-*b*-PTMSS-*b*-PS BCPs [16].

However, several improvements are still needed to translate this proof of concept into a robust method for the lithographic industry. Indeed, the design of these specific TCs is tedious. The emphasis of the balance between neutrality and solubility is not always possible to achieve depending on the BCP systems. The optimization of the chemistry between the various monomers (solubility switch *vs* neutrality) needs to be repeated for each new BCP system and probably even for each variation in composition, rendering this approach difficult to generalize [17].

Willson's team thus developed, in 2013, new TC materials to overcome these drawbacks. The maleic anhydride unit is still present but associated with two styrene units to form an alternating copolymer whose ratio of styrene units is supposed to extend the accessible range of surface energies although no surface energy measurements supported this hypothesis (Figure 3-4) [17], [18].

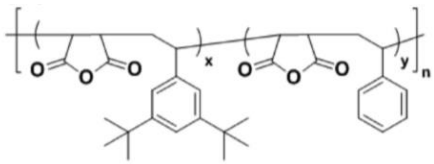

Figure 3-4: Structure of the TC used in order to obtain out-of-plane lamellae of PS-*b*-PTMSS and PVBD-*b*-PDSS [17].

Moreover, to avoid the formation of amide and imide after the annealing step, the ammonium hydroxide solution was replaced by a solution of trimethylamine, a tertiary amine which cannot therefore form an amide. Finally, they used this new TC to produce perpendicular lamellae of poly(styrene)-*b*-poly(trimethylsilyl styrene) (PS-*b*-PTMSS) with a periodicity of 18 nm and 22 nm. Recently, out-of-plane lamellae of poly(5-vinyl-1,3-benzodioxole)-*b*-poly(pentamethyldisilyl styrene) (PVBD-*b*-PDSS) with 10 nm periodicity were obtained and transferred into a chromium/SOC[9] substrate following the same strategy (Figure 3-5) [17].

[9] *"Spin-on carbon"*

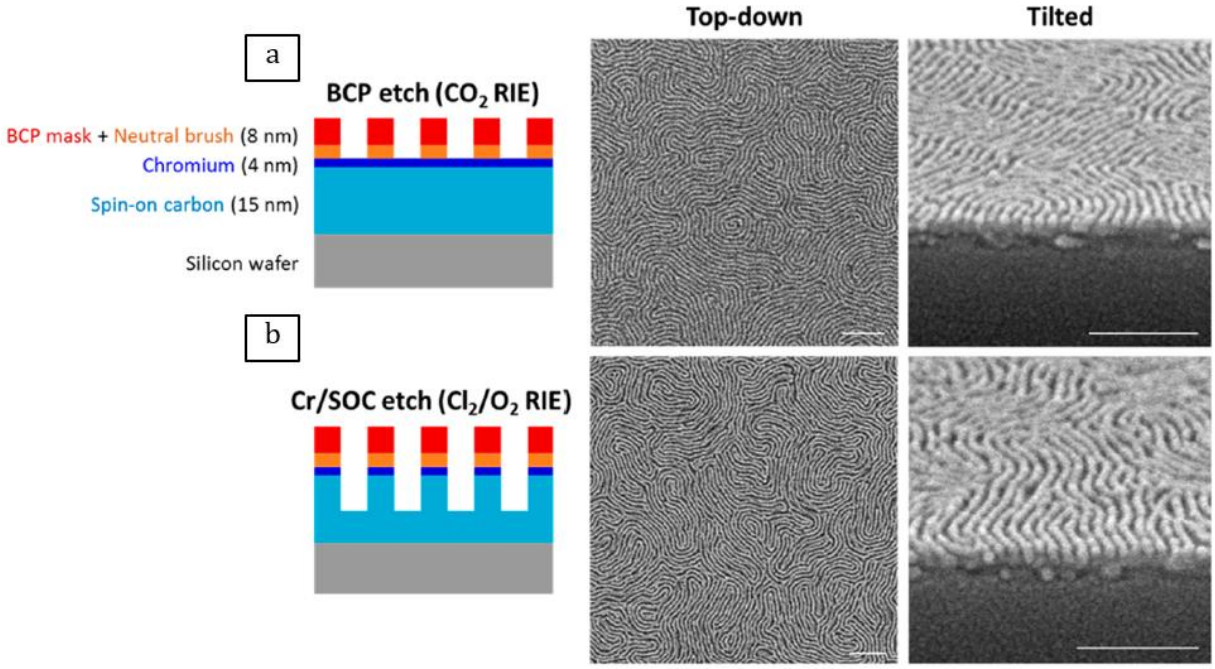

Figure 3-5: **SEM images of the lamellae of PVBD-*b*-PDSS obtained (a) after the etching treatment and (b) after their transfer into chrome/SOC substrate [17].**

These results are interesting since it is the first demonstration of the use of neutral TCs in a thermal annealing process for high-χ BCPs. These TC layers are thus of high interest for the next generation of sub-10nm masks. It would have been interesting to know the range of surface energies that is possible to achieve with the neutral layer, for instance, by varying the composition of the TC, in order to evaluate the potential of the material for other high-χ BCP systems.

b) Integration of additives into the BCP formulation

Hustad *et al.* proposed another strategy to neutralize the air/BCP interface for the perpendicular orientation of PS-*b*-P2VP lamellae based on the migration of low molecular weight (co)polymers at the free interface [19]. For this purpose, an additive was added to formulations of PS-*b*-P2VP in a mixture of PGMEA and gamma-butyrolactone. This additive was expected to migrate at the film surface during the spin-coating step and remain anchored during the thermal annealing allowing the neutralization of the interface (Figure 3-6) [6],[7].

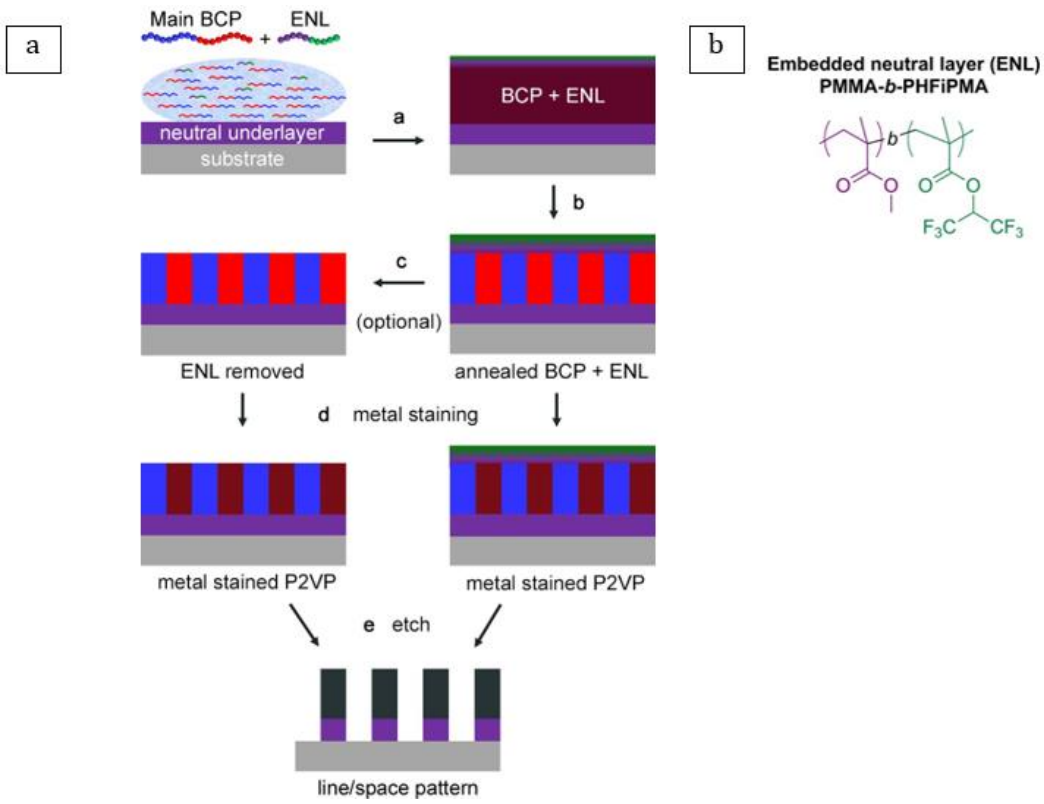

Figure 3-6: Principle of the neutralization method proposed to neutralize the upper interface of the PS-*b*-P2VP (a) using embedded neutral layer. (b) is the structure of the poly(methyl methacrylate)-*b*-poly(hexafluoro isopropyl methacrylate) BCP used as embedded neutral layer [19].

A poly(methyl methacrylate)-*b*-poly(hexafluoro isopropyl methacrylate) BCP was chosen as additive. Indeed, the fluorine-rich block has a low surface energy that will promote the migration of the additive at the top interface during the self-assembly process [21]. On the other hand, the methacrylate block confers the neutrality of the polymer with respect to PS-*b*-P2VP [22]. In addition, the poly(methyl methacrylate)-*b*-poly(hexafluoro isopropyl methacrylate) system was proven to be easily removed during the following process steps.

Using Gas Cluster Ion Beams - X-ray photoelectron spectroscopy (GCIB-XPS), a significant fluorine concentration was revealed on the first nanometers of the film which is consistent with the presence of a TC when the additives concentration is sufficiently high (20% weight compared to the BCP). Out-of-plane lamellae with a period of 28 nm were thus obtained with this process as shown in Figure 3-7(b) [19].

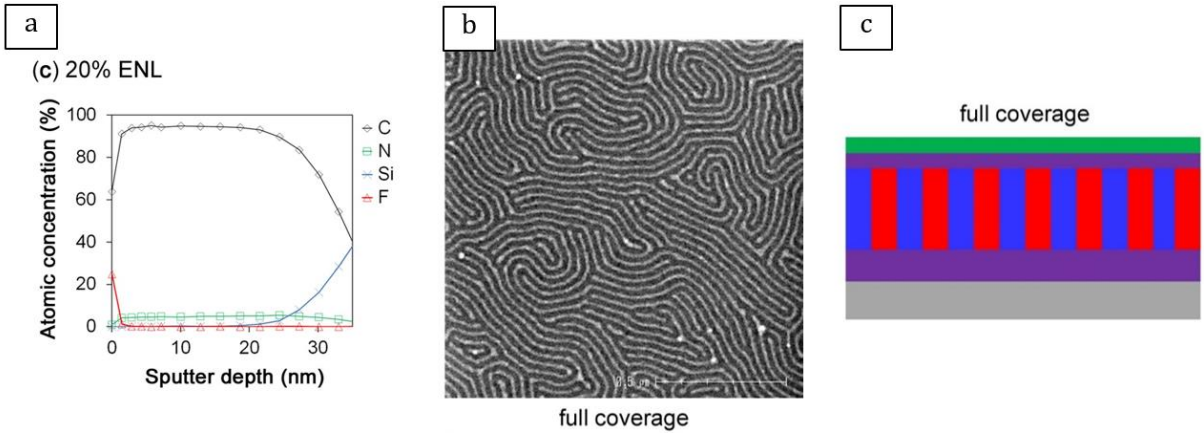

Figure 3-7: (a) Characterization of the air/PS-*b*-P2VP interface by GCIB-XPS highlighting the evidence of the fluorinated additive. (b) SEM image and (b) the associated integration scheme of out-of-plane PS-*b*-P2VP lamellae obtained thanks to the full coverage of the surface by the fluorinated additive [19].

This approach allows simplifying the self-assembly process and the orientation of the PS-*b*-P2VP because it does not require the additional step of a TC deposition. Consequently, it avoids the associated issues such as the compatibility between the solvents of the BCP and the TC. In addition, it is possible to anneal at a higher temperature (here, 250°C for 5 min) which decreases the self-assembly defects while this temperature is generally limited to the TC glass transition to prevent diffusion of the TC through the BCP layer [16]. However, a large load of additives is necessary to obtain the total covering of the surface and to minimize the mixing with the BCP leading to detrimental dewetting phenomenon.

Following a similar methodology, Ankit *et al.* added a hexafluoroalcohol polymer (PHFA) to the formulation of their high-χ poly(styrene)-*b*-poly(methyl 5-methyl-2-oxo-1,3-dioxane-5-carboxylate) (PS-*b*-PTMC-Me) BCP [23]. Similarly, the addition of fluorinated groups allows the orientation of the BCP at the air interface as shown in Figure 3-8(a)) [21]. Due to the presence of fluorinated tertiary alcohols, this additive only segregates on the top of the PTMC-Me domains thanks to hydrogen bonding with the polar carbonyl groups (Figure 3-8(b)) [10][11]. This approach reduces the high surface energy of the carboxylate block to compensate the BCP/air interfacial energy resulting in a perpendicular orientation of the lamellae (Figure 3-8(c)) [26]. In addition, it requires a much lower concentration of additive (2% weight) compared to the previous approach for which a total surface coverage was required [19].

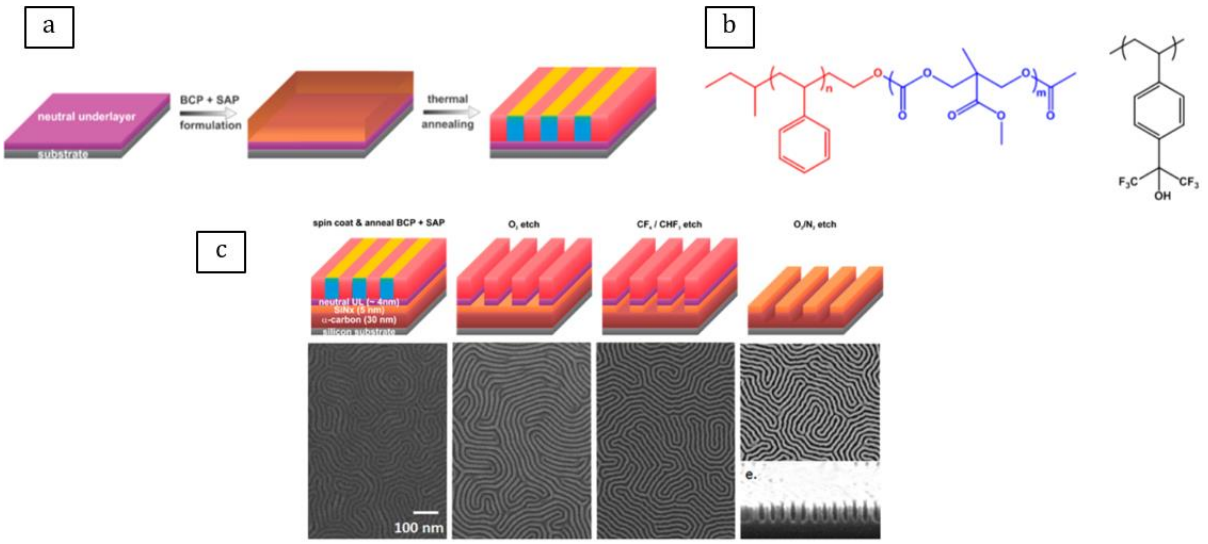

Figure 3-8: (a) General principle of the neutralization method used to control the air/BCP interface. (b) Structures of PS-*b*-PTMC-Me (right) and PHFA (left). (c) SEM images of the processing steps leading to the transfer of the lamellae into a SiN_x substrate [23].

An indirect demonstration was performed to highlight the preferential interaction of the additive with the block PTMC-Me. For this purpose, the BCP was deposited on top of a PHFA underlayer. As shown in Figure 3-9(a) and (b), islands with 21 nm height were observed which is characteristic of an asymmetric BCP wetting for the lamellar morphology. In addition, a phase separation was observed after the annealing of a homoPS/PHFA film while a homogeneous film was observed for a homoPTMC-Me/PHFA mixture (Figure 3-9(c) and (d)).

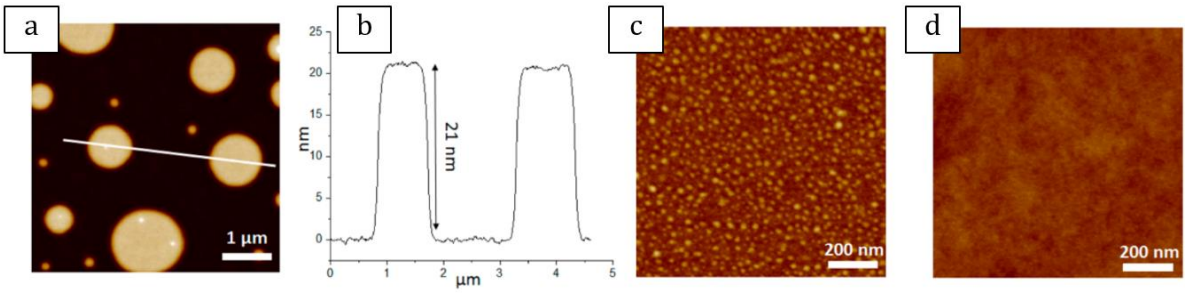

Figure 3-9: Highlight of the preferential interaction between the PHFA and the PTMC-Me block. (a) and (b): Obtention of $1L_0$ island after the BCP deposition PHFA underlayer (c) Heterogenous film obtained from a homoPS/PHFA blend (d) Homogeneous film film obtained from a homoPTMC-Me/PHFA blend [23].

This methodology led to the transfer of a 19 nm periodic pattern into a hydrogenated amorphous silicon nitride substrate (SiN_x) (Figure 3-9(c)), underlining the high potential of such additives for the controlled orientation of BCP domains.

c) Crosslinked top-coats

More recently, Nealey and co-workers reported the self-assembly of the P2VP-*b*-PS-*b*-P2VP into out-of-plane lamellae through the use of a TC [27]. The originality of this approach lies on the deposition process of the neutral layer as it is deposited in vapour phase by iCVD (Figure 3-10) [28]. For this purpose, monomer and initiator molecules are sent through hot tubes (200-300°C) in a vacuum chamber containing the BCP film. There is thus a decomposition of the initiator into free radicals with the temperature while the monomer, more stable, remains intact. By keeping the BCP film at a lower temperature (20-50°C), reactive molecules adsorbed on the surface of the film on which the radical polymerization of the monomers occurs [29], [30].

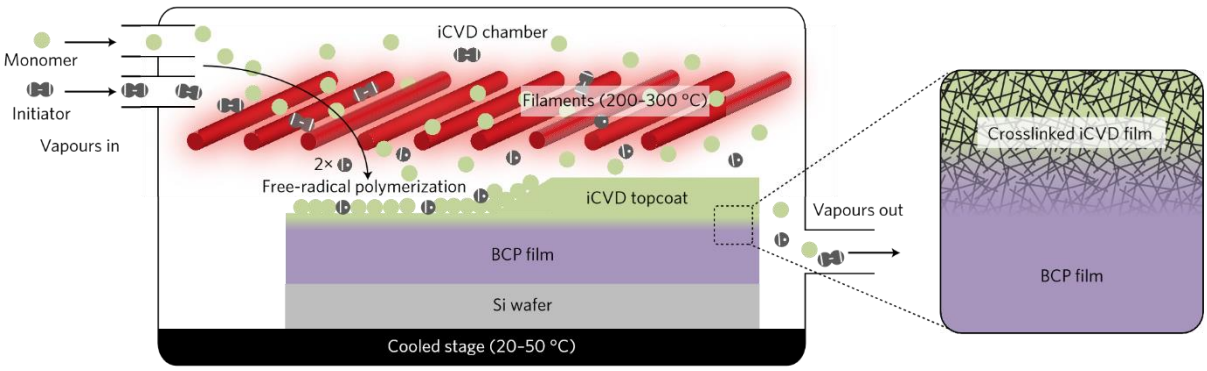

Figure 3-10: Scheme of the initiated chemical vapour deposition (iCVD) process used to produce a crosslinked TC on a BCP film. To generate this layer, vinyl monomer and initiator are sent in vapour phase into the iCVD chamber through heated filaments. The initiator decomposes into free radicals with the temperature. As the BCP film is maintained at a lower temperature, radical and monomer molecules diffuse at the film top surface where the free-radical polymerization occurs [27].

In this study, divinylbenzene (DVB) and di-*tert*-butyl peroxide were used as monomer and initiator, respectively. The temperature causes the cleavage of the O-O bond of the di-*tert*-butyl peroxide which is then separated into β-*tert*-butoxy radicals to form methyl radicals [31]. Nealey and co-workers hypothesized that these small and highly reactive molecules could be solvated and diffuse at the interface between the BCP and the PDVB layer being formed [30]. These radicals could activate the aromatic carbons of the P2VP and PS cycles present at the surface by extracting

protons and the resulting active sites would then be able to react with DVB [32], [33]. The existence of this layer grafted to the P2VP-*b*-PS-*b*-P2VP was confirmed by contact angle measurements, angle resolved X-Ray photoelectron spectroscopy (ARXPS) and attenuated total reflection-Fourier-transform infrared spectroscopy (ATR-FTIR), that showed the presence of pyridine and polysubstituted pyridine moieties. This grafted polymer interface is supposed to be responsible for neutralizing the P2VP-*b*-PS-*b*-P2VP/air interfacial energy and thus for the perpendicular orientation of the lamellae.

An inorganic mask of alumina was then obtained by selective infiltration of aluminium precursors into the P2VP domains, allowing the transfer of a 18.5 nm period pattern into a silicon substrate as shown in the Figure 3-11.

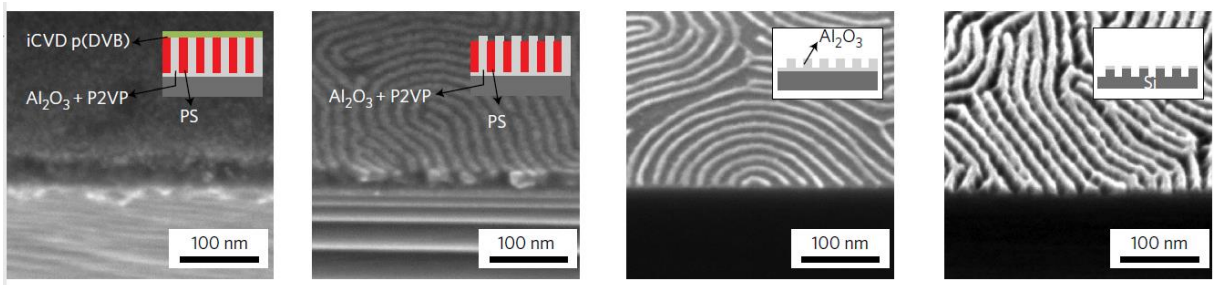

Figure 3-11: Process used to transfer the out-of-plane lamellae formed by a P2VP-*b*-PS-*b*-P2VP into a silicon substrate [27].

Finally, a chemo-epitaxy process was used to direct the self-assembly and a photosensitive resin was deposited on the TC to define patterns on a larger scale by electron beam lithography as shown in Figure 3-12.

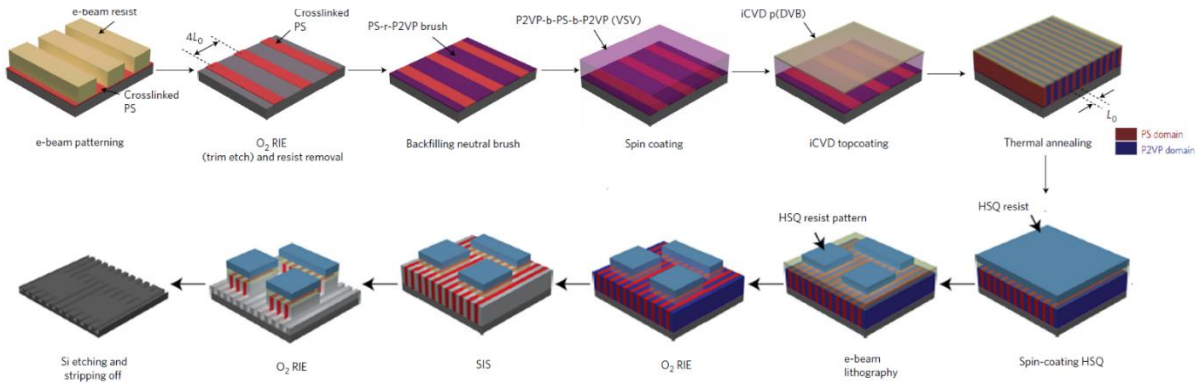

Figure 3-12: Scheme of the directed self-assembly of P2VP-*b*-PS-*b*-P2VP and use of e-beam lithography on the crosslinked TC to define a larger scale pattern [27].

However, this process is associated to some bottlenecks as regards to its implementation in microelectronics. First of all, the iCVD chamber is a very specific and expensive equipment, not readily available on common lithography tracks. Moreover, this approach is not versatile as it is limited to BCP systems bearing aromatic rings. Finally, dewetting issues during the TC deposition and the thermal annealing have also to be taken into account.

Oh et *al.* proposed a more general method to create out-of-plane orientations using a filtered argon plasma treatment of the BCP films (Figure 3-13) [34]. This specific plasma allows physical collisions between atoms to occur on the top-surface of the BCP film without damaging it. Indeed, the filter is supposed to block the ion bombardment and the generated VUV/UV, so that only the neutral argon species can interact with the first few nanometers of the BCP film to form a crosslinked layer. The integrity of the BCP film after the filtered plasma was confirmed by ARXPS. It is this crosslinking process freezing the BCP in its disordered (as-cast) state that is supposed to enable the neutralization at the free surface even if no surface energy measurements were reported to support this hypothesis.

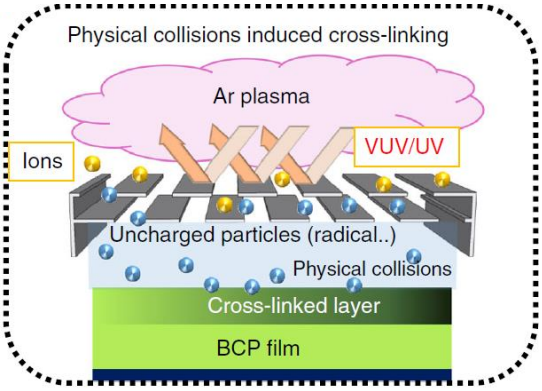

Figure 3-13: Scheme of the filtered plasma treatment to form the crosslinked layer for perpendicular orientation of BCP microdomains [34].

To show the versatility of their approach, the filtered Argon plasma method was applied to PS-*b*-PMMA, PS-*b*-PDMS, PS-*b*-P2VP, P2VP-*b*-PS-*b*-P2VP and PMMA-*b*-PDMS systems for which an out-of-plane orientation of the BCP structure obtained by thermal annealing was demonstrated after a subsequent non-selective plasma etching of the crosslinked layer (Figure 3-14).

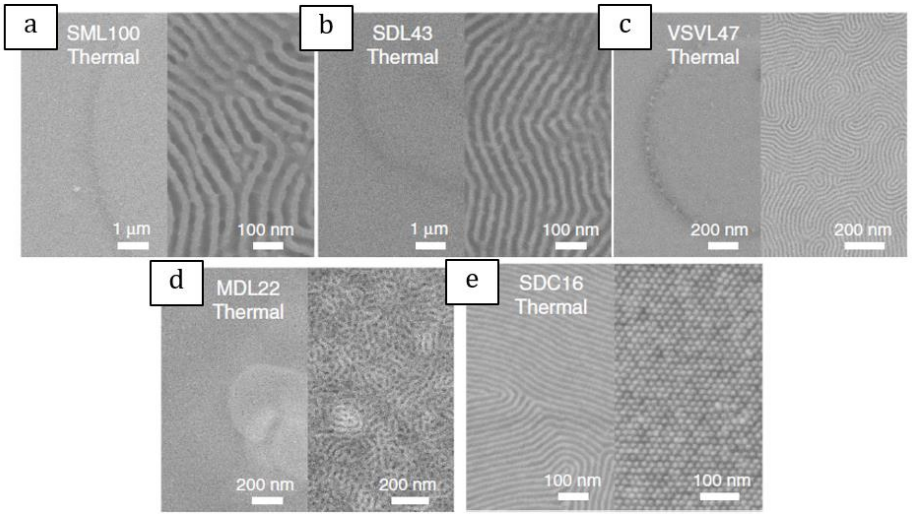

Figure 3-14: SEM images of various thermally-annealed BCP systems with (right) and without (left) the filtered plasma treatment. SML100, SDL43, VSVL47, MDL22, SDC16 refers to (a) lamellar-forming PS-*b*-PMMA, (b) lamellar-forming PS-*b*-PDMS, (c) lamellar-forming P2VP-*b*-PS-*b*-P2VP, (d) cylinder-forming PMMA-*b*-PDMS and (e) cylinder-forming PS-*b*-PDMS [34].

Finally, the crosslinked layer was used as a new susbtrate to build multi-layer stack of lamellar- and cylinder-forming PS-*b*-PDMS. For this purpose, plasma treatment was performed at each interface of the multilayer to obtain a perpendicular orientation of the BCP. To control the orientation of the different layers, an additional thin layer of P2VP was introduced between the crosslinked layer and the subsequent BCP layer in order to promote an in-plane orientation (Figure 3-15).

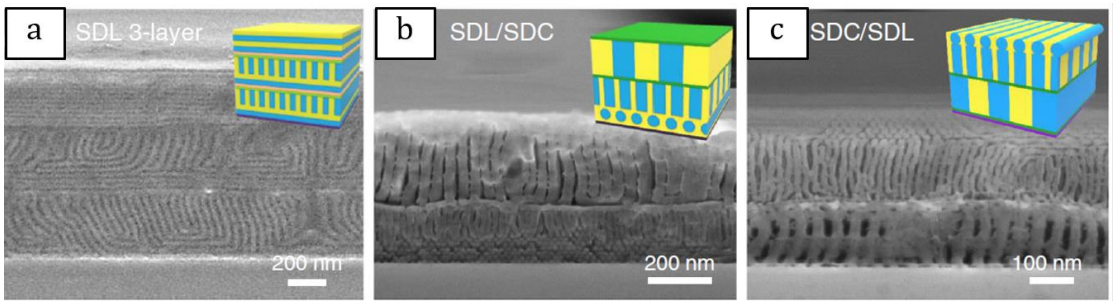

Figure 3-15: Filtered plasma method used to build 3D multilayer structures. (a) is the cross-sectional SEM image of a SDL43 stack using the following process: SDL43/P2VP/plasma/SDL43/P2VP/plasma/SDL43/ substrate, (b) is the cross-sectional SEM image of SDL43 and SDC16 stack using the following process: plasma/SDL43/plasma/thin SDL43/plasma/SDC/substrate and (c) is the cross-sectional SEM image of a SDL43 stack using the following process: SDC16/plasma/thin SDC16/plasma/SDL43/plasma/thin SDL43/substrate [34].

This approach is very powerful and can be applied to numerous BCP systems as the neutral layer is obtained through the disordered (and thus compositionally similar) BCP state.

These studies led us to establish the following list of criteria for the development of a neutral TC in order to control the self-assembly of high-χ lamellar-forming BCPs in thin film using a thermal annealing process:

- The TC has to be neutral for the targeted BCP, i.e. the mismatch of interfacial energy between the BCP domains and the interfaces should be minimized.
- The neutrality of the TC should be easily tunable in order to apply the methodology to various BCP systems with different molecular weights and compositions, i.e. macromolecular design through the variation of TC composition should allow to access a large range of surface energy.
- The deposition of the TC should keep the underlying BCP film intact.
- The deposition process has to be simple and at low cost to be viable at industrial level.
- The TC has to allow high temperature annealing of the BCP layer to promote the self-assembly while avoiding dewetting of the BCP layer during the thermal process, i.e. the kinetics of crosslinking has to be faster than the dewetting kinetics.
- The TC should be easily removed by either plasma or wet chemistries.

II. Development of a crosslinkable top-coat

Considering our industrial requirements and the previous studies, we choose to develop a crosslinkable neutral TC. The main advantage of using a crosslinked layer as neutral TC is to mechanically maintain the BCP film during the thermal annealing step to avoid dewetting issues (Figure 3-16). Indeed, the development of high-χ BCP to reach sub-20 nm features also implies the use of low molecular weight polymers which leads to the dewetting of the polymer film during the thermal annealing process especially since high temperatures are required to decrease the defect density in the self-assembled structures. Moreover, Si-containing BCPs such as the PDMSB-*b*-PS system tend to dewet due to a low surface energy of the silicon containing block.

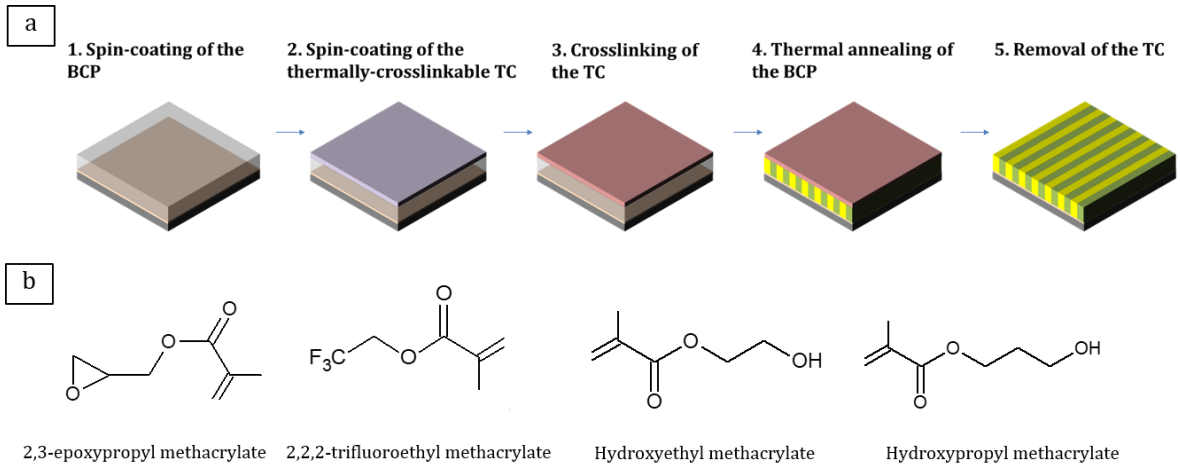

Figure 3-16: Design of the neutral crosslinkable TC. (a) Scheme of the process in order to achieve out-of-plane lamellae using the neutral crosslinkable TC. (b) Co-monomers used to synthetize the TC.

As several functionalities are needed for the design of an efficient TC, a random copolymer consisting of hydroxy-containing methacrylate (hydroxyethyl methacrylate or hydroxypropyl methacrylate), 2,2,2-trifluoroethyl methacrylate and 2,3-epoxypropyl methacrylate was developed as shown in Figure 3-16(b). A methacrylate chemistry was chosen because the polymerization of such compounds is well-established using (controlled) radical polymerization and each monomer is commercially available. Besides, thanks to the methacrylate backbone, the TC could also be selectively removed either by UV radiation or by dry etching after the BCP self-assembly process. The hydroxy-containing methacrylate unit will confer the solubility in polar solvents in order to deposit the TC without damaging the underlying BCP film. The 2,2,2-

trifluoroethyl methacrylate will allow the tuning of the surface energy in order to provide a neutrality window as regards to the PDMSB-*b*-PS domains. Finally, the 2,3-epoxypropyl methacrylate unit should allow the crosslinking of the TC, either by UV radiation or by thermal treatment through the ring-opening of the epoxy groups.

Moreover, a crosslinked neutral layer can also act as a new "substrate" to deposit a subsequent BCP layer [34]. By repeating the process, it would be thus possible to build multi-layer stacks with BCPs of different morphologies, periodicities or thicknesses independent of the BCP layers thanks to the intermediate TC layers. The orientation of the different BCP layers could be achieved by controlling the surface energy of each TC (by varying its chemical composition) in a simple manner.

III. Characterization of the top-coats

A series of random copolymers was synthetized *via* controlled free-radical polymerization in the Groupement de Recherche de Lacq (Arkema) with a molecular weight ranging from 2000 to 3000 g.mol^{-1}. The Table 3-1 summarizes the macromolecular characteristics of the polymers. In the following parts, the different polymers will be rated as $G_wM_xHe_yHp_z$ with *w*, *x*, *y* and *z* the respective molar fraction of 2,3-epoxypropyl methacrylate (so-called GMA for glycidyl methacrylate), 2,2,2-trifluoroethyl methacrylate (so-called Matrife), hydroxyethyl methacrylate (HEMA) and hydroxypropyl methacrylate (HPMA) in the polymer. Four polymers ($G_{25}M_{75}$, $G_{27}M_{47}He_{26}$, $G_{25}M_{37.5}He_{37.5}$, $G_{20}M_{24}He_{56}$) were synthetized with various Matrife/HEMA ratio while keeping the GMA content constant to study the effect of (i) the Matrife/HEMA ratio on the surface energy of the polymer; (ii) the HEMA content on the solubility of the polymer in polar solvents. The $G_{65}Hp_{35}$ was synthetized with a higher content of GMA to study its effect on the crosslinking reaction.

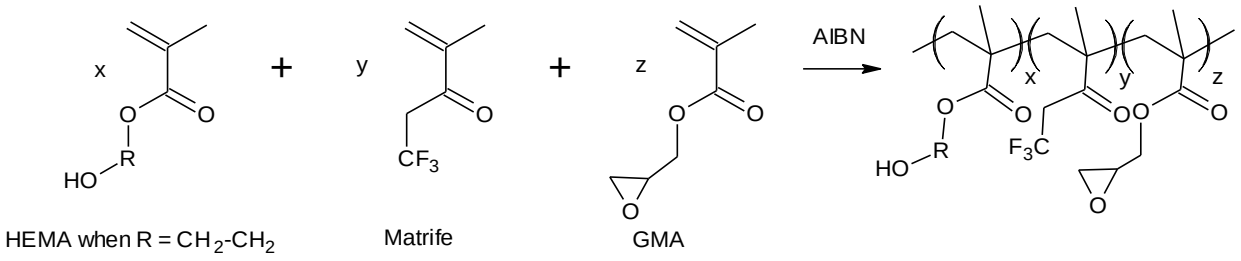

Figure 3-17: Synthetic scheme for the free-radical polymerization of random methacrylate-based copolymers. 1,1'-azo-bis-isobutyronitrile (AIBN) was used as initiator.

Table 3-1: Relevant macromolecular characteristics of the polymers.

Polymer	Tg (°C) [a]	f_{GMA} [b]	$f_{Matrife}$ [b]	f_{HEMA} [b]	f_{HPMA} [b]
$G_{25}M_{75}$	26	25	75	0	0
$G_{27}M_{47}He_{26}$	35	27	47	26	0
$G_{25}M_{37.5}He_{37.5}$	28.5	25	37.5	37.5	0
$G_{20}M_{24}He_{56}$	32.5	20	24	56	0
$G_{65}Hp_{35}$	28.5	65	0	0	35

a: Determined by differential scanning calorimetry from the second heating curve. Heating rate: 40°C.min^{-1}
b: Molar fraction (%) determined by ^{1}H NMR at the laboratory of the Groupement de Recherche de Lacq (Arkema)

Films of $G_{25}M_{75}$, $G_{27}M_{47}He_{26}$, $G_{25}M_{37.5}He_{37.5}$, $G_{20}M_{24}He_{56}$ and $G_{65}Hp_{35}$ were prepared by spin-coating 2% wt. solution of the polymers in 1-methoxy-2-propanol on silicon substrate. As shown in Figure 3-18(a), it is possible to finely tune the surface energy of the polymer from 30 $mN.m^{-1}$ to 40 $mN.m^{-1}$ by playing with the Matrife/HEMA ratio. Indeed, for a high molar fraction of Matrife, the surface energy of the polymer is lowered by the presence of the trifluoromethyl group. With the decrease of the Matrife molar fraction as well as the increase of the HEMA content, there is an increase of the surface energy of the polymer reflected by an increase of the polar component due to the presence of the HEMA hydroxy groups as shown in the Figure 3-18(b).

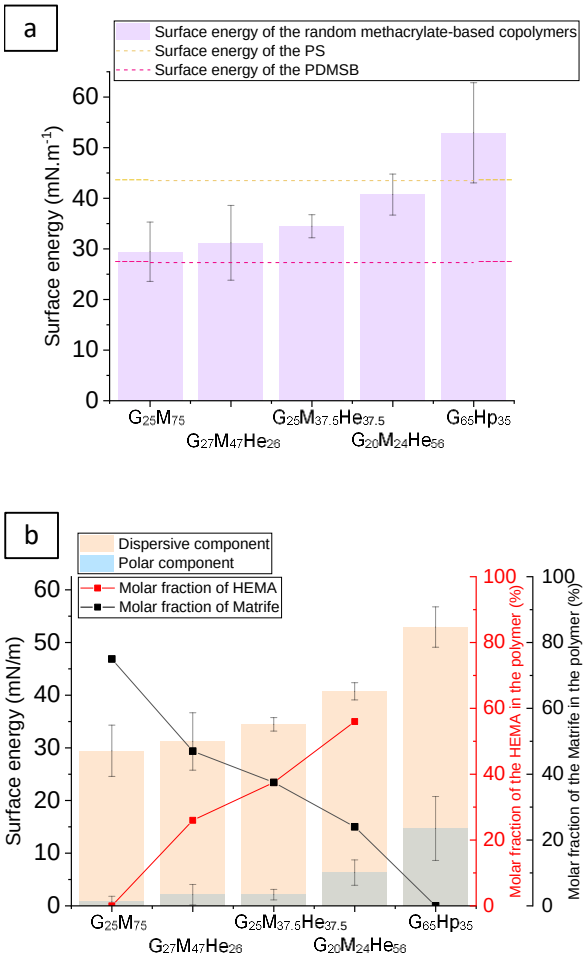

Figure 3-18: (a) Surface energy measurements of the $G_{25}M_{75}$, $G_{27}M_{47}He_{26}$, $G_{25}M_{37.5}He_{37.5}$, $G_{20}M_{24}He_{56}$ and $G_{65}Hp_{35}$ with the respect to PS and (b) PDMSB surface energies and correlation of the surface energy values with the content of Matrife and HEMA in the polymer. Surface energies were determined using the three typical liquids (water, diiodomethane and ethylene glycol) and the OWRK model.

IV. Crosslinking characterization

The crosslinking reaction of the TCs developed in this study is based on the catalysed ring-opening of the epoxy group, similarly to the one involved within CARs (see Introduction section). Indeed, the carbons of an epoxide group are considered as reactive electrophiles mainly due to the strained ring that can be opened upon a nucleophilic attack. The catalyst of this reaction is an acid that can be thermally-activated. In this work, the ammonium trifluoromethanesulfonate (ATMS) was chosen as thermally-activated acid to initiate the crosslinking reaction of the TC (see the structure in Figure 3-19(a)). Upon heating, the ATMS undergoes a thermal decomposition releasing a proton that will induce the opening of the epoxy group (Figure 3-19(b)).

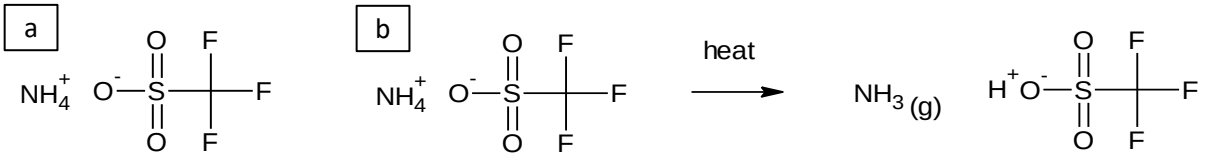

Figure 3-19: Structure of the ammonium trifluoromethanesulfonate (ATMS) (a) and its decomposition upon heating (b).

The crosslinking reaction of the TCs was followed by DSC. For this purpose, solutions of 20% wt. in ethanol of $G_{25}M_{75}$, $G_{27}M_{47}He_{26}$, $G_{25}M_{37.5}He_{37.5}$, $G_{20}M_{24}He_{56}$, $G_{65}Hp_{35}$ and ATMS were prepared. 60 µL of TC/ATMS blends (9:1) were drop-casted into DSC pans and dried in open air until the complete evaporation of the solvent. The polymer/ATMS blends were first annealed for 3 min above the T_g of the TCs at 90°C and quenched at -70°C. A temperature ramp was then performed until 240°C to follow the crosslinking exotherm. Finally, a second quenching followed by a heating ramp was performed in order to verify that the polymer was fully crosslinked. Figure 3-20(a) shows the resulting DSC traces. The crosslinking exotherm is clearly visible for the five TCs with the presence of a broad peak between 182 and 203°C. As expected, the crosslinking enthalpy of the $G_{65}Hp_{35}$ is significantly higher than the other polymers due to the higher content in GMA (Figure 3-20(a) and (d)). The second run did not show any extra exothermic peak confirming that the TCs were fully crosslinked during the first heating treatment (Figure 3-20(b)). Furthermore, blank tests were also performed with $G_{25}M_{75}$, $G_{27}M_{47}He_{26}$, $G_{25}M_{37.5}He_{37.5}$, $G_{20}M_{24}He_{56}$ and $G_{65}Hp_{35}$

without ATMS. As shown in the Figure 3-20(c), no crosslinking reaction was observed in the absence of ATMS.

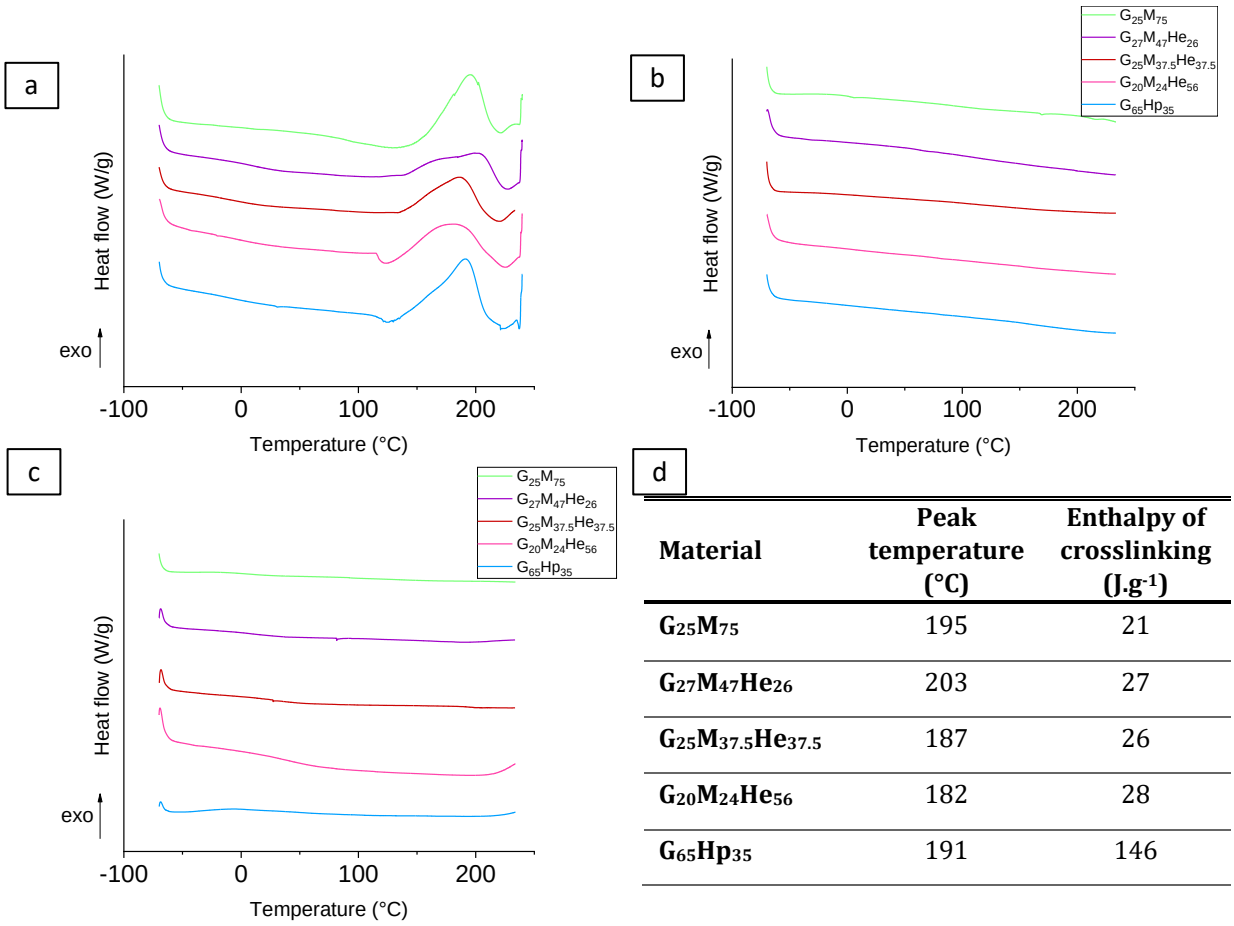

Material	Peak temperature (°C)	Enthalpy of crosslinking ($J.g^{-1}$)
$G_{25}M_{75}$	195	21
$G_{27}M_{47}He_{26}$	203	27
$G_{25}M_{37.5}He_{37.5}$	187	26
$G_{20}M_{24}He_{56}$	182	28
$G_{65}Hp_{35}$	191	146

Figure 3-20: DSC traces of crosslinkable $G_{25}M_{75}$, $G_{27}M_{47}He_{26}$, $G_{25}M_{37.5}He_{37.5}$ and $G_{20}M_{24}He_{56}$ during the heating process. (a) and (b) are the DSC traces of the polymers in the presence of the ATMS. (a) the exothermic peak of the crosslinking reaction is visible when the polymer is in the presence of ATMS (b) the second run confirmed that the polymers were fully crosslinked as there is no extra exothermic peak. (c) are the DSC traces of the polymers without ATMS. (d) Summary of the thermal characteristics. The enthalpy of crosslinking was calculated using the weight fraction of the GMA units. Heating rate: 20°C.min^{-1}.

To follow the crosslinking reaction in a thin film configuration, 2% wt. solutions of $G_{25}M_{75}$, $G_{27}M_{47}He_{26}$, $G_{25}M_{37.5}He_{37.5}$, $G_{20}M_{24}He_{56}$ and $G_{65}Hp_{35}$ were prepared in 1-methoxy-2-propanol. 2% wt. solution of ATMS was prepared in ethanol and added to the polymer solution with a volume ratio of 9:1. Films were then obtained by spin-coating at 2000 rpm the polymer/ATMS solution on silicon substrate in order to reach a film thickness of 60 nm. Finally, the films were heated at 90°C to initiate the crosslinking of the TCs. Figure 3-21 shows the insoluble fraction of the five polymers as a function of the heating time. The insoluble fraction was determined by the ratio of the film thickness before and after dipping the crosslinked film in ethanol (for $G_{65}Hp_{35}$, $G_{25,5}M_{75}$,

$G_{27}M_{47}He_{26}$, $G_{25}M_{37.5}He_{37.5}$, $G_{20}M_{24}He_{56}$) or methanol (for $G_{25}M_{75}$). As shown the Figure 3-21, the crosslinking reaction of the $G_{25}M_{75}$, $G_{27}M_{47}He_{26}$, $G_{25}M_{37.5}He_{37.5}$ and $G_{20}M_{24}He_{56}$ is rapid and the polymer films are fully crosslinked after only 3 minutes at 90°C. One can note that the crosslinking reaction of the $G_{25}M_{75}$ is slower than the crosslinking reaction of the other polymers, which means that the hydroxy-block is also involved in the crosslinking mechanism.

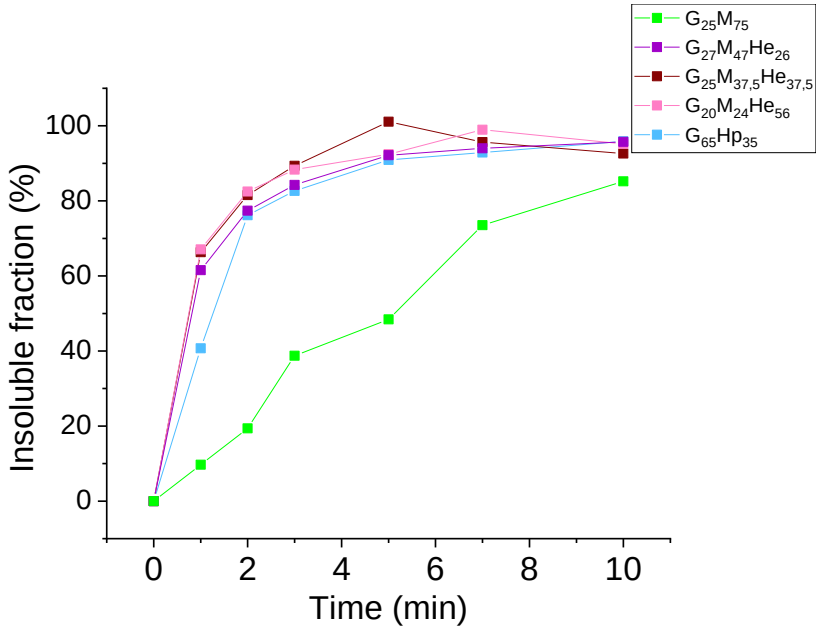

Figure 3-21: Insoluble fraction of the $G_{25}M_{75}$, $G_{27}M_{47}He_{26}$, $G_{25}M_{37,5}He_{37,5}$, $G_{20}M_{24}He_{56}$ and $G_{65}Hp_{35}$ formulated with ATMS as a function of the heating time at 90°C. The thicknesses were measured with an error of ± 5 nm.

In order to probe the crosslinking mechanism of the polymer, ATR-FTIR measurements were performed on drop-casted films as a function of the heating time. Figure 3-22 shows the FTIR spectrum of an as-cast $G_{25}M_{37.5}He_{37.5}$ film. The spectrum corresponds to the typical spectrum of a methacrylate-based polymer with the presence of the characteristic peaks of the ester and of the aliphatic carbons. The hydroxyl groups of the HEMA units are also visible with the presence of the O-H and C-O bonds stretching at 3500 cm^{-1} and 1070 cm^{-1}, respectively. Moreover, the C-O bond stretching of the epoxy group can be observed at 1220 cm^{-1} (see Table 3-2 for the detailed assignments [35]). However, it was not possible to clearly identify the characteristic signal of the trifluoromethyl group due to an overlap of the C-F signal with the stretching modes of the -C-O-C- group between 1400 cm^{-1} and 1000 cm^{-1}.

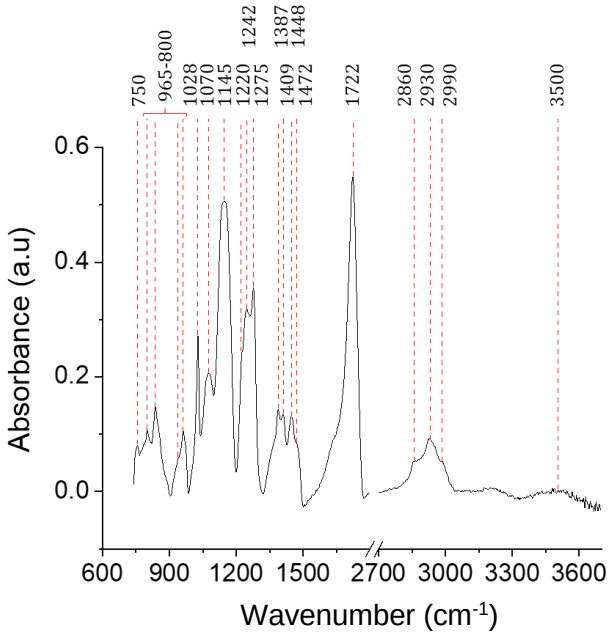

Figure 3-22: **ATR-FTIR spectra of the $G_{25}M_{37.5}He_{37.5}$ drop-casted film.**

Table 3-2: **Assignment of the vibration peaks corresponding to the ATR-FTIR spectra of the $G_{25}M_{37.5}He_{37.5}$. Here, ν is the bond stretching; δ, the bending; ω, the wagging; γ, the rocking and τ, the torsion.**

Group vibrations	Wavenumber (cm^{-1})	Group vibrations	Wavenumber (cm^{-1})
ν(OH)	3500	**[ω(CH_2), δ(CH)]**	1275
[ν(CH_3)$_{as}$, ν(CH_2)$_{as}$]	2990	**ν(C-O)**	1242
[ν(CH_2)$_s$, ν(CH_3)$_s$]	2930	**[ν(C-O), epoxy]**	1220
δ(CH_3)	2860	**[γ(CH_3), τ(OH)]**	1145
ν(C=O)	1722	**[ν(O-C), alcohol]**	1070
δ(CH_2)	1472	**[ν(O-C), ester]**	1028
[ν(CH_2), ν(CH_3)$_{as}$]	1448	**[ν(C-C), γ(CH_3), γ(CH_2)]**	965-800
δ(CH_3)$_s$	1409	**δ(O=C-O)**	750
ω(CH_2)	1387		

The Figure 3-23(a) shows the evolution of the $G_{25}M_{37.5}He_{37.5}$ IR spectra as a function of the heating time. As expected, there is a decrease of the C-O bond stretching of the epoxy group at 1220 cm^{-1} consistent with the ring-opening during the crosslinking reaction (Figure 3-23(b)). One can also see the decrease of the C-O bond at 1028 cm^{-1} of the ester which means that several intermolecular reactions are involved in the crosslinking reaction. Indeed, we can hypothesize that once the ring-

opening occurs, the carbocation being formed is able to attack the surrounding available nucleophile sites such as the oxygens of the ester groups or the ones of the hydroxy groups.

It is possible to determine the degree of conversion of the C-O bond as a function of the heating time using the following equation : $Conversion\ (\%) = \frac{A_{t=0s} - A_t}{A_{t=os}}$ with $A_{t=0s}$ the area of the C-O peak of the as-casted $G_{25}M_{37.5}He_{37.5}$ film and A_t the area of the C-O peak at each time. As shown the Figure 3-23(d), 50% conversion is reached after 2 minutes of reaction which is consistent with the formation of a crosslinked film (Figure 3-21). The final conversion was evaluated as the mean value of three to five experiments to ensure a good reproducibility.

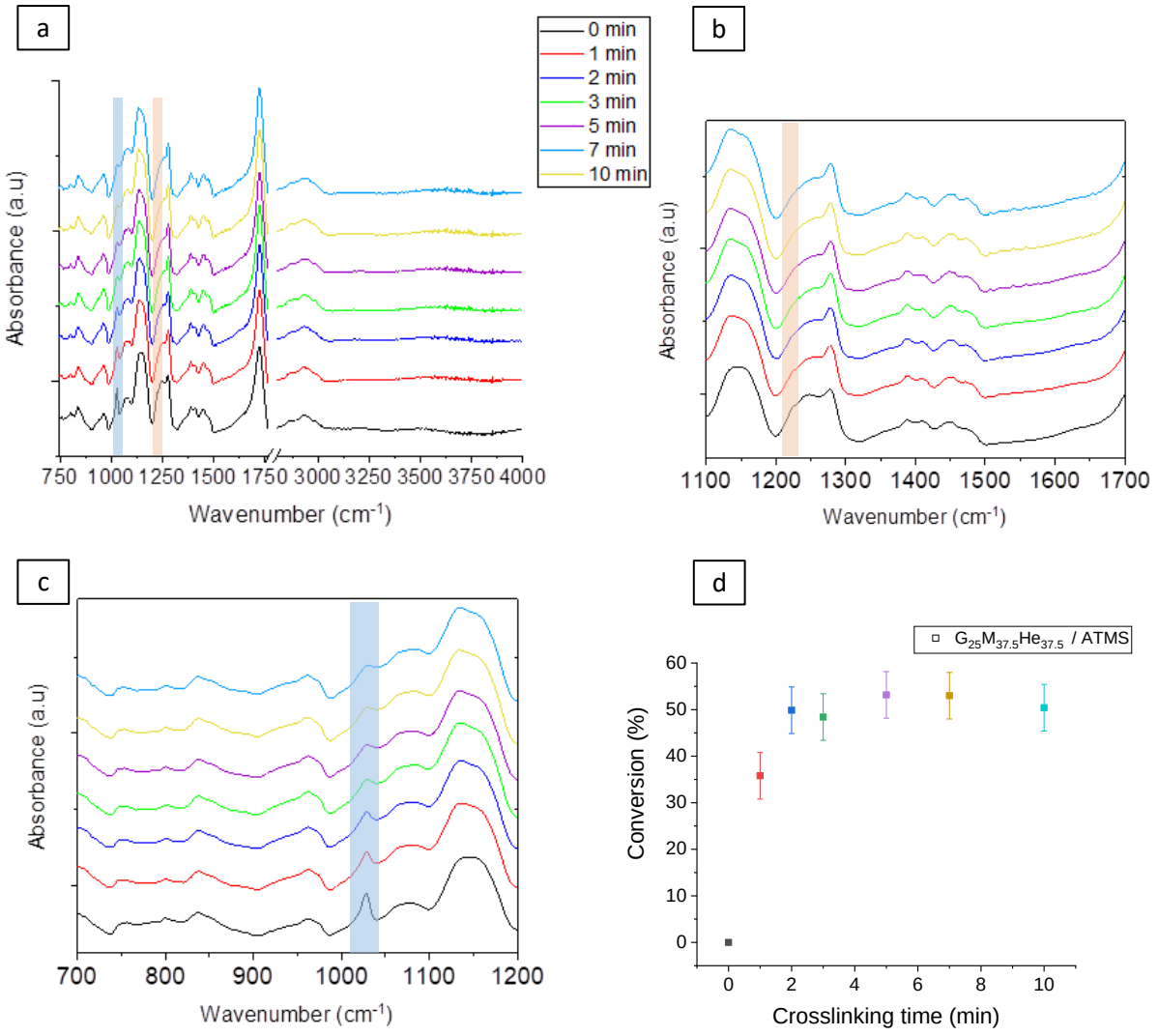

Figure 3-23: (a) ATR-FTIR measurements performed on a $G_{25}M_{37.5}He_{37.5}$/ATMS drop-casted film as a function of the heating time. ATR-FTIR spectrum of the $G_{25}M_{37.5}He_{37.5}$ (the entire spectrum is not shown). (b) Zoom on the area between 1100 and 1700 cm^{-1} showing the decrease of the C-O bond stretching of the epoxy group at 1220 cm^{-1}. (c) Zoom on the area between 900 and 1200 cm^{-1} showing the decrease of the C-O bond at 1028 cm^{-1} of the ester group. (d) Conversion of the C-O bond of the ester deduced from (c) which allows to obtain a rough estimation of the crosslinking kinetics.

Finally, as the main objective of developing a crosslinkable neutral material was to mechanically maintain the BCP film to avoid its dewetting during thermal annealing, mechanical measurements were performed. We measured the Young modulus of $G_{25}M_{37.5}He_{37.5}$/ATMS by AFM to have an insight into the hardness of the material. As shown the Figure 3-24, there is an increase of the Young modulus with the heating time, in line with a crosslinking reaction of the TC layer.

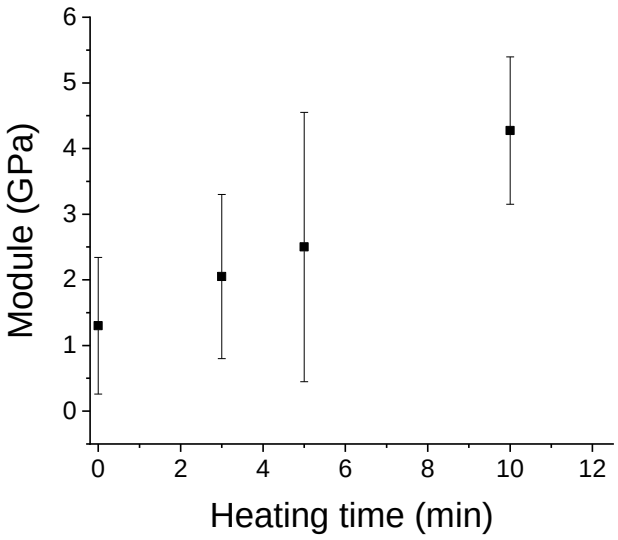

Figure 3-24: Measurements of the Young modulus of the $G_{25}M_{37.5}He_{37.5}$/ATMS thin film as a function of the heating time.

V. Self-assembly of the PDMSB-*b*-PS with the crosslinkable top-coat

The self-assembly of the lamellar-forming $PDMSB_{120}$-*b*-PS_{143} (see relevant characteristic in the Table 3-3) was performed using the crosslinkable TCs. For this purpose, we investigated the effect of the TC composition on the BCP self-assembly. $G_{27}M_{47}He_{26}$, $G_{25}M_{37.5}He_{37.5}$, $G_{20}M_{24}He_{56}$ and $G_{65}Hp_{35}$ were chosen as TCs while $G_{27}M_{47}He_{26}$ and $G_{25}M_{37.5}He_{37.5}$ were used as underlayers (ULs) to tune the surface energy of the substrate. Moreover, we decided to use a hydroxyl-terminated poly(methyl heptyl acrylate) (PMHA) as a third UL. This polymer has nearly the same surface energy as the $G_{27}M_{47}He_{26}$ which would allow us to eventually determine the effect of the polymer structure on the final BCP assembly. The $G_{27}M_{47}He_{26}$, $G_{25}M_{37.5}He_{37.5}$ and PMHA were thus grafted onto silicon substrates *via* their hydroxyl groups before performing the self-assembly of the $PDMSB_{120}$-*b*-PS_{143} using different TCs. The same procedure was used for all the tests and is described below:

i. Grafting of the UL at 200°C for 75 s followed by a rinsing step,
ii. spin-coating of the 1% wt. solution of the $PDMSB_{120}$-*b*-PS_{143} in methyl isobutyl ketone at 2000 rpm (to reach $2L_0$ thickness),
iii. spin-coating of the TC at 2000 rpm,
iv. baking at 90°C for 4 min,
v. thermal annealing of the BCP at 240°C for 5 min.

Table 3-3: Macromolecular characteristics of the lamellae-forming $PDMSB_{120}$-*b*-PS_{143}.

Material	M_n (g.mol^{-1}) [a]	f_{PDMSB} [b]	BCP morphology [c]
$PDMSB_{120}$-*b*-PS_{143}	17140	0.5	Lamellar (L_0=18.2 nm)

a: Molecular weight determined by SEC using PS standards.
b: PDMSB volume fraction determined by ^{1}H NMR.
c: Bulk morphology assigned from SAXS and the periodicity L_0 was calculated using the first order diffraction peak.

First of all, the impact of the TC is directly visible after the thermal annealing of the BCP. Indeed, Figure 3-25 shows the microscopic characterization of the thermally-annealed $PDMSB_{120}$-*b*-PS_{143} films with and without the crosslinked TC. In the absence of the crosslinked TC, the $PDMSB_{120}$-*b*-PS_{143} film dewets on the UL with the typical hole and rim instability observed on the microscopy image (Figure 3-25(a)). When using the crosslinked TC, a homogenous film of $PDMSB_{120}$-*b*-PS_{143} is obtained after the thermal annealing as demonstrated by the optical microscopy image of the $PDMSB_{120}$-*b*-PS_{143} film after removal of the TC (see the Figure 3-25(b)).

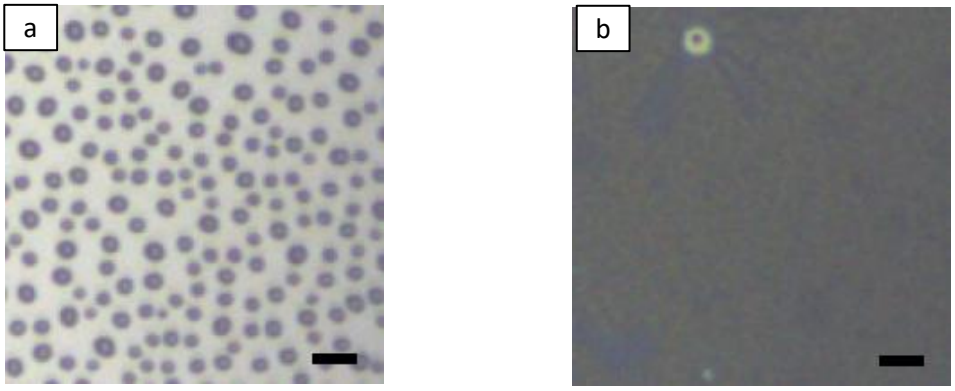

Figure 3-25: Optical microscopy images of the $PDMSB_{120}$-*b*-PS_{143} after the thermal annealing of the films at 240°C for 5 min without (a) and (b) with the crosslinked TC. In the case of (b), the crosslinked TC was removed by plasma. Scale bar: 10 µm.

Ar/O_2 (80 sccm of Ar, 40 sccm of O_2 and 200W) and CF_4/O_2 (17 sccm of CF_4, 3 sccm of O_2 and 40W) plasma etching recipes were used in order to remove the TC layer after the self-assembly process. Indeed, Ar/O_2 is generally used to etch methacrylate-based polymers as it is known to cause breakage of the polymer backbone, side chain scission and depolymerization leading to an efficient etching [36]. CF_4/O_2 plasma allows to slightly etch the PDMSB domains to provide contrast for further microscopy characterizations [37]. Figure 3-26 shows the Ar/O_2 etching rate measurement that was performed by measuring the thickness of a single crosslinked layer of $G_{25}M_{37.5}He_{37.5}$ as a function of the etching time. The etching rate is the 4 $nm.s^{-1}$ which allows to remove the TC after 20 s of plasma.

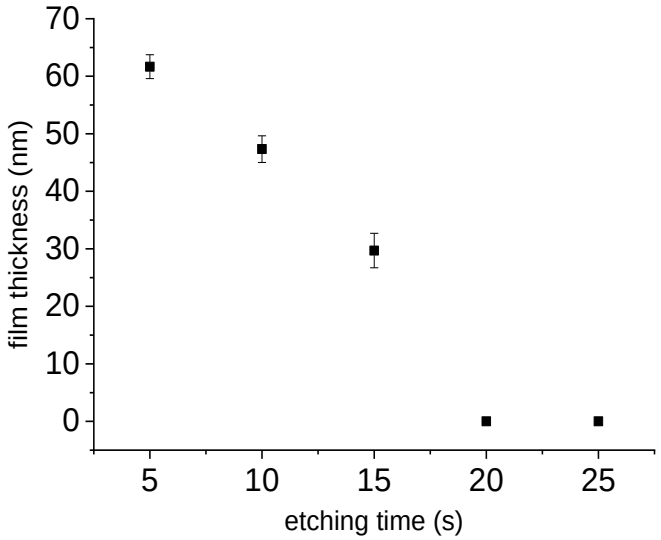

Figure 3-26: Measurements of film thicknesses of $G_{25}M_{37.5}He_{37.5}$/ATMS films as a function of the etching time in order to determine the etching rate of the Ar/O_2 plasma.

The Figure 3-27 summarizes the different orientations of the PDMSB_{120}-*b*-PS_{143} that were observed by SEM after the removal of the TCs. In-plane lamellae are obtained when using the $G_{65}Hp_{35}$ as TC for almost all the ULs which could be expected from the surface energy measurements (Figure 3-18). In the same way, an in-plane orientation is observed when using the $G_{27}M_{47}He_{26}$ as TC associated to the $G_{27}M_{47}He_{26}$ and $G_{25}M_{37.5}He_{37.5}$ as ULs. When we keep decreasing the surface energy of the TC, we start to observe out-of-plane lamellae until a fully-perpendicular lamellar structure (pitch: 17.2 nm) is obtained with the use of $G_{27}M_{47}He_{26}$ regardless of the ULs. Interestingly, when we use the PMHA as UL, out-of-plane lamellae are obtained for almost all the TCs. It can thus be assumed that there is an "orientational field" induced by the neutrality of the UL which can be sufficient to drive the out-of-plane orientation of the lamellae through the thickness of the film.

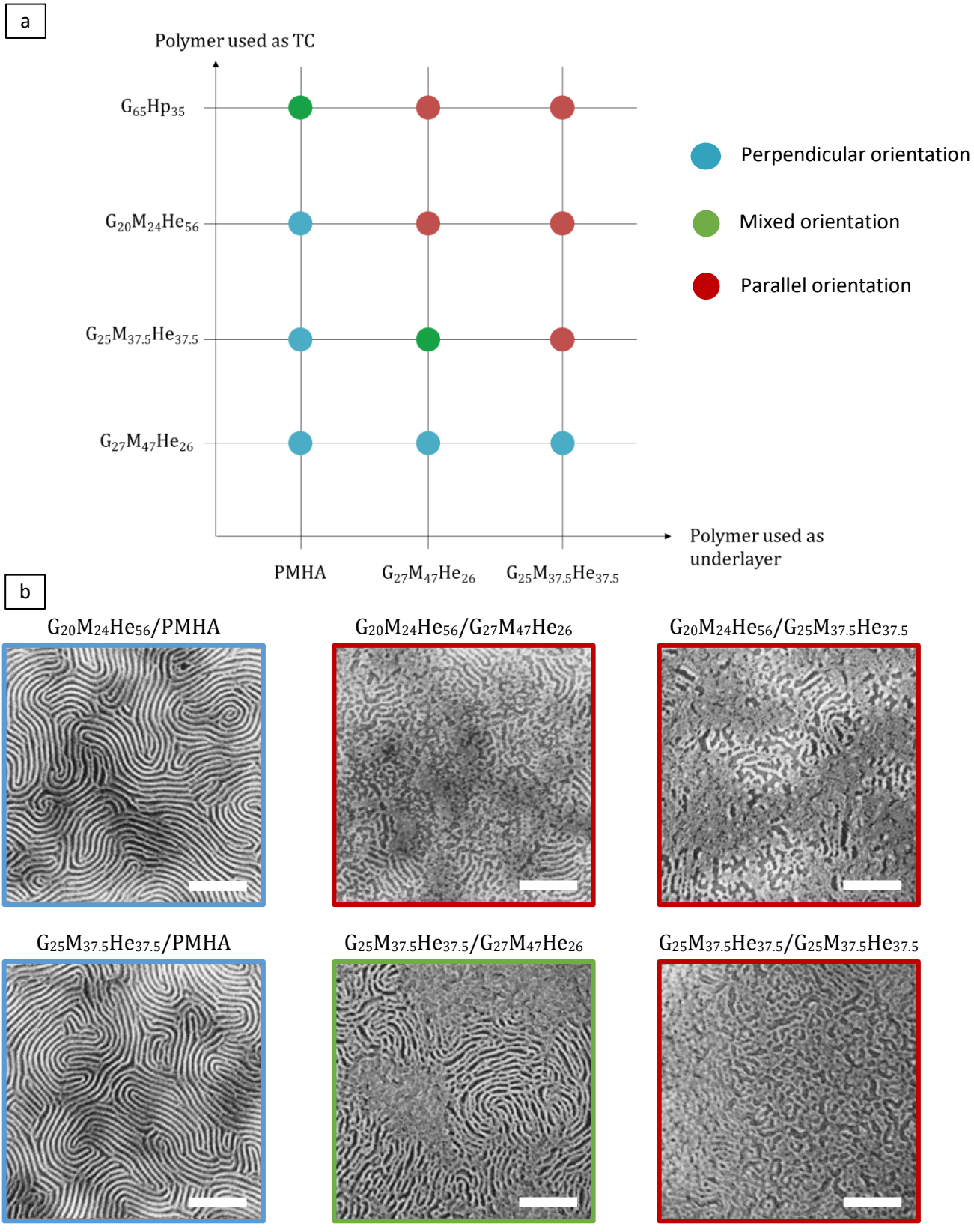

Figure 3-27: Self-assembly of the lamellar-forming PDMSB$_{120}$-*b*-PS$_{143}$ using different sets of TC and UL. (a) summarizes the different PDMSB$_{120}$-*b*-PS$_{143}$ orientations that have been observed by SEM using G$_{27}$M$_{47}$He$_{26}$, G$_{25}$M$_{37.5}$He$_{37.5}$, G$_{20}$M$_{24}$He$_{56}$ and G$_{65}$Hp$_{35}$ as TC and PMHA, G$_{20}$M$_{24}$He$_{56}$ and G$_{25}$M$_{37.5}$He$_{37.5}$ as UL. (b) are some selected SEM images of the lamellar-forming PDMSB$_{120}$-*b*-PS$_{143}$ using six sets of TC/UL. The ULs were grafted onto the silicon substrates. The blue and red frames refer to out-of-plane and in-plane orientations, respectively, while the green frame refers to a mixed orientation. Scale bars: 200 nm.

To further understand these results, the interfacial energies of both PDMSB and PS with the UL and TC were estimated using a harmonic mean equation describing the polymer-surface interfacial interactions [38]:

$$\gamma_{polymer-surface} = \gamma_{polymer} + \gamma_{surface} - \frac{4\,\gamma^{d}_{polymer}\,\gamma^{d}_{surface}}{\gamma^{d}_{polymer} + \gamma^{d}_{surface}} - \frac{4\,\gamma^{p}_{polymer}\,\gamma^{p}_{surface}}{\gamma^{p}_{polymer} + \gamma^{p}_{surface}}$$

where $\gamma_{polymer\text{-}surface}$ is the interfacial energy between the PDMSB or PS block and the UL or TC. γ is the total surface energy while γ^{d} and γ^{p} are the dispersive and polar components of the total surface energy, respectively.

The respective interfacial energy of the PDMSB and PS blocks with each UL and TC layer were calculated using the surface energy measurements performed on PDMSB-OH and PS-OH grafted on Si wafers as described in the previous chapter, while the surface energy of the crosslinked TCs and the grafted ULs were determined using the estimation of the contact angle with three typical liquids (water, diiodomethane and ethylene glycol) by the OWRK model (Figure 3-28).

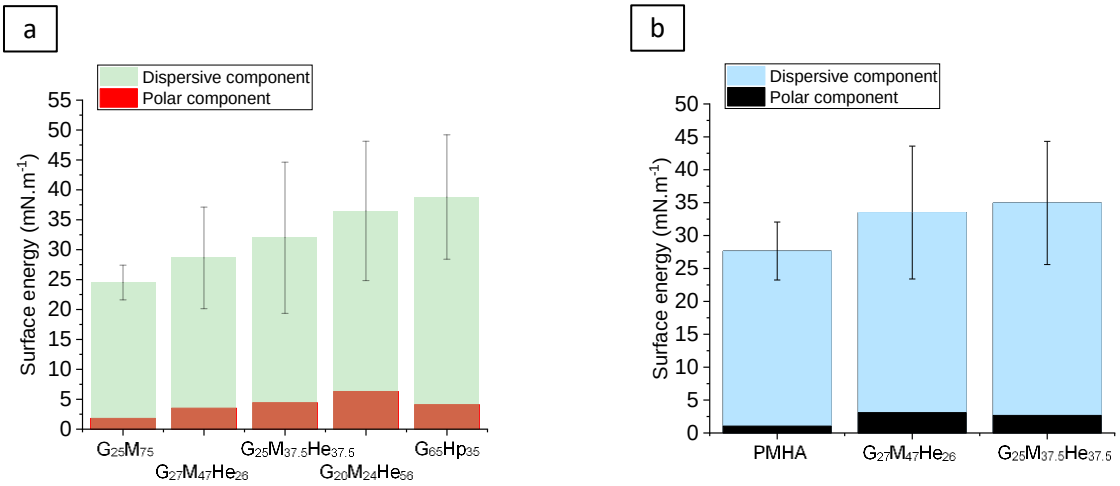

Figure 3-28: Surface energy measurements of (a) the crosslinked TCs and (b) the grafted ULs. Surface energies were determined by contact angle measurements using the three typical liquids (water, diiodomethane and ethylene glycol) and the OWRK model.

The main objective of using neutral layers at the bottom and top interfaces is to avoid a preferential interaction of one of the domains with the substrate and/or the air. When appropriately chosen, these materials should thus lead to a minimization of the interfacial energy difference between the domains and the interfaces resulting in a perpendicular orientation of the domains. Contrary to our expectations, the ULs and TCs allowing an out-of-plane orientation of

the $PDMSB_{120}$-*b*-PS_{143} lamellae (PMHA and $G_{27}M_{47}He_{26}$, respectively) are the ones for which the interfacial energy difference, $\Delta\gamma_{PS\text{-}PDMSB} = \gamma_{PS\text{-}surface} - \gamma_{PDMSB\text{-}surface}$, is the highest (see Table 3-4 and Table 3-5).This apparent lack of correlation could be attributed to the harmonic mean equation that has been used for the calculation of the interfacial energies. Indeed, we used a harmonic mean to predict the interfacial energy between polymers and low energy materials which might not be the most suitable approximation for such layers [39]. Moreover, the temperature is not taken into account in the evaluation of the surface energy. As the self-assembly of the BCP occurs at 240°C, it means that the measurements performed at RT do not reflect the actual surface energies of the layers during the thermal annealing process [40].

Nevertheless, it is noteworthy that the out-of-plane lamellae are obtained for the smallest values of $\gamma_{PDMSB\text{-}surface}$. Consequently, it appears that the lowering of the interfacial energy between the PDMSB and both interfaces is the driving force inducing the perpendicular orientation of the BCP domains (making the assumptions that our surface energy measurements correctly reflected the state of the system during the thermal annealing).

Table 3-4: Calculation of the interfacial energy of the PDMSB and PS with the various ULs.

$\gamma_{polymer\text{-}surface}$ (mN.m^{-1})	PMHA	$G_{27}M_{47}He_{26}$	$G_{25}M_{37.5}He_{37.5}$
PS	3.6	2.5	1.7
PDMSB	0.5	0.7	0.9
$\lvert\Delta_{PS\text{-}PDMSB}\rvert$	3.1	1.9	0.7

Table 3-5: Calculation of the interfacial energy of the PDMSB and PS with the various TCs.

$\gamma_{polymer\text{-}surface}$ (mN.m^{-1})	$G_{65}Hp_{35}$	$G_{20}M_{24}He_{56}$	$G_{25}M_{37.5}He_{37.5}$	$G_{27}M_{47}He_{26}$
PS	2.0	5.1	4.6	5.2
PDMSB	2.1	2.4	0.9	0.3
$\lvert\Delta_{PS\text{-}PDMSB}\rvert$	0.1	2.6	3.8	4.9

In order to validate the ability of our crosslinkable layers to obtain out-of-plane lamellae, we also performed the self-assembly of two other BCPs ($PDMSB_{84}$-*b*-PS_{123} and $PDMSB_{165}$-*b*-PS_{195}), by

preparing 1% wt. solutions of the polymers in methyl isobutyl ketone (see Table 3-6 for the relevant macromolecular characteristic of the BCPs). A $G_{25}M_{37.5}He_{37.5}$/ATMS system was used as both TC and UL following the common procedure:

i. crosslinking of the $G_{25}M_{37.5}He_{37.5}$/ATMS at 240°C for 2 min,
ii. spin-coating of the BCP solution at 2000 rpm,
iii. spin-coating of the TC at 2000 rpm,
iv. baking at 90°C for 4 min,
v. thermal annealing of the BCP at 240°C for 5 min,
vi. and removal of the TC.

Table 3-6: Macromolecular characteristics of the lamellar-forming PDMSB-*b*-PS BCPs.

Material	M_n (g.mol^{-1}) [a]	f_{PDMSB} [b]	BCP morphology [c]
PDMSB$_{84}$-*b*-PS$_{123}$	13600	0.45	Lamellar
PDMSB$_{165}$-*b*-PS$_{195}$	23000	0.51	Lamellar

a: Molecular weight determined by SEC using PS standards
b: PDMSB volume fraction determined by ^{1}H NMR
c: Bulk morphology assigned from SAXS

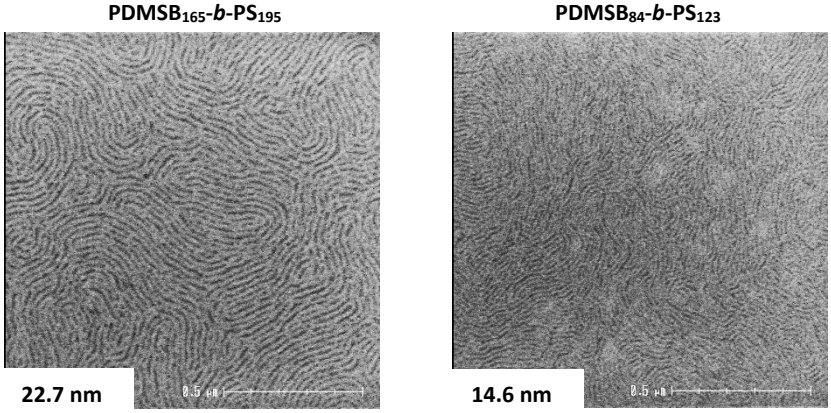

Figure 3-29: SEM images of the PDMSB$_{165}$-*b*-PS$_{195}$ and PDMSB$_{84}$-*b*-PS$_{123}$ BCP after the etching of the crosslinked $G_{25}M_{37.5}He_{37.5}$/ATMS layer using a Ar/O_2 plasma for 25 s followed by a CF_4/O_2 plasma for 45 s.

As shown the Figure 3-29, the $G_{25}M_{37.5}He_{37.5}$/ATMS system allowed to obtain non-dewetted films of out-of-plane lamellae with a periodicity of 22.7 nm and 14.6 nm, respectively. This result confirms the neutrality of the crosslinked TC for lamellae-forming PDMSB-*b*-PS with different molecular weights.

VI. PDMSB-*b*-PS multi-layers

Finally, we decided to use the crosslinked layer as a new "substrate" to deposit a subsequent BCP layer. As shown in the Figure 3-30, it is possible to build a multi-layer stack of BCP layers in a simple manner. Indeed, after performing the self-assembly of the first BCP layer, one can use the TC as a substrate to deposit a second BCP layer. Finally, a subsequent TC can be deposit on the BCP film prior to perform the self-assembly of the BCP (see pathway 1 of the Figure 3-30). In another pathway, it is also possible to deposit and crosslink all the layers and perform a unique thermal annealing to self-assemble the two BCP layers (see pathway 2 of the Figure 3-30). Moreover, we saw in the previous section that is was possible to control the orientation of the lamellar-forming BCPs by varying the chemical composition of the TC and UL. Consequently, by choosing the appropriate sets of UL/TC, we could thus be able to control the orientation of each BCP layer in an independent manner.

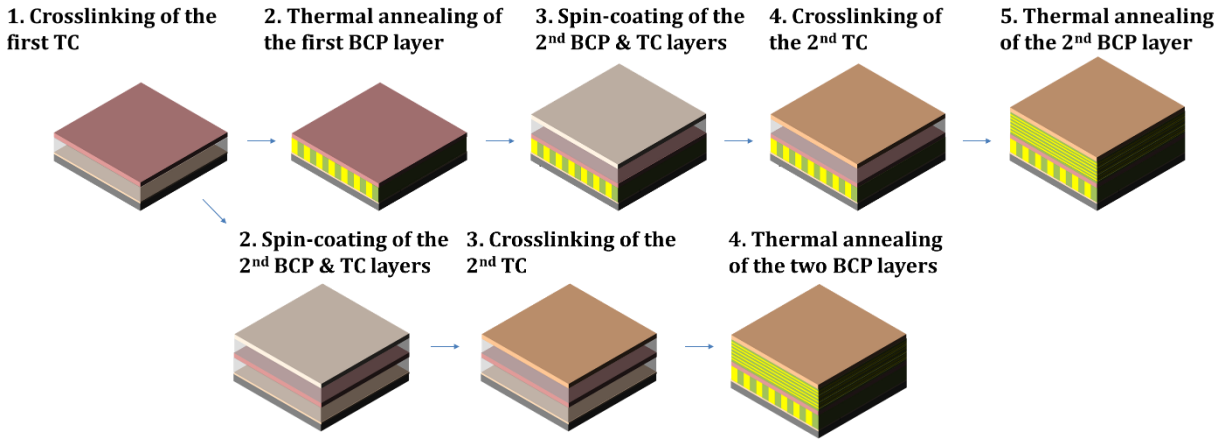

Figure 3-30: Scheme of the process used in order to achieve a two-layers stack of lamellae having different orientations and periodicities using crosslinkable layers.

As a proof of concept, we decided to stack two lamellar-forming PDMSB-*b*-PS BCPs having (i) different periodicities, (ii) different orientations and (iii) different thicknesses. For this purpose, we prepared 1.5% wt. and 1% wt. solutions in methyl isobutyl ketone of $PDMSB_{120}$-*b*-PS_{143} and $PDMSB_{220}$-*b*-PS_{238}, respectively (Table 3-7).

Table 3-7: Macromolecular characteristics of the lamellae-forming PDMSB-*b*-PS BCPs used to build the two-layers stack.

Material	M_n (g.mol^{-1}) [a]	f_{PDMSB} [b]
PDMSB$_{120}$-*b*-PS$_{143}$	17140	0.5
PDMSB$_{220}$-*b*-PS$_{238}$	29150	0.54

a: Molecular weight determined by SEC using PS standards
b: PDMSB volume fraction determined by ^{1}H NMR

With the aim to obtain a thick layer of in-plane PDMSB$_{120}$-*b*-PS$_{143}$ lamellae above a thin layer of out-of-plane lamellae of PDMSB$_{220}$-*b*-PS$_{238}$, we consequently performed the following protocol:

i. grafting of the PMHA at 200°C for 75 s followed by a rinsing step,
ii. spin-coating of 1% wt. solution of PDMSB$_{220}$-*b*-PS$_{238}$ film at 2000 rpm,
iii. spin-coating of G$_{20}$M$_{24}$He$_{56}$/ATMS (9:1) solution at 2000 rpm,
iv. baking at 90°C for 4 min followed by a rinsing step,
v. thermal annealing of the BCP at 240°C for 5 min,
vi. spin-coating of 2% wt. solution of PDMSB$_{120}$-*b*-PS$_{143}$ film at 1500 rpm,
vii. spin-coating of G$_{65}$Hp$_{35}$/ATMS at 2000 rpm,
viii. baking at 90°C for 4 min,
ix. thermal annealing of the BCP at 240°C for 5 min.

The PMHA was chosen as the first UL for the self-assembly PDMSB$_{220}$-*b*-PS$_{238}$ because it offers a high versatility as regards to the choice of the top coat due to a strong "orientational field" inducing lamellar out-of-plane orientation independently of the TC (Figure 3-27). We consequently choose one of the TCs that could lead to an in-plane orientation of the subsequent PDMSB$_{120}$-*b*-PS$_{143}$ layer, i.e. a G$_{20}$M$_{24}$He$_{56}$/ATMS layer. Finally, we choose a G$_{65}$Hp$_{35}$/ATMS layer as TC for the second BCP layer. The Figure 3-31 shows the characterization of the stack by FIB-STEM. We successfully obtain a layered stack with in-plane and out-of-plane lamellae of PDMSB$_{120}$-*b*-PS$_{143}$ and PDMSB$_{220}$-*b*-PS$_{238}$ with a periodicity of ~17 nm and ~24 nm, respectively. The bended shape can be attributed to the FIB preparation process (during the platinum deposition or during the cutting of the slide).

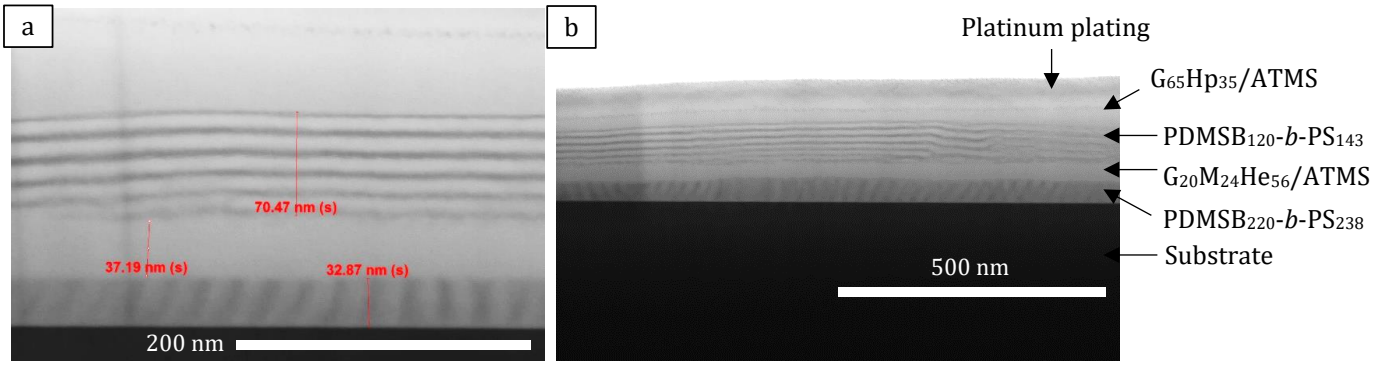

Figure 3-31: FIB-STEM characterization of the two-layers stack of PDMSB$_{220}$-*b*-PS$_{238}$ (1st layer) and PDMSB$_{120}$-*b*-PS$_{143}$ (2nd layer).

We have further implemented this iterative self-assembly method by stacking three different lamellar-forming PDMSB-*b*-PS layers (PDMSB$_{165}$-*b*-PS$_{195}$, PDMSB$_{120}$-*b*-PS$_{143}$ and PDMSB$_{84}$-*b*-PS$_{123}$) (Table 3-8).

Table 3-8: Macromolecular characteristics of the lamellar-forming PDMSB-*b*-PS BCPs used to build the third-layers stack.

Material	M_n (g.mol^{-1}) [a]	f_{PDMSB} [b]
PDMSB$_{165}$-*b*-PS$_{195}$	23000	0.51
PDMSB$_{120}$-*b*-PS$_{143}$	17140	0.5
PDMSB$_{84}$-*b*-PS$_{123}$	13600	0.45

a: Molecular weight determined by SEC using PS standards
b: PDMSB volume fraction determined by ^{1}H NMR

As out-of-plane lamellae of PDMSB$_{165}$-*b*-PS$_{195}$ and PDMSB$_{84}$-*b*-PS$_{123}$ were demonstrated using a G$_{25}$M$_{37.5}$He$_{37.5}$/ATMS layer as both bottom and top neutral layers, this TC composition was chosen for the self-assembly of these two BCPs. Moreover, we also saw in the same section that out-of-plane lamellae of PDMSB$_{120}$-*b*-PS$_{143}$ could be obtained using G$_{25}$M$_{37.5}$He$_{37.5}$/ATMS and G$_{27}$M$_{47}$He$_{26}$/ATMS as TC and UL, respectively. Consequently, to build a stack of PDMSB$_{165}$-*b*-PS$_{195}$ (1st layer), PDMSB$_{120}$-*b*-PS$_{143}$ (2nd layer) and PDMSB$_{84}$-*b*-PS$_{123}$ (3rd layer) having perpendicular orientation (such as the Figure 3-32), we performed the following protocol:

i. crosslinking of G$_{25}$M$_{37.5}$He$_{37.5}$/ATMS at 240°C for 2 min followed by a rinsing step,
ii. spin-coating of 2% wt. solution of PDMSB$_{165}$-*b*-PS$_{195}$ film at 1500 rpm,
iii. spin-coating of G$_{25}$M$_{37.5}$He$_{37.5}$/ATMS solution at 2000 rpm,

iv. baking at 90°C for 4 min followed by a rinsing step,

v. spin-coating of 2% wt. solution of PDMSB$_{120}$-*b*-PS$_{143}$ film at 1500 rpm,

vi. spin-coating of G$_{25}$M$_{37.5}$He$_{37.5}$/ATMS solution at 2000 rpm,

vii. baking at 90°C for 4 min followed by a rinsing step,

viii. spin-coating of G$_{27}$M$_{47}$He$_{26}$/ATMS solution at 2000 rpm,

ix. baking at 90°C for 4 min followed by a rinsing step,

x. spin-coating of 2% wt. solution of PDMSB$_{84}$-*b*-PS$_{123}$ film at 1500 rpm,

xi. spin-coating of G$_{25}$M$_{37.5}$He$_{37.5}$/ATMS solution at 2000 rpm,

xii. baking at 90°C for 4 min followed by a rinsing step,

xiii. thermal annealing of the BCP at 240°C for 5 min.

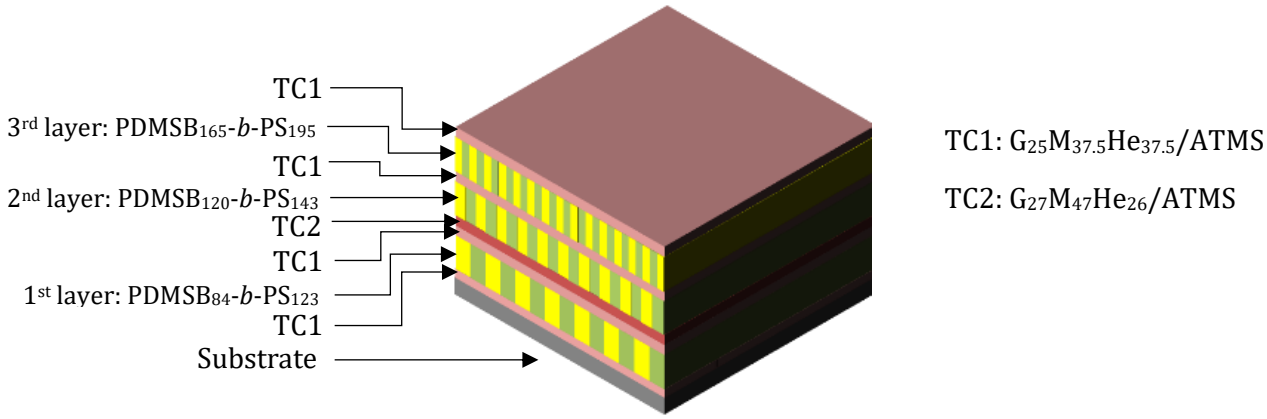

Figure 3-32: Scheme of the expected three-layers stack of lamellae-forming PDMSB-*b*-PS having different molecular weights using crosslinkable layers.

The Figure 3-33 shows the characterization of the stack by FIB-STEM. A flat and non-dewetted stack is obtained after the thermal annealing as shown the Figure 3-33(a). Despite the limited contrast, we can see that out-of-plane lamellae of PDMSB$_{120}$-*b*-PS$_{143}$ are obtained (2nd layer) while PDMSB$_{84}$-*b*-PS$_{123}$ (3rd layer) and PDMSB$_{165}$-*b*-PS$_{195}$ (1st layer) exhibit a mixed orientation (Figure 3-33(b) and (c)). It seems that the set of parameters (crosslinked layers composition, temperature and time of the thermal annealing) chosen for the self-assembly of the PDMSB$_{84}$-*b*-PS$_{123}$ and PDMSB$_{165}$-*b*-PS$_{195}$ were not suitable to induce a complete out-of-plane orientation when increasing the thickness of the films (61 nm and 117 nm for the PDMSB$_{84}$-*b*-PS$_{123}$ and PDMSB$_{165}$-

b-PS$_{195}$, respectively as shown the Figure 3-33). An optimization of the crosslinked layer composition and of the self-assembly parameters should be performed in order to obtain fully perpendicular orientations.

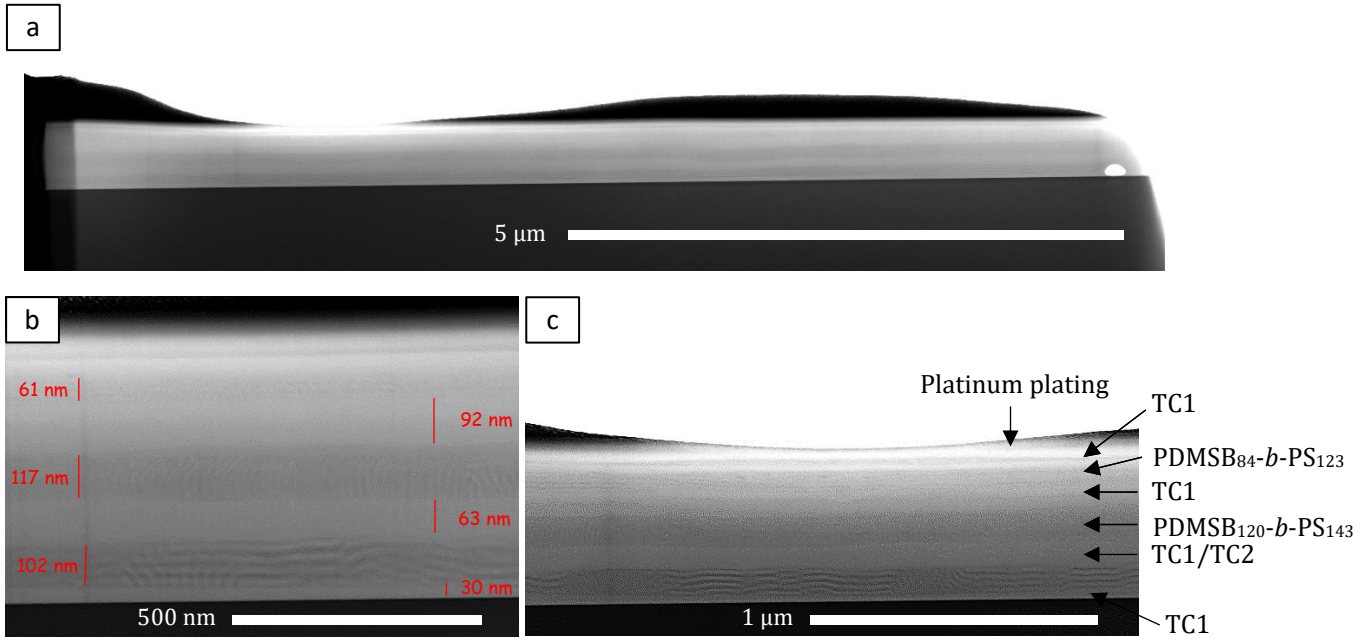

Figure 3-33: FIB-STEM characterization of the three-layers stack of PDMSB$_{165}$-*b*-PS$_{195}$ (1st layer), PDMSB$_{120}$-*b*-PS$_{143}$ (2nd layer) and PDMSB$_{84}$-*b*-PS$_{123}$ (3rd layer). (a) is the low magnification view of the characterized slice to highlight the homogeneity of the stack. (b) and (c) are FIB-STEM images highlighting the structure and the orientation of the different PDMSB-*b*-PS layers.

VII. Conclusion

In this chapter, an approach relying on the use of TC layers to control the BCP self-assembly in thin film was developed for the production of out-of-plane PDMSB-*b*-PS lamellae. Indeed, we have designed a TC material that (i) prevents the lower surface energy PDMSB block to segregate at the top interface during thermal annealing (and leading to an in-plane orientation) and (ii) limits the dewetting of the BCP film during the annealing. The design of the TC layers was rationalized through the different functionalities provided by a methacrylate-based random copolymer architecture providing an easy deposition of the material on the BCP, a tuning of its surface energy and its crosslinking ability. This latter property constitutes the major originality of our approach as compared to the current state of art.

We have demonstrated the crosslinking ability of the TC using a thermal crosslinking agent that allows a fast crosslinking of the material in 3 min. This crosslinked TC was further used for the self-assembly of the lamellar-forming $PDMSB_{120}$-*b*-PS_{143} in thin film and leads to the achievement of a smooth film of out-of-plane lamellae with a 17.2 nm pitch. These results were extended to two other lamellar-forming PDMSB-*b*-PS BCPs in order to obtain films of out-of-plane lamellae with 14.6 nm and 22.7 nm periodicities showing the versatility of the approach.

Finally, taking advantage of the crosslinking ability of our TC material, we have built two- and three-layers stacks of lamellar PDMSB-*b*-PS. By controlling the surface energy of the crosslinked material at bottom and top interfaces, it was possible to control the orientation of each BCP layer in an independent way. Consequently, we successfully obtained a two-layer stack of in- and out-of plane lamellae with two BCPs having different periodicities and film thicknesses. We also performed the stacking of three lamellar PDMSB-*b*-PS BCPs although an optimization of the process remains to be done to achieve a perfect control of BCP alignment within the stack.

VIII. References

[1] H. S. Wang, K. H. Kim and J. Bang, "Thermal Approaches to Perpendicular Block Copolymer Microdomains in Thin Films: A Review and Appraisal", *Macromolecular Rapid Communications*, vol. 40, nº 4, p. 1800728, févr. 2019.

[2] R. D. Peters, X. M. Yang, T. K. Kim *et al.*, "Using Self-Assembled Monolayers Exposed to X-rays to Control the Wetting Behaviour of Thin Films of Diblock Copolymers", *Langmuir*, vol. 16, nº 10, p. 4625-4631, mai 2000.

[3] T. K. Kim, X. M. Yang, R. D. Peters *et al.*, "Chemical Modification of Self-Assembled Monolayers by Exposure to Soft X-rays in Air", *The Journal of Physical Chemistry B*, vol. 104, nº 31, p. 7403-7410, août 2000.

[4] A. P. Smith, J. F. Douglas, J. C. Meredith *et al.*, "Combinatorial Study of Surface Pattern Formation in Thin Block Copolymer Films", *Physical Review Letters*, vol. 87, nº 1, juin 2001.

[5] A. Niemz, K. Bandyopadhyay, E. Tan, K. Cha and S. M. Baker, "Fabrication of Nanoporous Templates from Diblock Copolymer Thin Films on Alkylchlorosilane-Neutralized Surfaces", *Langmuir*, vol. 22, nº 26, p. 11092-11096, déc. 2006.

[6] T. H. Epps, D. M. DeLongchamp, M. J. Fasolka *et al.*, "Substrate Surface Energy Dependent Morphology and Dewetting in an ABC Triblock Copolymer Film", *Langmuir*, vol. 23, nº 6, p. 3355-3362, mars 2007.

[7] P.-H. Liu, P. Thébault, P. Guenoun and J. Daillant, "Easy Orientation of Diblock Copolymers on Self-Assembled Monolayers Using UV Irradiation", *Macromolecules*, vol. 42, nº 24, p. 9609-9612, déc. 2009.

[8] P. Mansky, "Controlling Polymer-Surface Interactions with Random Copolymer Brushes", *Science*, vol. 275, nº 5305, p. 1458-1460, mars 1997.

[9] E. Han, K. O. Stuen, Y.-H. La, P. F. Nealey and P. Gopalan, "Effect of Composition of Substrate-Modifying Random Copolymers on the Orientation of Symmetric and Asymmetric Diblock Copolymer Domains", *Macromolecules*, vol. 41, nº 23, p. 9090-9097, déc. 2008.

[10] K. Sparnacci, D. Antonioli, V. Gianotti *et al.*, "Ultrathin Random Copolymer-Grafted Layers for Block Copolymer Self-Assembly", *ACS Applied Materials & Interfaces*, vol. 7, nº 20, p. 10944-10951, mai 2015.

[11] S. Ji, G. Liu, F. Zheng, G. S. W. Craig *et al.*, "Preparation of Neutral Wetting Brushes for Block Copolymer Films from Homopolymer Blends", *Advanced Materials*, vol. 20, nº 16, p. 3054-3060, août 2008.

[12] W. Gu, S. W. Hong and T. P. Russell, "Orienting Block Copolymer Microdomains with Block Copolymer Brushes", *ACS Nano*, vol. 6, nº 11, p. 10250-10257, nov. 2012.

[13] E. Kim, W. Kim, K. H. Lee, C. A. Ross and J. G. Son, "A Top Coat with Solvent Annealing Enables Perpendicular Orientation of Sub-10 nm Microdomains in Si-Containing Block Copolymer Thin Films", *Advanced Functional Materials*, vol. 24, nº 44, p. 6981-6988, nov. 2014.

[14] I. H. Ryu, Y. J. Kim, Y. S. Jung, J. S. Lim *et al.*, "Interfacial Energy-Controlled Top Coats for Gyroid/Cylinder Phase Transitions of Polystyrene- *block* -polydimethylsiloxane Block Copolymer Thin Films", *ACS Applied Materials & Interfaces*, vol. 9, nº 20, p. 17427-17434, mai 2017.

[15] Takeru. Higuchi, Lennart. Eberson and J. D. McRae, "Acid anhydride-free acid equilibria in water in some substituted succinic acid systems and their interaction with aniline", *J. Am. Chem. Soc.*, vol. 89, nº 12, p. 3001-3004, juin 1967.

[16] C. M. Bates, T. Seshimo, M.J. Maher *et al.*, "Polarity-Switching Top Coats Enable Orientation of Sub-10-nm Block Copolymer Domains", *Science*, vol. 338, nº 6108, p. 775-779, nov. 2012.

[17] M. J. Maher, C.M. Bates, G. Blachut *et al.*, "Interfacial Design for Block Copolymer Thin Films", *Chem. Mater.*, vol. 26, nº 3, p. 1471-1479, févr. 2014.

[18] J. G. Kennemur, M. A. Hillmyer and F. S. Bates, "Synthesis, Thermodynamics, and Dynamics of Poly(4-tert-butylstyrene-b-methyl methacrylate)", *Macromolecules*, vol. 45, nº 17, p. 7228-7236, sept. 2012.

[19] J. Zhang, M. B. Clark, C. Wu, M. Li, P. Trefonas and P. D. Hustad, "Orientation Control in Thin Films of a High-χ Block Copolymer with a Surface Active Embedded Neutral Layer", *Nano Lett.*, vol. 16, nº 1, p. 728-735, janv. 2016.

[20] P. Trefonas III, P.D. Hustad, D. Wang *et al.*, "Neutral layer polymers, methods of manufacture thereof and articles comprising the same" US Patent, 2016.
[21] D. K. Owens and R. C. Wendt, "Estimation of the surface free energy of polymers", *J. Appl. Polym. Sci.*, vol. 13, nº 8, p. 1741-1747, août 1969.
[22] H. Yoshida, H.S. Suh, A. Ramirez-Herunandez *et al.*, "Topcoat Approaches for Directed Self-Assembly of Strongly Segregating Block Copolymer Thin Films", *J. Photopol. Sci. Technol.*, vol. 26, nº 1, p. 55-58, juin 2013.
[23] A. Vora, K. Schmidt, G. Alva *et al.*, "Orientation Control of Block Copolymers Using Surface Active, Phase-Preferential Additives", *ACS Appl. Mater. Interfaces*, vol. 8, nº 43, p. 29808-29817, nov. 2016.
[24] O. Coulembier, D.P. Sanders, A. Nelson *et al.*, "Hydrogen-bonding catalysts based on fluorinated alcohol derivatives for living polymerization", *Angew. Chem. Int. Ed. Engl.*, vol. 48, nº 28, p. 5170-5173, 2009.
[25] S. Tempelaar, L. Mespouille, P. Dubois, and A. P. Dove, "Organocatalytic Synthesis and Postpolymerization Functionalization of Allyl-Functional Poly(carbonate)s", *Macromolecules*, vol. 44, nº 7, p. 2084-2091, avr. 2011.
[26] "Surfactant-Assisted Orientation of Thin Diblock Copolymer Films - Son - 2008 - Advanced Materials - Wiley Online Library". [En ligne]. Disponible sur: http://onlinelibrary.wiley.com/doi/10.1002/adma.200800670/abstract. [Consulté le: 10-janv-2018].
[27] H. S. Suh, P. Moni, S. Xiong *et al.*, "Sub-10-nm patterning via directed self-assembly of block copolymer films with a vapour-phase deposited topcoat", *Nat Nanotechnol*, vol. 12, nº 6, p. 575-581, juill. 2017.
[28] A. M. Coclite, R.M. Howden, D.C. Borrelli *et al.*, "25th Anniversary Article: CVD Polymers: A New Paradigm for Surface Modifi cation and Device Fabrication", *Adv. Mater.*, vol. 25, nº 38, p. 5392-5423, oct. 2013.
[29] A. M. Ross and J. Lahann, "Current Trends and Challenges in Biointerfaces Science and Engineering", *Annu Rev Chem Biomol Eng*, vol. 6, p. 161-186, 2015.
[30] "Organic Vapour Passivation of Silicon at Room Temperature - Yang - 2013 - Advanced Materials - Wiley Online Library". [En ligne]. Disponible sur: http://onlinelibrary.wiley.com/doi/10.1002/adma.201204382/abstract. [Consulté le: 10-janv-2018].
[31] G. Ozaydin-Ince and K. K. Gleason, "Transition between kinetic and mass transfer regimes in the initiated chemical vapour deposition from ethylene glycol diacrylate", *Journal of Vacuum Science & Technology A: Vacuum, Surfaces, and Films*, vol. 27, nº 5, p. 1135-1143, juill. 2009.
[32] R. Shelkov and A. Melman, "Free-Radical Approach to 4-Substituted Dipicolinates", *Eur. J. Org. Chem.*, vol. 2005, nº 7, p. 1397-1401, avr. 2005.
[33] F. Minisci, R. Bernardi, F. Bertini *et al.*, "Nucleophilic character of alkyl radicals—VI: A new convenient selective alkylation of heteroaromatic bases", *Tetrahedron*, vol. 27, nº 15, p. 3575-3579, janv. 1971.
[34] J. Oh, H.S. Suh, Y. Ko *et al.*, "Universal perpendicular orientation of block copolymer microdomains using a filtered plasma", *Nature Communications*, vol. 10, nº 1, déc. 2019.
[35] L. Ferreira, M. M. Vidal and M. H. Gil, "Evaluation of poly(2-hydroxyethyl methacrylate) gels as drug delivery systems at different pH values", *International Journal of Pharmaceutics*, vol. 194, nº 2, p. 169-180, janv. 2000.
[36] Y.-H. Ting, C.-C. Liu, S.-M. Park *et al.*, "Surface Roughening of Polystyrene and Poly(methyl methacrylate) in Ar/O2 Plasma Etching", *Polymers*, vol. 2, nº 4, p. 649-663, déc. 2010.
[37] Y. Rho, K. Aissou, M. Mumtaz *et al.*, "Laterally Ordered Sub-10 nm Features Obtained From Directed Self-Assembly of Si-Containing Block Copolymer Thin Films", *Small*, vol. 11, nº 48, p. 6377-6383, déc. 2015.
[38] I. Keen, H.H. Cheng, K.S. Jack *et al.*, "Control of the Orientation of Symmetric Poly(styrene)- *block* -poly(D,L-lactide) Block Copolymers Using Statistical Copolymers of Dissimilar Composition", *Langmuir*, vol. 28, nº 45, p. 15876-15888, nov. 2012.
[39] S. Wu, *Polymer interface and adhesion*. New York: M. Dekker, 1982.
[40] K. GmbH, "Effect of Temperature on the Surface Energy of Solids", p. 2.

CHAPTER 4: Patterning of the top-coat

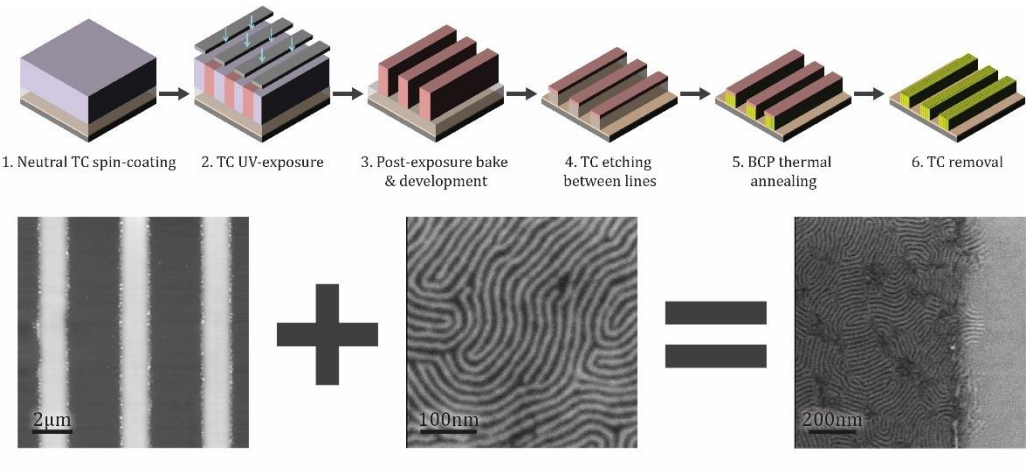

In this chapter, we have extended the potential ability of the TC to build complex structures by investigating the patternability of the material in order to guide the self-assembly of the lamellar BCP in specific areas of the film. Three different strategies have been studied to photocrosslink the TC layer in deep-UV and in the visible range. We have compared and optimized the crosslinking efficiency of the material with various photosensitive crosslinking agents to achieve fully-crosslinked films after 2 min and 1 s of flood exposure under UV-light and deep-UV, respectively. We have then performed the patterning of the TC above the PDMSB-*b*-PS film, which allowed a control the orientation of the lamellae in specific areas of the film with a good resolution.

I. Introduction

The fact that the developed TCs can be photocrosslinked is the major originality of our study as compared to the current state-of-the-art. By combining the neutralization functionality with the crosslinking ability, patterning strategies by standard UV lithography, electron-beam lithography or nanoimprint can be designed which would lead to the definition of chemical patterns in order to control the BCP orientation at specific locations of the film. Nealey and co-workers already demonstrated the potential of photoresists to define patterns at a second scale with the use of a commercial resist deposited on the top of the neutral layer after the self-assembly of the BCP [1]. Here, we propose to directly use the neutral TC material as a platform for the definition of patterns through a simple process as shown in Figure 4-1.

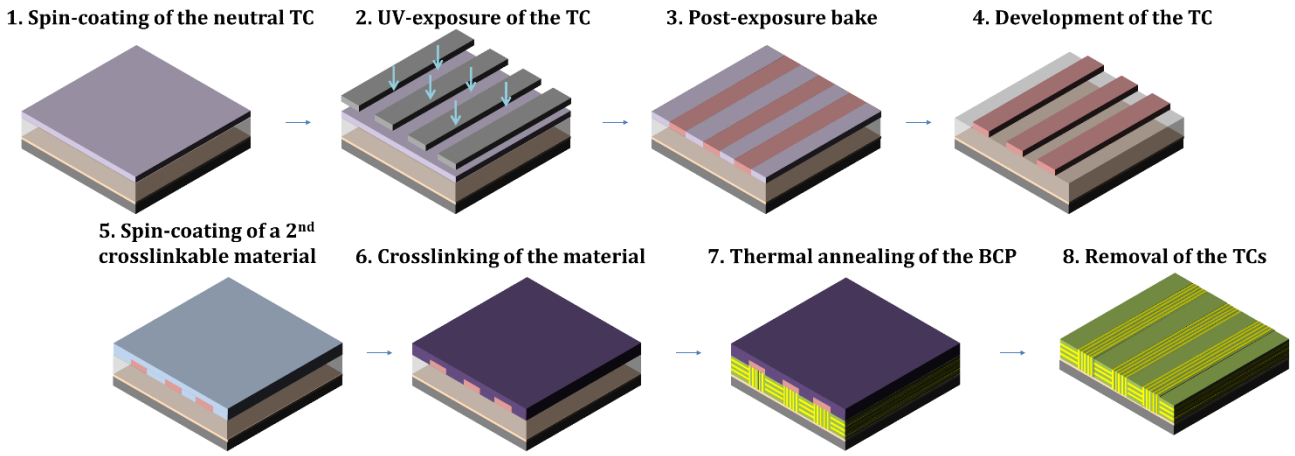

Figure 4-1: Scheme of the process in order to achieve out-of-plane lamellae using the neutral patternable TC.

The crosslinking reaction of the $G_wM_xHe_yHp_z$ TC is based on the photocatalysed ring-opening of the epoxy group in the same way the CARs presented in the first chapter are working. Indeed, the design of the TC material was inspired from the conventional CARs. First of all, the methacrylate backbone was chosen because methacrylate-based photoresists are widely used for the lithography at 193 nm owning their good transparency at such wavelengths as shown in the Figure 4-2 [2]. Moreover, the chemistry involving epoxy moieties is well-known and remains among the most used following the success of the SU-8 resins.

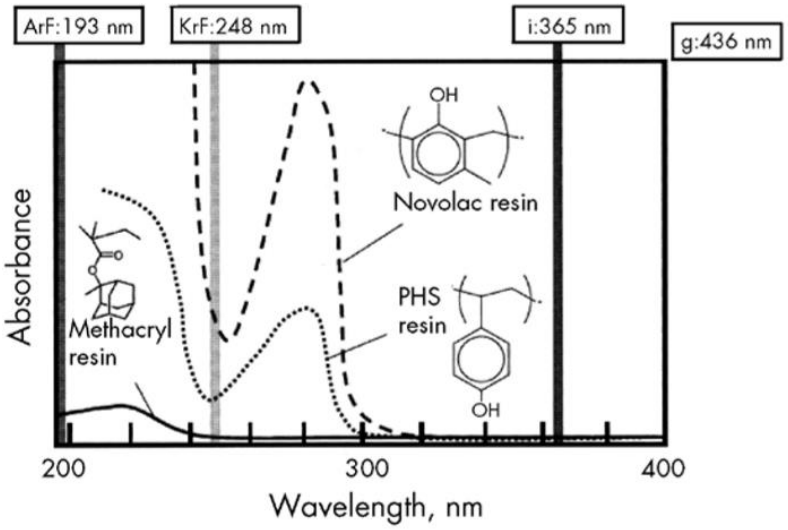

Figure 4-2: UV-visible spectrum showing the different light absorption of typical photoresists [2].

II. Evaluation of crosslinking systems for top-coat patterning

1. Crosslinking under deep-UV irradiation

a) Absorbance of the PAGs

To photocrosslink our TCs, we have decided to use a pathway involving the use of PAG. In this work, diphenyl iodonium and triaryl sulfonium salts were chosen as PAGs since they are reported to be the most stable, efficient and in high abundance at industrial scale [3]. A series of 5 PAGs (Table 4-1) were evaluated in order to investigate the effect on the PAG characteristics of (i) the counter-anion, (ii) the cation chemistry and (iii) the chemical structure. Indeed, the cation will determine the photochemistry of the molecule including the light sensitivity, the maximum of absorbance and the thermal stability. On the other hand, the anion will determine the strength of the acid that will be formed upon photochemical decomposition of the onium cation [3]. This preliminary study was designed to choose the best candidate for the crosslinking of the TCs.

Table 4-1: The different photoacid generators used for the photocrosslinking of the TCs.

<table>
<tr><td rowspan="2">Diphenyl iodonium salts</td><td>diphenyl iodonium p-toluenesulfonate
(dPi-TS)
 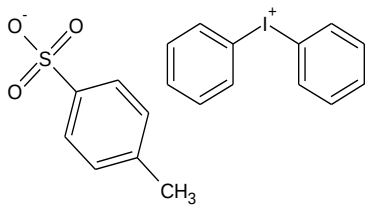
λ_{max} = 222 nm[10]</td><td colspan="2">(4-methylphenyl) [4-(2-methylpropyl) phenyl] iodonium hexafluorophosphate
(dPi-PF₆)
 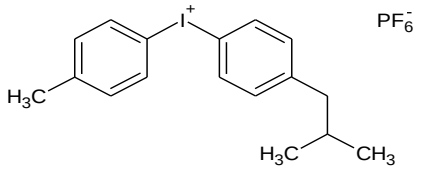
λ_{max} = 222 nm [4]</td></tr>
<tr><td>Triaryl sulfonium salts</td><td>diphenyl (4-(phenylthio)phenyl) sulfonium trifluoromethanesulfonate
(dPSPT-OTf)
 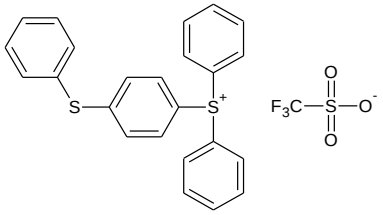
λ_{max} = 298 nm[10]</td><td>triphenyl sulfonium trifluoromethanesulfonate
(tPS-OTf)
 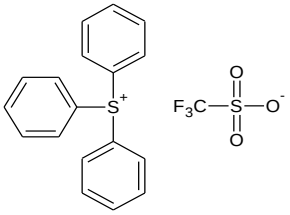
λ_{max} = 233 nm[10]</td><td>triphenyl sulfonium bromide
(tPS-Br)
 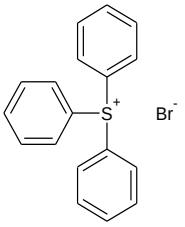
λ_{max} = 222 nm [4]</td></tr>
</table>

[10] *Obtained from the Sigma Aldrich datasheet*

The 5 PAGs studied here include : the diphenyl iodonium *p*-toluenesulfonate (dPi-TS), the (4-methylphenyl) [4-(2-methylpropyl) phenyl] iodonium hexafluorophosphate (dPi-PF_6), triphenylsulfonium bromide (tPS-Br), the triphenyl sulfonium trifluoromethanesulfonate (tPS-OTf) and diphenyl (4-(phenylthio)phenyl) sulfonium trifluoromethanesulfonate (dPSPT-OTf). As the triphenyl sulfonium cation contain chromophores, the maximum of absorbance, λ_{max}, is nearly the same for the tPS-Br and the tPS-OTf as shown the Table 4-1. In the case of the dPSPT-OTf, there is a red-shift of the λ_{max} due to the presence of the phenylthio substituent that increases the conjugation pathway. The dPi-TS has a maximum of absorbance at 222 nm which is due to the diphenyl iodonium. In the same way, there is a red-shift of the λ_{max} due to the presence of the substituents on the aromatic rings.

b) Evaluation of the efficiency of the PAGs

The dPi-TS, dPi-PF_6, tPS-Br and tPS-OTf were tested in order to photocrosslink $G_{65}Hp_{35}$ layers using deep-UV irradiation. For this purpose, 2% wt. solutions of $G_{65}Hp_{35}$ were prepared in ethanol with different volume ratio of a 2% wt. PAG solution. The films were obtained by spin-coating at 2000 rpm the polymer/PAG solution on silicon substrate. The exposure of the TC to deep-UV irradiation was performed in the CEA-LTM facilities using a UV unit provided by Screen (the UV wavelength is 172 nm with a power of 20 $mW.cm^{-2}$). After exposure, a post-bake was performed at 90°C for 2 min to ensure the complete crosslinking of the films. The films were dipped in ethanol in order to remove the non-crosslinked fraction. To evaluate the efficiency of the crosslinking reaction, we have measured the insoluble fraction of the $G_{65}Hp_{35}$ films as a function of the PAG load using the thickness loss as indicator of the crosslinking efficiency.

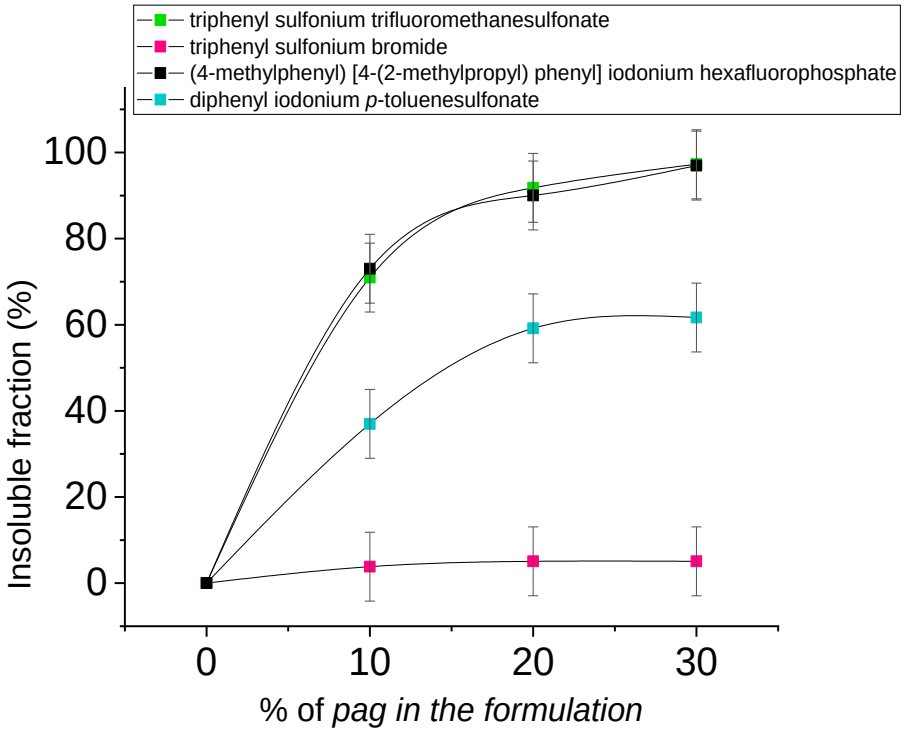

Figure 4-3: Insoluble fraction of the $G_{65}Hp_{35}$ formulated with different PAGs as a function of the PAG loading.

As shown in the Figure 4-3, different reaction kinetics were observed for the crosslinking of $G_{65}Hp_{35}$ layers depending on the PAG: the crosslinking is 2 times faster with the dPi-PF_6 and tPS-OTf than with the dPi-TS, while there is almost no reaction with the tPS-Br. Indeed, the kinetic of crosslinking is related to the nucleophilicity of the counter-anion. Weakly coordinating anions (WCA) are necessary to have a low nucleophilicity in order to reduce the ion-pairing decreasing the catalytic activity of the cations [3], [6]. To limit the nucleophilicity, the strategy is generally to shield the anion charge with phenyl groups or to surround it with poorly polarizable fluorine atoms. This is the reason why superacid-forming fluorinated anions such as hexafluorophosphate, tetrafluoroborate, hexafluoroarsenate, hexafluoroantimonate or triflate are classically used in PAG formulations. This explains the faster kinetics observed with dPi-PF_6 and tPS-OTf (Figure 4-3) [3], [7]. In the case of the tPS-Br, the negative charge is only located on the bromine atom leading to a much higher ion-pairing that completely inhibits the catalytic activity. Finally, in the case of the dPi-TS, the charge is delocalized over the oxygen which decreases the nucleophilicity of the anion explaining the intermediate kinetic profile.

Studying the reactivity of the PAGs enabled a first evalutation of the potential of theses different salts as efficient PAGs for the crosslinking of our TCs. At this stage, dPi-PF_6 and tPS-OTf are the best candidates allowing a fast crosslinking reaction of the film with a reasonable loading.

2. Crosslinking in UV-visible using a photosensitizer

It is also possible to use the PAGs in the visible range to crosslink the polymer using the principle of photosensitization. The photosensitization is based on sensitizing species that will interact with light in the visible region. Through a dominant electron transfer mechanism, the cationic photoinitiator will thus be able to initiate the crosslinking reaction without being directly excited (Figure 4-4) [3][5].

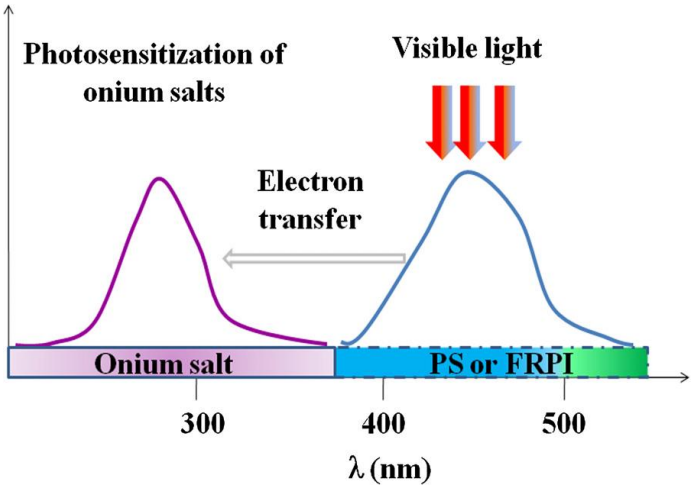

Figure 4-4: Principle of the photosensitization of conventional onium salts for their use in the visible range. PS and FRPI refers to photosensitizers and free radical photoinitiators, respectively [5].

The electron transfer process between the sensitizing species and the onium salts is the key step for the efficiency of photocrosslinking. The basic condition for the photosensitization depends on the thermodynamics of the photoinduced electron transfer reaction between the electron donating species (i.e. the sensitizing molecule) and the electron accepting species (i.e. the onium salt). The free energy of the reaction can be described by the Rehm-Weller equation:

$$\textbf{(eq. 4-1)} \quad \Delta G_{et} = F\left(E_{\frac{1}{2}}^{ox} - E_{\frac{1}{2}}^{red}\right) - E^{*} + C$$

where F is the Faraday constant, $E_{\frac{1}{2}}^{ox}$ and $E_{\frac{1}{2}}^{red}$ are the oxidation and reduction half-wave potentials, respectively, E^* the excitation energy of the sensitizing molecule and C a coulombic term often neglected. Consequently, the electron transfer reaction will be facilitated with onium salts having high reduction potential such as iodonium salts ($E_{\frac{1}{2}}^{red} = -0{,}2\ eV$) and sensitizing species having low oxidation potential such as anthracenes [3].

There are two main sensitizing species: photosensitizer (pS) and photoinitiator (pI). A pS absorbs the light energy to form excited species from which an electron transfer process occurs with the onium salt in order to give a pS-cation radical and an onium radical. The radical cation will then initiate the cationic ring-opening reaction by releasing a protonic acid through the hydrogen abstraction of a hydrogen donor specie (such as protic solvent or monomer) followed by coupling reactions (Figure 4-5)[5].

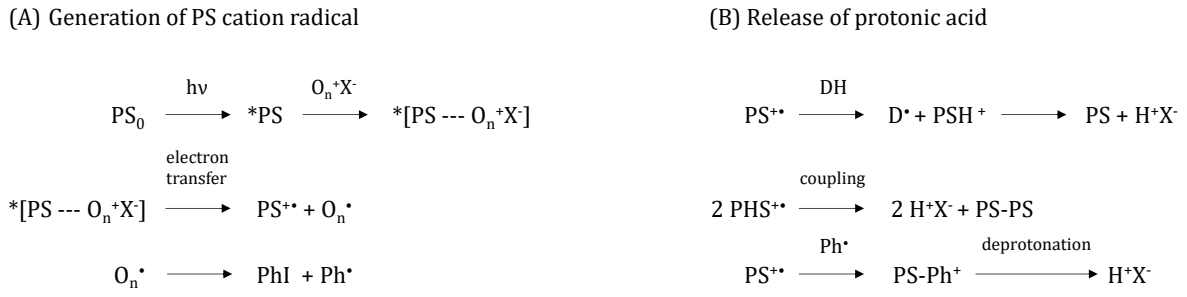

Figure 4-5: General photosensitization mechanism of onium salts using a photosensitizer. The mechanism involves two main steps: the generation of PS cation radical (step (A)) that will induce the release of the initiating protonic acid (step(B)). PS_0 refers to the non-excited state of the PS molecules while *PS refers to the excited state of the PS molecules. On^+X^- refers to the onium salt. DH refers to a hydrogen donor specie that can be a protic solvent or a monomer [5].

On the other hand, a pI undergoes unimolecular or bimolecular photochemical reactions to yield reactive species. Indeed, a type I pI undergoes unimolecular bond cleavage upon irradiation to produce two radical species. The majority of these radicals can then be oxidized directly or indirectly by onium salts leading to the formation of cationic initiating species. In the case of type II pIs, there is a bimolecular reaction upon irradiation that involves the exited state of the pI and

another molecule (generally a hydrogen donor molecule) in order to generate the radical species [5].

The typical type I pIs, i.e. 2,2-dimethoxy-2-phenylacetophenone (DMPAP) and diphenyl(2,4,6-trimethylbenzoyl) phosphine oxide (TPO), were selected for the photosensitization of the tPS-OTf PAG in $G_{65}Hp_{35}$ TC formulations (Figure 4-6). As example, Figure 4-7 shows the mechanism of the photoinduced cationic polymerization of vinyl ether monomer using a bi-component photoinitiating system with benzoin derivative as type I pI and an iodonium salt as PAG. Upon irradiation, there is a α-cleavage of the benzoin to generate hydroxybenzyl and benzoyl radicals that are electron donating and electron withdrawing, respectively. The radicals can then be oxidized by the iodonium salt leading to the corresponding cation initiating species of the polymerization [5]. In the same way, DMPAP and TPO can undergo a α-cleavage providing radicals that can be oxidized by tPS-OTf to generate the cation initiating species of the ring-opening of the epoxide of the GMA moieties.

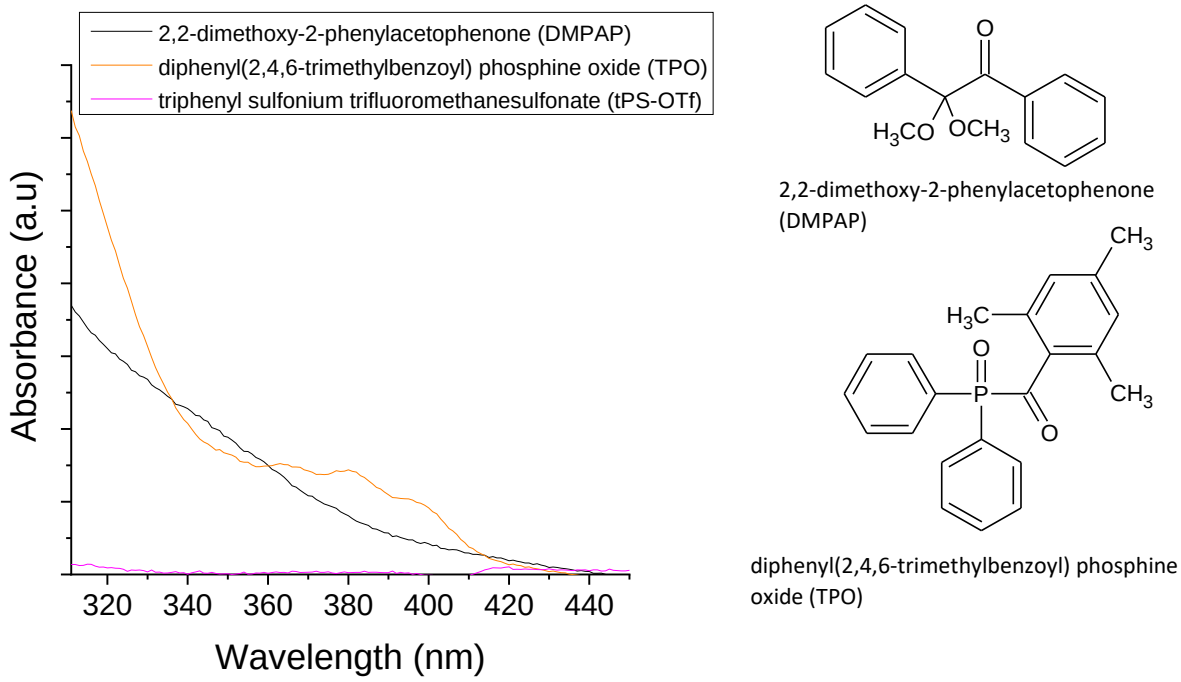

Figure 4-6: Absorption spectra of type I photoinitiators 2,2-dimethoxy-2-phenylacetophenone (DMPAP), diphenyl(2,4,6-trimethylbenzoyl) phosphine oxide (TPO) and triphenyl sulfonium trifluoromethanesulfonate (tPS-OTf) obtained from drop-cast films of 2% wt. solutions of each compound on quartz substrates.

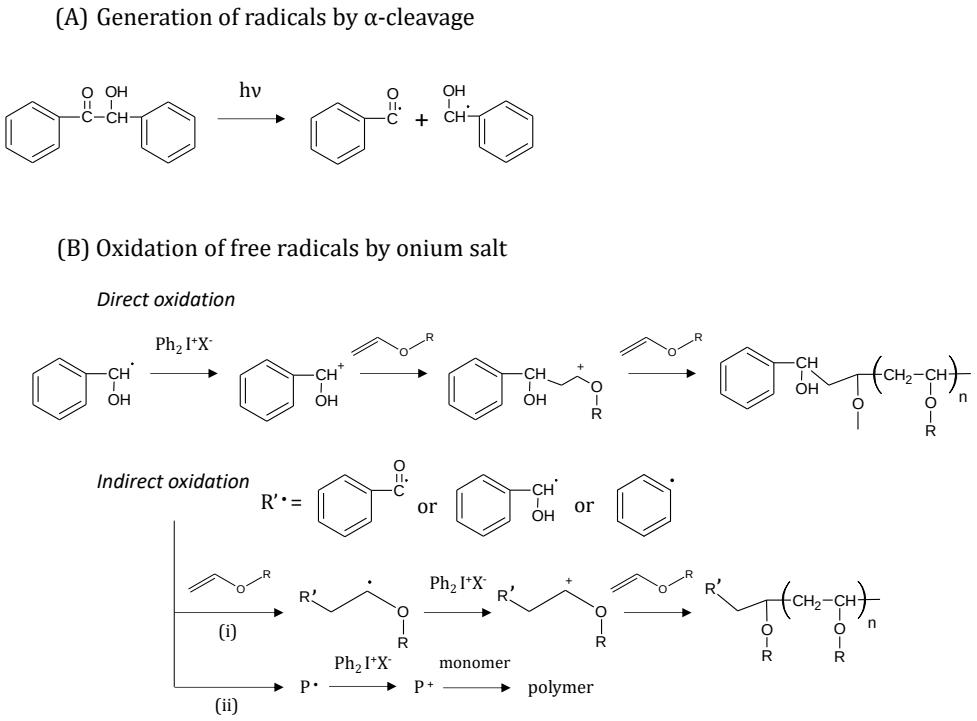

Figure 4-7 : Photosensitization mechanism of iodonium salts using benzoin inducing the polymerization of vinyl ether monomer. The mechanism involves two main steps: the generation of radicals upon irradiation (step (A)) that will be oxidized directly or indirectly by iodonium salts to form the cation initiating species of the polymerization (step(B)). When the radical is too difficult to oxidize by the onium salt, one can use another functional molecule (P). The radical will convert the P molecule into an electron-rich radical (P°) that can be further oxidized by the onium salt to form the corresponding cation initiating species of the polymerization [5].

Films of $G_{65}Hp_{35}$/tPS-OTf/pI were thus prepared to evaluate the crosslinking ability of the $G_{65}Hp_{35}$ in the visible range using the two-components photoinitiating system. For this purpose, 2% wt. solutions of tPS-OTf/pI (DMPAP or TPO) were prepared in ethanol with a molar ratio of 0.7 and added to a 2% wt. solution of $G_{65}Hp_{35}$ at different volume ratio. The solution was then spin-coated at 2000 rpm on silicon substrate and exposed to irradiation in the visible range for different irradiation times using a UVP 280 lamp provided by Eleco Panacol. The exposure was followed by a post-exposure bake at 90°C for 1 min. As shown in Figure 4-8, by increasing the photoinitating system loading, there is an increase of the photogenerated acids leading to an improvement of the crosslinking reaction of the $G_{65}Hp_{35}$ layer. It is thus possible to obtain a fully crosslinked film of $G_{65}Hp_{35}$ within 5 minutes with a volume ratio of 9:1 using tPS-OTf/DMPAP and tPS-OTf/TPO as photoinitiating system.

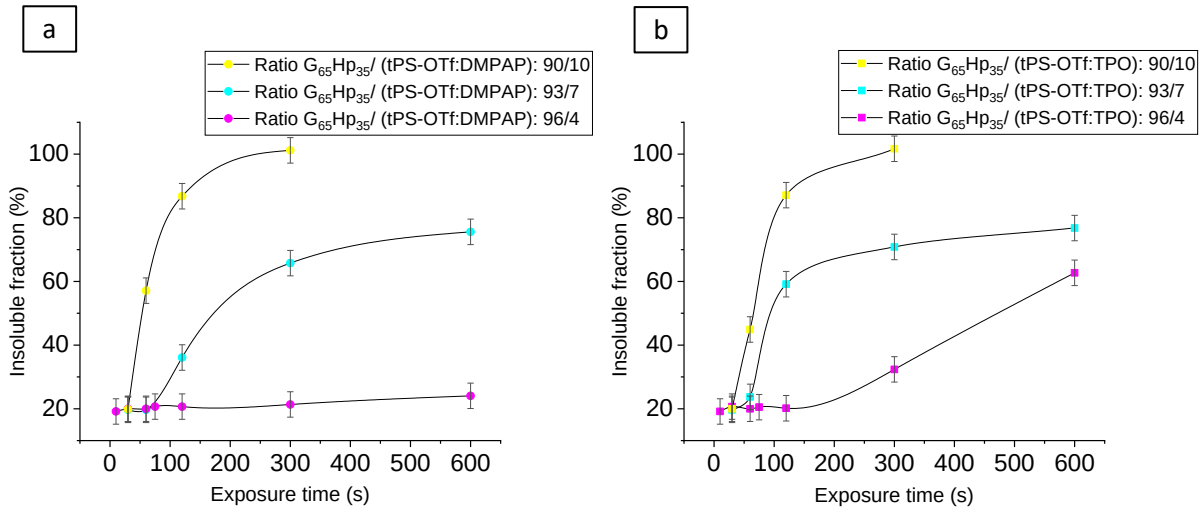

Figure 4-8: Insoluble fractions of the $G_{65}Hp_{35}$ formulated with the tPS-OTf as PAG and (a) DMPAP or (b) TPO as type I pI. The pI system (tPS-OTf/pI) content was varied from 4% to 10% while keeping the molar ratio of tPS-OTf/pI constant in order to evaluate the effect of the pI system loading on the crosslinking kinetics.

To further decrease the exposure time without increasing too much the pI system loading, we investigated the effect of the tPS-OTf/pI molar ratio on the crosslinking kinetics. Several molar ratios of tPS-OTf and pI were prepared using 2% wt. solutions and added to a 2% wt. solution of $G_{65}Hp_{35}$ with a volume ratio of 9:1. As shown in the Figure 4-9, there is an increase of the crosslinking rate with the increase of the tPS-OTf/pI molar ratio. It means that the decrease of pI loading results in an improvement of the crosslinking kinetics. Indeed, the increase in DMPAP or TPO molar loadings results in the formation of more initiating radial species that can favour termination reactions [3]. By plotting the insoluble fraction of the $G_{65}Hp_{35}$ as a function of the tPS-OTf/pI molar ratio, one can see that the insoluble fraction reaches a plateau from 0.7 tPS-OTf/pI molar ratio (Figure 4-9(c)). The value of the plateau is nearly the same for both pI at a given exposure time with 90% of insoluble fraction for 2 min exposure and 100% of insoluble fraction for 5 min exposure. The value of the plateau is increasing with the exposure time as a higher photoacid concentration is generated.

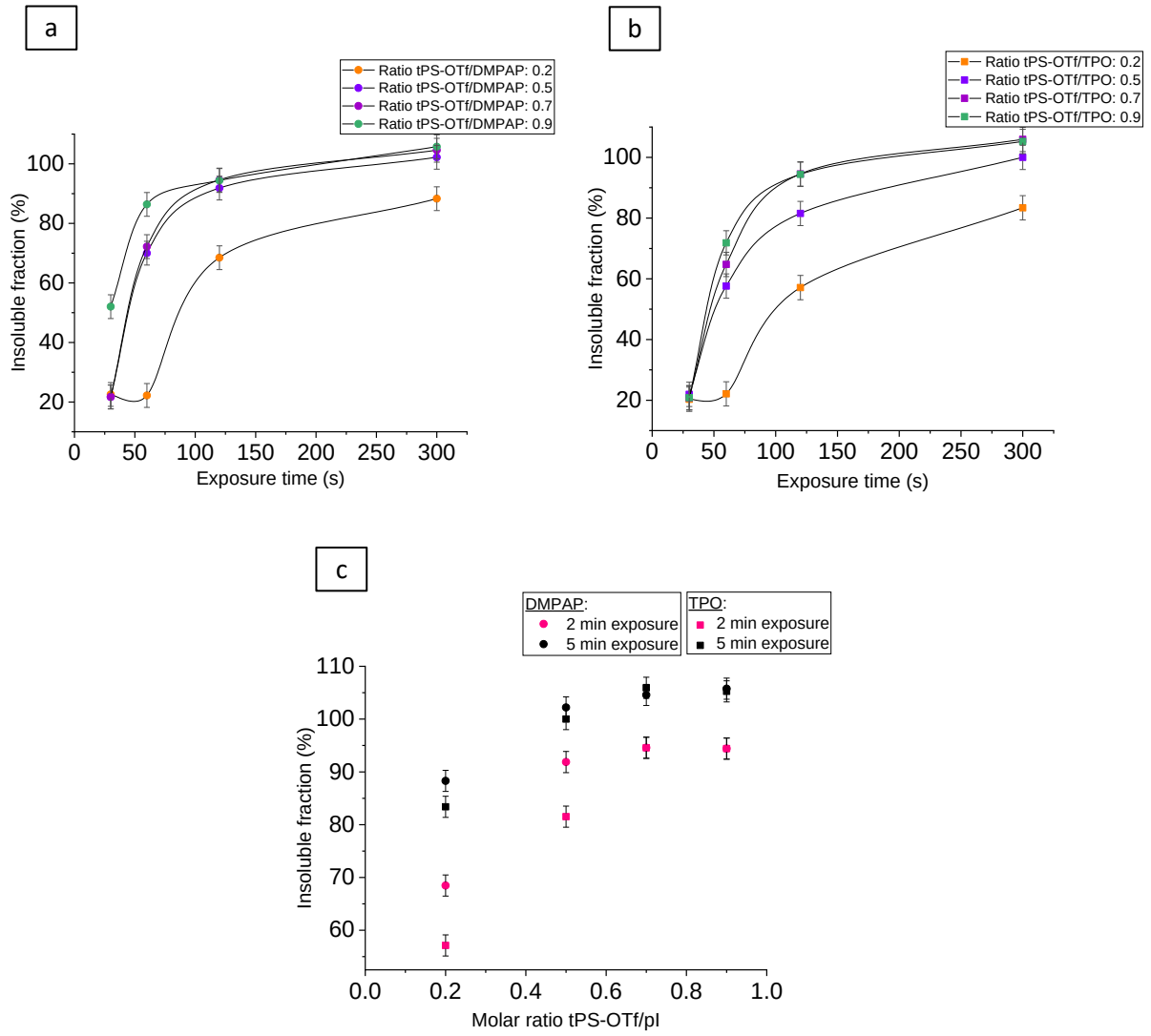

Figure 4-9: **Insoluble fractions of the $G_{65}Hp_{35}$ formulated with the tPS-OTf as PAG and (a) DMPAP or (b) TPO as type I pIs. The tPS-OTf/pI molar ratio was varied from 0.2 to 0.9 while keeping the overall tPS-OTf/pI loading constant to evaluate the effect of the tPS-OTf/pI molar ratio on the crosslinking kinetics. (c) is the insoluble fraction of the $G_{65}Hp_{35}$ formulated with tPS-OTf and DMPAP or TPO as a function of the tPS-OTf/pI molar ratio to compare both pIs.**

One can also note that the photosensitization also worked for (4-methylphenyl) [4-(2 methylpropyl) phenyl] iodonium hexafluorophosphate (dPi-PF_6) using the DMPAP and TPO while it did not lead to conclusive results for the diphenyl iodonium p-toluenesulfonate (dPi-TS) which is consistent with the observations deduced from Figure 4-3.

3. Crosslinking in UV-visible range using a structurally modified PAG

The last strategy that has been employed to UV-crosslink the polymer was the use of a structurally modified PAG: diphenyl(4-(phenylthio)phenyl) sulfonium trifluoromethanesulfonate (dPSPT-OTf). Indeed, owing to the phenylthiol substituent, there is an increase of the conjugation pathway of the triphenyl sulfonium cation which allows to extend the absorption of the PAG in the visible range.

Several films of $G_{65}Hp_{35}$/dPSPT-OTf were prepared to evaluate the crosslinking ability of the $G_{65}Hp_{35}$ in the visible range using this particular PAG. For this purpose, 2% wt. solution of dPSPT-OTf was prepared in ethanol and added to a 2% wt. solution of $G_{65}Hp_{35}$ with a volume ratio of 9:1. The solution was then spin-coated at 2000 rpm onto silicon substrate and exposed in the visible range for different irradiation times. The exposure was followed by a post-exposure bake at 90°C for 1 min. The films were then rinsed in ethanol to remove the non-crosslinked part. As shown in Figure 4-10, it is possible to obtain a fully crosslinked film of $G_{65}Hp_{35}$ within 2 minutes with a volume ratio of 9:1 underlining the efficiency of such structurally modified PAG.

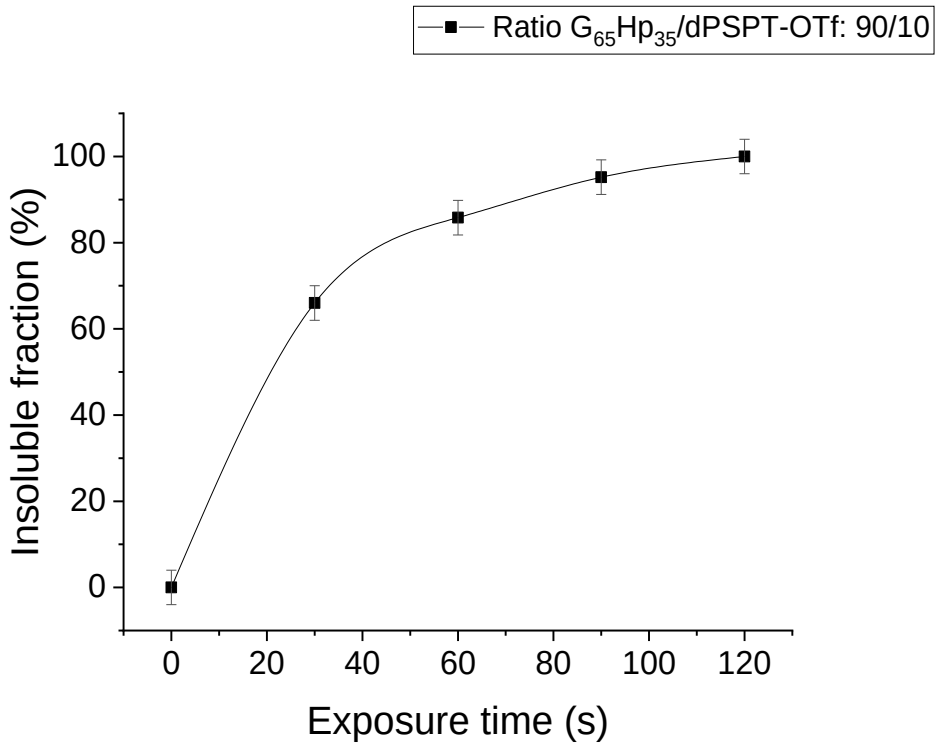

Figure 4-10: Insoluble fraction of the $G_{65}Hp_{35}$ formulated with dPSPT-OTf as a function of exposure time.

In summary, three strategies have been presented in order to photocrosslink our TC materials. Conventional PAGs have been used to photocrosslink the TCs using deep-UV. The crosslinking rate was found to be strongly related to the structure of the PAG, especially depending of the structure of the anion that is responsible for the salt reactivity. On the other hand, the polymer can also be crosslinked in the visible range using a structurally modified PAG or *via* a sensitizing molecule. In the latter case, it was shown that the crosslinking efficiency was determined by the termination reactions induced by the radical species of the sensitizing molecule. By optimizing the composition of the photoinitiating system, it was thus possible to reach a fully-crosslinked film in 2 min.

III. Top-coat patterning under deep-UV irradiation

1. Patterning of the TC under deep-UV irradiation on silicon substrate

In the previous section, we have demonstrated the crosslinking ability of the TCs under deep-UV irradiation using the dPi-TS, dPi-PF_6 and tPS-OTf. Consequently, the self-assembly of the $PDMSB_{120}$-*b*-PS_{143} was performed using the three TC/PAG formulations in order to evaluate the effect of the PAG on the TC surface energy, and subsequently on the BCP self-assembly behaviour. For this purpose, $G_{65}Hp_{35}$ was chosen as the reference TC material for the self-assembly of the lamellar $PDMSB_{120}$-*b*-PS_{143}: as the material is non-neutral for the BCP, in-plane lamellae are expected as seen in Chapter 3.

2% wt. solutions of $G_{65}Hp_{35}$ were formulated with the dPi-TS, dPi-PF_6 and tPS-OTf (2% wt. in ethanol) with a volume ratio of 9:1 for the dPi-PF_6, 9:1 for the tPS-OTf and 8:2 for the dPi-TS according to the results of the Figure 4-3. The thickness of the $PDMSB_{120}$-*b*-PS_{143} was fixed at 35 nm ($\sim 2L_0$) using 1% wt. solution in methyl isobutyl ketone spin-coated at 2000 rpm for 30 sec. As the BCP thickness is low, the structure will also be strongly affected by the surface energy of the substrate. Consequently, thermally-crosslinked $G_{27}M_{47}He_{26}$, $G_{25}M_{37.5}He_{37.5}$, $G_{20}M_{24}He_{56}$ and $G_{65}Hp_{35}$ were used as ULs to vary the surface energy of the substrate and evaluate its effect on the orientation of the self-assembled structure. The UL/ATMS solutions (2% wt. solution of the polymer in a mixture of ethanol and 1-methoxy-2-propanol (9:1) with 2% wt. solution of ATMS in ethanol (9:1)) were thus spin-coated on silicon substrates and crosslinked at 240°C for 2 min. The $PDMSB_{120}$-*b*-PS_{143} was spin-coated on top of the ULs which was followed by the spin-coating of the different $G_{65}Hp_{35}$/PAG TCs. The TCs were irradiated at 172 nm for 1 sec and baked at 90°C for 2 min. Finally, the BCP was thermally-annealed at 240°C for 5 min. The TCs were then etched with an Ar/O_2 plasma (10 mTorr, 80 sccm of Ar, 40 sccm of O_2 and source power: 200 W - bias power: 20 W) for 10 s using a decoupled plasma source (DPS).

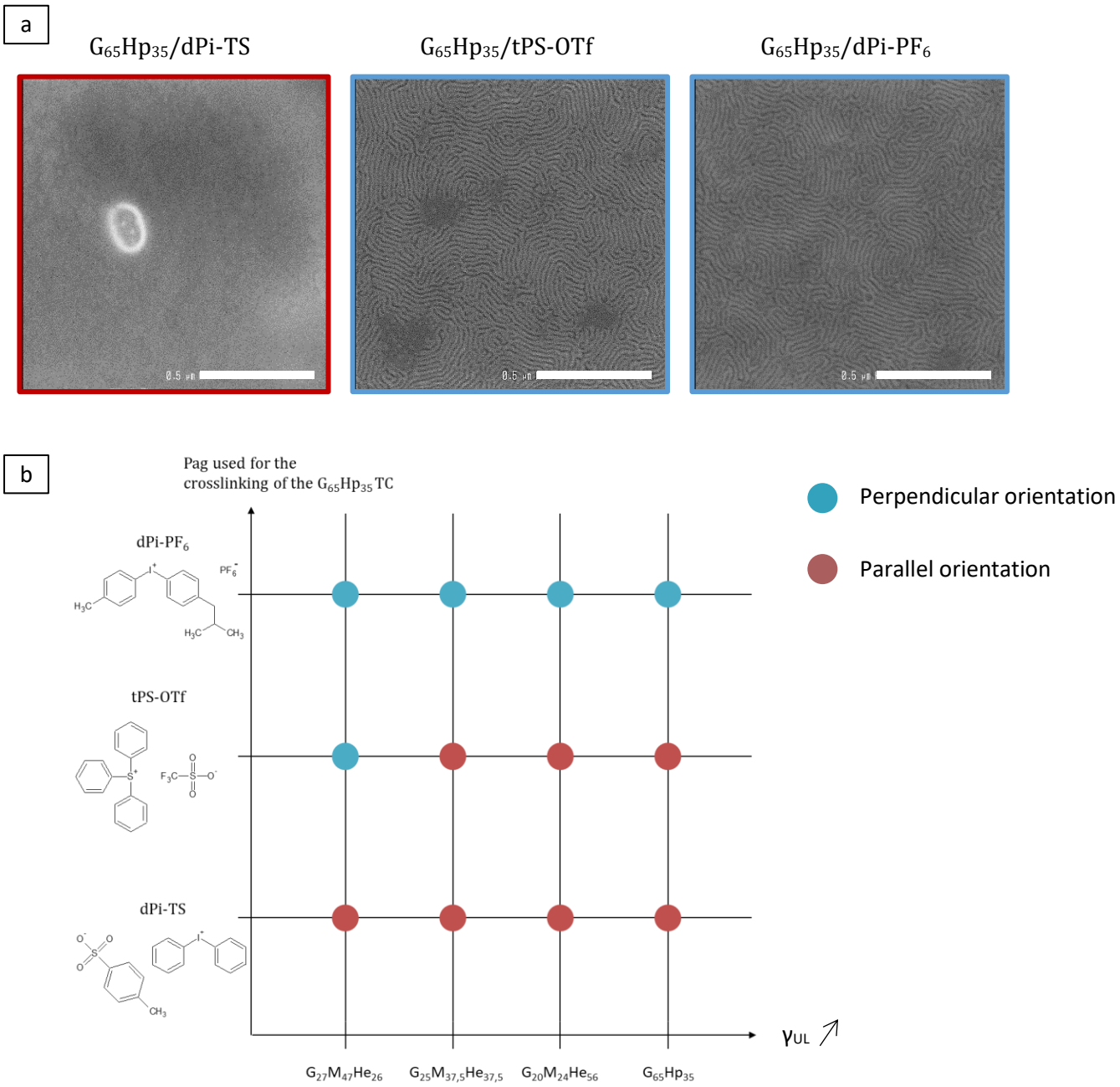

Figure 4-11: Effect of the PAG chemistries on the surface energy of the $G_{65}Hp_{35}$ TC. (a) are the SEM images of the lamellar-forming $PDMSB_{120}$-*b*-PS_{143} using the three $G_{65}Hp_{35}$/PAG TCs and the $G_{27}M_{47}He_{26}$/ATMS as UL. (b) summarizes the different $PDMSB_{120}$-*b*-PS_{143} orientations that have been observed by SEM as a function of the PAG used to crosslink the TC. The self-assembly of the $PDMSB_{120}$-*b*-PS_{143} was performed on ULs having different surface energies. The ULs were crosslinked with the ATMS thermal crosslinking agent. The blue and red circles refer to out-of-plane and in-plane orientations, respectively. Scale bars: 500 nm.

The Figure 4-11 summarizes the different orientations of the $PDMSB_{120}$-*b*-PS_{143} observed by SEM after the removal of the TCs. Although the initial surface energy of the $G_{65}Hp_{35}$ was out of the neutrality range, out-of-plane lamellae were observed when using the dPi-PF_6 as PAG regardless of the ULs. In the case of the tPS-OTf PAG, out-of-plane orientation was only observed when the $G_{27}M_{47}He_{26}$ was used as ULs. Finally, in-plane lamellae were observed when using the dPi-TS as

PAG regardless of the UL. Looking at the PAG structures, the only main difference is the anion. Indeed, the hexafluorophosphate anion of the dPi-PF_6 contains 6 fluorine atoms which could be responsible for the decrease of the surface energy of the $G_{65}Hp_{35}$ film shifting this particular TC towards the BCP neutrality window. As the trifluoromethanesulfonate anion of the tPS-OTf contains only 3 fluorine atoms, it can be assumed that there is a slight decrease of the surface energy which is not enough to obtain out-of-plane lamellae for most of the ULs. In the case of the dPi-TS, as there is no fluorine atoms on the anion, there is not a strong evolution of the surface energy of the $G_{65}Hp_{35}$ film leading to in-plane orientation of the lamellae regardless of the ULs.

One can also note that out-of-plane lamellae were observed using the $G_{65}Hp_{35}$/tPS-OTf as TC and $G_{27}M_{47}He_{26}$/ATMS as UL which means that the "orientational field" induced by the neutrality of the UL can be sufficient to drive the out-of-plane orientation of the lamellae through the thickness of the film. On the other hand, out-of-plane lamellae were observed with the $G_{65}Hp_{35}$/dPi-PF_6 regardless the surface energy of the UL. Consequently, it could also mean that the neutrality of the TC is sufficient to drive the perpendicular orientation through the film even with a non-neutral UL.

Studying the impact of the PAGs on the polymer surface energy together with the study of their reactivity (section I.1.b)) led us to highlight two main criteria for the evaluation of the salts as pertinent PAGs for the patterning of our polymers. Indeed, the PAG should allow the crosslinking of the polymers with a low loading and within a short exposure time to be viable at industrial scale. Consequently, only dPi-PF_6 and tPS-OTf can be considered. Moreover, the PAG should have minimum impact on the surface energy of the polymer in order to have further control of the interfacial energy between the crosslinked layer and the BCP. This is the key reason why the tPS-OTf was chosen as PAG for the patterning of the TC on top of the BCP thin film.

2. Top-coat patterning under deep-UV irradiation on top of BCP thin films

By combining the neutrality with the patternability of the TCs, it is possible to control the orientation of the BCP structure at specific locations of the film. For this purpose, 1% wt. solution of $PDMSB_{120}$-*b*-PS_{143} was prepared in methyl isobutyl ketone. On the other hand, the neutral TC was prepared using 2% wt. solution of $G_{25}M_{37.5}He_{37.5}$ in a mixture of ethanol and 1-methoxy-2-propanol (9:1) mixed with 2% wt. solution of tPS-OTf in ethanol (9:1). In order to neutralize the surface energy of the substrate, the PMHA was grafted onto the silicon substrate. For this purpose, a 2% wt. solution of the polymer was prepared in methyl isobutyl ketone and spin-coated (700 rpm – 1 min) on silicon substrates. Thermal treatment was then performed at 200°C for 75 s to promote the grafting of the polymer chains. The film was subsequently rinsed with methyl isobutyl ketone to remove the excess of non-grafted polymer chains. Finally, the BCP was spin-coated (2000 rpm – 30 sec) followed by the spin-coating of the $G_{25}M_{37.5}He_{37.5}$/tPS-OTf TC formulation.

To selectively UV-crosslinked the neutral TC, a part of the film was covered by a portion of silicon substrate in order to mask the covered parts from deep-UV irradiation while exposing the non-covered parts as shown in Figure 4-12 (see steps 2 and 3). After performing a post-exposure bake at 90°C for 3 min, the film was rinsed in ethanol in order to remove the non-crosslinked parts. To avoid the dewetting of the $PDMSB_{120}$-*b*-PS_{143} film that is not covered by the neutral TC, the non-neutral $G_{65}Hp_{35}$/tPS-OTf formulation was spin-coated and UV-crosslinked (1 sec at 172 nm – 90°C for 2 min) before performing the thermal annealing of the BCP.

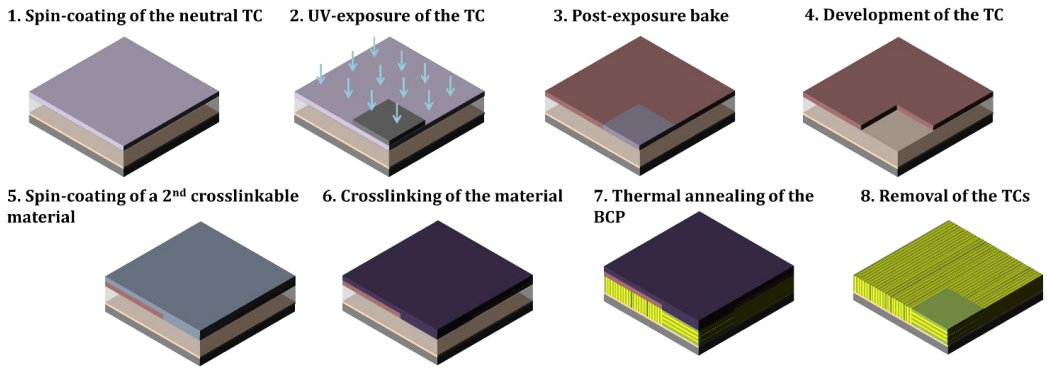

Figure 4-12: Scheme of the process in order to achieve out-of-plane lamellae using a neutral TC patterned at 172 nm.

Figure 4-13 shows the SEM characterization of the PDMSB$_{120}$-*b*-PS$_{143}$ after the removal of the two crosslinked TCs (neutral G$_{25}$M$_{37.5}$He$_{37.5}$/tPS-OTf and non-neutral G$_{65}$Hp$_{35}$/tPS-OTf) using an Ar/O$_2$ plasma (10 mTorr, 80 sccm of Ar, 40 sccm of O$_2$ and source power: 200 W- bias power: 20 W) for 20 s. As shown in Figure 4-13(a), the PDMSB$_{120}$-*b*-PS$_{143}$ exhibits a mixed orientation in the area previously covered by the non-neutral material (G$_{65}$Hp$_{35}$/tPS-OTf) while fully oriented out-of-plane lamellae are obtained in the area that was covered by the neutral TC (G$_{25}$M$_{37.5}$He$_{37.5}$/tPS-OTf) (see Figure 4-13(b)).

To confirm the orientation of the PDMSB$_{120}$-*b*-PS$_{143}$ of the Figure 4-13(a), a blank test was performed on a simple stack of UL/PDMSB$_{120}$-*b*-PS$_{143}$/[G$_{65}$Hp$_{35}$/tPS-OTf] following the same procedure:

i. grafting of the UL at 200°C for 75 s followed by a rinsing step,
ii. spin-coating of the PDMSB$_{120}$-*b*-PS$_{143}$ film at 2000 rpm,
iii. spin-coating of the G$_{65}$Hp$_{35}$/tPS-OTf at 2000 rpm,
iv. exposure at 172 nm for 1 s followed by a post-exposure bake at 90°C for 2 min,
v. and thermal annealing of the BCP at 240°C for 5 min.

As shown on the FIB-STEM image presented in Figure 4-14), a flat film is obtained with parallel lamellae. We can thus conclude that the small number of domains with out-of-plane lamellae observed in Figure 4-13(a) do not propagate into the thickness of the BCP film.

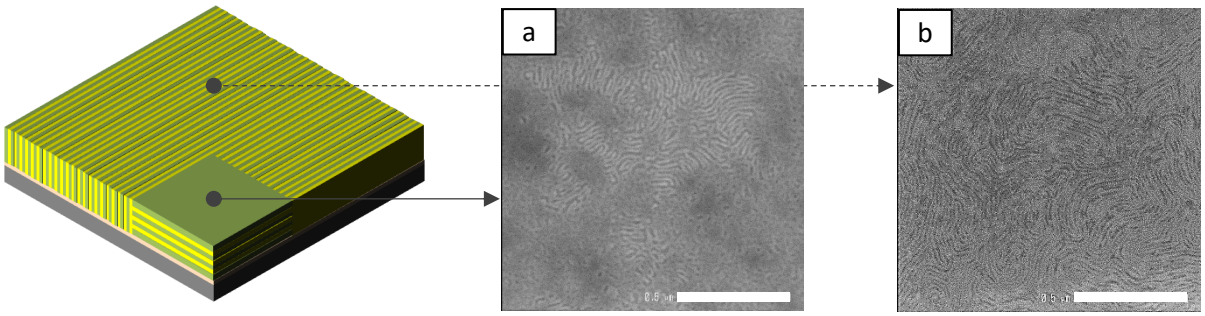

Figure 4-13: SEM images of the PDMSB$_{120}$-*b*-PS$_{143}$ after the removal of the patterned TC in (a) the non-neutral area and in (b) the neutral area as illustrated by the scheme. Scale bar: 500 nm.

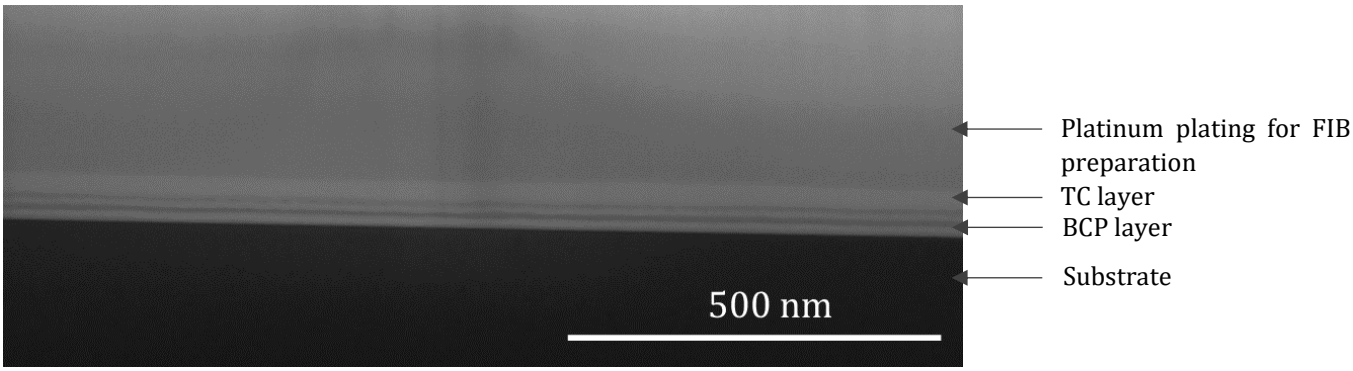

Figure 4-14: FIB-STEM image of the lamellar-forming PDMSB$_{120}$-*b*-PS$_{143}$ using the non-neutral TC: G$_{65}$Hp$_{35}$/tPS-OTf. An in-plane orientation of the lamellae is retrieved using this particular TC composition.

IV. Top-coat patterning under UV-visible irradiation

1. Mask aligner as tool for selective exposure

To selectively pattern the TC in the UV-visible range, a mask aligner was used. A mask aligner is an instrument enabling the selective exposure of the photoresist through a mask with a precise alignment of the mask and the resist. Figure 4-15 shows the standard principle of the machine. The source is generally a mercury lamp that is emitting UV light. An ellipsoidal reflector is used to collect the light while an optical system allows to collimate, redistribute, homogenize and send the light through the mask [8].

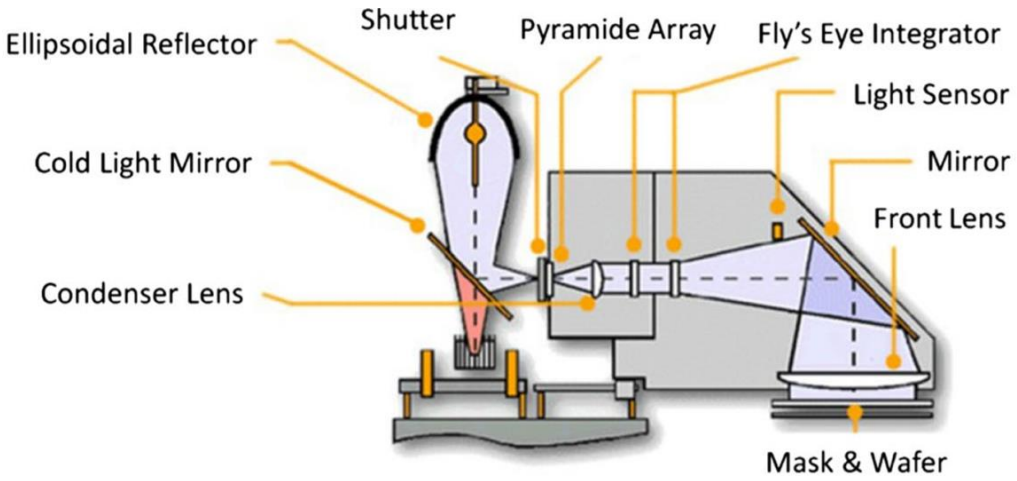

Figure 4-15: Scheme of the general principle of a mask aligner.

In this work, two mask aligners were used. The MJB4® mask aligner (SUSS MicroTec) was used at the CEA-LTM facilities while the EVG6200® mask aligner (EV Group) was used in the ELORPrintTec facility (Figure 4-16 (a) and (b), respectively). The light intensity of the mercury lamp of the MJB4® mask aligner was measured to be 15 $mW.cm^{-2}$ at 365 nm while the one of the EVG6200® mask aligner was measured to be 10.4 $mW.cm^{-2}$ at the same wavelength.

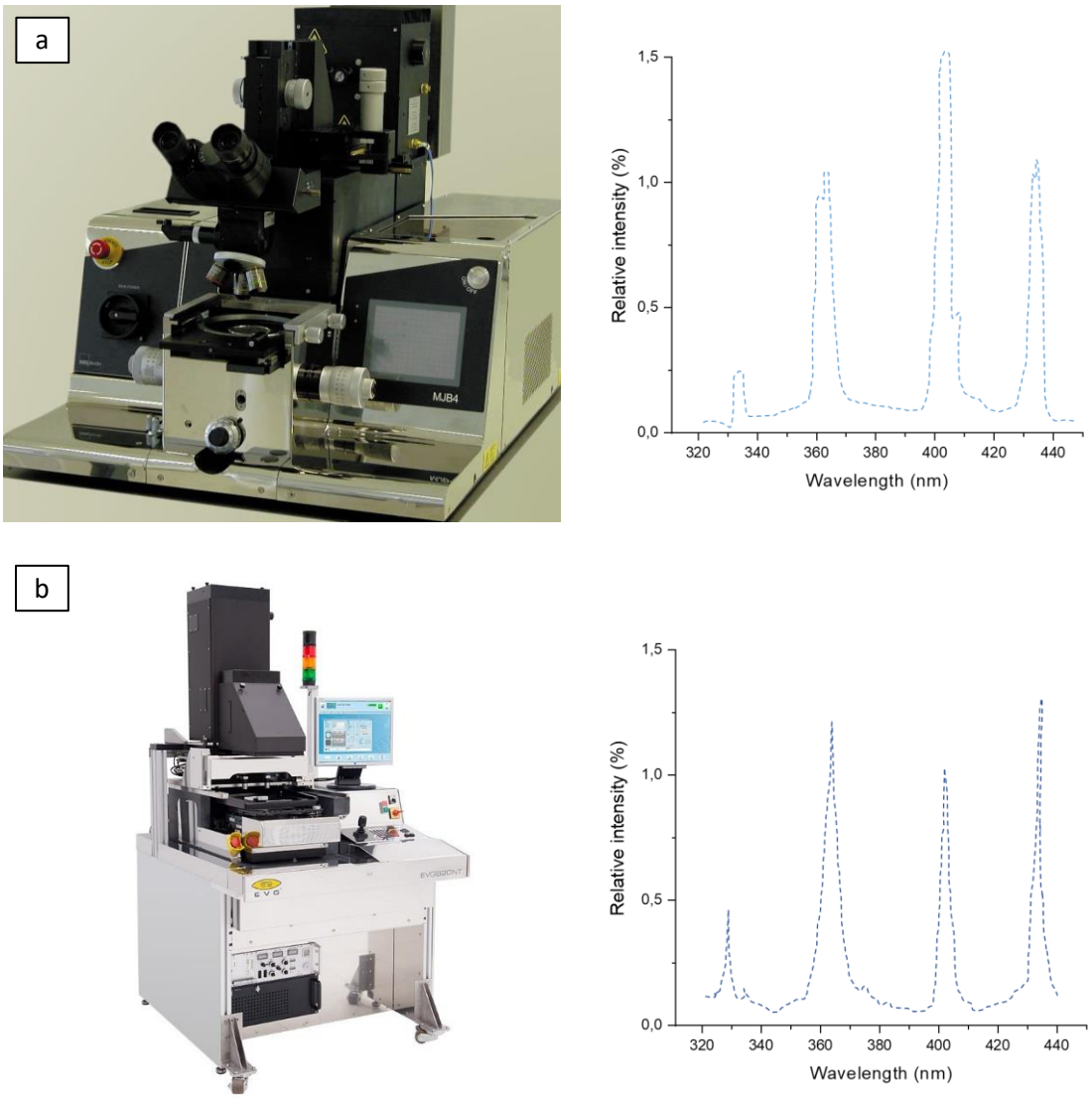

Figure 4-16: Pictures of the (a) MJB4® and (b) EVG6200® mask aligners and the emission spectra of their respective mercury lamps. Pictures and emission spectra are extracted from SUSS MicroTec and EV Group websites.

2. Patterning of the TC in UV-visible using a photosensitizer

Before performing the patterning of the TCs using the mask aligner, we initially checked the crosslinking kinetic in flood exposure (i.e. exposure of the resist to blanket radiation (all over) with no pattern). According to the optimization process performed on the photoinitiating system (see Section II.2), 2% wt. solutions of tPS-OTf/DMPAP were prepared in ethanol with a molar ratio of 0.9 and added to a 2% wt. solution of $G_{65}Hp_{35}$ with a volume ratio of 9:1. The solution was then spin-coated at 2000 rpm on silicon substrate and exposed with the MJB4® in flood exposure mode

for different irradiation times. The exposure was followed by a post-exposure bake at 90°C for 1 min.

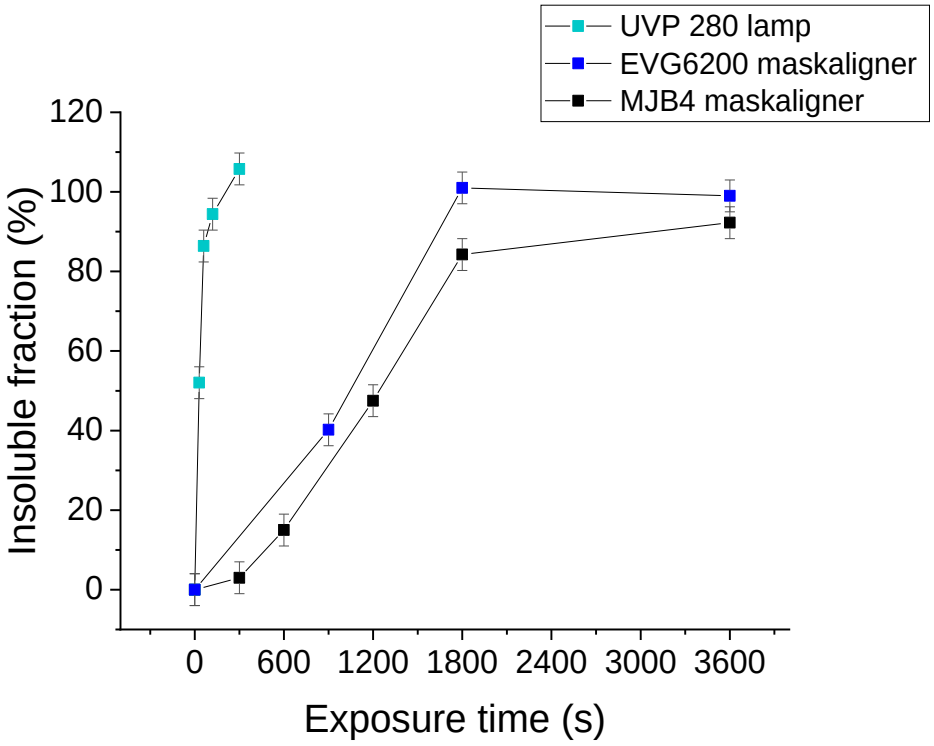

Figure 4-17: Insoluble fractions of the $G_{65}Hp_{35}$ formulated with bi-component photoinitiating system tPS-OTf/DMPAP as a function of exposure time and comparison of the crosslinking kinetics depending on the lamp.

As shown in the Figure 4-17, the crosslinking kinetics is drastically slowed down when using a mask aligner. Indeed, 30 min are necessary to achieve a complete crosslinking of the film while only 2 min was needed using the UVP 280 lamp. The same rate of crosslinking was found using the EVG6200® mask aligner as shown in the Figure 4-17.

To increase the efficiency of the crosslinking reaction and thus decrease the exposure time, post-exposure bake (PEB) optimization was performed. Indeed, the PEB is a crucial step in the crosslinking process as it allows an acceleration of the crosslinking reaction. Generally, the PEB temperature range is 80-100°C to promote the diffusion of the photoacid as well as to ensure the mobility of polymer chains improving thus the crosslinking rate [9]. Consequently, films of $G_{65}Hp_{35}$/tPS-OTf/DMPAP were prepared, exposed for 15 min using the EVG6200® and baked following different post-exposure conditions. The objective was to find the set of PEB parameters {temperature, time} allowing a complete crosslinking of the $G_{65}Hp_{35}$ films in 15 min exposure. As

shown in the Figure 4-18, an increase of the PEB temperature and time allows the achievement of a complete crosslinking of the $G_{65}Hp_{35}$ film within the 15 min exposure.

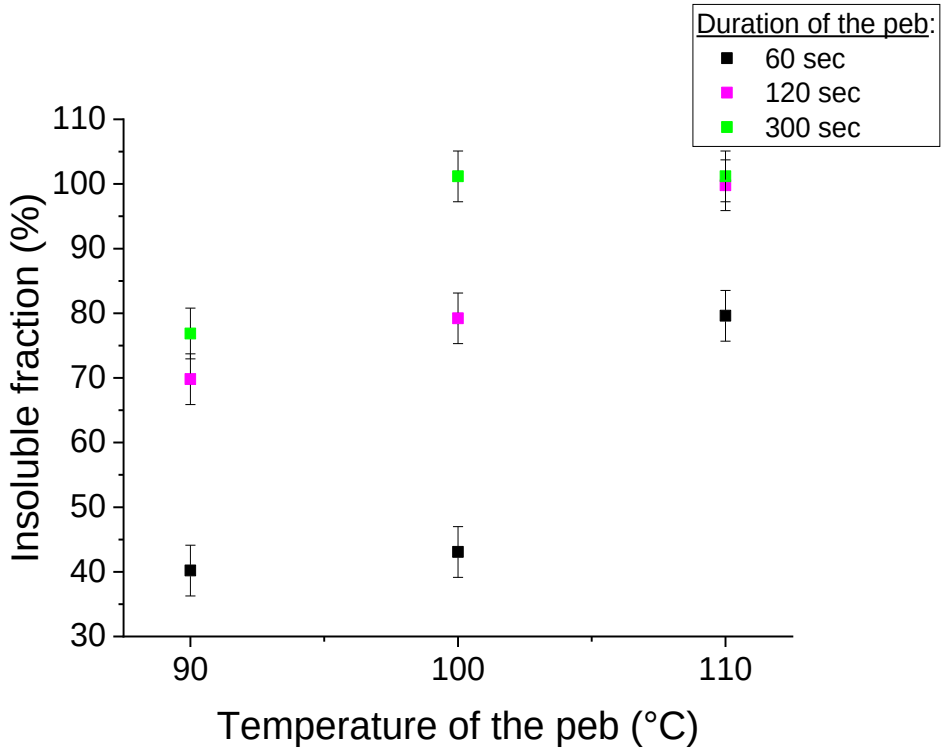

Figure 4-18: Insoluble fraction of the $G_{65}Hp_{35}$ formulated with the tPS-OTf/DMPAP after 15 min exposure as a function of the PEB temperature. PEB was performed for 60 s, 120 s and 300 s to evaluate the effect of the PEB duration on the crosslinking efficiency.

The patterning of $G_{65}Hp_{35}$ layers was performed with the EVG6200® mask aligner following the three sets of parameters giving the best results in flood exposure mode [{100°C-5min};{110°C-2min};{110°C-5min}] to compare the profile of the patterned lines. For this purpose, the films were exposed for 15 min through a mask with 50 µm-width lines and baked under the different predefined conditions. The films were then developed by dipping the films in ethanol and dried with compressed air. The quality of the patterns was characterized by profilometry and compared to the patterns that were obtained with the reference procedure (15 min exposure followed by a post-exposure bake at 90°C for 1 min). Figure 4-19 shows the height profile of the resulting lines obtained after exposure and baking under the different conditions while Figure 4-20 shows the characteristic dimensions of the lines (height and width) with respect to the initial mask and film thickness. The height was taken at the central part of the line while the

value of the width was determined as a mean value of the bottom, middle and top of the line. These measurements were performed on three to five lines to ensure good reproducibility.

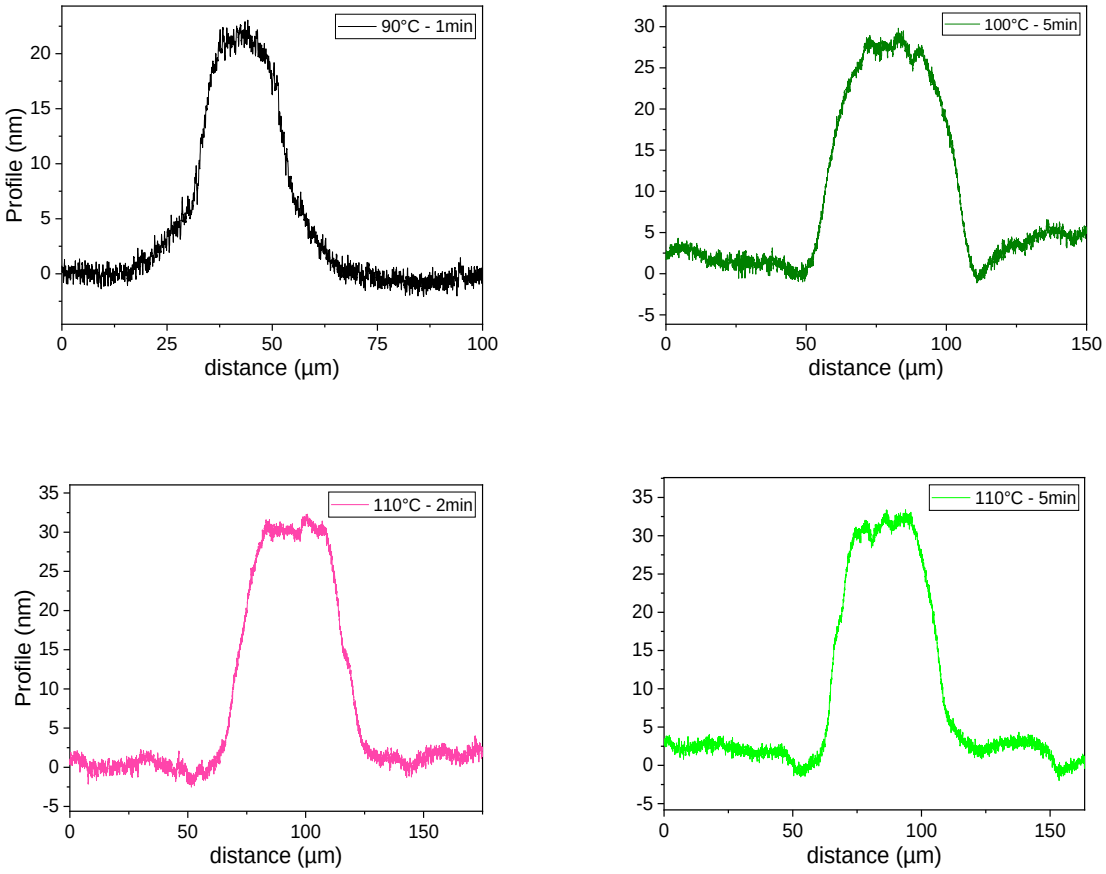

Figure 4-19: **Profiles of the lines obtained after the patterning of the $G_{65}Hp_{35}$ under different baking conditions.**

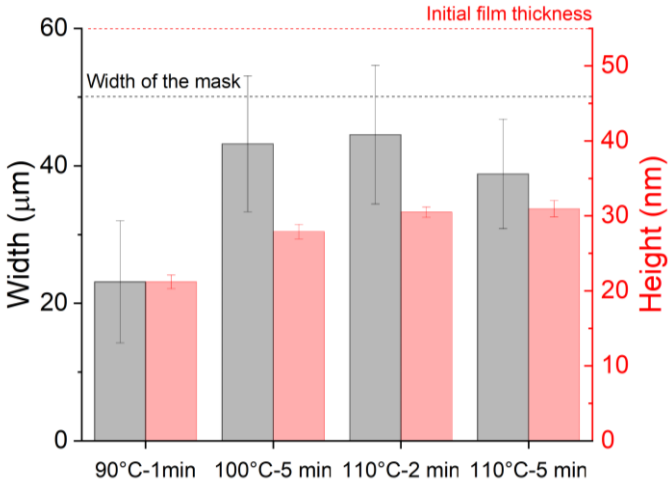

Figure 4-20: **Characteristic dimensions (height and width) of the profile of the lines obtained after the patterning of the $G_{65}Hp_{35}$ exposed during 15 min and baked under different conditions.**

First, a thickness loss between 40% and 60% was observed when passing from flood exposure mode to the patterning mode. This thickness loss is reduced as the post-exposure bake temperature increases which is consistent with an enhancement of the photoacid diffusion improving the crosslinking efficiency. Moreover, one can also notice a poor development of the lines when long PEB (5 min) are applied (see in the Figure 4-19). It can be explained by a diffusion of the photoacid into the non-exposed areas leading to a blurring of the original mask pattern.

We can thus conclude that is it possible to pattern $G_{65}Hp_{35}$ films using the bi-component photoinitiating system. An optimization of the PEB conditions allowed an increase of the crosslinking efficiency leading to the well-defined lines of the $G_{65}Hp_{35}$ films after 15 min exposure. Indeed, performing a fast baking at high temperature {110°C-2min} improves the diffusion of the photoacid in the exposed part (by reducing the thickness loss) while avoiding its lateral diffusion in the non-exposed parts (by limiting a blurring of the original mask pattern). However, the exposure time remains very long (15 min) which is a critical issue for industrial considerations. Further increase of the baking temperature above 110°C was considered but did not result in a significant decrease of the exposure time. Besides higher temperature treatment could induce a dewetting of the BCP film when performing the TC patterning on top of it during the full process (Figure 4-1) and, consequently, should be avoided. We tentatively linked the low crosslinking efficiency to the small reduction potential of the sulfonium salt ($E_{\frac{1}{2}}^{red} = -1{,}2\ eV$), rendering the sensitization process difficult [5]. The use of the corresponding iodonium salt could be a way to improve the electron transfer reaction and thus the crosslinking efficiency.

3. Top-coat patterning upon UV-visible exposure using a structurally modified PAG

a) Patterning of the TC on silicon substrates

Following the same strategy, a study of the crosslinking kinetic of the $G_{65}Hp_{35}$ was performed in flood exposure using the dPSPT-OTf prior to the patterning. For this purpose, 2% wt. solution of dPSPT-OTf was prepared in ethanol and added to a 2% wt. solution of $G_{65}Hp_{35}$ with a volume ratio of 9:1. The solution was then spin-coated at 2000 rpm on silicon substrates and exposed with the EVG6200® mask aligner for different irradiation times. The exposure was followed by a PEB at 90°C for 1 min. The films were then rinsed in ethanol to remove the non-crosslinked part. As shown the Figure 4-21(a), the crosslinking kinetic is comparable with the one obtained with the previous UVP 280 lamp as 2 min is sufficient to obtain a fully crosslinked film. By increasing the PEB duration, it is even possible to divide by two the exposure time that is necessary to reach 100% of insoluble fraction as shown the Figure 4-21(b).

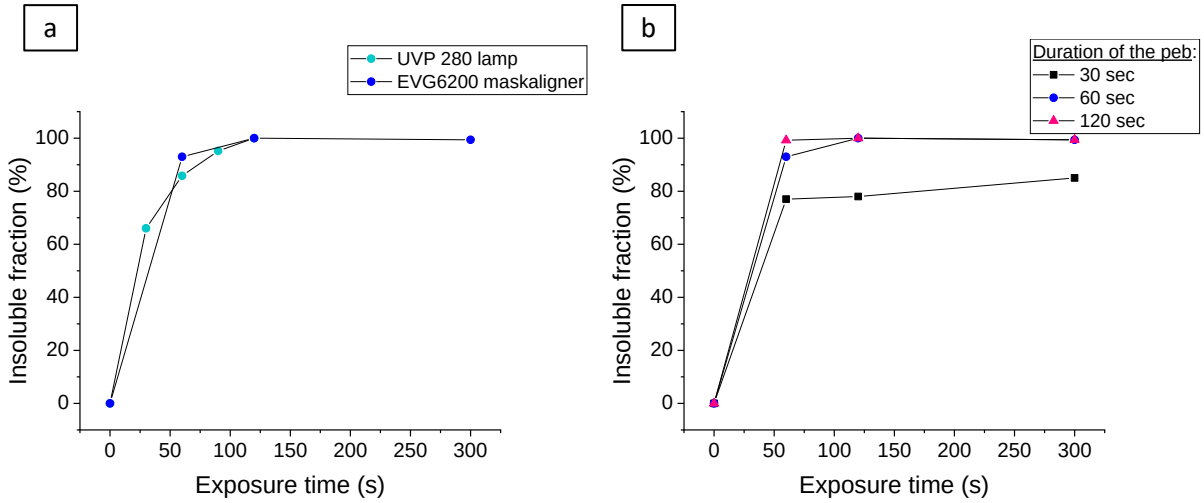

Figure 4-21: Insoluble fractions of the $G_{65}Hp_{35}$ formulated with the dPSPT-OTf (a) as a function of exposure time and comparison of the crosslinking kinetic depending on the lamp. The exposure was followed by a post-exposure bake at 90°C for 1 min (b) as a function of the exposure time. The exposure was followed by a post-exposure bake at 90°C for different baking time to see the effect of the PEB duration on the crosslinking efficiency.

The patterning of the $G_{25}M_{37.5}He_{37.5}$ was performed with the EVG6200® mask aligner at different exposure times between 30 s and 120 s followed by a PEB at 90°C for 2 min to compare the profile of the patterned lines. The films were then developed by dipping the films in ethanol and dried with compressed air. The quality of the patterns was characterized by AFM as shown the Figure

4-19. For 2 min exposure, it is possible to obtain lines with 45 nm height which correspond to only 20% of thickness loss compare to the initial film thickness (Figure 4-22(a)). However, the lines are not well-defined as seen in Figure 4-22(c) and the width of the lines is too large as regards to the width of the mask (see Figure 4-22(b)). All these features are consistent with an overexposure of the film. For 1 min exposure, lines with 36 nm height are obtained with a better definition and the line width is closer to the one of the mask. There is, however, a poor development of the pattern as crosslinked polymer traces can be seen between the lines (Figure 4-22(d)). By decreasing the exposure time, one can achieve more-resolved lines as shown in Figure 4-22(e) and (f).

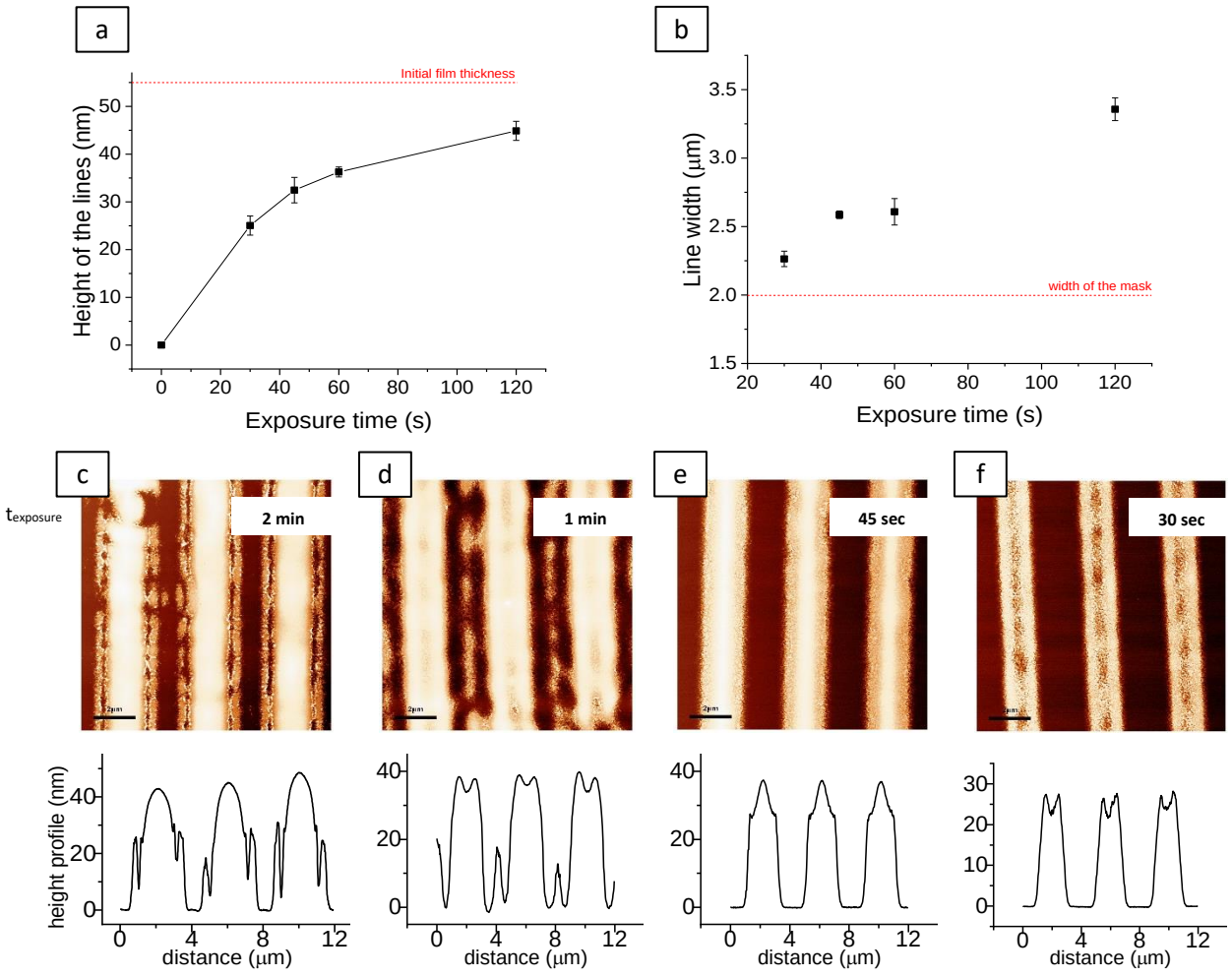

Figure 4-22: Characterization of the profile of the lines obtained after the patterning of the $G_{25}M_{37.5}He_{37.5}$ at different exposure times which was followed by a post-exposure bake at 90°C for 2 min. (a) and (b) are the height and the width of the lines at the different exposure time, respectively. (c) to (f) are the (12 µm x 12 µm) AFM (height) images of the lines at the different exposure time with their corresponding height profiles.

Besides, we noticed a deviation from the expected rectangular shape of the features after patterning even for overexposed films. This heterogeneity is most likely related to the development step which predominantly affects the top surface of the films. Indeed, the compressed air drying might mechanically damage the top of the patterned lines. In order to remove the ethanol after the development step, one more step was added to the protocol. After rinsing the films with ethanol, the films were dipped in water. Water was chosen for its miscibility with ethanol while being a bad solvent for the polymer. As shown in the Figure 4-22, the quality of the pattern was significantly improved with the patterning of 40 nm height lines of rectangular shape.

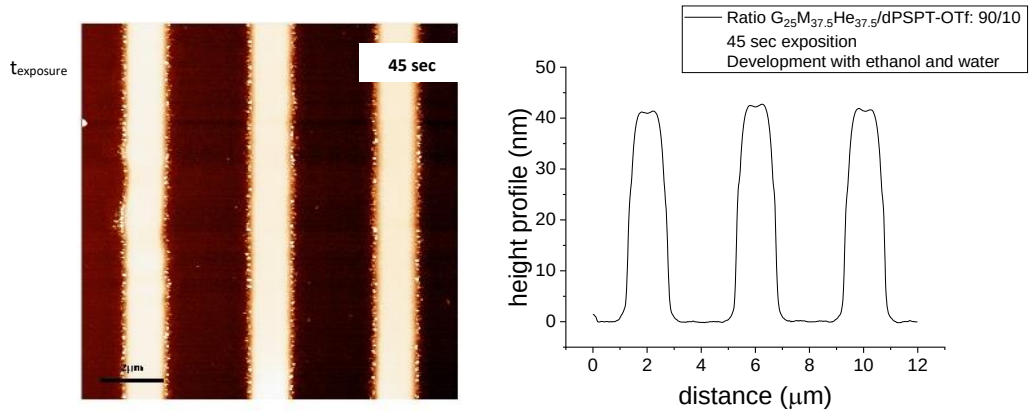

Figure 4-23: (12 µm x 12 µm) AFM (height) image of the lines obtained with the $G_{25}M_{37.5}He_{37.5}$ and the corresponding height profile. The film was exposed for 45 s followed by a post-exposure bake at 90°C for 2 min. The film was then developed in ethanol and dipped in water.

b) Patterning of the TC on top of the BCP film

In the previous section (IV.3.a)), we have demonstrated the ability to obtain well-defined lines of $G_{25}M_{37.5}He_{37.5}$ using the dPSPT-OTf using a fast and industrially-friendly process. In order to pattern the TC on the lamellar-forming PDMSB-*b*-PS, the effect of the PAG on BCP self-assembly was investigated. For this purpose, self-assembly of $PDMSB_{120}$-*b*-PS_{143} was performed using $G_{27}M_{47}He_{26}$, $G_{25}M_{37.5}He_{37.5}$ and $G_{20}M_{24}He_{56}$ as crosslinked TC while $G_{27}M_{47}He_{26}$, $G_{25}M_{37.5}He_{37.5}$ and $G_{20}M_{24}He_{56}$ were used as grafted ULs to vary the surface energy of the substrate and following the same procedure:

i. grafting of the UL at 200°C for 75 s followed by a rinsing step,

ii. spin-coating of the 1% wt. solution of the $PDMSB_{120}$-*b*-PS_{143} in methyl isobutyl ketone at 2000 rpm (to reach $2L_0$ thickness),

iii. spin-coating of the TC at 2000 rpm,

iv. exposure with the UVP 280 lamp for 3 min,

v. baking at 90°C for 3 min,

vi. thermal annealing of the BCP at 240°C for 5 min,

vii. removal of the TC.

The Figure 4-24 summarizes the different orientations of $PDMSB_{120}$-*b*-PS_{143} that were observed by SEM after the removal of the UV-crosslinked TCs. Well-defined out-of-plane lamellae are obtained when using $G_{27}M_{47}He_{26}$, $G_{25}M_{37.5}He_{37.5}$ as TC and UL which is consistent with the results obtained in the Chapter 3.

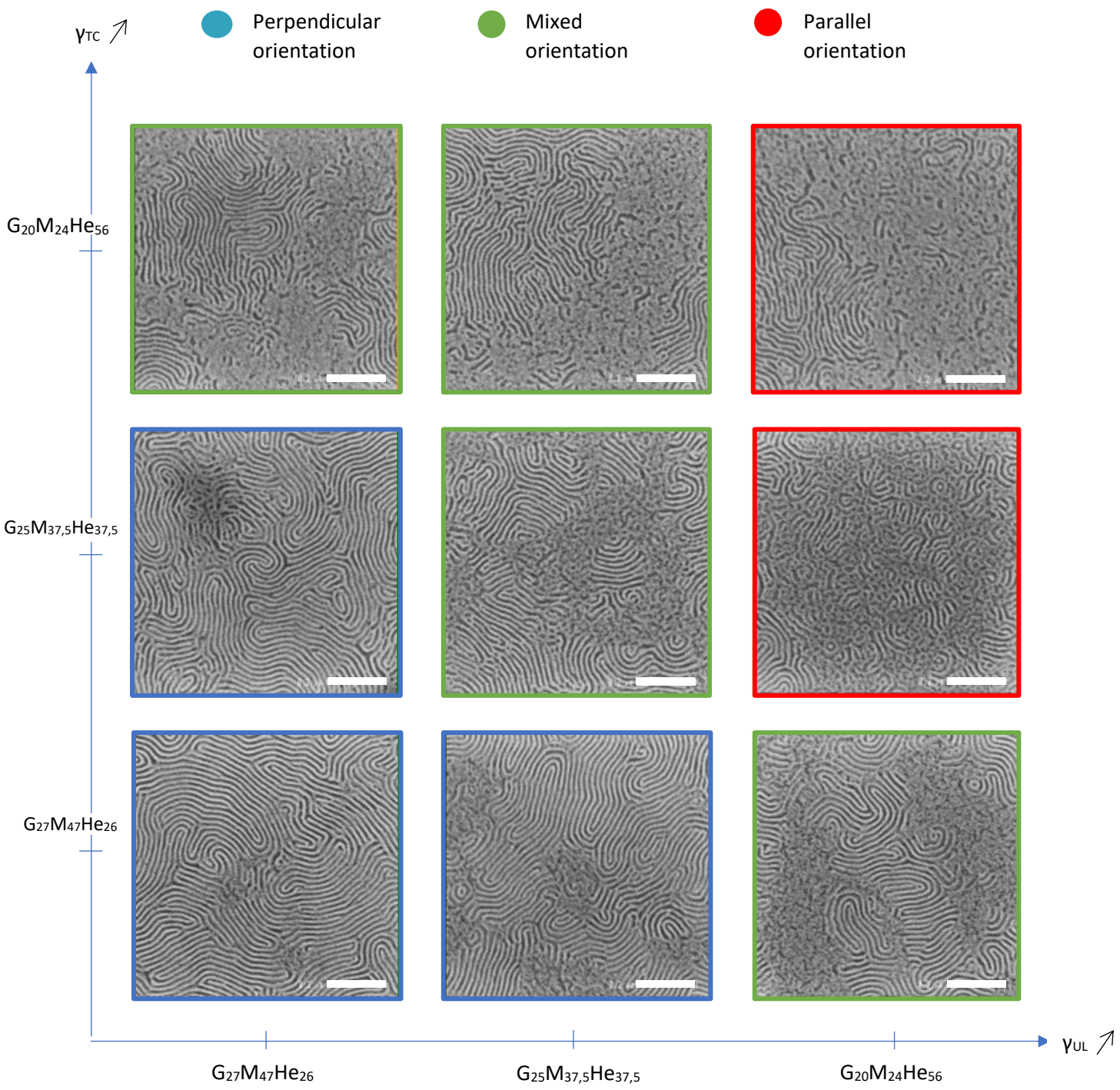

Figure 4-24: **SEM images of the lamellar-forming PDMSB$_{120}$-*b*-PS$_{143}$ using the G$_{27}$M$_{47}$He$_{26}$, G$_{25}$M$_{37,5}$He$_{37,5}$ and G$_{20}$M$_{24}$He$_{56}$ as crosslinked TCs (using the dPSPT-OTf) on different grafted G$_{27}$M$_{47}$He$_{26}$, G$_{25}$M$_{37,5}$He$_{37,5}$ and G$_{20}$M$_{24}$He$_{56}$ underlayers. The blue, red and green circles refer to out-of-plane, mixed and mostly in-plane orientations, respectively. Scale bar: 200 nm.**

The patterning of $G_{25}M_{37.5}He_{37.5}$ was consequently performed above $PDMSB_{120}$-*b*-PS_{143} following the optimized protocol developed in section IV.2.a).:

i. 2% wt. solution of $G_{25}M_{37.5}He_{37.5}$ in a mixture of ethanol and 1-methoxy-2-propanol (9:1) mixed with a 2% wt. solution of dPSPT-OTf in ethanol (9:1) (2000 rpm for 30 sec),
ii. exposure with the EVG6200® mask aligner for 45 s and baked at 90°C for 2 min,
iii. development in ethanol and rinse with water.

Figure 4-25 shows the AFM characterization of the patterned $G_{25}M_{37.5}He_{37.5}$ line above the $PDMSB_{120}$-*b*-PS_{143} film after the development step. One can see that there is a uniform coating of the crosslinked $G_{25}M_{37.5}He_{37.5}$ on the BCP film while keeping the good definition of the line (Figure 4-25(b)). Moreover, the $PDMSB_{120}$-*b*-PS_{143} is not dewetted after the patterning of the $G_{25}M_{37.5}He_{37.5}$ due to the PEB performed at a relatively low temperature. This PEB is already sufficient to induce the self-assembly of the BCP into out-of-plane lamellae with a short-range ordering.

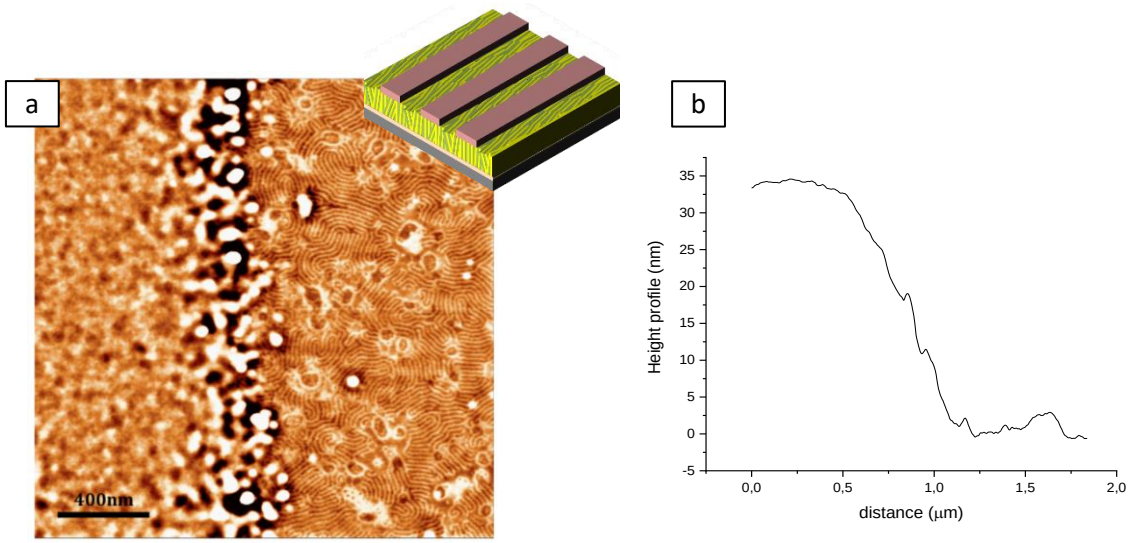

Figure 4-25: AFM image and the corresponding height profile of the patterned $G_{25}M_{37.5}He_{37.5}$ on top of the $PDMSB_{120}$-*b*-PS_{143} before the thermal annealing of the BCP.

Following the same protocol, it is also possible to pattern the other $G_wM_xHe_yHp_z$ TCs on the $PDMSB_{120}$-*b*-PS_{143} using dPSPT-OTf. These TCs have comparable crosslinking kinetics as shown in the Figure 4-26(a). Figure 4-26(b) shows the pictures of 1.5 x 1.5 cm silicon wafers coated with

stacks of UL, $PDMSB_{120}$-*b*-PS_{143} and patterned $G_{65}Hp_{35}$, $G_{25}M_{75}$, $G_{27}M_{47}He_{26}$ and $G_{20}M_{24}He_{56}$ at specific exposure time; the pattern is becoming more defined as we increase the exposure time.

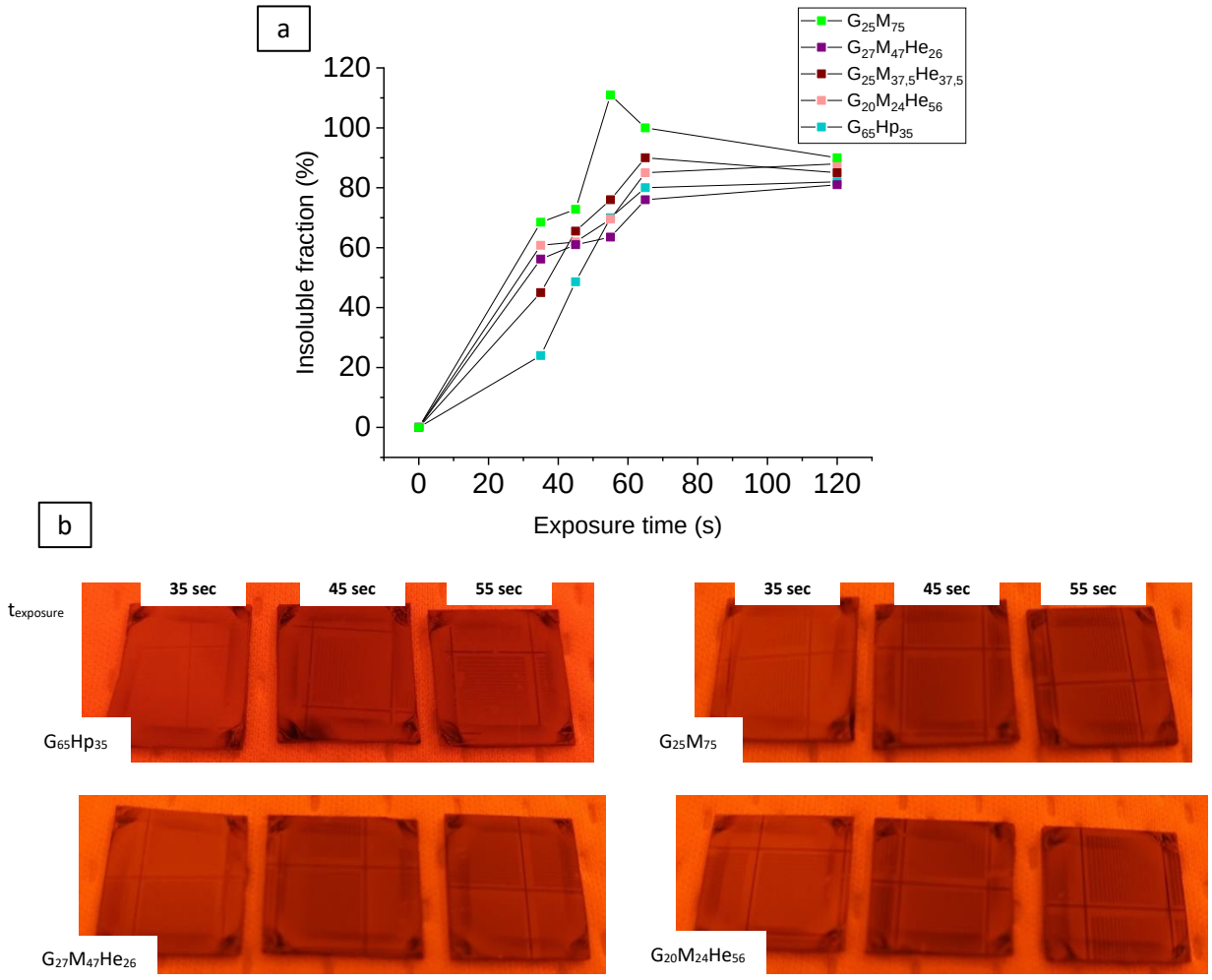

Figure 4-26: **(a) Insoluble fractions of the $G_{65}Hp_{35}$, $G_{25}M_{75}$, $G_{25}M_{37.5}He_{37.5}$, $G_{27}M_{47}He_{26}$ and $G_{20}M_{24}He_{56}$ formulated with the dPSPT-OTf as a function of the exposure time and (b) pictures of 1.5 x 1.5 cm silicon wafers with patterned $G_{65}Hp_{35}$, $G_{25}M_{75}$, $G_{27}M_{47}He_{26}$ and $G_{20}M_{24}He_{56}$ after 35, 45 and 55 sec exposure times. The thicknesses were measured with an error of ± 5 nm.**

However, when performing the thermal annealing of the $G_{25}M_{37.5}He_{37.5}$ at 240°C for 5 min, dewetting of the $PDMSB_{120}$-*b*-PS_{143} film between the patterned lines was noticed as shown on the SEM images (Figure 4-27). The complete dewetting of the BCP film was confirmed with Energy-dispersive X-ray (EdX) spectroscopy (Figure 4-28). Indeed, the signal of the carbon (green) is strong on the TC lines while the silicon signal is predominant in-between the lines which is consistent with a dewetting of the BCP layer leaving exposed the bare silicon substrate. The thickness of the grafted UL is so thin that its carbon signal is not detectable.

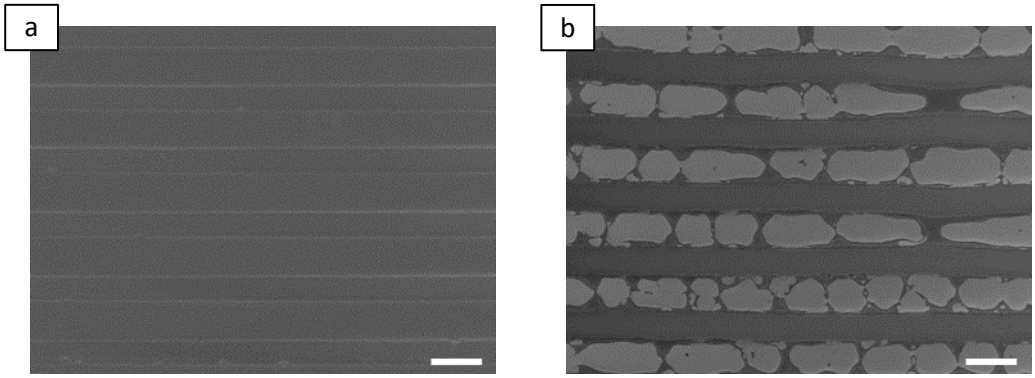

Figure 4-27: SEM images of the patterned lines of $G_{25}M_{37.5}He_{37.5}$ on top of $PDMSB_{120}$-*b*-PS_{143} (a) before and (b) after the thermal annealing. Scale bar 10 µm.

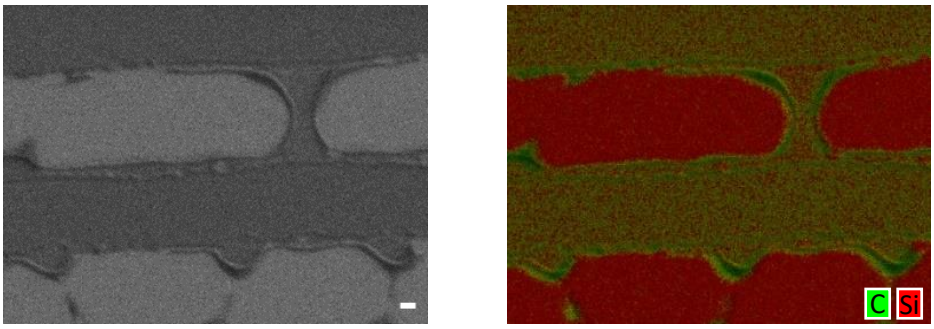

Figure 4-28: SEM images of the patterned lines of $G_{25}M_{37.5}He_{37.5}$ on top of $PDMSB_{120}$-*b*-PS_{143} after the thermal annealing at 240°C of the BCP (left) and the corresponding EdX spectroscopy (right). Scale bar 1 µm.

However, when the TC is removed using the typical Ar/O_2 plasma, we can see that the BCP film below the patterned lines has also been strongly affected by the dewetting of the BCP layer between the lines. Indeed, there is a dislocation of the BCP film on the edges that are in contact with the dewetted parts of the film. Figure 4-29 shows the AFM characterization of the $PDMSB_{120}$-*b*-PS_{143} that were annealed at different temperature: 100°C, 150°C, 200°C and 240°C. Interestingly, the dislocation seems to be lower with the increase of the annealing temperature. However, the BCP lines are heterogeneous and it therefore renders the homogenous removal of the TC fastidious.

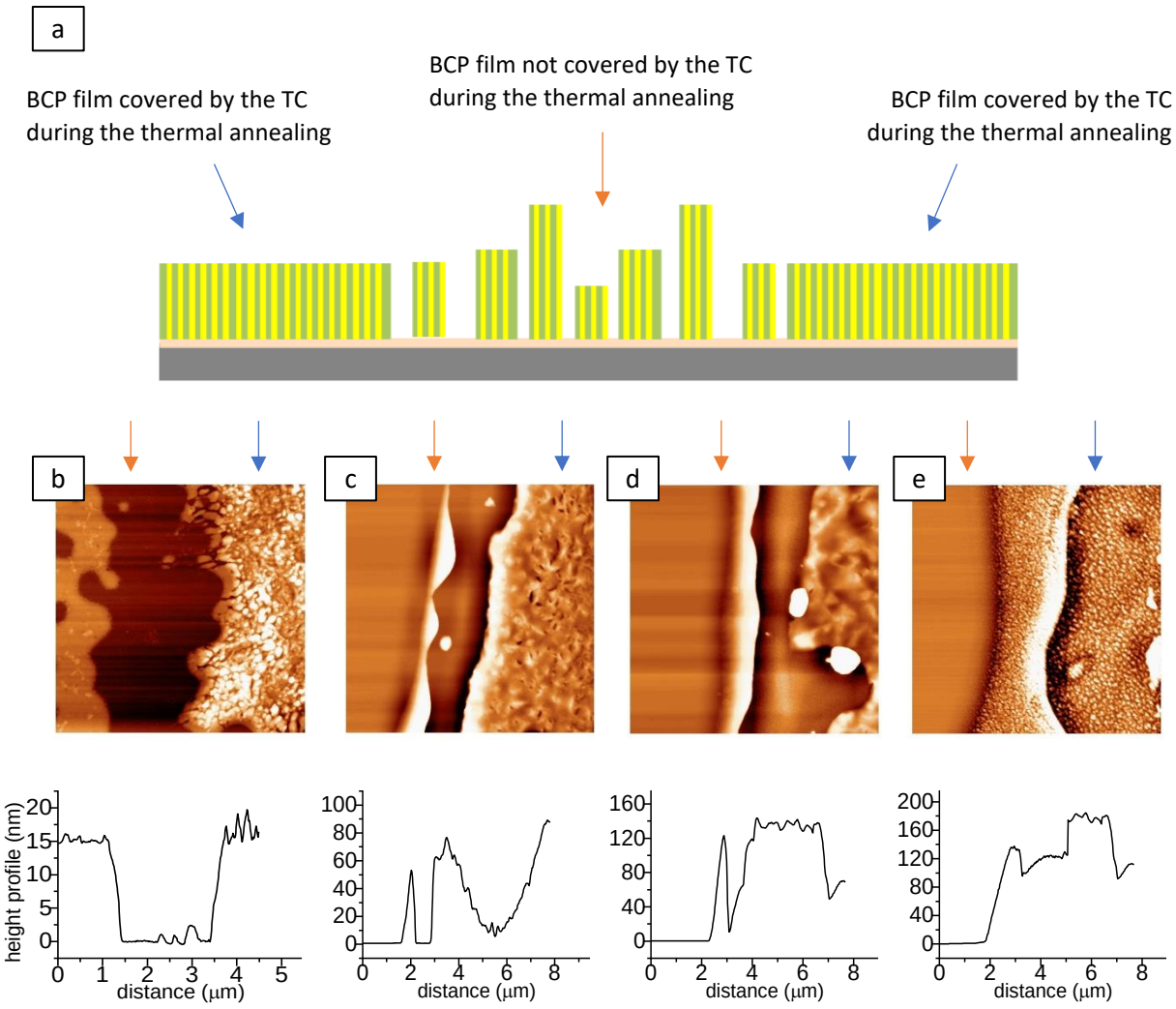

Figure 4-29: Characterization of the BCP films after the thermal annealing and the removal of the TC. (a) is the scheme representing the BCP film after the process and is illustrating the AFM images (5 µm x 5 µm) of thermally-annealed PDMSB$_{120}$-*b*-PS$_{143}$ at (b) 100°C, (c) 150°C, (d) 200°C and (e) 240°C after the removal of the patterned lines and their corresponding height profiles. The parts of the film that were not covered by the crosslinked TC dewet which impact the adjacent areas where the BCP film was covered by the TC.

In order to obtain a homogenous film with well-defined lines of out-of-plane lamellae and to avoid the dewetting of the BCP layer in-between the lines, we choose to refill the developed parts of the neutral TC pattern by a non-neutral crosslinkable material before performing the thermal annealing as already done in the section 2 (see Figure 4-12). Another possibility is to pattern a non-neutral material above the BCP film and refill the developed parts with the neutral TC, and this alternative was investigated by Dr. X. Chevalier (Arkema) and Dr. M. Zelsmann (LTM) in the CEA-LTM facilities. Figure 4-30 shows the SEM characterization of PDMSB$_{120}$-*b*-PS$_{143}$ after the removal of the two TCs. Well-defined lines of out-of-plane lamellae are obtained with a clear interface between parallel and the perpendicular areas.

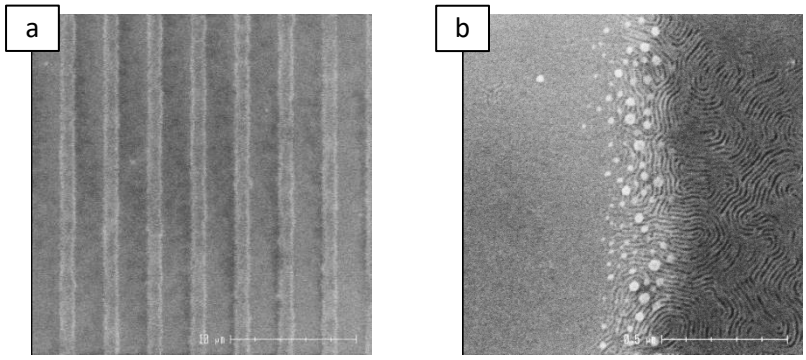

Figure 4-30: SEM images of the PDMSB$_{120}$-*b*-PS$_{143}$ obtained from a non-neutral patterned TC refilled with a neutral TC. (a) and (b) are two different magnifications.

We have developed another strategy consisting in the use of the crosslinked TC lines as mask for the selective etching of the BCP film prior the annealing process as shown the Figure 4-31.

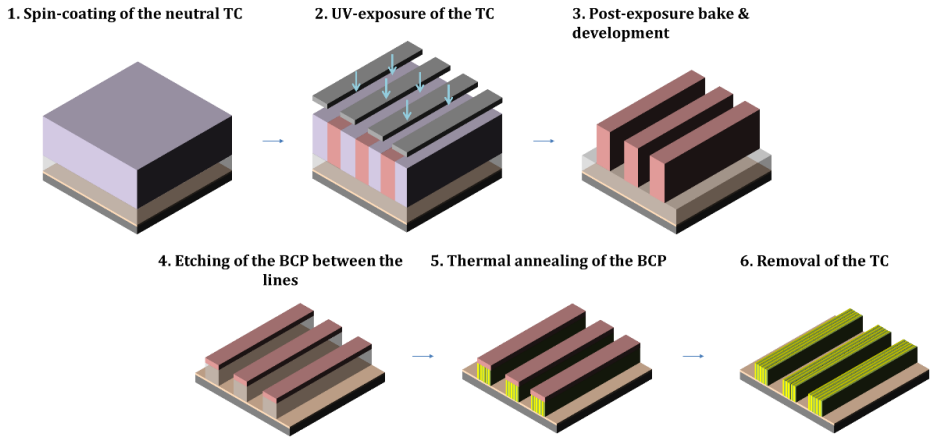

Figure 4-31: Scheme of the procedure used to obtain well-defined lines of out-of-plane lamellae. The TC is used as a mask to remove the BCP between the lines.

For this purpose, a CF_4/O_2 plasma (10 mTorr, 100 sccm of CF4, 10 sccm of O_2 and source power: 200 W- bias power: 10 W) was performed as it allows the removal of the BCP with a good selectivity. Figure 4-32 shows the CF_4/O_2 etching rate measurement that was performed by measuring the thickness of a single crosslinked layer of $G_{25}M_{37.5}He_{37.5}$/dPSPT-OTf and of a single PDMSB-*b*-PS layer as a function of the etching time. The etching rate of the $G_{25}M_{37.5}He_{37.5}$ layer is the ~ 2.2 nm.s^{-1} while the one of the PDMSB-*b*-PS layer is ~1.2 nm.s^{-1}.

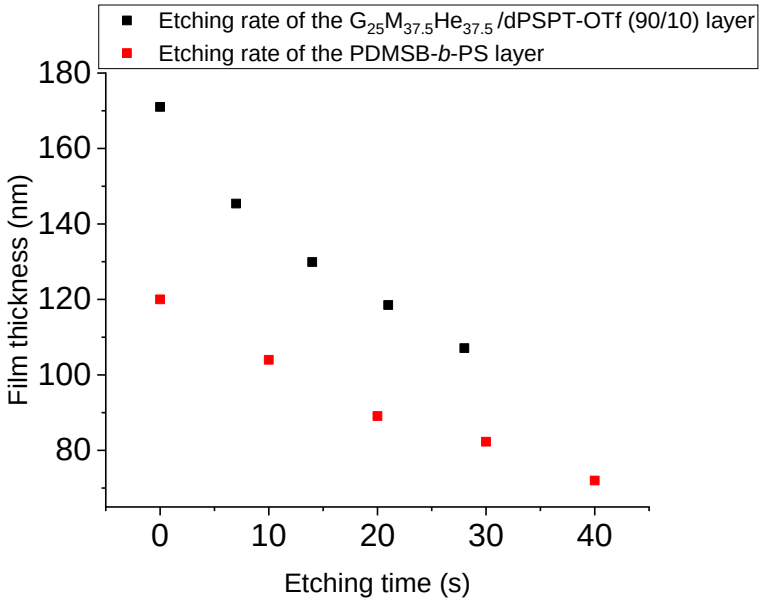

Figure 4-32: Measurements of film thicknesses of $G_{25}M_{37.5}He_{37.5}$/dPSPT-OTf and PDMSB-*b*-PS films as a function of the etching time to determine the etching rate of the CF_4/O_2 plasma.

To conserve enough TC material for the further thermal annealing of the BCP, the patterned TC has thus to be way thicker than the BCP film as the plasma will still etch a part of the TC. Consequently, the patterning of the $G_{25}M_{37.5}He_{37.5}$ was performed above the $PDMSB_{120}$-*b*-PS_{143} as shown in the Figure 4-33 and following the following protocol:

i. grafting of the UL at 200°C for 75 s followed by a rinsing step,

ii. spin-coating of the 1% wt. solution of the $PDMSB_{120}$-*b*-PS_{143} in methyl isobutyl ketone at 2000 rpm (to reach $2L_0$ thickness),

iii. 4% wt. solution of $G_{25}M_{37.5}He_{37.5}$ mixed with a 4% wt. solution of dPSPT-OTf (9:1) in a mixture of ethanol and 1-methoxy-2-propanol (85:15) (2000 rpm for 30 sec to reach ~90 nm thickness),

iv. exposure with the MJB4® mask aligner followed by a development step,

v. etching of the BCP between the patterned lines using the CF_4/O_2 plasma (10 mTorr, 100 sccm of CF4, 10 sccm of O_2 and source power: 200 W- bias power: 10 W)

vi. thermal annealing of the BCP at 240°C for 5 min,

vii. removal of the TC using the conventional Ar/O_2 plasma (10 mTorr, 80 sccm of Ar, 40 sccm of O_2 and source power: 200 W- bias power: 20 W) for 20 s followed by a CF_4/O_2 plasma

(10 mTorr, 40 sccm of CF_4, 40 sccm of O_2 and source power: 200 W- bias power: 10 W) for 13 s and again the Ar/O_2 for 10 s to ensure a good contrast between the domains for further microscopy characterization.

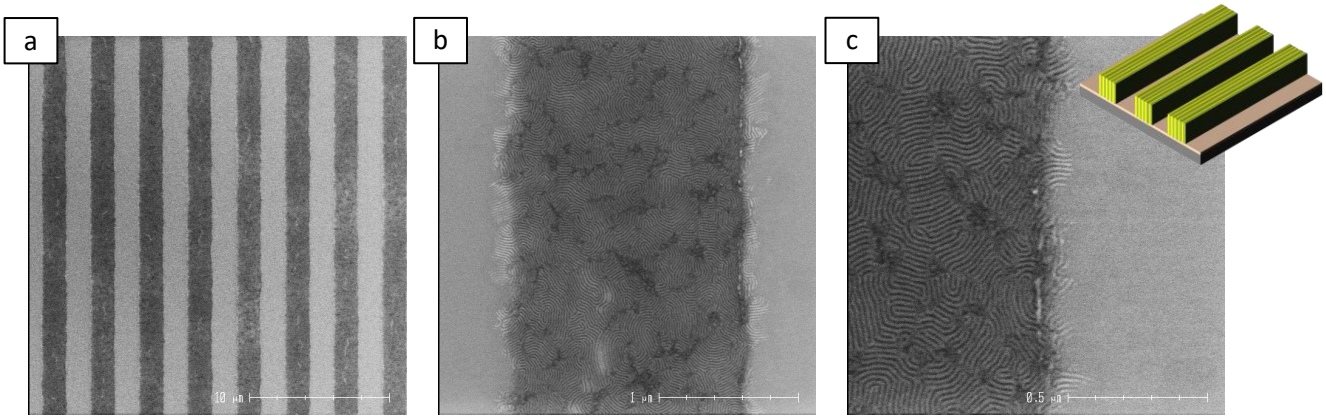

Figure 4-33: SEM images of the $PDMSB_{120}$-*b*-PS_{143} obtained from a patterned neutral TC. (a), (b) and (c) are three different magnifications.

Moreover, to mechanically maintain BCP between the patterned lines, it is also possible to refill the pattern with a crosslinkable neutral (or not) material followed by the thermal annealing of the BCP. The patterned TC can thus be used as mask for the etching of the BCP in between the lines using the same CF_4/O_2 plasma (10 mTorr, 100 sccm of CF_4, 10 sccm of O_2 and source power: 200 W- bias power: 10 W) as before (Figure 4-34(a)). Figure 4-34(b) shows the SEM images of $PDMSB_{120}$-*b*-PS_{143} after the removal of the $G_{25}M_{37.5}He_{37.5}$/dPSPT-OTf that was used as the patterned layer and as refilling material. The protocol is almost the same except that one has to add the covering of the BCP film between the patterned lines prior to the thermal annealing and the etching step now occurs after the thermal annealing.

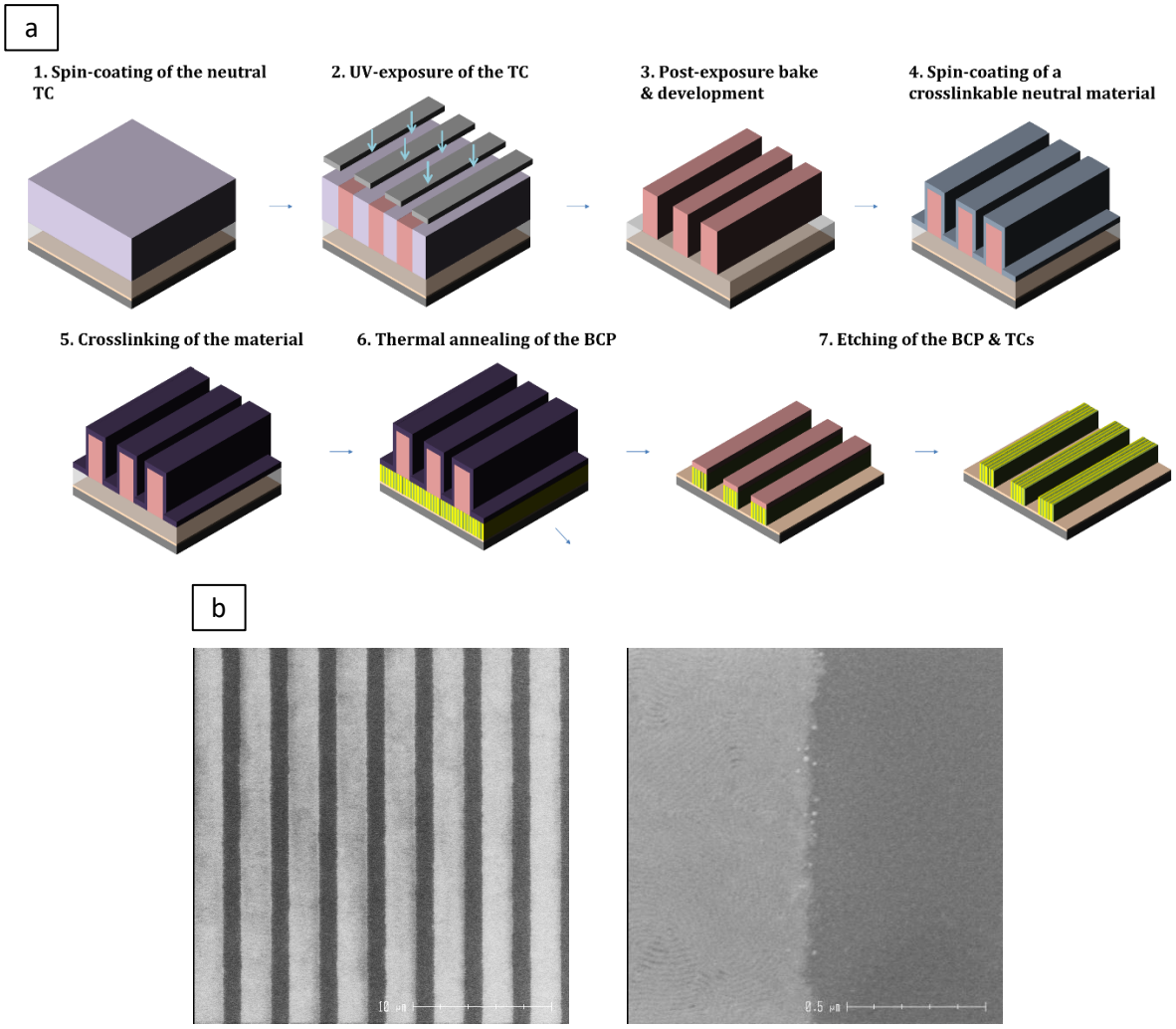

Figure 4-34: **(a) is scheme of the procedure used to obtain well-defined lines of out-of-plane lamellae. The TC is used as a mask to remove the BCP between the lines. Another TC material is deposited in order to mechanically maintain the BCP between the patterned lines during the thermal annealing. (b) are the SEM images of the resulting film with different magnifications.**

Finally, in an easier process, it is still possible to simply remove the dewetted BCP parts using the CF_4/O_2 plasma (Figure 4-35). However, as shown previously, the lines of out-of-plane lamellae are distorted which renders the homogenous removal of the TC fastidious due to variation of thickness on the edges of the lines (Figure 4-36).

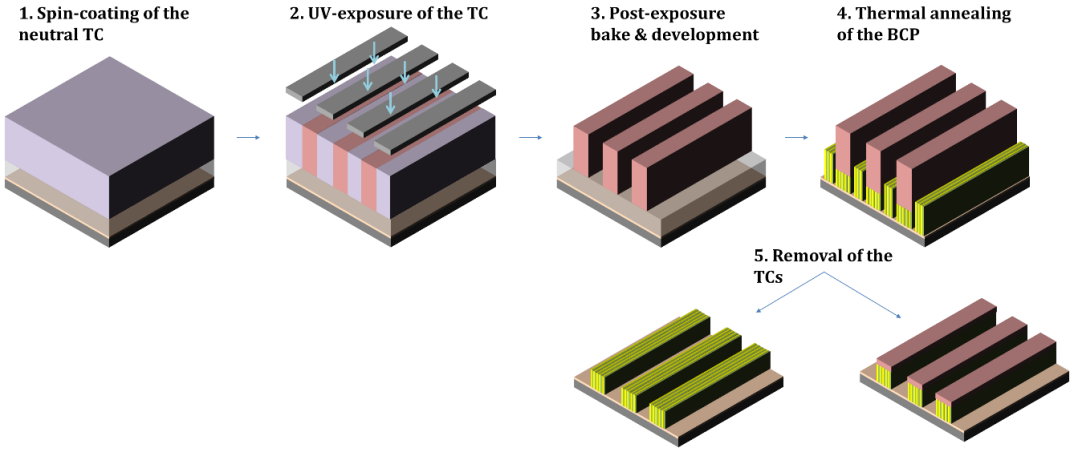

Figure 4-35: **Scheme of the procedure used to obtain well-defined lines of out-of-plane lamellae. The TC is used as a mask to remove the dewetted BCP between the lines.**

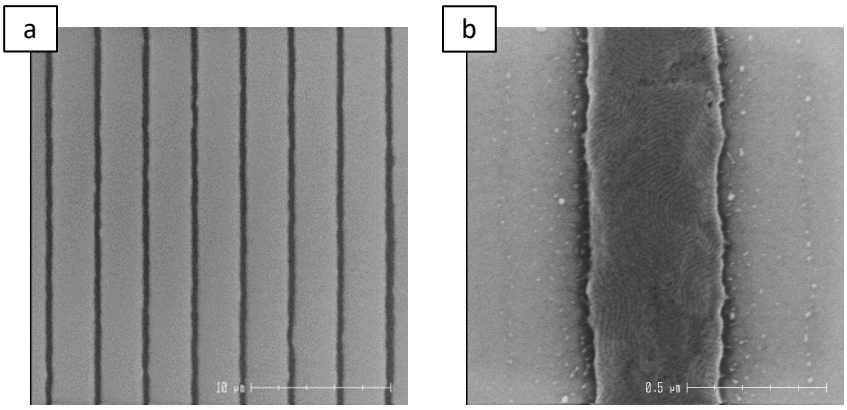

Figure 4-36: **SEM images of the PDMSB$_{120}$-*b*-PS$_{143}$ obtained from a patterned neutral TC after the removal of the TC and of the dewetted parts of the BCP film. (a) and (b) are two different magnifications.**

V. Conclusion

Our objective was to demonstrate the potential of our methacrylate-based material as patternable neutral TC to guide the self-assembly of lamellar-forming PDMSB-*b*-PS into an out-of-plane orientation in specific areas of the film. For this purpose, three different strategies have been presented in order to photocrosslink our TC layer in deep-UV and in the visible range (see Table 4-2). The reactivity of various pI systems has been investigated in order to obtain, for each approach, an efficient crosslinking reaction, which consequently resulted in fully-crosslinked films after 2 min and 1 s of flood exposure under UV-light and deep-UV, respectively. We have proposed two different approaches in order to pattern the TC material using (i) a two-component system with a PAG and a pI, and (ii) a structurally modified PAG. An optimization of the lithography conditions allowed to obtain well-defined patterned lines of the crosslinked TC for only 45 sec exposure when the polymer was formulated with the dPSPT-OTf while a slow crosslinking kinetic was observed when the polymer was formulated with the dPSPT-OTf/DMPAP and which is probably due to the small reduction potential of the sulfonium salt. The patterning of the TC/dPSPT-OTf above a lamellar PDMSB-*b*-PS BCP allowed a control the orientation of the lamellae in specific areas of the film with a good resolution. These results are very promising for the building of complexes nanostructures. For deep-UV conditions, the complexity of our objective led us to highlight and study the effect of the sensitive species on the surface energy of the initial material in order to be able to control de surface energy of the TC layer. This allowed us to demonstrate the patterning of our polymer/PAG formulation to produce out-of-plane lamellae at specific locations of the film within extremely short time. An appropriate lithography tool could allow to further explore the possibilities offered by this TC in order to define areas of out-of-plane lamellae with a high-resolution.

Table 4-2: **Summary of the different approaches investigated in this chapter for the patterning of the TC.**

	Potential of the different approaches for patterning of the TC		
	Visible light		**Deep-UV**
	one-component system	**two-component system**	**one-component system**
	dPSPT-OTf 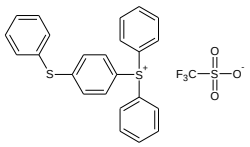	**DMPAP + dPSPT-OTf** 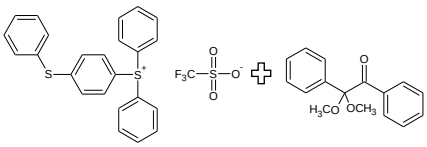	**tPS-OTf** 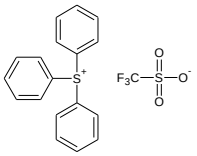
Crosslinking efficiency of the optimized system in flood exposure	 Fast: 2 min exposure	 Fast: 2 min exposure	 Very fast: 1 s exposure
Capability of the different approaches for patterning	*Using the mask aligner*		
	 Very fast after optimization of the process: 45 s exposure 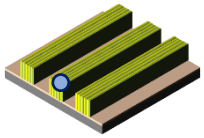 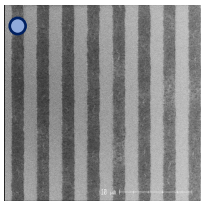 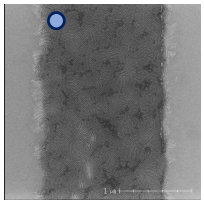	 Very slow crosslinking when selectively exposed: 15 min exposure	 Very fast: 1 s exposure 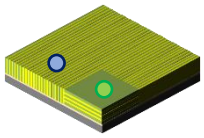 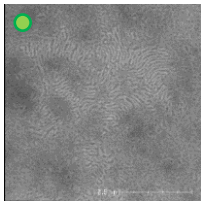 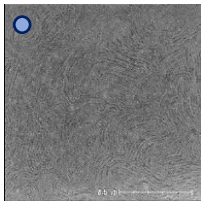

VI. References

[1] H. S. Suh, P. Moni, S. Xiong *et al.*, “Sub-10-nm patterning via directed self-assembly of block copolymer films with a vapour-phase deposited topcoat”, *Nat Nanotechnol*, vol. 12, nº 6, p. 575-581, juill. 2017.

[2] A. Soyano, “Application of polymers to photoresist materials”, vol. 39, nº 5, p. 8, 2012.

[3] N. Klikovits, P. Knaack, D. Bomze, I. Krossing and R. Liska, “Novel photoacid generators for cationic photopolymerization”, *Polymer Chemistry*, vol. 8, nº 30, p. 4414-4421, 2017.

[4] J. Liu, Y. Qiao, Z. Liu and L. Wang, “The preparation of a novel polymeric sulfonium salt photoacid generator and its application for advanced photoresists”, *RSC Advances*, vol. 4, nº 40, p. 21093, 2014.

[5] S. Shi, C. Croutxé-Barghorn and X. Allonas, “Photoinitiating systems for cationic photopolymerization: Ongoing push toward long wavelengths and low light intensities”, *Progress in Polymer Science*, vol. 65, p. 1-41, févr. 2017.

[6] I. M. Riddlestone, A. Kraft, J. Schaefer and I. Krossing, “Taming the Cationic Beast: Novel Developments in the Synthesis and Application of Weakly Coordinating Anions”, *Angewandte Chemie International Edition*, vol. 57, nº 43, p. 13982-14024, oct. 2018.

[7] J. P. Fouassier and J. F. Rabek, Éd., *Radiation curing in polymer science and technology. Vol. 4: Practical aspects and applications*. London: Elsevier Applied Science, 1993.

[8] R. Voelkel, U. Vogler, A. Bramati *et al.*, “Advanced mask aligner lithography (AMALITH) for thick photoresist”, *Microsystem Technologies*, vol. 20, nº 10-11, p. 1839-1842, oct. 2014.

[9] S. Keller, G. Blagoi, M. Lillemose, D. Haefliger and A. Boisen, “Processing of thin SU-8 films”, *Journal of Micromechanics and Microengineering*, vol. 18, nº 12, p. 125020, déc. 2008.

General conclusion

During this Ph.D., we have provided an understanding of the self-assembly behaviour of the PDMSB-*b*-PS system in bulk and in thin film. We have highlighted the potential of this semi-crystalline BCP to form sub-20 nm features using industrially-friendly processes thanks to a high Flory-Huggins interaction parameter (Chapter 2). With the aim of controlling the out-of-plane orientation of lamellar-forming PDMSB-*b*-PS BCPs in thin film, we have proposed an approach relying on the use of crosslinkable neutral TC layers. The versatility of this approach was demonstrated using BCPs having different macromolecular characteristics and further extended to the formation of multi-layer stacks through an iterative self-assembly process (Chapter 3). Taking advantage of the crosslinking ability of our TC material, we have demonstrated the patterning ability of the TCs using photosensitive crosslinking agents. The patterning of neutral TCs above the lamellar-forming PDMSB-*b*-PS BCPs further allowed a control of the orientation of the PDMSB-*b*-PS domains in specific areas of the film (Chapter 4).

Indeed, the phase behaviour of the PDMSB-*b*-PS system was deciphered using a platform of BCPs having different macromolecular characteristics. We have determined the temperature-dependent Flory-Huggins interaction parameter of this particular system that was found to be 0.13 ± 0.06 at RT (thus higher than the conventional PS-*b*-PMMA system with $\chi_{PS\text{-}b\text{-}PMMA}$ = 0.03 at RT). This highlights the potential of this BCP system for next-generation lithography as low molecular weight BCPs (i.e. segregating with a low periodicity) are able to form well-defined structures. As a complementary study, we have also explored the ability of PDMSB-*b*-PS BCPs to self-assemble into the cylindrical and gyroid nanostructures establishing the main processing parameters for a control of the organization and orientation of the BCP domains. Cylindrical nanostructures were thus obtained in thin film with periodicities ranging from 21.7 nm to 41.6 nm. Different orientations of the PDMSB cylinders were observed depending on the melting temperature of the semi-crystalline PDMSB block with an out-of-plane orientation of the cylinders when $T_{m,\ PDMSB} > RT$ and an in-plane orientation of the cylinders when $T_{m,\ PDMSB} < RT$. The

crystallization occurring for PDMSB-*b*-PS BCPs having $T_{m,\ PDMSB}$ results in a kinetically trapped perpendicular orientation of the nanodomains after the spin coating step. Consequently, it is possible to counter thermodynamics in order to obtain well-defined out-of-plane cylinders for different film thicknesses without using neutral layers. Finally, we have performed the self-assembly of gyroid-forming PDMSB-*b*-PS in thin film with the smallest unit cell reported to date using a short thermal annealing process. The stabilization of this 3D-structure required a rapid and high temperature annealing to kinetically trap the structure in films largely thicker than the gyroid unit cell in order to decrease the interactions between the BCP film and the interfaces (substrate and/or air). Further work should be performed on the cylinder-forming PDMSB-*b*-PS in thin film to give additional proofs of the underlying crystallization, for example, by using wide-angle X-ray scattering in order to access the crystalline structure of the PDMSB in thin film. Further studies could perform the same experiments with a PDMSB-*b*-PS where random units are incorporated in the PDMSB block in order to break the crystallinity and see the effect on the self-assembly. Additionally, the gyroid-forming PDMSB-*b*-PS film could serve as a template to build functional materials. By removing the PDMSB domains (using a fluorinated treatment), one could access to nanoporous film that could be used (i) as catalytic support in polymer/organic chemistry due to the high specific surface, (i) as template to build bulk heterojunction for solar cells, (iii) as membranes or (iv) as starting material for photonic applications.

On the other hand, as the main structure of interest for BCP lithography is the out-of-plane lamellar morphology, we have developed an approach in order to obtain perpendicular PDMSB-*b*-PS lamellae. This approach is based on the design of a methacrylate-based random copolymer that allows an easy deposition of the material on top of the BCP layer, a tuning of its surface energy and a crosslinking ability: these three properties were provided by the combination of the hydroxyethyl, matrife and glycidyl moieties, respectively. We have demonstrated that TC materials with finely tuned composition were able to prevent the lower PDMSB surface energy block to segregate at the top interface during thermal annealing. Importantly, we have shown that such crosslinked TCs were able to limit dewetting phenomena occurring in the BCP film during

the annealing. Consequently, smooth and non-dewetted films of out-of-plane lamellae with 14.6 nm, 17.2 nm and 22.7 nm periodicities were obtained after a high temperature process. Finally, we have built two- and three-layered stacks of lamellar PDMSB-*b*-PS BCPs. Indeed, the crosslinked TC was used as a "new" substrate for the deposition of a subsequent BCP layer. The stacking of BCP layers was demonstrated as an easy process to access more complex structures as compared to the ones obtained from a single layer of a diblock copolymer. As a proof of concept, stacking of two BCP layers of in- and out-of-plane lamellae with BCPs having different periodicities and film thicknesses was realized but further works have to be performed in order to provide a better control of these stacking methodologies.

We have further explored the crosslinking ability offered by our TC material to build even more complex nanostructures. Indeed, we have used the TCs as a patternable material to guide the self-assembly of lamellar-forming PDMSB-*b*-PS into an out-of-plane orientation in specific areas of the films. For this purpose, a set of photosensitive crosslinking agents were studied and tested to achieve an efficient photocrosslink of the TC in deep-UV and in visible light. Following an optimization process of the patterning conditions, we have demonstrated the patterning of the TC above the lamellar-forming BCP to obtain well-defined lines of out-of-plane lamellae in the visible range. This complex structuration of the BCP thin films could be useful for advanced nanolithography in semi-conductor industry as the process employs microelectronic-compatible solvents, a thermal annealing process and a simple methodology with tools that are already common on lithography tracks.

The "crosslinkability" as well as the "patternability" of TC layers developed in this study open new avenues for BCP nanotechnologies. In particular, such patternable layers were demonstrated to define chemically modified surfaces of high interest for the long-range ordering of BCPs through chemoepitaxy. It would be indeed possible through the use of TC layers to control both the orientation of the domains (in-plane *vs.* out-of-plane) and the overall translational correlation

length of the BCP structure (long-range order with improved defectivity). A second challenge linked to this study is the realization of BCP stacks with functional properties. One of the possibilities could be the insertion of functional materials between the crosslinked layers in order to build hybrid stacks. Another possibility to obtain such functional design would be to utilize selective hybridization methodologies of BCP domains (using sequential infiltration synthesis, metallic salt incorporation of sol-gel chemistry) in order to convert the BCP patterns into functional structured surfaces such as bit-patterned media, field effect transistors, optical metamaterials, filtration membranes or photonic structures. As most of these applications require the precise positioning or registration of the BCP nanostructure, the methods developed during this Ph.D. would constitute a great asset towards such realizations. Finally, the transposition of this work at the industrial level lays down a challenge for “technological integrators” and further optimization of the processes (considering the reproducibility, defectivity and scaling on large surfaces) will be needed to fully fulfil the technological potential of TC materials in BCP nanotechnology.

Annex

I. Characterization of the material in bulk

1. Differential scanning calorimetry

Differential scanning calorimetry is a thermoanalytical technique that allows the determination of the different phase transitions of a material (e.g. glass transition, melting transition, crystallization or crosslinking). The principle of the technic is based on the measure of the difference in the amount of heat that is required to increase the temperature of a sample and a reference as a function of temperature. Both the sample and reference (generally empty alumina capsule) are maintained at nearly the same temperature during the experiment and the reference has a well-known heat capacity over the range of temperatures to be scanned.

II. Thin film process

1. Spin-coating

The spin-coating process remains the most common technique to obtain polymeric thin films and is widely used in industry and in laboratories. The principle of the technique is depicted in the Figure 5-1. The main advantage of the technic is its ability to produce uniform films with controlled thicknesses of a few nanometers in an easy and quick process. A polymer solution is first deposited on a substrate (step 1 in the Figure 5-1). The substrate will then start rotating at a constant acceleration rate (step 2) until the desired rotation speed is reached (step 3). The majority of the solvent is ejected during the acceleration stage (step 2) while the airflow allows to evaporate the remaining solvent traces (step 3). The final thickness will depend on the rotation speed and on the solution concentration.

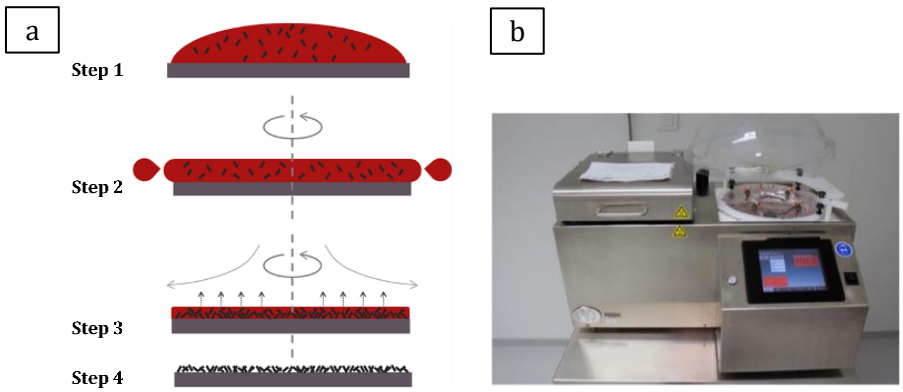

Figure 5-1: (a) is the scheme of the general procedure of the spin-coating in order to obtain thin films. (b) is the picture of spin-coater used during this study.

2. Etching plasma

After the spin-coating and thermal annealing processes, an etching treatment is necessary in order to (i) remove the PDMSB wetting layer in case a self-assembly process performed without TC (ii) remove the neutral TC (iii) provide contrast between the two phases for further microscopy characterization. Plasma etching has proven to be a great tool for surface modification or selective etching of polymeric materials and is widely used in semiconductor industry. A plasma is an electrically neutral ionized gas consisting of neutral particles and charged particles (ions and electrons), which can be generated by an electrical discharge. A plasma can etch in three different manners. Indeed, the material can be chemically etched by reactive species of the plasma (e.g. radicals or ions created in the plasma): one talk about chemical etching. The ion bombardment on a polymer surface, which causes sputtering of the surface, is referred to as physical process. Finally, UV radiation from the plasma can also lead to dissociation of chemical bonds, which leads to the formation of low molecular weight materials [1]–[3].

a) Reactive ion etching

Most of the plasma experiments presented in the manuscript were carried in the LCPO using a PE-100 Benchtop Plasma System (Figure 5-2). In the case of the reactive ion etching (RIE), those three mechanisms proposed above generally simultaneously occur during the plasma treatment inducing the formation of volatiles products in the plasma chamber. The main advantage of this technique is its selectivity regarding the chemical structure of the polymers.

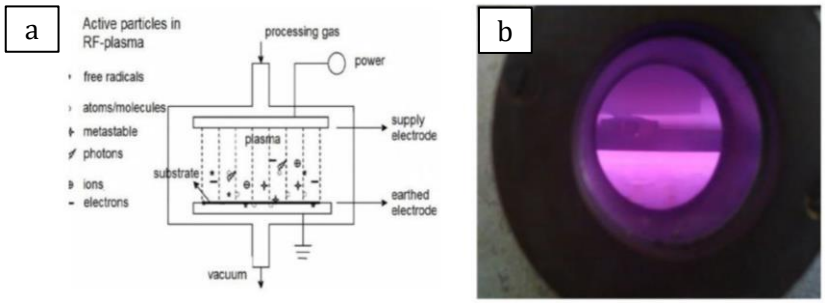

Figure 5-2: (a) Schematic representation of the plasma etching process and (b) plasma reactor chamber used in this work.

b) DPS 200 reactor

Some of the plasma experiments presented in the manuscript for the etching of the neutral TC were carried out in industrial plasma reactors installed in the cleanroom of the CEA-LETI in Grenoble. The reactor of the plasma is an inductively coupled reactor plasma (ICP) of the company Applied Materials (DPS Centura 5200) accepting substrates of 200 mm diameter. In this type of reactors, an intense alternating magnetic field is generated in the gas by a high frequency current. The electromagnetic field is strong enough to generate a current in some gases (typically Cl_2, HBr, O_2, BCl_3, CF_4, SF_6, Ar, CH_2F_2)[3], [4]. The gas is transformed into an intense and high-density plasma. Figure 5-3 shows the scheme of the plasma chamber. A RF generator connected to the antenna delivers a power of 200 W to 1500 W at 12.56 MHz to create and maintain the plasma in the chamber. This power is absorbed by the electrons and allow thus to control of their density (1010-1012 cm-3). The power delivered by this generator is commonly referred as the “power source”. On the other hand, a second RF generator (at 13.56 MHz) is connected to an electrode covered with an insulating layer. The substrate placed on this insulation is therefore negatively affected when the generator delivers power (between 0 and 250 W) which allow to control the energy of the ions bombarding the substrate (10-300 eV). The power delivered by this generator is commonly referred as the “power bias”[4].

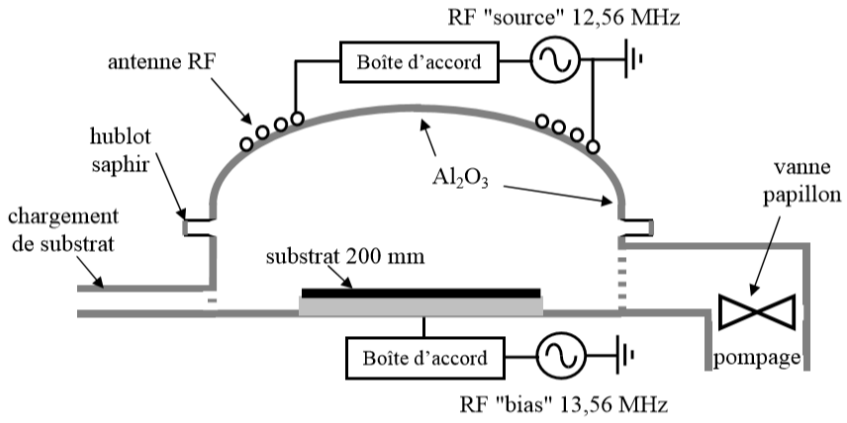

Figure 5-3: Schematic representation of the plasma etching process used in this work [4].

III. Thin film characterization

1. Atomic Force Microscopy

To characterize the structure of the self-assembled BCP thin films, the atomic force microscopy was used during this thesis. AFM is a high-resolution type of scanning probe microscopy technique. It is one of the foremost tools for imaging and measuring surface features at the nanoscale level. The Figure 5-4 shows the general scheme of the AFM. A tip is mounted on a reflective cantilever (the cantilever and the tip together are known as the probe) made of silicon nitride, silicon oxide or pure silicon fabricated with standard techniques used in semiconductor industry. In Tapping mode (or intermittent contact mode atomic force microscopy), the cantilever is oscillating up and down at or near its resonance frequency, in a direction normal to the sample surface. A laser beam is focused onto the back of the reflective cantilever (Figure 5-4(a)); as the tip scans the surface of the sample, the tip deflects and the laser beam is bounced of the cantilever. Depending on the interaction between the tip and the sample, there will be a difference in the intensity of the reflected light. This difference is measured by the photodetector and the signal is sent off to the controller feedback loop. The feedback loop will attempt to keep the cantilever deflection constant by maintaining a constant distance between the cantilever and the sample. This can be done by moving the piezoelectric scanner (by applying a voltage) in the Z direction at each point. The voltage is then converted to a cantilever deflection.

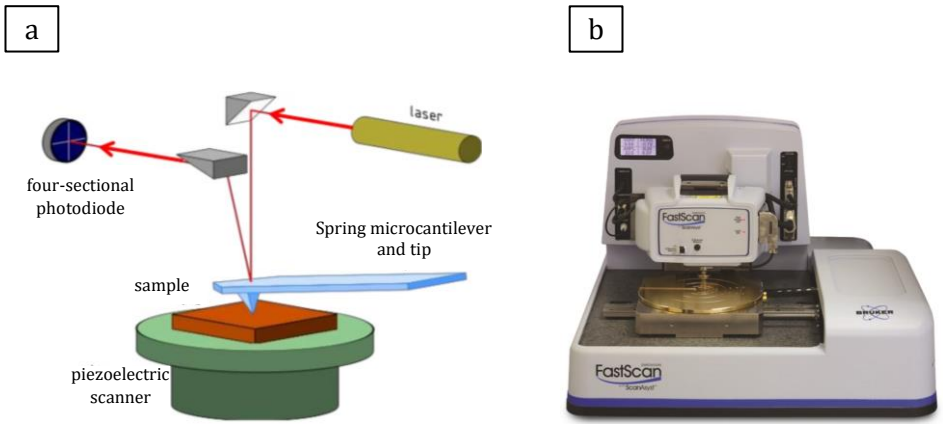

Figure 5-4: (a) Schematic illustration of the principle of AFM. The scanner is composed of three piezo components that control the horizontal (x and y) and vertical (z) movement of the sample. The photodiode will detect the laser beam bouncing while the tip scans the surface of the sample. (b) is the AFM apparatus used during this study.

In this work, a Dimension Fast Scan AFM of the company Bruker was used in tapping mode to characterize the surface morphology of the different films (Figure 5-4(b)). Silicon cantilevers (Fastscan-A) with a nominal tip radius of 5 nm and a spring constant of 18 $N.m^{-1}$ were used. The resonance frequency of the cantilevers was 1400 KHz. The images were analysed using the NanoScope Analysis software and Matlab code developed in the LCPO.

2. Electron microscopy

a) Scanning Electron Microscopy

The signals used by a scanning electron microscope (SEM) to produce an image result from interactions of the electron beam with atoms at various (small) depths within the sample. The observation can be performed in two different imaging modes: secondary electron imaging (SEI) and backscattered electron imaging (BSEI). SEI refers to the most common SEM mode, which is detection of secondary electrons emitted by surface atoms excited by the electron beam. By scanning the sample and collecting the emitted secondary electrons using a specific detector, an image displaying the topography of the surface is created. BSEI refers to backscattered electron imaging (Figure 5-5), which is formed using an optional backscattered electron detector and is mostly sensitive to the chemical contrast in the sample, with heavier and electron-rich elements scattering more, and appearing brighter in the images [5]. Consequently, in the case of our PDMSB-*b*-PS BCP, the PDMSB domains will appear brighter than the PS ones.

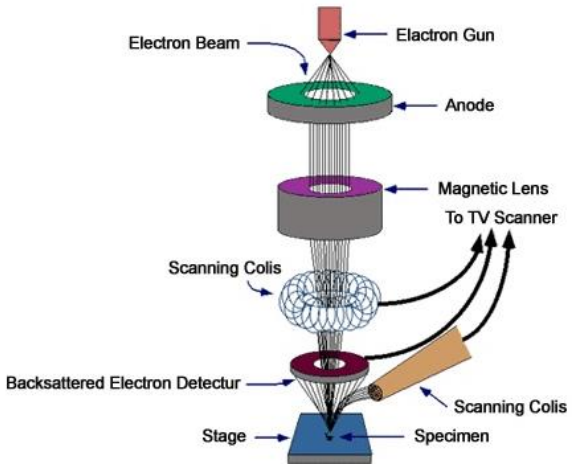

Figure 5-5: Schematic of the SEM principle.

During this study, a Jeol 7800-E Prime microscope at low acceleration voltage (1 kV) in the super high-resolution gentle beam mode (GBSH) was used to characterize the structure of the BCP nanostructure in the LCPO (Figure 5-6(a)). Gentle Beam (GB) is a technique of applying a bias voltage to the sample to reduce the speed of the incident electrons and increase the speed of the emitted electrons. The low acceleration voltages used in this study allows us to measure the samples without any metallization. On the other hand, a HITACHI H9300A microscope of the company Hitachi was used in CEA-LETI facilities (Figure 5-6(b)).

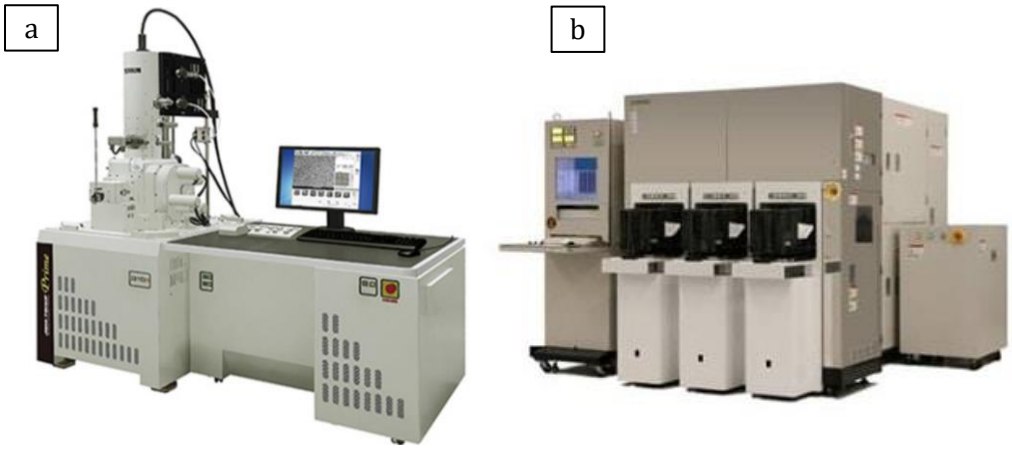

Figure 5-6: SEM apparatus used in this study. (a) is the Jeol microscope and (b) is the Hitashi microscope.

b) Focus Ion Beam- Scanning transmission electron microscopy

In order to investigate the structure of the BCP systems through the thickness of the film (multi-layer stacking in the Chapter 2 and in-plane lamellae-forming PDMSB-*b*-PS in the Chapter 3, we used the Focus Ion Beam- Scanning transmission electron microscopy (FIB-STEM) technic. The principle of transmission electron microscopy is based on the interactions of atoms within the sample and the electron beam transmitted through the it. STEM is a type of TEM. Indeed, in the STEM technic, the electron beam is focused to a fine spot (typically 0.05 nm – 0.2 nm) which is then scanned over the sample to form the image in the same way the conventional scanning electron microscopy is working. The resolution of the image is thus linked to the diameter of the electronic probe.

To allow the electrons to easily pass through the sample and obtain the highest transmitted signal, it is necessary to have a very thin sample. For this purpose, a slice of the film is extracted from the initial sample and thinned down using a Focused Ion Beam: the main steps are summarized in Figure 5-7.

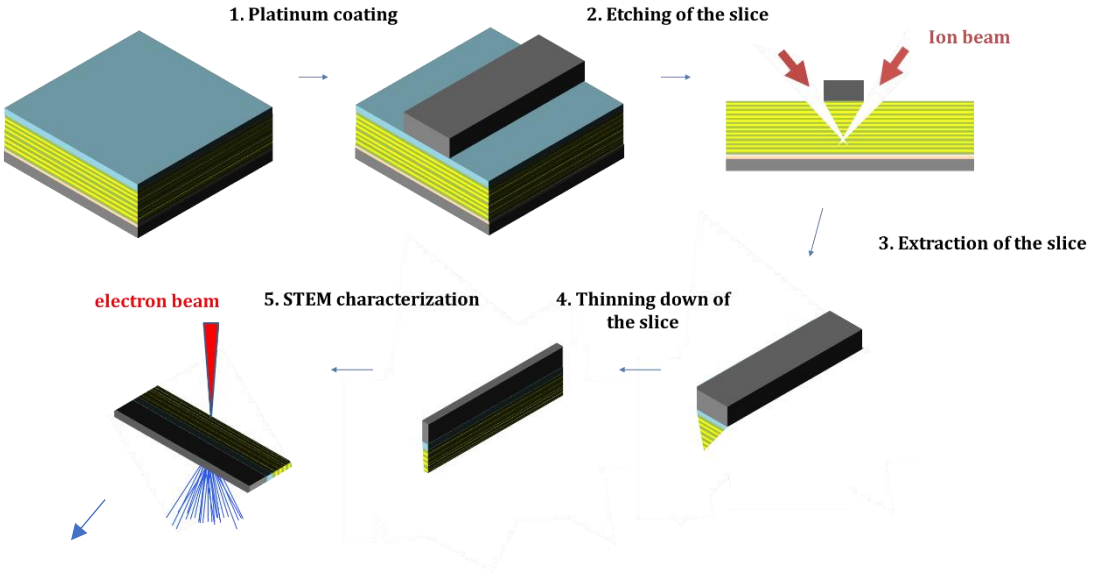

6. Resulting image:

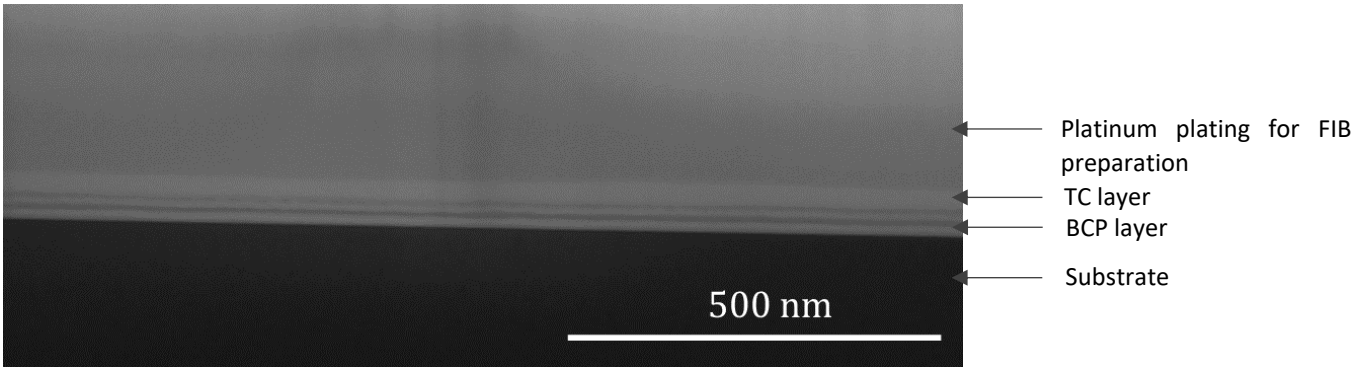

Figure 5-7: General procedure for FIB-STEM characterization. The main steps involve the protection of the areas of interest using a platinum coating followed by an etching of the slice using the ion beam and finally, the slice is thinning down to be characterized on a STEM grid.

IV. X-rays characterization

a) Small angle X-ray scattering

SAXS is a powerful technique enable to provide information about the dimensions and space group symmetry of a mesostructure. This method is particularly useful because it is non-destructive and provide statistical information of the whole probed sample. The technic is especially interesting in the study of BCP as it can probe the ~1-100 nm length scale (in a typical set-up) that is typically characteristic of BCP morphologies [6], [7].

The principle is based on the interaction between the oscillating incident X-ray radiations and the electrons of the material. Indeed, the electrons in the material placed in the X-ray beam will oscillate at the frequency of the incident X-rays. These oscillating electron clouds (namely scattering centers) will then emit spherical waves of radiation that propagate radially and thus scatter the incident X-rays. In the case the energies of the incident and scattered waves are equal, the scattering is said to be elastic. Only elastic scattering is discussed in this section as it does not carry any structure information. The basic scattering event of a single scattering center is illustrated in Figure 5-8. The wave vector of the incident and scattered radiation is rated as k_i and k_d, respectively.

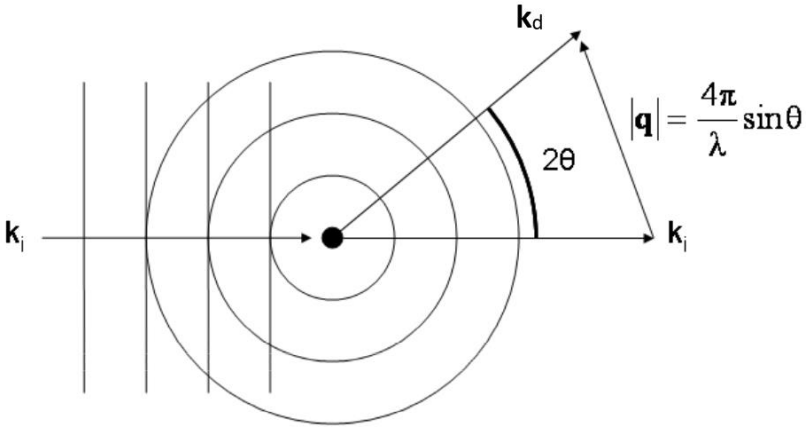

Figure 5-8: Schematic representation of the relationship between the incident plane wave k_i and the scattered spherical waves k_d. The scattering vector q is defined as the difference between the incident and scattered wave vectors k_d and k_i, respectively. Note that the emitted wave vectors are pointing radially from the scattering center in all directions (spherical waves) such that k_d is drawn arbitrarily [7].

As the scattering is elastic, the frequencies and amplitudes of the two waves are equal in elastic scattering events. The scattering vector q can thus be defined as the difference between the incident and scattered wave vectors: $\mathbf{q} = \mathbf{k}_d - \mathbf{k}_i$. This vector, q, represents the change in momentum incurred by the radiation due to the scattering event. If the angle between $\mathbf{k}_d$ and $\mathbf{k}_i$ is defined as 2θ, $|\boldsymbol{q}|$ can be defined as:

$$\textbf{(eq.5-1)} |\boldsymbol{q}| = \frac{4\pi}{\lambda} \sin\theta$$

where λ is the wavelength. It is well common to use this expression because it includes the scattering angle and the wavelength used in a given experiment.

If now, one considers more than one scattering center in a material, the superposition of the scattered waves leads to an interference pattern that depends on the arrangement of the atoms in the material. These interferences can be either constructive (if the scattered waves are in phase) or destructive (if the scattered waves are out of phase) depending on the distance between the scatters and on the observation angle, 2θ.

To understand how the scattering pattern provide structural information about the structure of the material, it is possible to simply describe the different scattering centers as semi-reflective planes, n, with an interplanar spacing *d* [7]. The Figure 5-9 depicts the pathway of an incident wave upon infinite series of semi-reflective planes. The reflection through the first plane (n=1) is interfered with by reflections from the other planes. Indeed, these reflections must travel an additional distance, 2.d.n.sinθ, to penetrate the layer n and reflect back to the reference plane (n=1) which result in a shift of the phase angle, φ, of 2.d.n.sinθ. This phase shift leads to destructive interference except δ is an integral multiple of the wavelength, a condition known as Bragg's Law: 2.d.sinθ = n.λ.

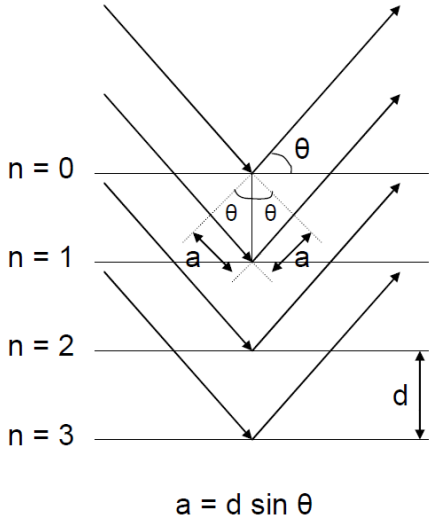

Figure 5-9: Scheme used to derive Bragg's Law. The scattering centers are defined as semi-reflective planes, n, with an interplanar spacing *d* [7].

Combining Bragg's Law with the magnitude of the scattering vector leads to:

$$\textbf{(eq.5-2)} |\boldsymbol{q}| = \frac{2n\pi}{d}$$

The Bragg's law applies to scattering from planes of atoms in a unit cell and will define the allowable reflections for a given space group. The unit cell for a perfect crystal describes the location of the scattering centers and can be represented using the lattice vector:

$$\textbf{(eq.5-3)}\ \boldsymbol{R_{hkl}} = \boldsymbol{R_0} + u\boldsymbol{a} + v\boldsymbol{b} + w\boldsymbol{c}$$

where $\mathbf{R_o}$ is the coordinate of scattering center o, the integers *u*, *v*, and *w* are basis coefficients, and **a**, **b**, and **c** are the basis vectors describing the unit cell.

The vector $\mathbf{R}_{hkl}$ can be used to determine the conditions that satisfy Bragg's Law as only specific distances between planes of atoms satisfy the Bragg criteria and allow scattering. To determine these specific distances, it is convenient to introduce the reciprocal space in order to recover the characteristic distances from the angle of the scattered waves.

The reciprocal lattice can thus be defined using the following vector:

$$\textbf{(eq. 5-4)}\ \boldsymbol{r}^* = h\boldsymbol{a}^* + k\boldsymbol{b}^* + l\boldsymbol{c}^*$$

where *h*, *k*, and *l* are the Miller indices describing a plane in the real space lattice and **a***, **b*** and **c*** the vectors reciprocal to the vectors **a**, **b**, and **c**. The magnitude of the reciprocal lattice vector can also be deduced and defined as:

$$\textbf{(eq.5-5)}\ |\boldsymbol{r}^*| = \sqrt{(h\boldsymbol{a}^* + k\boldsymbol{b}^* + l\boldsymbol{c}^*).(h\boldsymbol{a}^* + k\boldsymbol{b}^* + \boldsymbol{l}\boldsymbol{c}^*)} = \frac{1}{d_{hkl}}$$

where d_{hkl} are the distances between real space planes of atoms defined by *h*, *k*, and *l* that satisfy Bragg's Law. Finally, combining equations 5-2 and 5-5 leads to the expression for all $|q_{hkl}|$ that satisfy the Bragg criteria *i.e.* the positions at which the scattering peaks can appear for a given Bravais lattice:

$$\textbf{(eq.5-6)}\ |\boldsymbol{q_{hkl}}| = \frac{2\pi}{d_{hkl}} = 2\pi|\boldsymbol{r}^*|$$

These q_{hkl} values can be expressed using a series of Dirac delta functions that is known as the form factor ($F(q)$).

However, the form factor does not take into account the positions of the scatters within the unit cell. Indeed, the scattered wave of an atom will also be affected by the neighborhood. This additional contribution is called the structure factor (S(q)) as it contains information about the specific arrangements of the atoms within the unit cell. S(q) is the sum of the waves scattered by all the individual atoms:

$$\textbf{(eq.5-7)}\ S(q) = \sum_1^N f_n e^{2i\pi(h\boldsymbol{u_n}+k\boldsymbol{v_n}+l\boldsymbol{w_n})}$$

where f_n is the atomic scattering factor, and $\mathbf{u}_n$, $\mathbf{v}_n$, and $\mathbf{w}_n$ the coordinates of the atom within the unit cell. One can thus understand that the scattered wave of an atom can destructively interfere with the ones of the neighboring atoms if the arrangement of the atoms within the cell includes symmetry operations such as mirror planes, inversion center or screw axes. A structure factor of zero for specific *h*, *k*, and *l* values indicates the scattering peaks that will not be present for those Miller indices and lead to systematic extinctions even when the reflections satisfy the Bragg criteria.

Finally, the third factor that influences the scattering intensity of a material is the electronic contrast. Indeed, in the case of a A-*b*-B diblock copolymer, the A nanodomains embedded in a matrix of B must have an electron density different from the one of B in order to be visible in SAXS experiments otherwise, there would be no scattering even if reflections are permitted by the form and structure factors (other technic such as small-angle neutron scattering should thus be

investigated). The contrast scales as the square of the difference in electron densities between domains:

$$\textbf{(eq.5-8)}\ I(q) \propto (\rho_i - \rho_j)^2$$

where ρ_i and ρ_j the electron density of i and j, respectively.

To summarize, the form factor dictates the allowable reflections while the structure factor and contrast govern the relative intensities of the allowed peaks. Taking into account these three contributions to the scattering intensity lead consequently to the following equation:

$$\textbf{(eq.5-9)}\ I(q) \propto \left(\rho_i - \rho_j\right)^2 F(q)S(q)$$

In addition to the positional order, preferential orientation can also be developed within the material. In the case of crystals, only few grains are generally observed while BCPs contain distribution of randomly oriented grains. These latter are reflected by a 2D pattern[11] consisting in series of concentric rings with equal intensities having radius q_{hkl}. By performing an azimuthal integration of these 2D patterns, one can reduce the data to plot the scattered intensity as a function of q. The resulting plot result in a succession of peaks at q_{hkl} allowed by the form factor, with the intensities dictated by the structure factor, contrast, and long-range mesostructural order (Figure 5-10).

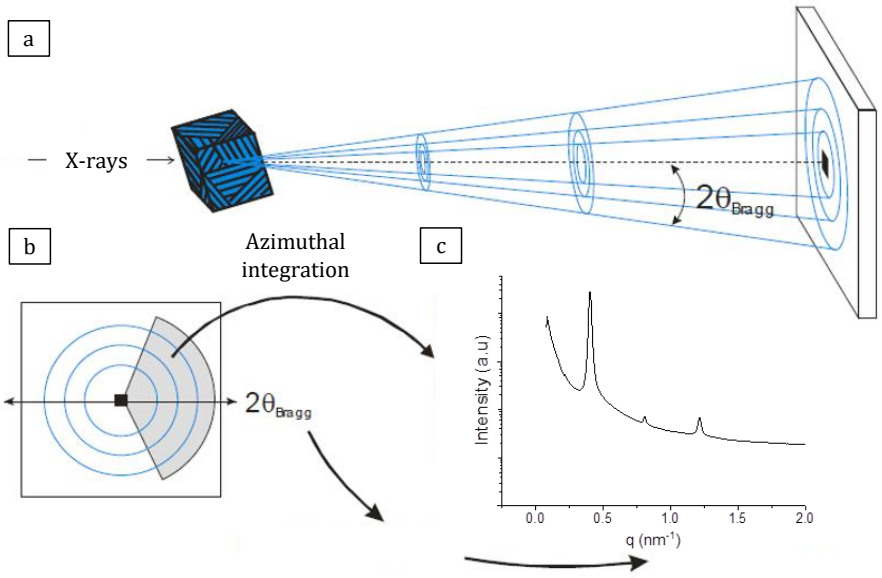

Figure 5-10: Scheme of a typical SAXS experiment that allows to recover the characteristic 1D pattern of the structure of the probed material [8].

[11] The scattering intensity is measured radially in a circle close to the primary beam.

Finally, to determine the BCP nanostructures, the positions of the peaks can be compared to the allowed positions of given space group symmetries. To determine the values, the magnitude of the reciprocal lattice vector is determined using the unit cell parameters of the space group. The allowable q_{hkl} for the given space group is then deduced by replacing $|\boldsymbol{r}^*|$ in the equation 5-6. Table 5-1 summarizes the allowable q_{hkl} values of the commonly encountered space groups in BCP systems.

Table 5-1: Allowed reflections for certain BCP morphologies.

Morphology	Space group	q_{hlk}/q_{001}
Lamellae	$\bar{1}$	1, 2, 3, 4, 5, …
BCC	$Im\bar{3}m$	$\sqrt{2}, \sqrt{4}, \sqrt{6}, \sqrt{8}, \sqrt{10}$, …
Hexagonal cylinders	$P\bar{6}$nm	$\sqrt{1}, \sqrt{3}, \sqrt{4}, \sqrt{7}, \sqrt{9}$, …
Gyroid	$Ia\bar{3}d$	$\sqrt{6}, \sqrt{8}, \sqrt{14}, \sqrt{16}, \sqrt{20}$, …

The domains spacings that are accessible in a scattering experiment depends on λ and θ (equations 5-1 and 5-2). In this work, the majority of the SAXS experiments presented in the Chapter 2 were performed on the Dutch-Belgian Beamline (DUBBLE) at the European Synchrotron Radiation Facility (ESRF) station BM26B in Grenoble [9]. The energy of the x-ray beam was 11 keV, which corresponds to a wavelength of 1.127 Å. One experiment was performed at the Centre de Recherche Paul Pascal using the Xeuss 2.0 (provided by XENOCS). The X-rays are generated with a Cu-Kα source. The energy of the x-ray beam was 8 keV, which corresponds to a wavelength of 1.549 Å in such way that the angle of observation θ~5° to access the 5-50 nm length scale. In practice, the observation angle is adjusted by changing the sample-to-detector distance which allows to vary the q range for the targeted domain spacings.

b) Grazing-incidence Small angle X-ray scattering

GISAXS is a surface-sensitive scattering technique used to probe the nanostructure of thin films. It is a powerful technic for the study of BCP nanostructures as it gives statistical information about the morphology as well as its orientation through the thickness of the film.

The concepts previously described are still applicable except that in GISAXS experiments, the geometry is in reflection mode (while in SAXS it is a transmission mode). Indeed, the incident beam hit the sample with a grazing-incidence angle carefully controlled using a sample-tilt stage and is typically on the order of 0.05° to 0.50°. At these angles, the X-ray beam is efficiently reflected off the sample or substrate surfaces. In order to limit the penetration of the X-rays to the probed film (and not the substrate), the choice of the incident angle is crucial. The critical angle is the angle below which the material becomes totally reflecting which means that the X-rays cannot penetrate the surface of the sample. Consequently, to penetrate the BCP film without penetrating the silicon substrate, the incident angle has to be comprised between the one of the BCP and the one of the silicon substrate. In practice, the incident angle is kept close to the critical angle of the studied BCP system. The critical angle of a material can be either calculated (as it depends on the refractive index of the material, intrinsic to the material) or determined via X-rays reflectivity [6]. For the GISAXS experiment performed on a gyroid-forming PDMSB-*b*-PS in thin film (Chapter 2), the incidence angle was set in the range of 0.1° – 0.14°, which is between the critical angle of the PDMSB-*b*-PS film and the silicon. The experiment was performed on the Dutch-Belgian Beamline at the ESRF station BM26B in Grenoble.

The scattering from the sample is recorded in the ($\mathbf{q_y}$, $\mathbf{q_z}$) plane where $\mathbf{q_y}$ and $\mathbf{q_z}$ are the components of the scattering vector, $\mathbf{q}$ as shown the Figure 5-11 [10]. The structure of the BCP film was then deduced by fitting the scattering pattern with the GIXSGUI matlab code developed by Jiang [11].

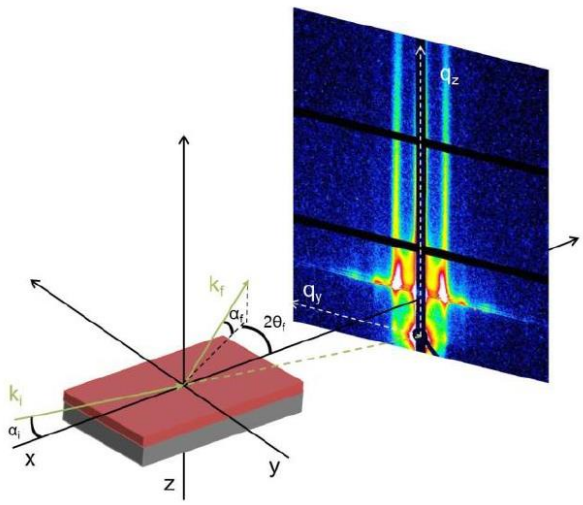

$$q_y = \frac{2\pi}{\lambda}\left[sin(2\theta_f)\,cos(\alpha_f)\right]$$

$$q_z = \frac{2\pi}{\lambda}\left[sin\left(\alpha_f\right) + sin(\alpha_i)\right]$$

Figure 5-11: Schematic representation of GISAXS geometry. The scattering from the sample is then recorded with a two-dimensional X-ray detector. The position of a point on the detector is defined by q_y and q_z which are the components of the scattering vector, q. α_i is the incident beam angle along the vertical direction, $2\theta_f$ and α_f are the scattered beam angles along the horizontal and vertical directions, respectively [10].

V. References

[1] F. D. Egitto, “Plasma etching and modification of organic polymers”, *Pure and Applied Chemistry*, vol. 62, nº 9, p. 1699-1708, janv. 1990.

[2] L. A. Pederson, “Structural Composition of Polymers Relative to Their Plasma Etch Characteristics”, *Journal of The Electrochemical Society*, vol. 129, nº 1, p. 205, 1982.

[3] P. Bézard, “Développement de procédés de gravure plasma innovants pour les technologies sub-14 nm par couplage de la lithographie conventionnelle avec l’approche auto-alignée par copolymère à blocs”, LABORATOIRE DES TECHNOLOGIES DE LA MICROELECTRONIQUE, 29-janv-2016.

[4] R. Ramos, “Interactions entre les plasmas de gravure à couplage inductif et les parois du réacteur”, LABORATOIRE DES TECHNOLOGIES DE LA MICROELECTRONIQUE, 29-sept-2008.

[5] J. A. Venables et C. J. Harland, “Electron back-scattering patterns—A new technique for obtaining crystallographic information in the scanning electron microscope”, *Philosophical Magazine*, vol. 27, nº 5, p. 1193-1200, mai 1973.

[6] H. Schnablegger et Y. Singh, *The SAXS Guide: : Getting acquainted with the principles.*, 3rd éd. Anton Paar GmbH, 2013.

[7] A. J. Meuler, “Network Morphologies in Monodisperse and Polydisperse Multiblock Terpolymers”, University of Minnesota, 2009.

[8] T. H. Epps, “Locating network phases in linear ABC triblock copolymers.”, University of Minnesota, 2004.

[9] W. Bras *et al.*, “Recent experiments on a small-angle/wide-angle X-ray scattering beam line at the ESRF”, *Journal of Applied Crystallography*, vol. 36, nº 3, p. 791-794, juin 2003.

[10] P. Andreazza, “Probing nanoalloys structure and morphology by x-ray scattering and absorption methods.”, in *Nanoalloys : Synthesis, Structure & Properties.*, 1re éd., Springer-Verlag London, 2012, p. 412.

[11] Z. Jiang, “*GIXSGUI* : a MATLAB toolbox for grazing-incidence X-ray scattering data visualization and reduction, and indexing of buried three-dimensional periodic nanostructured films”, *Journal of Applied Crystallography*, vol. 48, nº 3, p. 917-926, juin 2015.

Titre : Stratégies d'auto-assemblage dirigé pour le contrôle de l'orientation de domaines de copolymères à blocs en lithographie avancée

Résumé : L'objectif de ce travail était de mettre en évidence le potentiel du PDMSB-*b*-PS pour des applications en nanolithographie avancée. Pour cela, nous avons fourni une compréhension du comportement d'auto-assemblage du PDMSB-*b*-PS en masse et en film mince. Nous avons réalisé l'auto-assemblage de ce copolymère semi-cristallin en cylindre et gyroïde bien définis avec des périodicités inférieures à 20 nm grâce à un paramètre d'interaction de Flory-Huggins élevé (Chapitre 2). Nous avons par la suite proposé une approche pour obtenir des lamelles perpendiculaires du PDMSB-*b*-PS en film mince grâce à l'utilisation de sur-couches neutres réticulables. La polyvalence de cette approche a été démontrée à l'aide de CPBs de masses moléculaires différentes et s'est ensuite étendue à la formation d'empilements *via* un processus d'auto-assemblage itératif (chapitre 3). Enfin, nous avons réticulé la sur-couche neutre à l'aide d'agents photo-sensibles ce qui nous a permis d'obtenir un motif par photolithographie au-dessus du film CPB. Ainsi, il a été possible de contrôler l'orientation du CPB à des endroits spécifiques du film (Chapitre 4).

Mots clés : Auto-assemblage – Copolymères à blocs – Lithographie – Haut-χ

Title: Directed self-assembly strategies for orientation-controlled block copolymers for advanced lithography

Abstract: The objective of our work was to highlight the potential of the high-χ PDMSB-*b*-PS BCP for advanced nanolithography applications. For this purpose, we have demonstrated the ability of our system to self-assemble into well-defined nanostructures in bulk and we have performed the self-assembly of cylinder- and gyroid-forming PDMSB-*b*-PS BCPs in thin film using industrially-friendly processes (Chapter 2). With the aim of controlling the out-of-plane orientation of lamellar-forming PDMSB-*b*-PS BCPs in thin film, we have proposed an innovative approach relying on the use of crosslinkable neutral TC layers. The versatility of this approach was demonstrated using BCPs having different macromolecular characteristics and extended to the formation of multi-layer stacks through an iterative self-assembly process (Chapter 3). Taking advantage of the crosslinking ability of our TC material, we have outlined the patterning ability of the TCs using photosensitive crosslinking agents. The patterning of neutral TCs above the lamellar-forming PDMSB-*b*-PS BCPs further allowed a control of the orientation of the PDMSB-*b*-PS domains in specific areas of the film (Chapter 4).

Keywords: Self-assembly - Block copolymers – Lithography - High-χ

Unité de recherche

Laboratoire de Chimie des Polymères Organiques (LCPO), UMR 5629,
Bâtiment B8, Allée Geoffroy Saint Hilaire, 33615 Pessac Cedex, France